

UNIVERSITY OF PRETORIA
DEPARTMENT OF CIVIL ENGINEERING

INVESTIGATING CAVITY
PROPAGATION IN DENSE SAND
USING CENTRIFUGE TRAPDOOR
EXPERIMENTS

October 2017

**INVESTIGATING CAVITY PROPAGATION TO THE
SURFACE THROUGH CENTRIFUGE TRAPDOOR
EXPERIMENTS**

BENJAMIN MATTHYS BEUKES OBERHOLZER

**A project report submitted in partial fulfilment of the requirements for the degree of
MASTERS OF ENGINEERING (GEOTECHNICAL ENGINEERING)**

**In the
FACULTY OF ENGINEERING
UNIVERSITY OF PRETORIA**

October 2017

INVESTIGATING CAVITY PROPAGATION TO THE SURFACE THROUGH CENTRIFUGE TRAPDOOR EXPERIMENTS

BMB OBERHOLZER

Supervisor: Professor SW Jacobsz
Department: Civil Engineering
University: University of Pretoria
Degree: Masters of Engineering (Geotechnical Engineering)

The theory of soil arching can aid a study into the field of sinkhole development to enable researchers to understand possible mechanisms that may mobilise in the overburden material when existing underground cavities propagate to the surface to ultimately manifest as sinkholes. An understanding of these failure mechanisms could lead to improved estimations of the likely sinkhole diameter which is required for the design of infrastructure in sinkhole-prone environments. Current methods for the estimation of sinkhole size are very conservative, leading to an over-prediction of sinkhole size, often rendering sinkhole-prone land too costly to develop. A need exists for improved guidelines to assess probable sinkhole size which should eventually culminate in less stringent building regulations in sinkhole-prone environments.

Preliminary studies indicated that cavities propagate upwards in a near-vertical fashion, raising questions about the conical funnel-shape as suggested by current building regulation for dolomitic areas in South Africa. This prompted further investigation. Plane-strain deep trapdoor experiments were performed using two different grades of silica sand (a fine and coarse sand) in which active displacement of a trapdoor underneath the soil was modelled to simulate progressive failure of cavity walls and roof. These experiments were performed under dry and moist conditions with varying trapdoor widths and were carried out in a geotechnical centrifuge. Photographs of the models were analysed using Particle Image Velocimetry (PIV) to produce plots of displacement and strain that indicated the geometry of failure mechanisms in the overburden material as the trapdoor displacement increased. Surface settlements were also measured during the experiments using a combination of LVDT surface readings and PIV analyses. These results were compared to form an understanding of the influence of the said variables on failure mechanisms and surface settlement.

Zones of influence above trapdoors in all tests tended to propagate vertically upwards rather than in a funnel shape. Surface settlement initially tended to follow a Gaussian shape, but rapidly deepened once

the influence zone above the trapdoor (failure mechanism) reached the soil surface so that the Gaussian shape was no longer accurate. The trapdoor size tended to have very little effect on the general failure mechanism, but the propagation of the zone of influence above the trapdoor did advance more rapidly towards the surface when considering surface settlement versus normalised trapdoor settlement. The spatial frequency of shear zone formation in the sand was found to be related to the trapdoor width, with narrow trapdoors resulting in a denser shear band spacing. Increased trapdoor widths resulted in more symmetric shear zone formation.

DECLARATION

I, the undersigned hereby declare that:

- I understand what plagiarism is and I am aware of the University's policy in this regard;
- The work contained in this report is my own original work;
- I did not refer to work of current or previous students, lecture notes, handbooks or any other study material without proper referencing;
- Where other people's work has been used this has been properly acknowledged and referenced;
- I have not allowed anyone to copy any part of my report;
- I have not previously in its entirety or in part submitted this report at any university for a degree.

Benjamin Matthys Beukes Oberholzer

Student nr: 29136858

2 October 2017

ACKNOWLEDGEMENTS

This dissertation was made possible by the assistance of various persons and organizations. I wish to express my sincere appreciation and thanks to the following:

- a) First and foremost, My Lord and Saviour for strength, wisdom, guidance and the incredible opportunity.
- b) My supervisor, Prof. SW Jacobsz for his enthusiasm, motivation, guidance and continued support throughout this project. This man is an incredible geotechnical engineer with an immense knowledge and understanding of the field and I would not have been able to complete this dissertation without his guidance.
- c) My fiancée and love of my life, Lee-Anne Visagie, for her continued support, motivation and words of encouragement throughout the process.
- d) My father, Pieter Oberholzer, for his financial assistance, practical advice and motivation in times of hardship.
- e) My close family for their support throughout the study.
- f) Ruhann Steyn for his friendship, motivation, support, and for proof-reading my dissertation.
- g) The head of the Civil Engineering Department of the University of Pretoria at the time, Prof. Elsabe Kearsley, for her assistance and guidance regarding the centrifuge.
- h) The staff of the Civil Laboratory at the University of Pretoria – Mr. Johan Scholtz for creating and assembling the test frame, Mr. Jurie van Staden for assistance with geotechnical lab tests, Mr. Rikus Kock for his invaluable advice regarding electronics, and also Mrs. Jenny Callanan and Mrs. Vanessa Doman for assistance with lab equipment and procurement.
- i) Mr. W.A. Take and Mr. D.J. White for the use of their Particle Image Velocimetry (PIV) software, GeoPIV.
- j) The Civil Engineering Department of the University of Pretoria in general for the use of equipment, office space and other resources required to complete this dissertation.

TABLE OF CONTENTS

1	INTRODUCTION	1-1
1.1	Background	1-1
1.2	Objectives of the Study	1-2
1.3	Scope of the Study	1-2
1.4	Methodology	1-3
1.5	Organization of the Report	1-3
2	LITERATURE REVIEW	2-1
2.1	Dolomite	2-1
2.1.1	Composition of Dolomite	2-1
2.1.2	Weathering of Dolomite	2-2
2.1.3	Dolomite Land	2-4
2.1.4	Regions of Occurrence in South Africa	2-4
2.1.5	Human Settlement on Dolomite Land in South Africa	2-5
2.2	Sinkholes	2-6
2.2.1	Types of Sinkholes	2-6
2.2.2	Conditions Necessary for Sinkhole Formation	2-8
2.2.3	Shape and Size of Sinkholes	2-9
2.2.4	Quantification of Sinkhole Risk	2-12
2.2.5	Codes of Practice in South Africa	2-13
2.2.6	Previous Studies on Sinkhole Stability Charts	2-14
2.3	Soil Arching	2-16
2.3.1	Technical Definition of Soil Arching	2-16
2.3.2	Classical Arching Theory	2-18
2.3.3	Typical Results of Physical Trapdoor Studies	2-24
2.4	Remaining Questions	2-40
3	EXPERIMENTAL METHOD	3-1
3.1	Introduction	3-1
3.2	Geotechnical Centrifuge	3-1
3.3	Centrifuge Test Package	3-4
3.3.1	Test Frame	3-4
3.3.2	False Floor	3-7
3.3.3	Trapdoor Mechanism	3-8
3.3.4	Measurement of Trapdoor Settlement	3-12
3.3.5	Measurement of Surface Settlement	3-14
3.3.6	Introduction of Moisture	3-15
3.3.7	Calibration of Instruments	3-16
3.3.8	Data Acquisition and Photographic Equipment	3-18
3.4	Material properties	3-20
3.4.1	Particle Size Distribution	3-21
3.4.2	Density	3-23
3.4.3	Specific Gravity	3-23
3.4.4	Strength Parameters from Triaxial Tests	3-24
3.5	Model Preparation	3-27
3.5.1	Preparation of the Test Frame and Trapdoor System	3-27
3.5.2	Sand placement	3-28
3.5.3	Preparation of Centrifuge	3-30
3.5.4	Centrifuge Acceleration and Lowering of the Trapdoor	3-30

3.5.5	Post-experiment Procedures	3-31
3.5.6	Test schedule	3-32
3.6	Particle Image Velocimetry	3-34
3.6.1	Introduction	3-34
3.6.2	GeoPIV Software	3-34
3.6.3	Analysis Technique	3-35
3.6.4	Cleaning of Data	3-40
3.6.5	Calibration and Correcting for Parallax	3-41
3.6.6	Displacement and Strain Plots	3-42
4	RESULTS AND DISCUSSIONS	4-1
4.1	Introduction	4-1
4.2	Settlement of Trapdoor	4-1
4.3	Presentation and Discussion of Results	4-2
4.3.1	Test 1DC – Dry Coarse Sand	4-4
4.3.2	Test 2MC – Moist Coarse Sand	4-19
4.3.3	Test 3DF – Dry Fine Sand	4-26
4.3.4	Test 4MF-50 – Moist Fine Sand with 50mm Trapdoor	4-38
4.3.5	Test 5MF-75 – Moist Fine Sand with 75mm Trapdoor	4-46
4.3.6	Test 6MF-100 – Moist Fine Sand with 100mm Trapdoor	4-54
4.4	Comparison of Shear Behaviour in Various Conditions	4-62
4.4.1	Comparison Between Coarse and Fine Material	4-62
4.4.2	Comparison Between Dry and Moist Material	4-65
4.4.3	Comparison Between Different Trapdoor Widths	4-70
4.5	Progression of Failure Mechanisms	4-72
4.6	Discussion on Surface Settlement	4-73
4.7	Implications for Actual Sinkholes	4-74
5	CONCLUSIONS AND RECOMMENDATIONS	5-1
5.1	Conclusions	5-1
5.2	Recommendations	5-3
6	REFERENCES	6-1

LIST OF FIGURES

Figure 1-1: Method of determining maximum potential development space (SABS, 2012; Buttrick & Van Schalkwyk, 1995).....	1-1
Figure 2-1: Dolomite as a mineral (King, 2017).....	2-1
Figure 2-2: Dolomite as a rock (King, 2017).....	2-2
Figure 2-3: Small-scale example of pinnacle dolomite rock (Richardson, 2013).....	2-3
Figure 2-4: Distribution of major dolomitic groups in South Africa (Wagener, 1984).....	2-4
Figure 2-5: Location of carbonate rocks in South Africa (SABS, 2012).....	2-5
Figure 2-6: Types of sinkholes (Nel and Haarhoff, 2011).....	2-7
Figure 2-7: Shapes of a sinkhole (adapted from Hyatt et al. (1996)).....	2-9
Figure 2-8: Geometry forms associated with whole number VRI values (Hyatt et al., 1996).....	2-10
Figure 2-9: Sinkhole forming within confines of MPS (Buttrick & Van Schalkwyk, 1995).....	2-11
Figure 2-10: Determining MPS using the scenario supposition method (Buttrick and Van Schalkwyk, 1995).....	2-13
Figure 2-11: Shape of failure in cemented sand layers where (a) $H_c/D < 0.25$, (b) $H_c/D = 0.25$ and (c) $H_c/D > 0.31$ (Abdulla & Goodings, 1996).....	2-14
Figure 2-12: Dimensionless stability chart (Abdulla & Goodings, 1996).....	2-15
Figure 2-13: Stability chart showing effects of friction angle (Drumm et al., 2009).....	2-15
Figure 2-14: Pressure distributions in (a) active arching vs. (b) passive arching (Evans, 1983).....	2-17
Figure 2-15: Stress distribution in soil above a yielding base (Bierrum, et al., 1972; Revised by Evans, 1983).....	2-17
Figure 2-16: Typical setup of a trapdoor experiment.....	2-18
Figure 2-17: Results of Terzaghi's trapdoor experiment, normalized vertical force on trapdoor against normalized displacement of trapdoor (Terzaghi, 1936; Revised by Evans, 1983).....	2-19
Figure 2-18: Results of Terzaghi's trapdoor experiment: horizontal and vertical stresses in the soil above the trapdoor at various stages of trapdoor displacement (Terzaghi, 1936; Revised by Evans, 1983).....	2-20
Figure 2-19: Coefficient of lateral earth pressure in trapdoor experiment (Terzaghi, 1936; Revised by Evans, 1983).....	2-21
Figure 2-20: Assumed vs. actual sliding surfaces in a soil mass above a yielding trapdoor (Terzaghi, 1943).....	2-22
Figure 2-21: Free body diagram of a slice of soil in the yielding zone (Terzaghi, 1943).....	2-22
Figure 2-22: Derivation of K_K as a coefficient of lateral earth pressure (Iglesia et al. 1991).....	2-23
Figure 2-23: Normalized stress vs. trapdoor displacement for various H/B ratios (Ladanyi & Hoyaux, 1969).....	2-25
Figure 2-24: Normalized stress vs. trapdoor displacement (Evans, 1983).....	2-25
Figure 2-25: Typical loading vs. trapdoor displacement plot (Iglesia et al., 2014).....	2-26

Figure 2-26: Comparison of load-displacement curves of several H/B ratios (Iglesia et al., 2014) ..	2-27
Figure 2-27: Different behaviour of trapdoor tests above and below an H/D ratio of 2 (Dewoolkar, 2007)	2-27
Figure 2-28: Comparison of trapdoor load readings across several H/B ratios (Iglesia et al. 2014) ..	2-28
Figure 2-29: (a) Failure mechanism (with camera moving simultaneously with trapdoor) (Ladanyi & Hoyaux, 1969) and (b) Failure mechanism after large trapdoor displacements (Vardoulakis et al. (1981))	2-29
Figure 2-30: Comparison of pressure distributions above a trapdoor as measured by (a) Evans (1983) and (b) Harris (1974) (after Evans (1983))	2-30
Figure 2-31: Three phases of failure mechanisms observed by Chevalier et al. (2009)	2-30
Figure 2-32: Three phases of failure mechanisms observed by Iglesia et al. (2014)	2-31
Figure 2-33: Comparison of dilation angle with depth for soils of various relative densities (D_r)....	2-32
Figure 2-34: Shear band propagation at (a) single gravity and (b) in a centrifuge at 75g (Dewoolkar, 2007)	2-33
Figure 2-35: Schematic of propagation of shear bands above an active trapdoor (Costa et al., 2009) ..	2-33
Figure 2-36: Shear bands of tests with similar ratios of trapdoor settlement (Δ_B) to D_{50} (Stone, 1988)	2-34
Figure 2-37: Normal curve resembling the shape of a settlement trough (Peck (1969) revised by Evans (1983))	2-36
Figure 2-38: Shape of a settlement trough compared to a normal curve (Evans, 1983)	2-36
Figure 2-39: Gaussian curve resembling the shape of a settlement trough (Costa et al., 2009)	2-37
Figure 2-40: Surface depressions in (a) single gravity and (b) in a centrifuge at 75g (Dewoolkar, 2007)	2-37
Figure 2-41: Relationship between graphs of (a) surface settlement to trapdoor displacement, and (b) trapdoor load to trapdoor displacement, with increasing trapdoor displacement (Dewoolkar, 2007) ...	2-38
Figure 2-42: Typical maximum shear strain distributions in sand above a trapdoor at incremental trapdoor displacements (Stone, 1992)	2-39
Figure 2-43: Plots of vertical strain (ϵ_z) for three stages during a trapdoor test performed at 45g acceleration (Costa et al., 2009)	2-40
Figure 3-1: (a) Relationship of shear modulus to shear strain and shear stress and (b) non-linear behaviour of shear-modulus at small strains	3-1
Figure 3-2: Geotechnical centrifuge at the University of Pretoria	3-3
Figure 3-3: Top view of test frame (no sand loaded)	3-5
Figure 3-4: Front view of test frame (no sand loaded)	3-5

Figure 3-5: Schematic of test frame	3-6
Figure 3-6: Front view of test frame (with sand loaded)	3-7
Figure 3-7: False floor with trapdoor mechanism.....	3-8
Figure 3-8: Trapdoor mechanism used in tests 1 and 2	3-9
Figure 3-9: Trapdoor mechanism (with load cell) used in tests 3 through 6	3-10
Figure 3-10: Piston 2 connected to stepper motor	3-11
Figure 3-11: Trapdoor plumbing network	3-12
Figure 3-12: Pressure transducer (from O'Brien, 2013)	3-12
Figure 3-13: Back view of test frame and positioning of LVDTs tracking trapdoor settlement	3-13
Figure 3-14: Image of Solartron Amatek S015.0 LVDT (LVDT 1).....	3-14
Figure 3-15: Arrangement of surface settlement LVDTs above sand body	3-15
Figure 3-16: Perforated pipe on layer of Bidim, used to introduce moisture to the sample	3-15
Figure 3-17: LVDT calibration rig.....	3-16
Figure 3-18: Voltage against displacement readings of LVDT 1, used in calibration procedures	3-17
Figure 3-19: Voltage against pressure readings of pressure transducer, used in calibration procedure	3-17
Figure 3-20: Digital data acquisition ports for the Digidaq system	3-18
Figure 3-21: Canon EOS 100D camera used to capture images of soil deformation	3-19
Figure 3-22: Actual image captured, used to illustrate parallax	3-19
Figure 3-23: Physical appearance of (a) Cullinan sand and (b) Consol sand	3-20
Figure 3-24: Particle size distribution of Cullinan sand (Archer, 2014) and Consol sand.....	3-21
Figure 3-25: Classification of typical particle size ranges (Knappett & Craig, 2012).....	3-22
Figure 3-26: Consolidation curve of 20% RD 200eff test on Cullinan sand (Archer, 2014).....	3-24
Figure 3-27: Consolidation curve of 100% RD 450eff for Consol sand.....	3-25
Figure 3-28: Stress paths of Cullinan sand at 80% D_r at various effective stresses (Archer, 2014) ..	3-26
Figure 3-29: Stress paths of Consol sand at 100% D_r at various effective stresses	3-26
Figure 3-30: Sand being pluviated from a hopper into test frame	3-29
Figure 3-31: Principles of PIV analysis (from White & Take, 2002).....	3-35
Figure 3-32: Finding displacement vector using PIV by (a) determining a correlation plane, (b) enlarging the peak of the correlation plane and (c) fitting a cubic function over the peak (White et al., 2003)	3-36
Figure 3-33: PIV precision against patch size (White et al., 2003)	3-37
Figure 3-34: Typical mesh used in PIV analysis	3-37
Figure 3-35: Illustration of leapfrog parameter (grey blocks represent updated reference images) ..	3-39
Figure 3-36: Error induced in horizontal displacements by various leapfrog parameters	3-40
Figure 3-37: Typical vector displacement field	3-41
Figure 4-1 Settlement of trapdoor with time during Test 3DF	4-1

Figure 4-2: First analysed photo of Test 1DC.....	4-5
Figure 4-3 Upwards movement of the zone of influence.....	4-8
Figure 4-4 Progression of failure mechanisms	4-9
Figure 4-5: Settlement plots of test 1DC	4-10
Figure 4-6: Distribution of total maximum shear strain above the trapdoor showing the location of selected points 1 to 4 in Test 1DC	4-11
Figure 4-7: Total maximum shear strain of points 1 to 4 in Test 1DC (entire strain spectrum)	4-12
Figure 4-8: Total maximum shear strain of points 1 to 4 in Test 1DC (small strains)	4-12
Figure 4-9: Distribution of total maximum shear strain above the trapdoor showing the location of selected points 6 to 10 in Test 1DC	4-13
Figure 4-10: Total maximum shear strain of points 6 to 10 in Test 1DC (entire strain spectrum) ...	4-14
Figure 4-11: Total maximum shear strain of points 6 to 10 in Test 1DC (small strains)	4-14
Figure 4-12: Distributions of volumetric strains at the end of Test 1DC.....	4-16
Figure 4-13: Surface settlement distribution of Test 1DC.....	4-17
Figure 4-14: Ratio of normalized surface settlement against normalized trapdoor settlement during Test 1DC	4-18
Figure 4-15: Moisture content with soil depth (Test 2MC)	4-20
Figure 4-16: First analysed photo of Test 2MC	4-20
Figure 4-17: Settlement plots of test 2MC.....	4-24
Figure 4-18: Surface settlement distribution of Test 2MC	4-25
Figure 4-19: Ratio of normalized surface settlement against normalized trapdoor settlement during Test 2MC	4-25
Figure 4-20: First analysed photo of Test 3DF	4-27
Figure 4-21 Possible shear band locations in (a) fine vs. (b) coarse sand.....	4-30
Figure 4-22: Settlement plots of Test 3DF.....	4-31
Figure 4-23: Distribution of maximum shear strain above the trapdoor showing the location of selected points 1 to 5 in Test 3DF.....	4-32
Figure 4-24: Maximum shear strain of points 1 to 5 in Test 3DF (entire strain spectrum)	4-33
Figure 4-25: Maximum shear strain of points 1 to 5 in Test 3DF (small strains).....	4-33
Figure 4-26: Distribution of maximum shear strain above the trapdoor showing the location of selected points 6 to 10 in Test 3DF.....	4-34
Figure 4-27: Maximum shear strain of points 6 to 10 in Test 3DF (entire strain spectrum)	4-35
Figure 4-28: Maximum shear strain of points 6 to 10 in Test 3DF (small strains).....	4-35
Figure 4-29 Surface settlement distribution of Test 3DF.....	4-36
Figure 4-30 Surface settlement (LVDT bank) - Test 3DF.....	4-37
Figure 4-31: Ratio of normalized surface settlement to normalized trapdoor settlement during Test 3DF	4-37

Figure 4-32: Moisture content with soil depth (Test 4MF-50)	4-39
Figure 4-33: First analysed photo of Test 4MF-50	4-39
Figure 4-34: Images illustrating visible dilation along shear bands	4-40
Figure 4-35: Settlement plots of Test 4MF-50.....	4-44
Figure 4-36: Surface settlement distribution of Test 4MF-50	4-45
Figure 4-37: Ratio of normalized surface settlement against normalized trapdoor settlement during Test 4MF-50	4-45
Figure 4-38: Moisture content with soil depth (Test 5MF-75)	4-47
Figure 4-39: First analysed photo of Test 5MF-75	4-47
Figure 4-40: Settlement plots of Test 5MF-75.....	4-51
Figure 4-41: Surface settlement distribution for Test 5MF-75	4-52
Figure 4-42: Surface settlement (LVDT bank) - Test 5MF-50.....	4-53
Figure 4-43: Ratio of normalized surface settlement against normalized trapdoor settlement during Test 5MF-75	4-53
Figure 4-44: Moisture content with soil depth (Test 6MF-100)	4-55
Figure 4-45: First analysed photo of Test 6MF-100.....	4-55
Figure 4-46: Settlement plots of Test 6MF-100.....	4-59
Figure 4-47: Surface settlement distribution of Test 6MF-100	4-60
Figure 4-48: Surface settlement (LVDT bank) - Test 6MF-100.....	4-61
Figure 4-49: Ratio of normalized surface settlement against normalized trapdoor settlement during Test 6MF-100	4-61
Figure 4-50: Comparison of normalized settlement between coarse and fine conditions in dry material	4-64
Figure 4-51: Comparison of normalized settlement between coarse and fine conditions in moist material	4-65
Figure 4-52: Comparison of normalized settlement between dry and moist conditions in coarse material	4-67
Figure 4-53: Mohr circle diagram of the strength of a cavity roof	4-69
Figure 4-54: Comparison of normalized settlement between dry and moist conditions in fine material	4-69
Figure 4-55: Comparison of normalized settlement between tests with different trapdoor widths in moist fine material	4-71
Figure 4-56: Summary of failure mechanisms as the sinkhole propagates to the surface	4-72
Figure 4-57: Comparison of normalized surface settlement across all tests	4-73

LIST OF TABLES

Table 2-1: Sinkhole size and their classification (Buttrick & Van Schalkwyk, 1995)	2-11
Table 3-1: Applicable centrifuge scaling factors (Taylor, 1995).....	3-2
Table 3-2: Specifications of the geotechnical centrifuge at the University of Pretoria (Jacobsz et al., 2014).....	3-3
Table 3-3: Specifications of pistons used in trapdoor mechanism.....	3-9
Table 3-4: Specifications of Amatek S015.0 LVDT (LVDT 1) used for tracking surface settlement ..	3-14
Table 3-5: Particle size distribution parameters of both soils (including data by Archer, 2014).....	3-22
Table 3-6: Maximum and minimum dry densities of both sands (including data by Archer, 2014) ..	3-23
Table 3-7: Particle density of Cullinan sand (Archer, 2014) and Consol sand.....	3-24
Table 3-8: Initial conditions of triaxial test samples on Consol sand	3-25
Table 3-9: Strength parameters of Cullinan sand at 80% RD (Archer, 2014) and Consol sand at 100% RD.....	3-27
Table 3-10: Centrifuge test schedule	3-33
Table 4-1 Sequence of presentation of results	4-2
Table 4-2: Test arrangement parameters of Test 1DC	4-4
Table 4-3 Selected results of Test 1DC	4-6
Table 4-4: Test arrangement parameters for Test 2MC	4-19
Table 4-5: Selected results of Test 2MC.....	4-21
Table 4-6: Test arrangement parameters of Test 3DF	4-26
Table 4-7: Selected results of Test 3DF.....	4-28
Table 4-8: Test arrangement parameters for Test 4MF-50	4-38
Table 4-9: Selected results of Test 4MF-50.....	4-41
Table 4-10: Test arrangement parameters for Test 5MF-75	4-46
Table 4-11: Selected results of Test 5MF-75.....	4-48
Table 4-12: Test arrangement parameters for Test 6MF-100	4-54
Table 4-13: Selected results of Test 6MF-100.....	4-56
Table 4-14: Comparison between coarse and fine material	4-62
Table 4-15: Comparison of failure mechanisms between coarse and fine conditions in dry material at $\delta/B = 53\%$	4-63
Table 4-16: Comparison of failure mechanisms between coarse and fine conditions in moist material at $\delta/B = 91\%$	4-65
Table 4-17: Comparison between dry and moist material	4-66
Table 4-18: Comparison of failure mechanisms between dry and moist conditions in coarse material at $\delta/B = 73\%$	4-66

Table 4-19: Comparison of failure mechanisms between dry and moist conditions in fine material at $\delta/B = 53\%$ 4-68

Table 4-20: Comparison of failure mechanisms between tests with different trapdoor widths in moist fine material at $\delta/B = 50\%$ 4-70

1 INTRODUCTION

1.1 BACKGROUND

Sinkholes are natural hazards that originate when soil spanning an underground cavity becomes too weak to support itself and then collapses, leaving behind a hole in the ground or a surface depression. This could result in catastrophic influences on urban environments, failure of buildings and infrastructure and even loss of life.

Considering that large regions of South Africa is underlain by dolomite rock (providing geological conditions prone to the formation of sinkholes), various codes and standards have been developed to regulate development on dolomite land. To estimate the maximum potential size of a sinkhole that might result from a discovered underground cavity, these codes propose a sinkhole diameter that is obtained by extrapolating a funnel upwards from the cavity at slopes equal to the “angles of draw” of various soil layers in between (SABS, 2012; Buttrick & Van Schalkwyk, 1995), as seen in Figure 1-1.

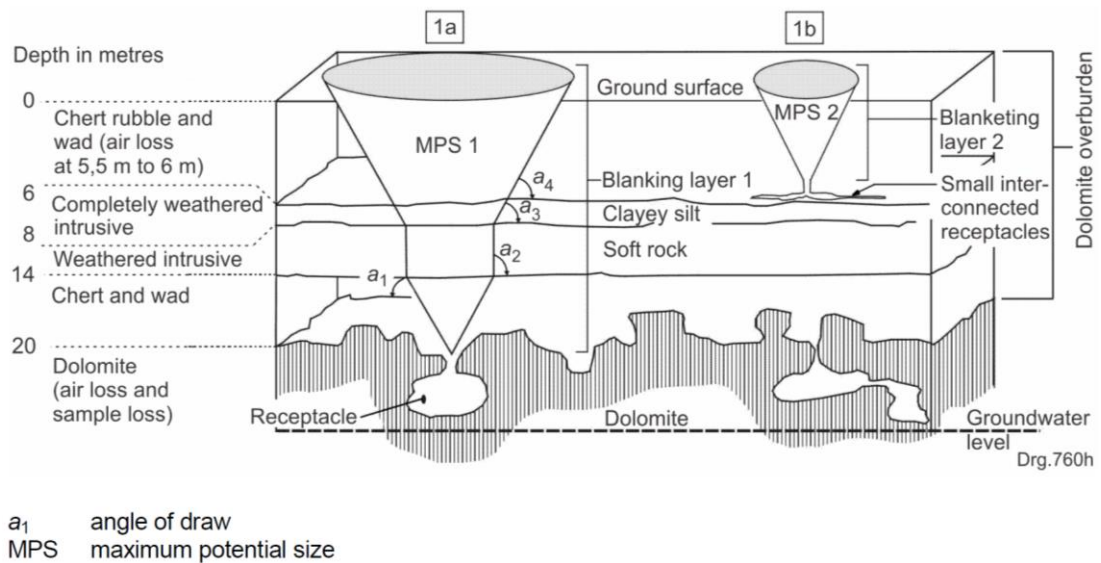


Figure 1-1: Method of determining maximum potential development space (SABS, 2012; Buttrick & Van Schalkwyk, 1995)

This concept is challenged in this study. Preliminary studies at the University of Pretoria have indicated that cavities propagate upwards in a chimney-like fashion instead of a funnel shape (Jacobsz, 2014). If this is indeed the case, building regulations can be relaxed and greater portions of dolomite land can be developed.

To test this hypothesis, failure of dense sand above an underground cavity was simulated with trapdoor tests, as pioneered by Terzaghi (1936), in which a trapdoor was lowered beneath a body of soil. These experiments were conducted in a geotechnical centrifuge at the University of Pretoria. Variables that were tested in this study include soil moisture content, particle size and trapdoor size.

1.2 OBJECTIVES OF THE STUDY

The main objective of this study was to investigate the development of failure mechanisms above a cavity by simulating cavity collapse using a centrifuge trapdoor experiment and to determine the geometric extents of the resulting sinkhole at the surface. Other objectives included:

- Investigate the influence of soil properties such as moisture content (used to impose a small amount of matric suction) and particle size on the relative size and shape of a resulting failure mechanism.
- Investigate the influence of trapdoor size on the relative size and shape of a resulting failure mechanism.
- Measure surface settlement and trapdoor settlement during cavity propagation.

1.3 SCOPE OF THE STUDY

The research in this study is limited to the following aspects:

- Sinkholes were simulated in a plane-strain trapdoor test. Three-dimensional models were not considered.
- The influence of the following soil properties on cavity propagation was investigated:
 - Moisture content (to impose matric suction) – moist and dry
 - Particle size – fine and coarse
- All soils were placed and tested at a high relative density.
- Soils used in this study were single layers of homogenous, well-graded sands. The response of natural, non-homogenous material and that of a combination of different soil layers were not investigated.
- The influence of trapdoor size on sinkhole propagation was investigated. Other geometric properties such as overburden depth were not investigated. A single overburden depth corresponding to a “deep” trapdoor (Costa et al., 2009) was investigated.

- Results of the study included data extracted from analyses of images taken during trapdoor settlement such as plots of displacements and strains, as well as direct measurements of trapdoor settlement and surface settlement.

1.4 METHODOLOGY

The methodology of this study was as follows:

- A literature study was conducted to determine the current state of knowledge applicable to dolomite land, sinkholes, soil arching and experimental methods used to study soil arching and sinkhole development. This information informed the experimental method and discussions of the current study.
- Failure of an underground cavity was simulated with trapdoor tests in plane-strain conditions. The experiments were performed in a geotechnical centrifuge. Parameters such as moisture content, particle size and trapdoor size were investigated.
- Images taken of the soil failures were analysed using Particle Image Velocimetry (PIV) and plots of displacements and strains were created, which provided insight into the size and shape of failure mechanisms. The failure mechanisms of various models were compared to one another to assess the influence of the named variables.
- Finally, conclusions were drawn from the study and recommendations for future work were made.

1.5 ORGANIZATION OF THE REPORT

The report consists of the following chapters and list of references:

- **Chapter 1** is an introduction to the report and provides a brief overview of the topic. It also describes the objectives and scope of the study, the methodology followed and the organizational structure of the report.
- **Chapter 2** presents an overview of the current literature on dolomite, sinkholes, soil arching theory and previous studies that investigated soil arching and sinkhole formation experimentally.
- **Chapter 3** describes the experimental work conducted in this study. The equipment is discussed in detail and typical steps followed in each experiment are presented, after which the material is described in terms of geotechnical parameters. The section ends with an overview of particle image velocimetry (PIV) and how it was used to analyse data from the experiments.

- **Chapter 4** discusses the results obtained from the trapdoor experiments as analysed using PIV. The results of all 6 tests are presented individually after which comparisons are made to illustrate the influence of various parameters on the propagation of a cavity to the surface.
- **Chapter 5** presents conclusions made from this study and recommendations for future work.

2 LITERATURE REVIEW

This literature review serves as background information supporting the current study. It starts with a discussion on dolomite, including its composition, locations where it occurs in South Africa and its role in sinkhole formation. This leads to a discussion of sinkholes including types of sinkholes, conditions necessary for formation and codes of practice regarding development of sinkhole-prone land. Since this study focuses on the propagation of a cavity to the surface, a discussion on soil arching and strength of soils is also included. The chapter ends with a review of existing literature on soil arching, specifically focusing on trapdoor tests performed both at normal gravity and in a geotechnical centrifuge. Typical results of this phenomenon are discussed, such as load-displacement graphs, failure mechanisms, surface settlement and strain distributions.

2.1 DOLOMITE

Dolomite is a type of carbonate rock found prolifically in South Africa, the weathering of which is responsible for most of the sinkhole formations in the country. Confusion often arises when the term *dolomite* is used since this term could refer to either dolomite as a mineral or dolomite as a rock. The latter definition is implied whenever the term is used in this dissertation.

2.1.1 Composition of Dolomite

Dolomite (the mineral) is a major constituent of dolomite (the rock), but is also found in many other rock types. Dolomite as a mineral (shown in Figure 2-1) is composed mainly of alternating arrangements of calcium and manganese that are separated by layers of carbonate (CO_3) (Richardson, 2013).



Figure 2-1: Dolomite as a mineral (King, 2017)



Figure 2-2: Dolomite as a rock (King, 2017)

Dolomite as a rock (shown in Figure 2-2) is a carbonate rock composed of at least 90% mineral dolomite ($(\text{CaMg}(\text{CO}_3)_2)$), up to 10% calcite (CaCO_3) and small traces of chert and other minerals (Trollip, 2006). Extensive descriptions of the exact mineral composition of dolomite in various regions of South Africa are given by Wagener (1984) while the formation and deposition of dolomite is described in detail by Trollip (2006) and Richardson (2013).

2.1.2 Weathering of Dolomite

Dolomite dissolves easily in the presence of weakly acidic water. Although generally impervious with a porosity of approximately 0.3% (Nel & Haarhoff, 2011), the rock often contains an extensive network of fissures, joints and cracks through which water can enter easily. Dolomite is insoluble in pure water (Richardson, 2013) but highly susceptible to dissolution by weakly acidic fluids such as rainwater and percolating groundwater that have acidified through carbon dioxide enrichment (Buttrick & Van Schalkwyk, 1995) as it falls through the atmosphere or flows through overburden soil. This water enters the dolomite rock through cracks and fissures and dissolves the rock into bicarbonates. The bicarbonate-rich water is then brought to the surface at springs after which it is carried away (Trollip, 2006). This weathering phenomenon expands the network of joints and fissures and forms a series of underground cavities, caves and other karst-related features that creates large voids underground. The top of the dolomite layer is often characterized by pinnacle dolomite formations as seen in Figure 2-3 below.



Figure 2-3: Small-scale example of pinnacle dolomite rock (Richardson, 2013)

There are several ways in which acidified water infiltrates onto dolomite rock to start the weathering process. Although it is possible for dolomitic weathering to occur naturally, this is very seldom the case. This process is often attributed to human infrastructure and activities with an estimated 96% of dolomitic activity in South Africa being related to human development (SABS, 2012). Some man-induced causes of this are:

- groundwater level drawdown (often due to mining activities)
- leaking reticulation such as water and sewer pipes
- leaking water-bearing services such as reservoirs, canals and swimming pools
- poor management of storm-water and surface-water runoff

The dissolution of dolomite occurs mostly above the groundwater table (Trollip, 2006) since ingress water speedily becomes less acidic after mixing with groundwater. This explains why groundwater level drawdown (by means of mine dewatering, for example) could accelerate weathering of dolomite by exposing ever-increasing volumes of bedrock to ingress water.

The process of dolomite weathering occurs over long periods of geological time, and although the dissolution of dolomite occurs at a rate much faster than that of other rocks, it often takes years for significant weathering to be observed.

2.1.3 Dolomite Land

The South African National Standard for Development on Dolomite Land (SANS 1936) defines dolomite land as any portion of land that is underlain by bedrock of a carbonate nature such as dolomite or limestone, to a depth of no more than 60m in locations where groundwater levels are being monitored and no dewatering has occurred, or to a depth of no more than 100m where no monitoring of groundwater levels are present and where dewatering *has* occurred (SABS, 2012). As described in subsequent sections, this type of land is especially prone to dolomite weathering and ground instability and thus the risk of sinkhole/subsidence formation in these regions is high.

2.1.4 Regions of Occurrence in South Africa

Two main dolomite groups are found in South Africa, namely the Chuniespoort Group and the Ghaap Group (also known as the Campbell Group) as shown in Figure 2-4 and Figure 2-5. These two groups cover 3% of South Africa's geographic area and represent 98% of all soluble rocks in the country (Van Schalkwyk, 1981).

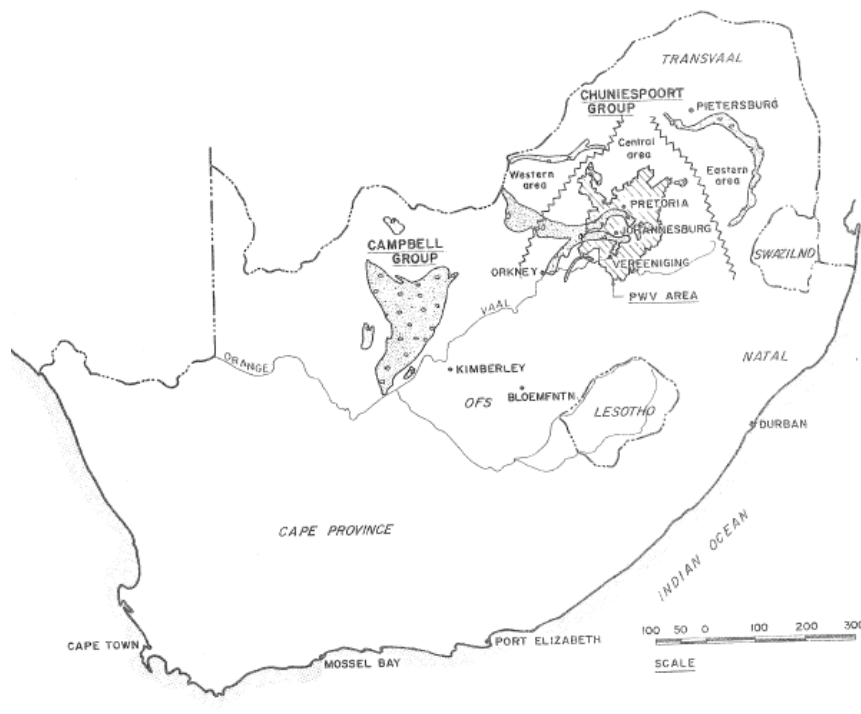


Figure 2-4: Distribution of major dolomitic groups in South Africa (Wagener, 1984)

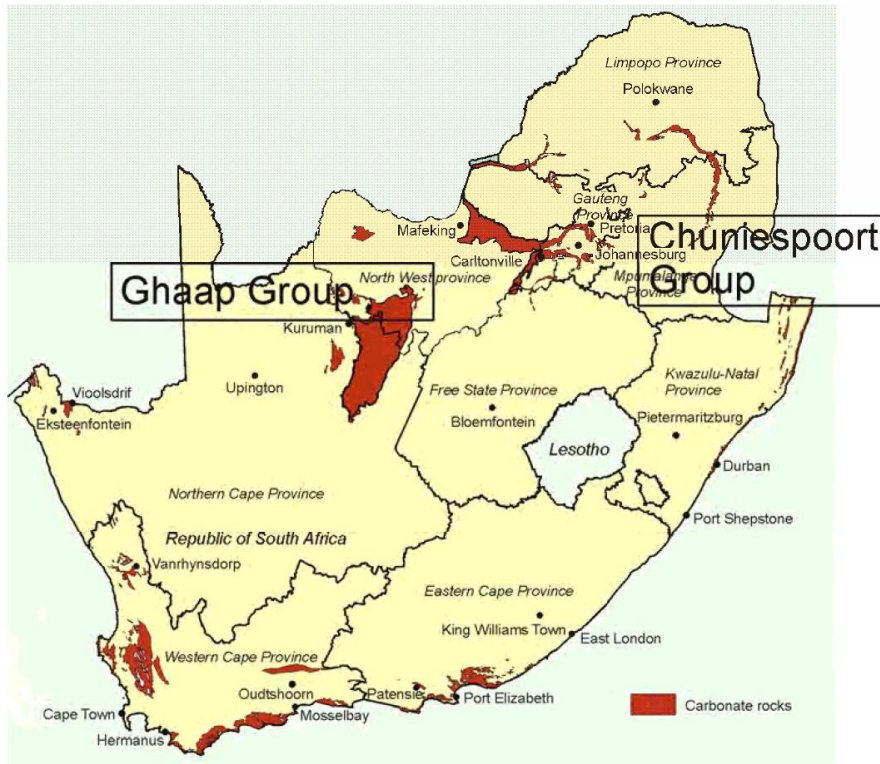


Figure 2-5: Location of carbonate rocks in South Africa (SABS, 2012)

The Chuniespoort Group is divided into three regions:

1. Western area – A thin band stretching from Gabarone (Botswana) eastward to Thabazimbi and Bela-Bela.
2. Eastern area – Thin band stretching from Polokwane/Mokopane in a south-eastern direction towards Nelspruit and then turning south-western up to Ermelo.
3. Central area – This area is much wider than the other two regions. It stretches from Mahikeng to Ventersdorp as a wide band from where it divides into two smaller bands, one stretching to Pretoria and the other to Johannesburg. A third thin band stretches from Ventersdorp in a south-western direction and ends at Orkney.

The Ghaap group is triangular and includes the towns of Kuruman, Vryburg, Kimberly and Hopetown. Other less prominent traces of carbonate rocks appear in western regions of the Eastern Cape and Western Cape as seen in Figure 2-5.

2.1.5 Human Settlement on Dolomite Land in South Africa

Human settlement on dolomite land is quite high in South Africa, with Buttrick & Van Schalkwyk (1995) estimating that around 20% of the Gauteng province is underlain by dolomite land. This percentage has been updated to 25% in 2012 as noted in SABS (2012) and

it is now estimated that between 4 and 5 million South Africans work and reside on dolomite land, constituting about 7 - 9% of the entire population.

As seen in Figure 2-4, the Chuniespoort Group overlays much of the Gauteng province, an economic hub that covers 1.5% of the country's geographic area but houses 23.5% of its population according to the 2014 census. This makes for a densely-populated region with large amounts of infrastructure and reticulation that further increases the likelihood of man-induced dolomitic activity. In addition, mining activities are common in this area which further increases the risk of sinkhole formation through ground dewatering practices. Due to the abundance of dolomite and likelihood of failure in this area, it is clear why dolomitic activity is much more noticeable in Gauteng than in other parts of the country and why sinkhole awareness in South Africa is largely focused in and around this region (Richardson, 2013).

2.2 SINKHOLES

When underground dolomite rock is dissolved and weathered away by percolating groundwater a cavity is left in its place. The cavity grows over time and at some stage the overbearing soil is no longer strong enough to span the void. The overburden soil shears off at the sides and falls into the cavity, leaving a hole in the ground or a surface depression. A hole formed in this way is known as a sinkhole while a surface depression is known as a subsidence (the term *doline* is often found in literature but has been deprecated) (SABS, 2012).

Failure of the overbearing soil may occur suddenly and catastrophically with little or no warning and thus the resulting damage to infrastructure and property could be excessive. Sinkholes have been known to swallow entire houses or span the width of freeways, disrupting traffic flow and causing damage to service infrastructure. Sinkholes also pose a threat to human life with a total of 38 people having been swallowed by sinkholes between 1965 and 1995 (Buttrick & Van Schalkwyk, 1995). The author is not aware of fatalities since 1995.

2.2.1 Types of Sinkholes

Nel and Haarhoff (2011) suggested three types of overburden collapse mechanisms which are shown in Figure 2-6 and reiterated here.

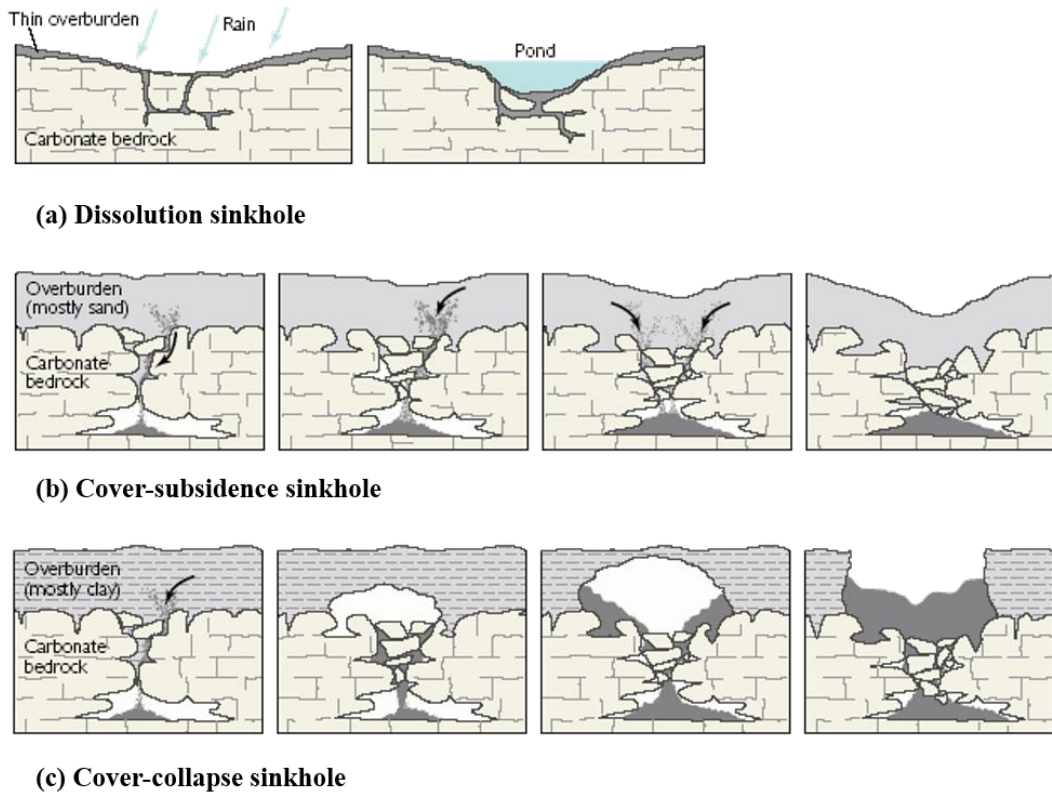


Figure 2-6: Types of sinkholes (Nel and Haarhoff, 2011)

The three types of sinkholes shown in Figure 2-6 are:

- a. **Dissolution sinkholes.** These sinkholes form at locations where dolomite bedrock is visible at the land surface as shown in Figure 2-6a. Weathering of the rock causes a top-down collapse over time and a pond of surface water is formed which accelerates the process. This type of collapse poses little threat to society due to its visibility above ground both before and after weathering has started. Any damages resulting from this collapse would be in the form of differential settlement of buildings and infrastructure and would occur over a long period of time with ample warning and evidence.
- b. **Cover subsidence sinkholes.** This type of sinkhole form at locations where the dolomite bedrock is overlain by a soil overburden of sand as shown in Figure 2-6b. Infiltrated water dissolves the dolomite and creates voids and cavities. The overlying soil gradually migrates downward and creates a shallow, basin-like depression that is round or oval-shaped, often called a subsidence. Subsidence can range in diameter from 50-300m and form slowly over time (Buttrick & Van Schalkwyk, 1998). Damages caused by this type of collapse are like that of dissolution sinkholes.

- c. Cover collapse sinkholes.** This type of sinkhole also forms in locations where a soil overburden is present above the dolomite bedrock, albeit at a greater depth. As the roof of a subsurface cavity becomes unstable, it caves in and forms a second cavity closer to the surface. This process repeats and the cavity propagates upwards towards the surface until it finally emerges as a hole in the ground as shown in Figure 2-6c. Cover-collapse sinkholes can be up to 50m in diameter and although formation of underground cavities occurs over several years, final failure of the top layer could happen suddenly and catastrophically (Buttrick & Van Schalkwyk, 1998). The initial opening in the surface may be smaller than the cavity diameter due to cohesive forces causing overhang of the side walls and the maximum diameter of the sinkhole may only be realized later when sections of the side overhangs collapse into the void (Augarde et al., 2003). Throughout this study, the term *sinkhole* will be used to refer specifically to cover collapse sinkholes.

2.2.2 Conditions Necessary for Sinkhole Formation

Ultimate formation of cover collapse sinkholes requires several natural phenomena to be present. Jennings et al. (1965) suggested the following list of factors that must be present for a soil arch above a cavity to collapse, which also provides a good indication of the chain of events leading up to failure. Items 1 to 3 relate to conditions necessary for cavity formation while items 4 to 6 relate to cavity propagation and ultimate failure.

1. *Presence of sufficiently strong material adjacent to the underground cavity.*

The material adjacent to the underground cavity should have enough shear strength to act as an abutment for the cavity roof. The diameter of the resulting cavity dictates the required distance that the roof will have to span and thus also the required shear strength of the material. If the material is not strong enough, arching may not be possible and failure is imminent.

2. *Arching capability of soil within the overburden.*

Some form of tensile strength, possibly in the form of negative pore pressures or a cementation agent, should be present in the overburden material. According to Jacobsz (2014), full arching occurs when the intrados of the arch experiences zero vertical stress, indicating that a form of tensile strength must be present.

3. *Development of a void or cavity below the arch.*

This happens due to weathering of the dolomite bedrock through moisture ingress and occurs over a long period of geological time.

4. *Presence of a large enough receptacle below the void to accept mobilized material.*

For collapse to occur, a receptacle must exist to receive the overburden material that ultimately caves in. If the receptacle is not capable of receiving all the mobilized material failure may occur as a cover subsidence sinkhole instead.

5. *Presence of a downward transportation agent for the overburden material.*

Gravity is the most common transportation agent in this case although moisture ingress, often the same moisture that causes dolomite weathering, can speed up the process.

6. *Presence of a final triggering mechanism or disturbing agent.*

Some disturbance is required to cause ultimate collapse of the arch, such as ground vibrations from seismic activity or mining tremors. It could also be due to loss of partial support from groundwater pressure, especially following groundwater level drawdown. Although the presence of this final trigger does indeed accelerate the process, loss of strength could also occur gradually over the span of several years.

2.2.3 Shape and Size of Sinkholes

The conditions listed in the previous section may lead to sinkhole formation, but the shape of the resulting sinkhole will differ widely based on soil parameters. Work done by Hyatt et al. (1996) distinguishes between three basic sinkhole shapes as seen in Figure 2-7:

1. Shaft – steep, vertical side slopes with a flat bottom.
2. Undercut – like a shaft but with visibly overhanging side slopes.
3. Bowl – depression with side slopes less than 90°.

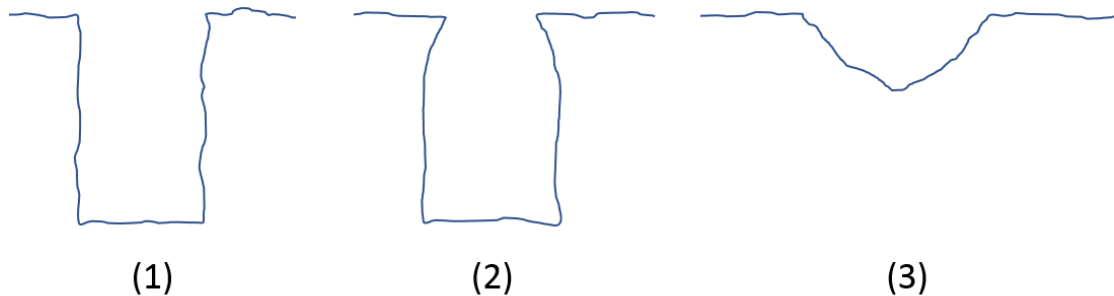


Figure 2-7: Shapes of a sinkhole (adapted from Hyatt et al. (1996))

Hyatt et al. (1996) further developed a volume ratio index (VRI) equal to the ratio of the volume of the sinkhole to the volume of an elliptic cone with the same major and minor radii and depth as the sinkhole in question. This allowed categorization of sinkhole shape as visualized in Figure 2-8. A shape corresponding to a VRI of 1 is similar to a cone, one with a VRI of 2 is similar to a hemi-ellipsoid and one with a VRI of 3 is similar to a cylinder. The VRI values of

several sinkholes in Albany, Georgia were then graphed against their surface diameter showing that shapes of sinkholes vary widely with a diameter of 4-5m or less, but converge to a bowl-shaped depression with a VRI of 1.5 at higher diameters.

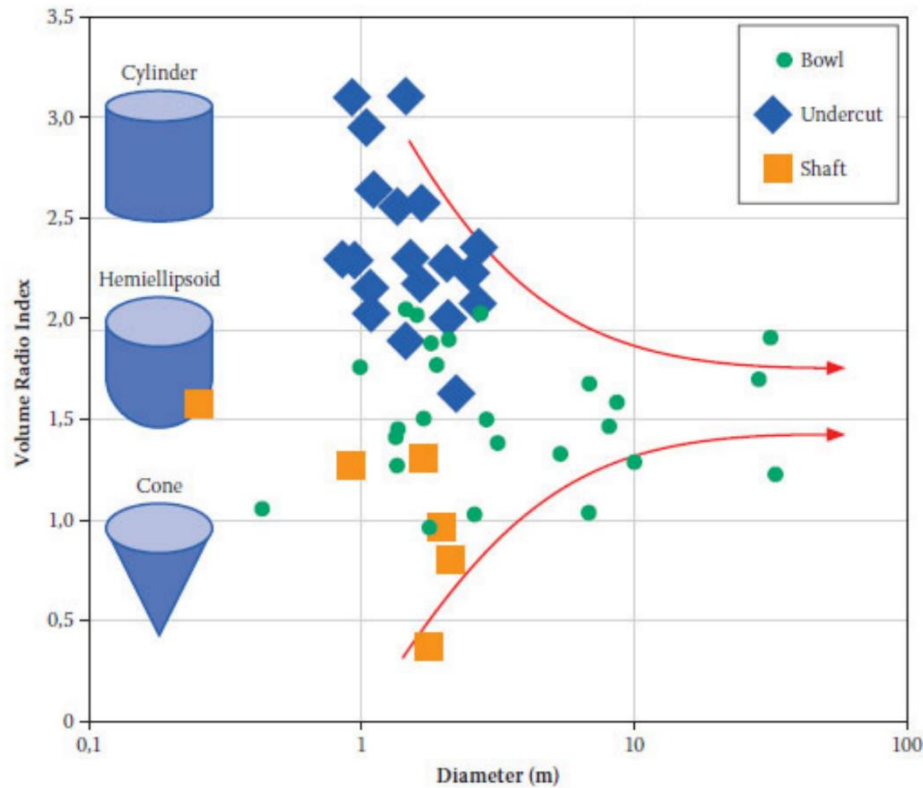


Figure 2-8: Geometry forms associated with whole number VRI values (Hyatt et al., 1996)

The ultimate surface diameter (size) of a sinkhole has been studied by several other researchers, most of which suggest the diameter to be a function of the original cavity diameter, overburden thickness and internal friction angle of the overlying soil. Pilecki et al. (2006) suggested the following relationship which predicts that the sinkhole diameter is directly proportional to the radius of the cavity, thickness of the overburden layer and internal friction angle.

$$D_{sh} = 2z \tan(90 - \varphi) + 2r_s$$

Where:

- D_{sh} = surface diameter of sinkhole (m)
- z = thickness of overburden layer (m)
- φ = internal friction angle of overburden material ($^{\circ}$)
- r_s = radius of cavity (m)

This reasoning also forms the basis for predicting the maximum potential development space or MPS of a sinkhole (an indication of the maximum potential size) as proposed by Buttrick & Van Schalkwyk (1995) in their method of scenario supposition, more thoroughly described in Section 2.2.4. This method suggests the same relationships between diameter, overburden thickness, cavity throat size and internal friction angle as that of Pilecki et al. (2006). Buttrick & Van Schalkwyk further noted that a sinkhole may not always realize the entire potential development space when it fails as seen in Figure 2-9 but rather create a smaller sinkhole within the confines of the MPS. Conservative measures therefore treat the entire potential development space as an unsafe zone, regardless of the final diameter of the sinkhole.

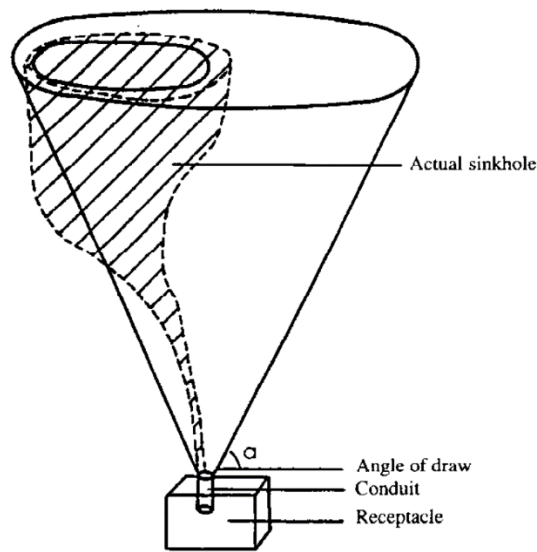


Figure 2-9: Sinkhole forming within confines of MPS (Buttrick & Van Schalkwyk, 1995)

Buttrick & Van Schalkwyk (1995) further categorized sinkhole diameters as small, medium, large, or very large as shown in Table 2-1, which has also been adopted in SANS 1936 (SABS, 2012).

Table 2-1: Sinkhole size and their classification (Buttrick & Van Schalkwyk, 1995)

Maximum diameter of surface manifestation (m)	Sinkhole size classification
< 2	Small size
2 to 5	Medium size
5 to 15	Large size
> 15	Very large size

2.2.4 Quantification of Sinkhole Risk

Codes of practice in South Africa base building regulations and recommendations on a rating mechanism described in SANS 1936 (SABS, 2012) that quantifies the risk of sinkhole formation as a hazard rating representing the number of sinkhole events that may occur per hectare per 20 years. A tolerable hazard rating of 0.1 has been agreed upon (that is, one event per hectare per 200 years).

Several natural conditions affect the risk of sinkhole formation, including the following (SABS, 2012):

1. Surface topography
2. Drainage conditions and changes
3. Nature and thickness of overburden material
4. Nature of underlying bedrock formations
5. Depth and fluctuations of the groundwater level
6. Presence of underlying structural features such as faults, fracture zones and dykes

Quantification of this risk is therefore a subjective process due to the number of variables involved and assumptions are required. SANS 1936 therefore incorporates a “worst-case scenario” method of risk assessment developed by Buttrick and Van Schalkwyk (1995) known as *scenario supposition*. It consists of a checklist of factors that identifies the worst-case scenario of a dolomite region. The method tries to predict future uses of the land and deduce the amount of water ingress based on that.

Calculation of the hazard rating is preceded by calculation of the maximum potential development space or MPS, defined as the maximum diameter of a resulting sinkhole at the soil surface depending on the overburden depth, cavity throat size and angles of draw of every layer of material in the overburden. The overburden material is divided into layers based on soil properties and a funnel is then extrapolated upwards from the cavity with side slopes equal to the angle of draw of the material in each layer (Figure 2-10). The full MPS will be realized if the receptacle is large enough to accommodate the mobilized material (which is conservatively assumed to be true) if all materials in the blanketing layer can be mobilized and if a sustainable mobilizing agent is present.

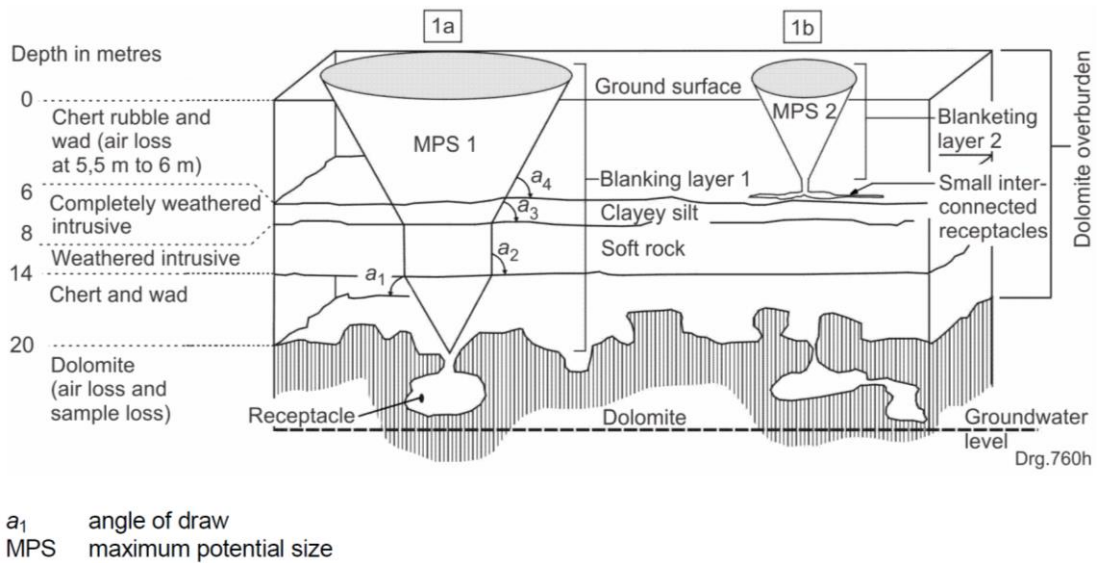


Figure 2-10: Determining MPS using the scenario supposition method (Buttrick and Van Schalkwyk, 1995)

An area is then given a risk rating by comparing the hazard rating and MPS to tabulated values. Keeping with conservative measures, the method suggests that the assumption should be made that any given area of land might be “abused” by poor management of infrastructure and storm water runoff in future. The method also suggests the continued evaluation of groundwater fluctuations or artificial drawdown in the future.

2.2.5 Codes of Practice in South Africa

The abovementioned scenario supposition method forms an integral part of SANS 1936. This document provides definitions, background information, other methods of determining the risk of sinkhole formation in a dolomitic area and suggested building regulations depending on the risk classification. The standard requires development on dolomite land to be classified and approved by a competent person according to the land use category, dolomite area designation and hazard rating (SABS, 2012). Extensive building regulations are given for several combinations of the above.

SANS 1936 further advocates a pro-active stance to dolomitic activity and encourages correct management practices on the same level of importance as building regulations. Risk on dolomite land can be managed by enforcing designated land use restrictions, monitoring surface drainage and de-watering and following requirements for installation and maintenance of water-bearing structures both above and below ground, as well as buildings and other infrastructure. Considering this, the standard provides suggestions for the development of a dolomite risk management strategy (DRMS) that details continuous monitoring of dolomite

land, management of infrastructure, actions to be taken when warning levels are reached, emergency reaction programs and rehabilitation programs when sinkholes do occur and dolomite awareness campaigns (SABS, 2012).

2.2.6 Previous Studies on Sinkhole Stability Charts

Several studies were performed with the aim of creating so-called stability charts that predict the likelihood of an overburden layer collapse, based on several soil parameters and geometrical measurements. These studies were often targeted to specific locations and were often empirical in nature (Augarde et al., 2003). However, most of the tests described sinkhole stability in terms of dimensionless parameters, allowing for extrapolation and application elsewhere.

Centrifuge modelling of sinkholes was performed by Abdulla & Goodings (1996) in which they tested the ability of weakly cemented sand slabs to span a cavity. They tested 49 models of different variations of overburden thickness (H_c), cavity diameter (D), unit weight (γ_c) and cohesion (c) and recorded the gravity multiple (N) at which failure occurred. As shown in Figure 2-11, they found that models with $H_c/D < 0.25$ failed along a near-linear failure plane sloping at an average angle of 61° to the horizontal, models with $H_c/D = 0.25$ failed along a curved failure plane with a slight overhang while models with $H_c/D > 0.31$ did not fail entirely to the surface, but rather formed a stable arch underground. Results were summarized into a stability chart with dimensionless axes (Figure 2-12) allowing for extrapolation to full-scale scenarios.

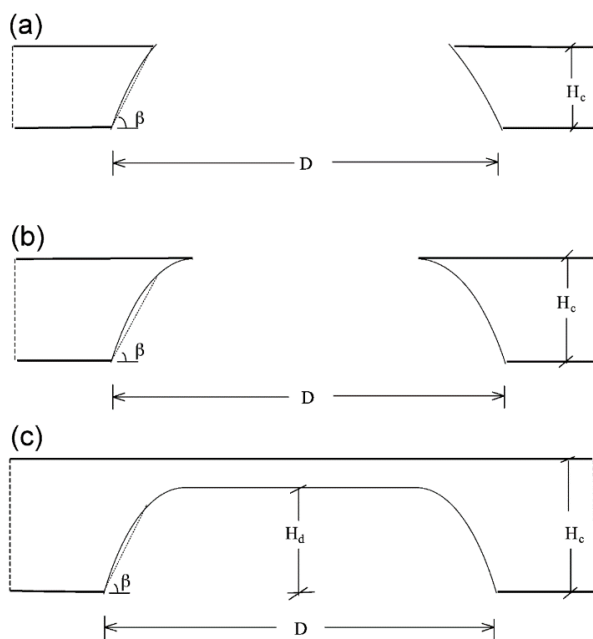


Figure 2-11: Shape of failure in cemented sand layers where (a) $H_c/D < 0.25$, (b) $H_c/D = 0.25$ and (c) $H_c/D > 0.31$ (Abdulla & Goodings, 1996)

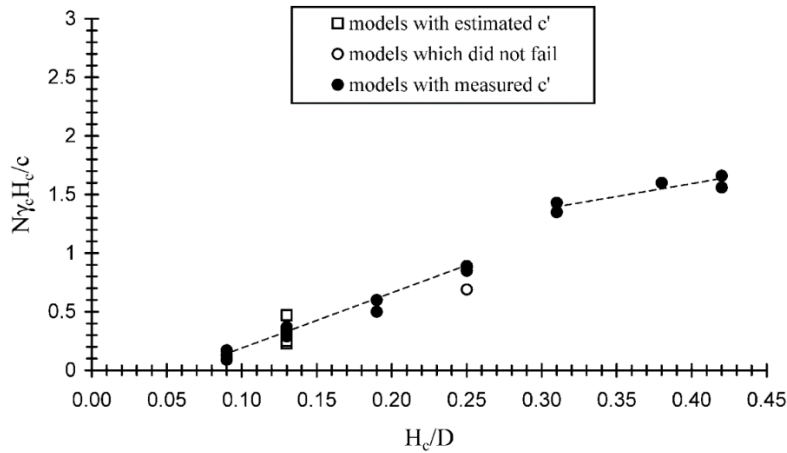


Figure 2-12: Dimensionless stability chart (Abdulla & Goodings, 1996)

Drumm et al. (2009) performed finite element analysis on a spherical cavity of diameter D at a depth of h and developed a stability chart based on a dimensionless stability number $N_{c\phi} = \gamma h/c_u$ and the cavity's h/D ratio. Stability curves for several values of ϕ' are given in Figure 2-13, indicating the effects of friction angle on stability. Other numerical studies include work by Augarde et al. (2003) who used the finite element limit analysis to determine upper and lower bounds for the loads that dictate stability of an underground cavity.

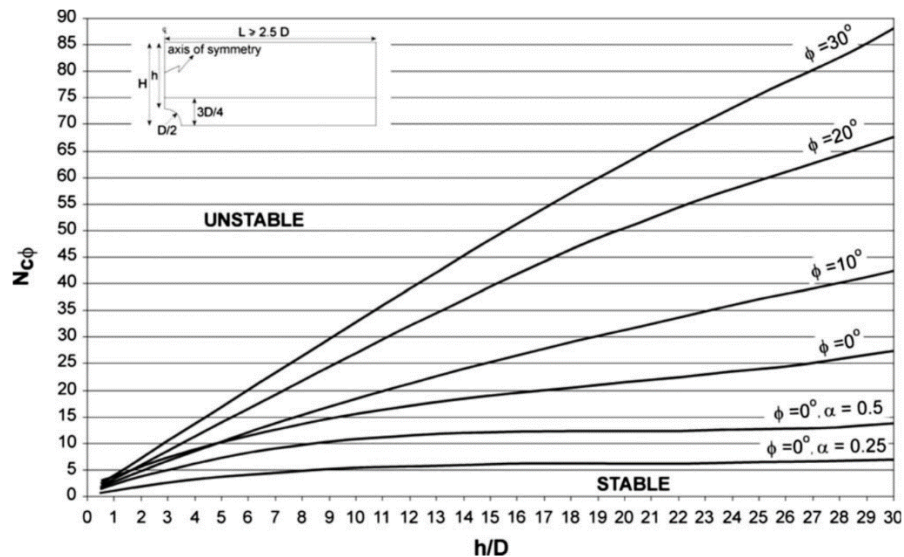


Figure 2-13: Stability chart showing effects of friction angle (Drumm et al., 2009)

Stability charts provide a way to quantify the risk of sinkhole formation given various soil parameters and geometric measurements, but provide little understanding regarding the actual mechanisms of a sinkhole collapse. This can be better studied using the so-called trapdoor test, a physical experiment geometrically similar to a sinkhole. The trapdoor experiment has been pioneered by Terzaghi (1936) to investigate the arching capabilities of soil and has been used by various researchers to study sinkholes. A review of soil arching, trapdoor experiments, and their application to sinkhole studies is thus provided next.

2.3 SOIL ARCHING

Soil arching, defined as the transfer of stresses between a moving soil mass and an adjacent stationary mass, is used extensively in the design of tunnels and underground conduits and pipelines (Tien, 1990) but is equally applicable for the study of sinkhole formation, since the ability of soil to span a cavity is directly correlated to its strength. Some of this strength could be due to suctions in the soil which might very well be present in a situation where groundwater lowering has occurred, but for a cohesionless, granular soil the primary strength contributor is the lateral stresses that result from soil arching (Tien, 1990). Most literature on the subject focused on dry soil with little to no cohesion where soil arching is the major contributor of strength, and no literature could be found on soil arching in moist, cohesion-strengthened soil. A much broader literature review on the subject can be found in Tien (1990).

2.3.1 Technical Definition of Soil Arching

Soil arching can be defined as a progressive shifting of load-bearing forces between a yielding soil mass and an adjacent stationary mass (Terzaghi, 1943). When a soil body fails, particles on either side of the line of failure tend to slide past one another and roll over one another in deformation. Interlock between the particles creates a shear resistance that opposes movement and attempts to keep the yielding soil mass in its original position.

Soil arching can be either active or passive depending on the stiffness of the yielding soil mass (inclusion) relative to the soil around it (Tien, 1990). An inclusion that is more compressible (less stiff) than the surrounding soil causes active arching in which load-bearing forces are transferred from the inclusion to the adjacent soil (Figure 2-14a). The opposite happens when the inclusion is less compressible (stiffer) than the adjoining soil, causing passive arching in which forces are transferred from the adjacent soil mass onto the inclusion (Figure 2-14b). The focus of the current study is mainly on active arching.

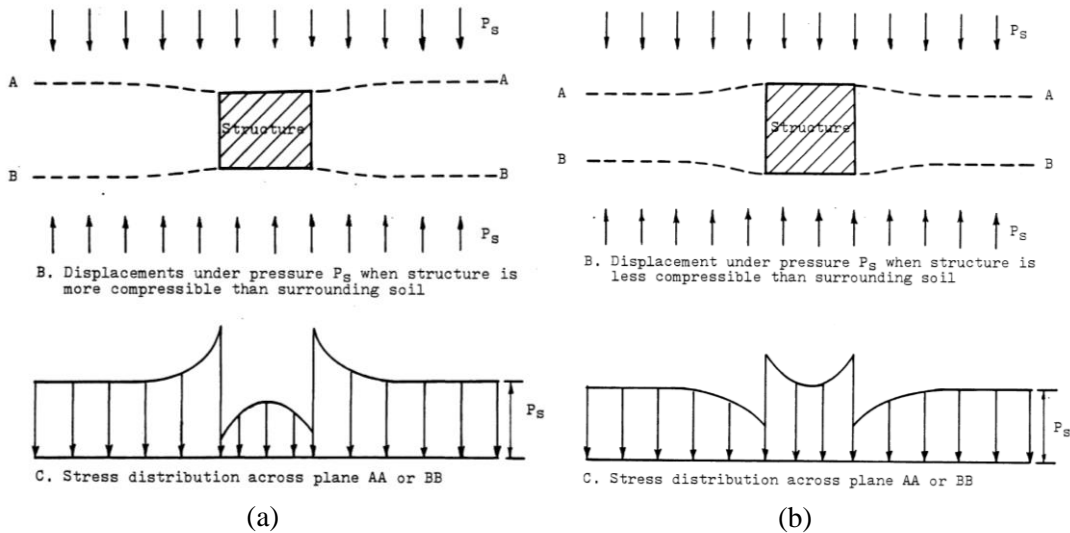


Figure 2-14: Pressure distributions in (a) active arching vs. (b) passive arching (Evans, 1983)

Active arching will typically occur when partial yielding of a support causes a section of the soil mass to move downward, thus increasing in volume and becoming more compressible than its surroundings (Figure 2-15). An increase in load-bearing forces on the adjacent soil will increase lateral stresses in the adjacent soil and could result in the formation of a stable arch, forming in the shape of an inverted parabola that extends from one edge of the inclusion to the other. The arch has sufficient strength to carry the weight of the soil above it, allowing the yielding inclusion to continue moving downward while the rest of the soil mass stays intact.

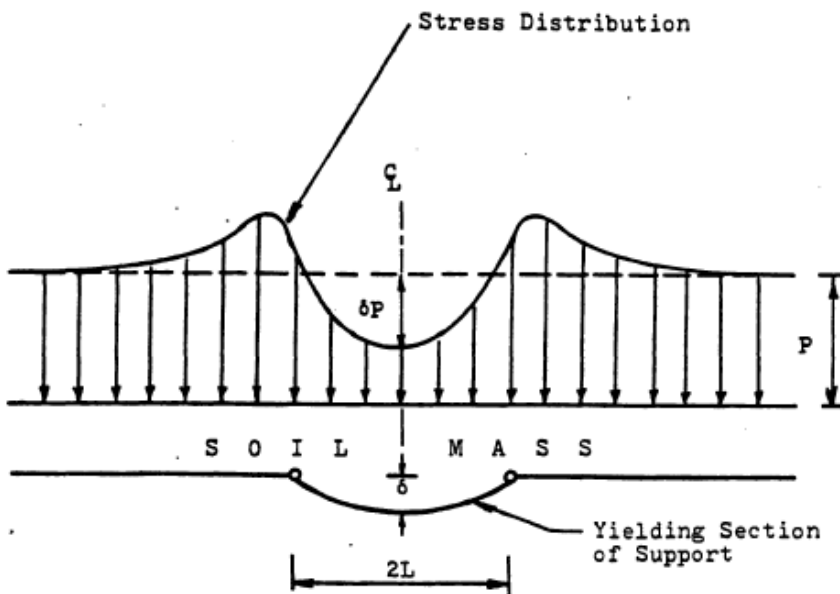


Figure 2-15: Stress distribution in soil above a yielding base (Bierrum, et al., 1972; Revised by Evans, 1983)

2.3.2 Classical Arching Theory

Researchers had known about soil arching since the early 1800s and research on the subject has often been sporadic, often directed to meet a particular need (Tien, 1990). The most famous work on the subject is that of Terzaghi (1936, 1943) who analysed the behaviour of soil above a yielding trapdoor in a laboratory. The physical results of this experiment were published in a paper (Terzaghi, 1936) and later used to develop a definition and working theory of soil arching in *Theoretical Soil Mechanics* (Terzaghi, 1943).

In a typical trapdoor experiment (Figure 2-16), a body of sand with height H is placed in a container. The base consists of a trapdoor of width B in the centre with fixed floor sections on both sides. The trapdoor is then lowered while the load on the trapdoor P and vertical displacement δ of the trapdoor is recorded.

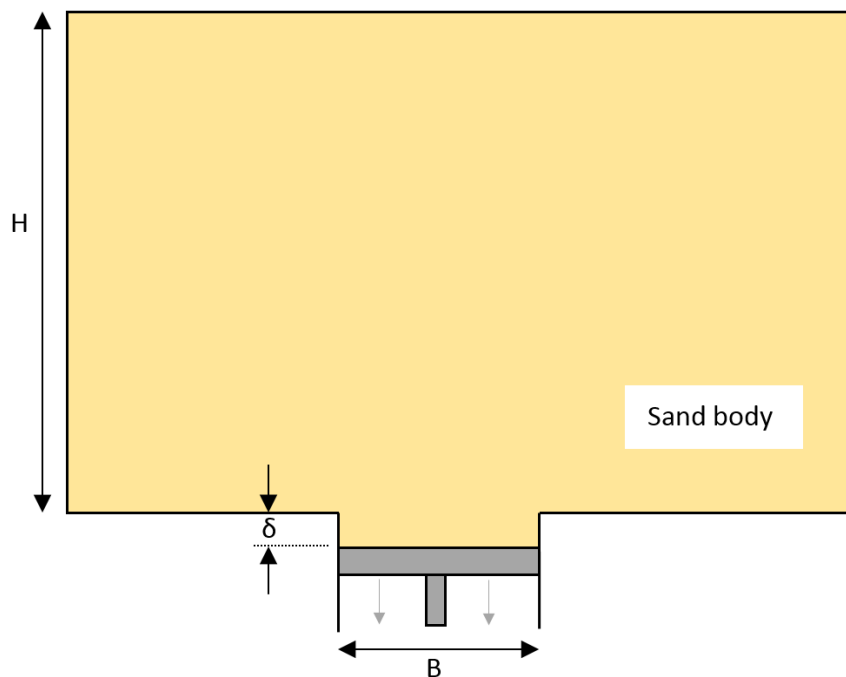


Figure 2-16: Typical setup of a trapdoor experiment

Terzaghi's experimental setup was identical to Figure 2-16 and typical results of his experiment are shown in Figure 2-17 as a plot of vertical load on the trapdoor normalized by initial load against vertical trapdoor displacement normalized by trapdoor width. It has since become common practice amongst researchers to normalize vertical load on the trapdoor by the initial load (F/F_0), normalize the overburden height by the width of the trapdoor (H/B) and normalize vertical trapdoor displacement by the width of the trapdoor (δ/B), thus providing dimensionless parameters that can be compared across publications.

Terzaghi's results in Figure 2-17 show that the load on the trapdoor decreased significantly at the initial removal of support, indicating that an amount of force was being transferred to adjacent soil. A minimum load was reached within a displacement of 1% of the trapdoor width. The force on the trapdoor then increased as the test progressed and the expanding mass of soil propagated upwards until a constant load was reached at a displacement of around 10% of the trapdoor width (note that Terzaghi chose $2B$ to represent the entire trapdoor width). The results were similar in both loose and dense sand although the amount of force transferred in the latter was greater than the former. However, both types of sand converged to the same constant load towards the end of the test (Terzaghi, 1936).

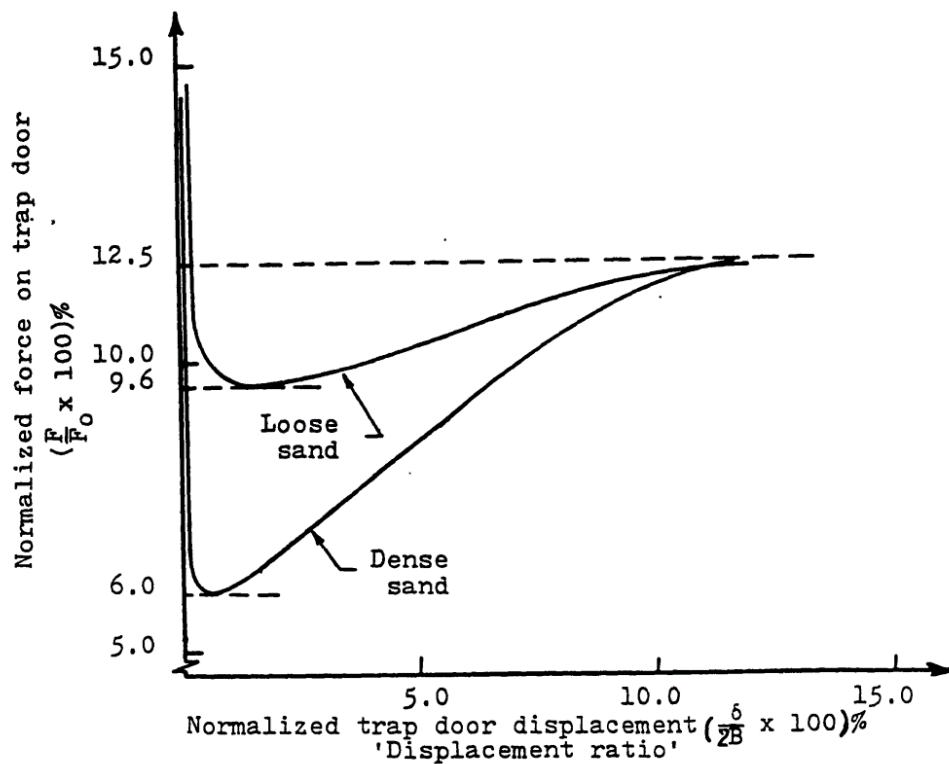


Figure 2-17: Results of Terzaghi's trapdoor experiment, normalized vertical force on trapdoor against normalized displacement of trapdoor (Terzaghi, 1936; Revised by Evans, 1983)

Horizontal and vertical forces were measured at several locations above the trapdoor using the friction tape method and results are shown in Figure 2-18. Vertical stresses decreased to almost 10% of the geostatic stress directly above the trapdoor, indicating that a transfer of stresses had indeed occurred for the overburden material to be supported. This reduction seemed to be present up to at least a height of $H/2$ above the trapdoor. As the door was lowered further the vertical stress increased but did not fully recover.

Horizontal stresses behaved in a similar manner to vertical stresses except for a slight increase above the geostatic value at a height of roughly $H/3$. Although not mentioned by Terzaghi, this behaviour supports the idea that a higher horizontal stress increased the shearing resistance of the soil at this location, thus forming a stable arch capable of carrying the weight of the soil above it. The coefficient of lateral stress K was calculated to be 1 directly above the trapdoor, increasing to 1.6 at a height of $H/3$ (Figure 2-19). The increase in K was evidence of greater lateral stresses which in turn provided an increased frictional shear resistance on vertical planes throughout the soil. This shear resistance supported the soil mass and is the basis of the arching mechanism. At a height of $H/2$ and above, the value of K decreased to essentially K_0 , leading Terzaghi to assume that the lowering of the trapdoor had no measurable effect above this height, and that all arching happened below it (Terzaghi, 1936; Tien, 1990). Evans (1983) also measured vertical and horizontal stresses at a single location directly above the trapdoor to investigate the change in K with trapdoor displacement, and showed that K increased from K_0 at $\delta/B = 0$ to a maximum value at $\delta/B = 0.01$, returned to about $1.6K_0$ at $\delta/B = 0.022$, and decreased slowly to reach K_0 at $\delta/B = 0.07$.

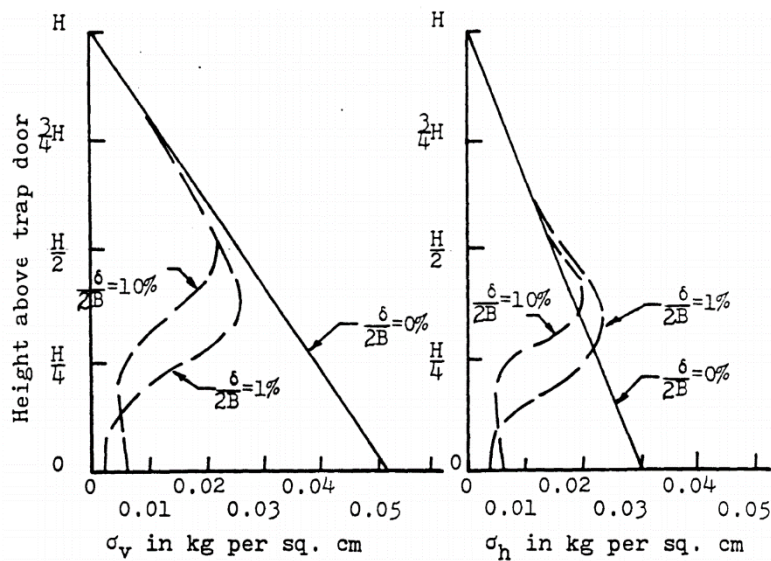


Figure 2-18: Results of Terzaghi's trapdoor experiment: horizontal and vertical stresses in the soil above the trapdoor at various stages of trapdoor displacement (Terzaghi, 1936; Revised by Evans, 1983)

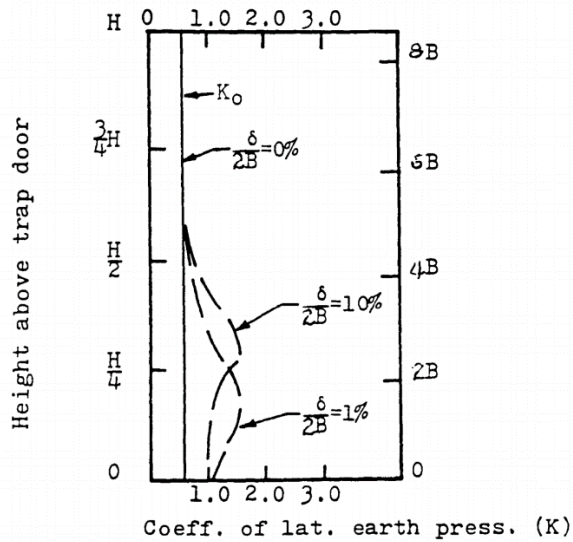


Figure 2-19: Coefficient of lateral earth pressure in trapdoor experiment (Terzaghi, 1936; Revised by Evans, 1983)

From the results given above Terzaghi developed a theoretical model for soil arching in plane strain problems (Terzaghi, 1943). This theory focused on the shearing resistance that develops on the failure plane between the moving soil mass above the trapdoor and the adjacent stationary soil mass. This shearing resistance allows for transfer of forces between the bodies. Terzaghi's approach is indicated in Figure 2-20 showing a yielding soil mass above a trapdoor **ab** of width $2B$. He simplified calculations by assuming two vertical sliding surfaces (**ae** and **bf**) as opposed to the actual sliding surfaces (**ac** and **bd**) which are curved outward from the trapdoor edges. A free body diagram showing all forces on an infinitesimal layer of soil in the yielding zone is shown in Figure 2-21. Horizontal stresses are taken to be $K\sigma_v$ where an empirical value of K equal to unity has been recommended by Terzaghi based on experimentation. Taking vertical equilibrium of the forces in the free body diagram and solving the differential equation yields an equation for the load on the trapdoor:

$$\sigma_v = \frac{B(\gamma - c/B)}{K \tan \varphi} (1 - e^{-K \tan \varphi z/B}) + qe^{-K \tan \varphi z/B}$$

Since the stress state of the soil above a height of $5B$ is not influenced by small displacements of the trapdoor, the soil above that height can be treated as a surcharge. Taking the height of the soil body above this level as n_1B and the height of the soil below this level as n_2B yields the following solution for the load on the trapdoor:

$$\sigma_v = \frac{B(\gamma - c/B)}{K \tan \varphi} (1 - e^{-K n_2 \tan \varphi}) + \varphi B n_1 e^{-K n_2 \tan \varphi}$$

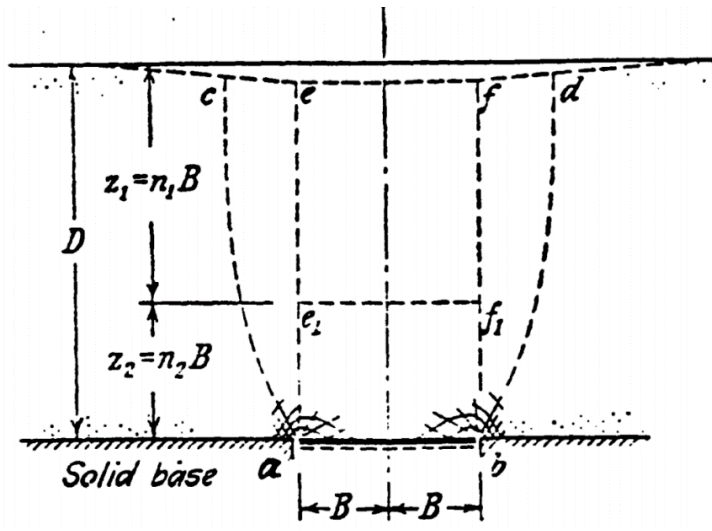


Figure 2-20: Assumed vs. actual sliding surfaces in a soil mass above a yielding trapdoor (Terzaghi, 1943)

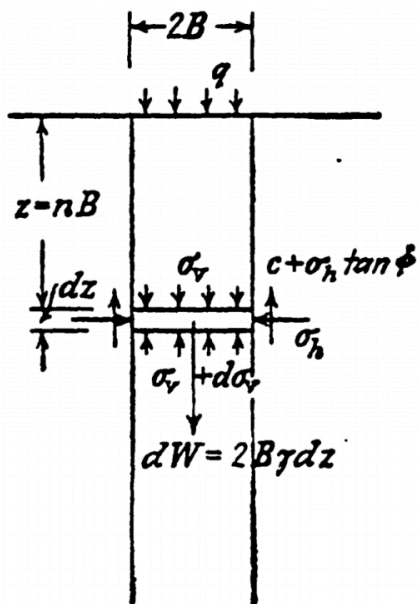


Figure 2-21: Free body diagram of a slice of soil in the yielding zone (Terzaghi, 1943)

Terzaghi (1943) and Evans (1983) noted that this model has several limitations, namely:

- a. The vertical stresses on the horizontal sliding surfaces are assumed to be uniform while the actual vertical stresses vary as is evident in Terzaghi's trapdoor experiments.
- b. The trapdoor is assumed to be rigid whereas the receding support is usually more flexible in reality.

- c. The assumed sliding surfaces are vertical whereas the actual sliding surfaces are parabolically shaped as seen in Figure 2-20.
- d. The coefficient of lateral earth pressure K is assumed to be unity as recommended by Terzaghi whereas experiments have shown it to vary between 0.6 and 1.6, as seen in Figure 2-19.

Due to the limitations regarding K in Terzaghi's design, researchers have proposed different values for this parameter. Marston (1930) suggested using the active Rankine ratio (K_a) in his work on tunnel design.

$$K_a = \frac{1 - \sin \phi}{1 + \sin \phi}$$

Iglesia et al. (1991) noted that this value is originally derived from the assumption that horizontal and vertical stresses are both principal stresses. The use of K_a in this case would thus only be valid if there are no shear stresses acting in the soil. Since shear stresses acting on the vertical failure planes form part of the definition of soil arching it is evident that shear stresses are present and thus K_a cannot be used. Iglesia et al. (1991) suggested a different method for calculating K by assuming the soil on the vertical bands to be in failure and using the geometry and principles of a Mohr circle to calculate horizontal and vertical stresses that are not principal, as seen in Figure 2-22. He suggested the value for K as given in the equation below. This value for K has been accepted and used by several other researchers (Ladanyi & Hoyaux, 1969; Evans, 1983; Iglesia et al., 2014).

$$K_K = \frac{1 - \sin^2 \phi}{1 + \sin^2 \phi} = \frac{\cos^2 \phi}{1 + \sin^2 \phi}$$

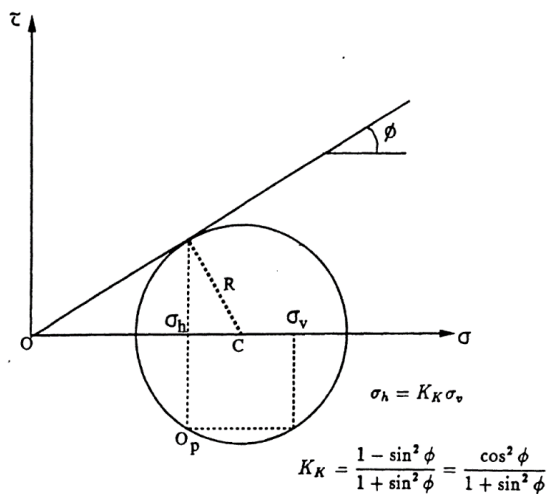


Figure 2-22: Derivation of K_K as a coefficient of lateral earth pressure (Iglesia et al. 1991)

2.3.3 Typical Results of Physical Trapdoor Studies

Since Terzaghi's initial experiments, numerous extensions of this study have been performed in physical laboratory experiments (McNulty, 1965; Ladanyi & Hoyaux, 1969; Vardoulakis et al., 1981; Evans, 1983; Chevalier et al., 2009) and more recently using scaled centrifuge modelling (Stone, 1988; Dewoolkar et al., 2007; Costa et al., 2009; Iglesia et al., 2011; Iglesia et al., 2014). Tien (1990) provides an extensive literature study on soil arching and discusses several of the older experiments in greater detail.

Previous studies on soil arching have focused on various aspects of the phenomenon including load-displacement curves (featuring a plot of normalized load on the trapdoor against normalized trapdoor displacement), failure mechanisms and surface settlement. Some recent studies have also measured local displacements of various regions in the soil to calculate strain distributions. The literature regarding each of these aspects is now discussed separately.

2.3.3.1 Load-Displacement Curves

To correct for stress distributions in the soil that was introduced by Terzaghi's small scale experiments, McNulty (1965) introduced a surcharge of air pressure at the soil surface to simulate more realistic stresses. He measured the load on the trapdoor in both active and passive arching tests and achieved results similar to that of Terzaghi. Ladanyi and Hoyaux (1969) performed similar experiments using an idealized medium of sanded aluminium rods instead of sand in a plane-strain environment. This test was performed with several H/B ratios and results showed that a greater overburden depth resulted in a greater reduction in the normalized load at the onset of trapdoor displacement (Figure 2-23). As in Terzaghi's results, an initial drop in pressure was observed followed by an eventual increase towards a constant pressure. Evans (1983) performed a similar test with a rectangular trapdoor in plane strain conditions and found similar results (Figure 2-24).

A more important aspect of the work of Ladanyi and Hoyaux (1969) was to investigate the validity of Terzaghi's simplifying assumption of two vertical sliding planes extending from the trapdoor to the surface as opposed to the actual slanted sliding planes (see Figure 2-20). They used the method proposed in Terzaghi (1943) to calculate pressures on the trapdoor for different overburden depths and found good correlation with measured results, concluding that Terzaghi's assumptions were reasonable when calculating pressure variations on a trapdoor.

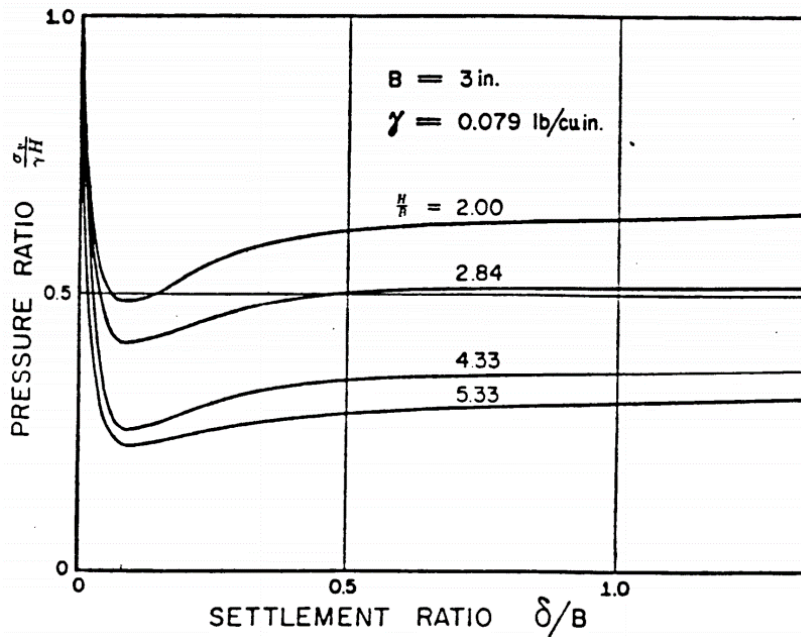


Figure 2-23: Normalized stress vs. trapdoor displacement for various H/B ratios (Ladanyi & Hoyaux, 1969)

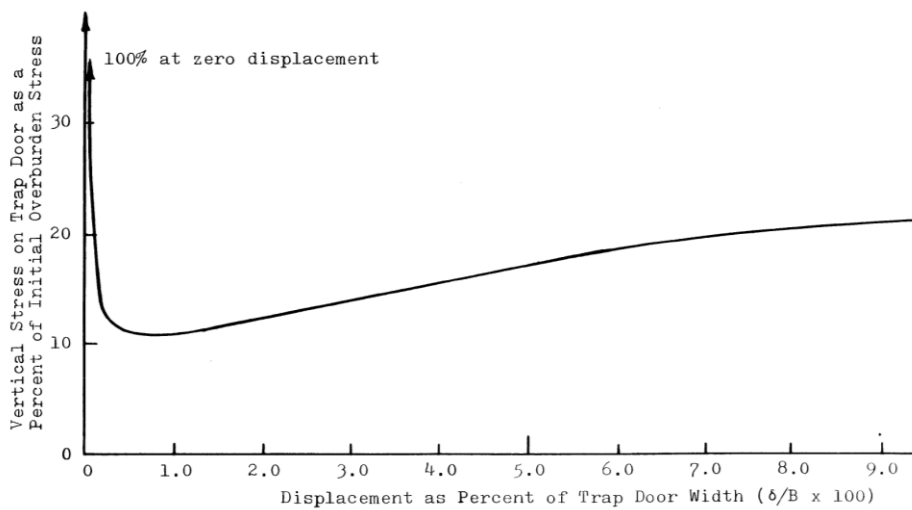


Figure 2-24: Normalized stress vs. trapdoor displacement (Evans, 1983)

Perhaps the best generalized explanation of observations regarding load-displacement curves was given by Iglesia et al. (2014) in one of several papers by this author stemming from an initial “modelling of models” experiment that was conducted to investigate the relationships of scaled trapdoor models in the centrifuge (Iglesia, 1991). Figure 2-25 shows a typical load-displacement curve plotting normalized load on the trapdoor P/P_0 against normalized trapdoor displacement δ/B . A sharp initial decrease in the load on the trapdoor is observed as soon as the trapdoor is retracted. A *breakpoint* or change in direction of this curve is reached at an average

of $0.1 \delta/B$ where load reduction stabilizes from a linear downward trend up to a point of *minimum load* corresponding to an area of “maximum arching” where the greatest amount of load is being carried by the arch. The load then gradually increases at a rate termed the load increase index and recovers up to an ultimate load where further retraction of the trapdoor will not result in a greater load on the trapdoor.

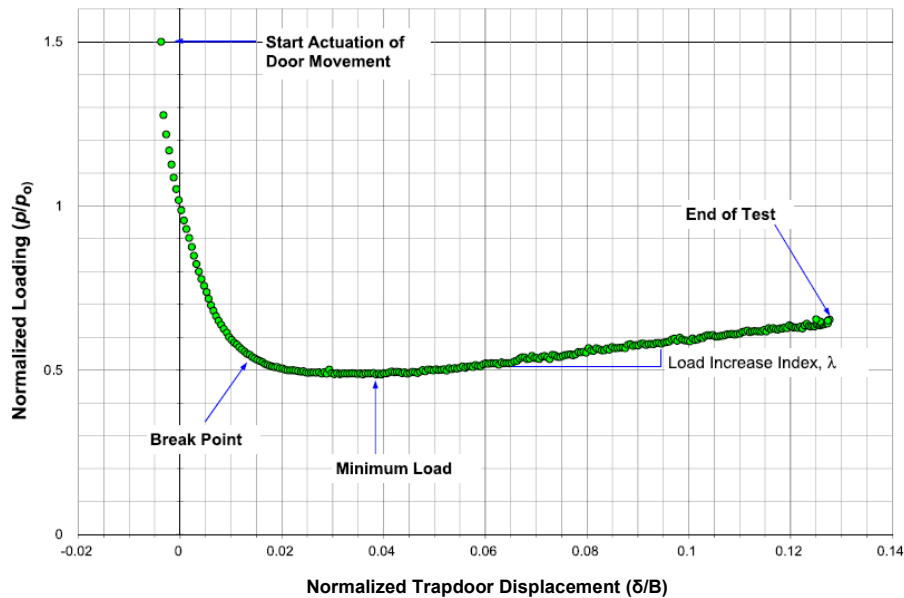


Figure 2-25: Typical loading vs. trapdoor displacement plot (Iglesia et al., 2014)

Actual results from tests performed by Iglesia et al. (2014) are shown in Figure 2-26 in which he compares load-displacement curves of tests with several H/B ratios. The breakpoints and points of minimum load are noticeable in each test, and it is seen that load recovery happens faster in tests with a lower H/B ratio. It is apparent that tests with similar H/B ratios (indicated by brackets in the table) demonstrated similar results even though the actual geometry of the respective setups varied. Evans (1983) noted similarly that soils with equal H/B ratios demonstrated similar arching behaviour.

It is commonly accepted by researchers that tests with an $H/B > 2$ behave differently than tests with $H/B < 2$ (Davis, 1968; Sloan et al., 1990). Terazghi (1943) suggested a lower limit to the overburden height below which soil arching cannot take place and set this limit at an H/B ratio of about 1.5 – 2. Tests by Dewoolkar et al. (2007) reinforced this when he plotted the minimum load P_{\min} and ultimate load P_{ult} on the trapdoor against H/D (using D as the width of the trapdoor) for several tests and found a definite change in behaviour between setups with $H/B > 2$ and setups with $H/B < 2$, as seen by the change in slope of trendlines in Figure 2-27. Evans (1983) noted that the load on the trapdoor decreased with increasing H/B for shallow soils (H/B

< 2), but that the maximum load changed little for deeper soil ($H/B > 2$), as is also evident in Iglesia's results in Figure 2-26.

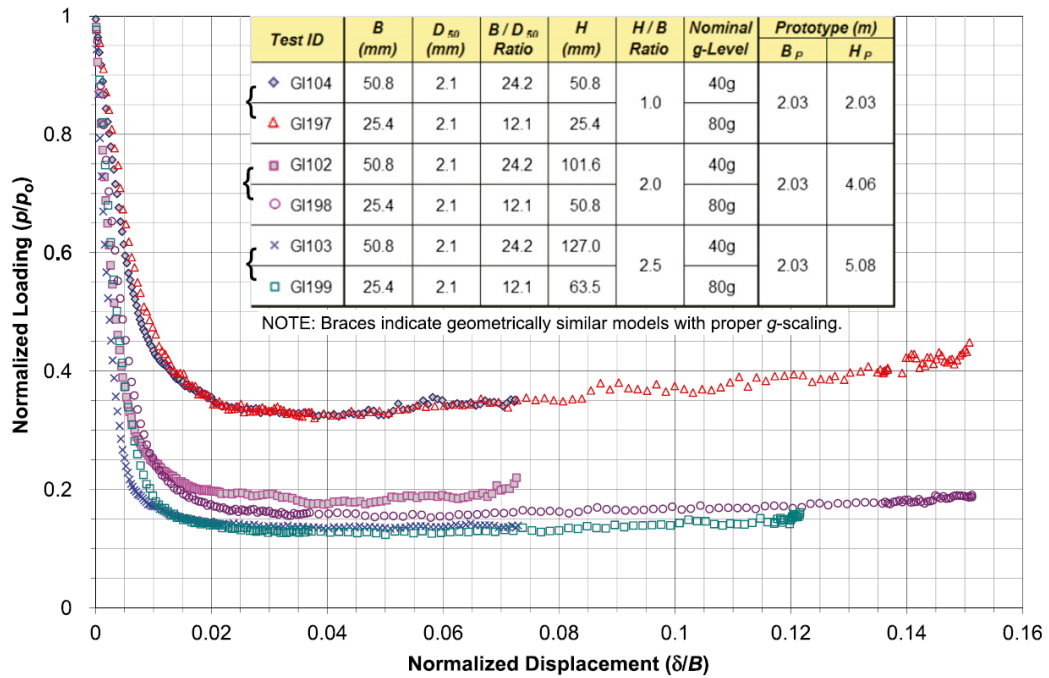


Figure 2-26: Comparison of load-displacement curves of several H/B ratios (Iglesia et al., 2014)

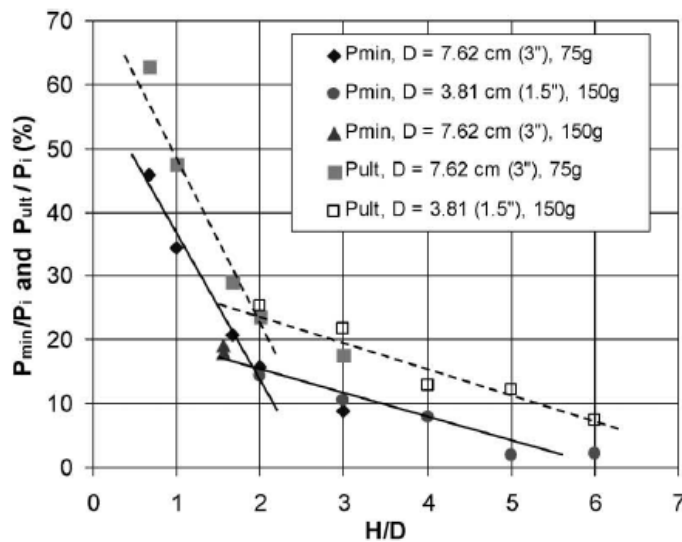


Figure 2-27: Different behaviour of trapdoor tests above and below an H/D ratio of 2 (Dewoolkar, 2007)

Iglesia et al. (2014) further compared the breakpoints and points of minimum load across several H/B ratios and found that, although the normalized minimum load decreased with an increase in H/B, the minimum load points occurred at roughly the same absolute stress as well

as the same normalized displacement (δ/B), regardless of the H/B ratio (Figure 2-28). This suggests that a similarly-sized stable arch formed directly above the trapdoor in each test and that the volume of soil underneath the arch in each test was independent of the H/B ratio. It is also interesting to note that the breakpoints of all tests occurred at roughly the same trapdoor displacement, further reinforcing this idea.

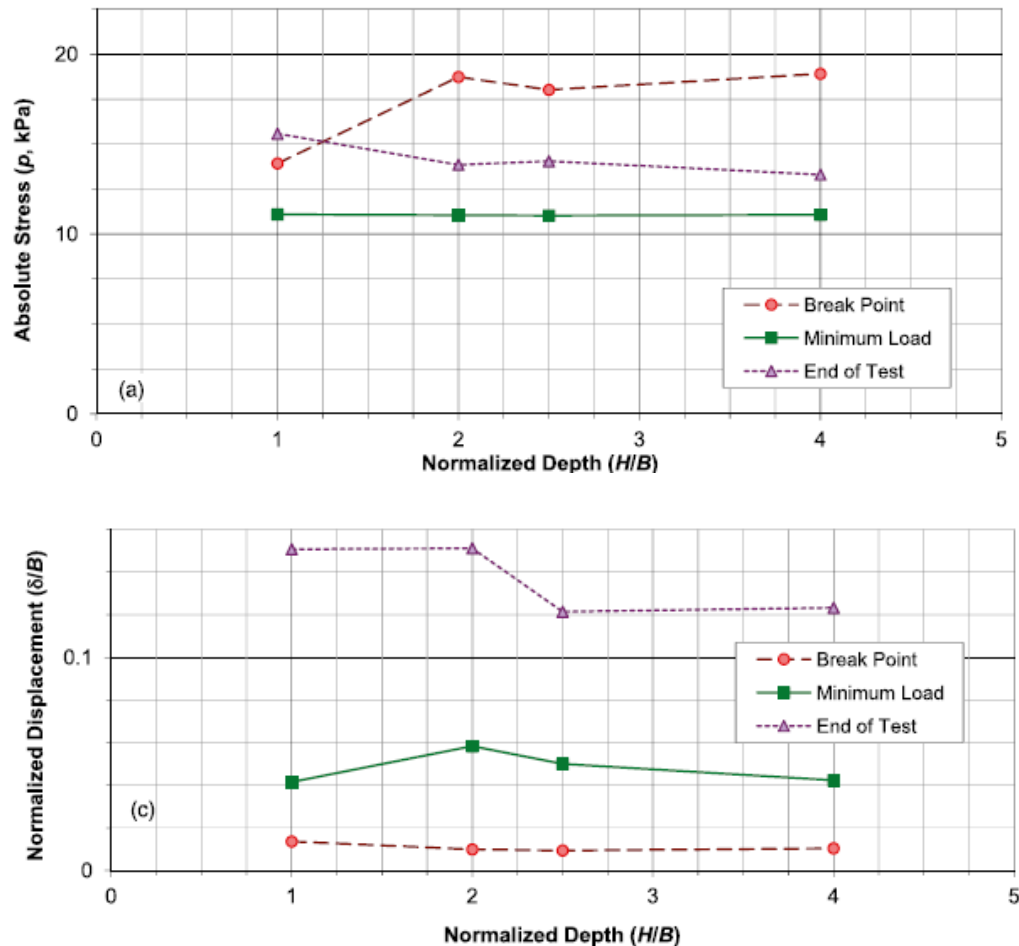


Figure 2-28: Comparison of trapdoor load readings across several H/B ratios (Iglesia et al. 2014)

It can be concluded from this section that the load on the trapdoor is sensitive to the H/B ratio rather than the exact geometry, that actual arching occurs only in tests with an H/B ratio greater than 2 and that the amount of load reduction is dependent on the H/B ratio and normalized trapdoor displacement.

2.3.3.2 Failure Mechanisms

In addition to load-displacement curves, researchers have also investigated the shape of failure mechanisms in a trapdoor test. Several methods have been used to record failure mechanisms

including photography, model dissection and measurements of load distributions on the trapdoor. Ladanyi & Hoyaux (1969) photographed their model during trapdoor drawdown with a camera that moved simultaneously with the trapdoor (Figure 2-29a), allowing visualization of the body of soil directly above the trapdoor but below the first mechanism, which consequently experienced no deformation for the entirety of the test. This body of soil took on a triangular to parabolic shape.

Vardoulakis et al. (1981) photographed coloured bands in a shallow body of soil (low H/D ratio) and recorded a triangular dilation zone like the one described above and later a final column-like mechanism, albeit with a small inward curve near the surface on the otherwise vertical boundary (Figure 2-29b). Stone (1988) deduced failure planes by tracking the locations of several buried markers through model dissection after the test. Evans (1983) used pressure transducers to measure the load distribution across several trapdoors where he simulated an advancing tunnel by lowering a series of adjacent trapdoors one after the other. The general load distribution took on the form of a triangle or parabola (seen in Figure 2-30a) at a δ/B ratio of 0.01 and closely resembled the results of Harris (1974) shown in Figure 2-30b. Evans noted that this mechanism agreed well with predictions made by his plasticity theory solution for the load on the trapdoor, developed in the same publication.

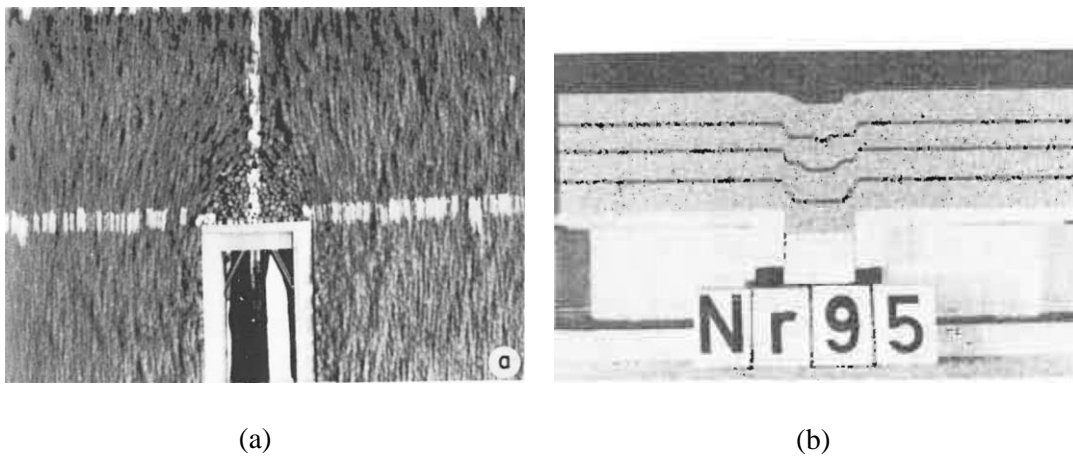


Figure 2-29: (a) Failure mechanism (with camera moving simultaneously with trapdoor) (Ladanyi & Hoyaux, 1969) and (b) Failure mechanism after large trapdoor displacements (Vardoulakis et al. (1981))

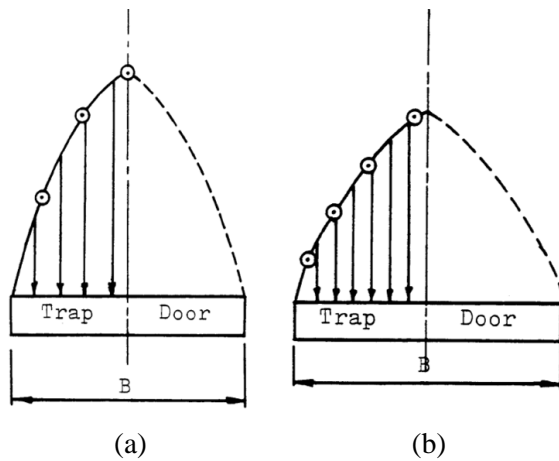


Figure 2-30: Comparison of pressure distributions above a trapdoor as measured by (a) Evans (1983) and (b) Harris (1974) (after Evans (1983))

The consensus between researchers regarding failure mechanisms is that failure occurs as a series of shear bands that originate at the trapdoor edges and form upwards and towards the trapdoor centreline, together creating a failure mechanism that divides the soil continuum. Most researchers observed three distinct failure phases (visible in Figure 2-31 and Figure 2-32), each with a different mechanisms: (1) an initial triangular or parabolic mechanism with the trapdoor as base and the apex above the centre of the trapdoor, progressing to (2) a transitional phase consisting of one or more parabolic mechanisms with roughly the same shape as the initial mechanism, dilating and progressing upwards through the soil body until ultimately reaching (3) a vertical column-like mechanism with the sides coinciding with the edges of the trapdoor (Vardoulakis, 1981; Tanaka, 1983; Chevalier et al., 2009; Iglesia et al., 2014).

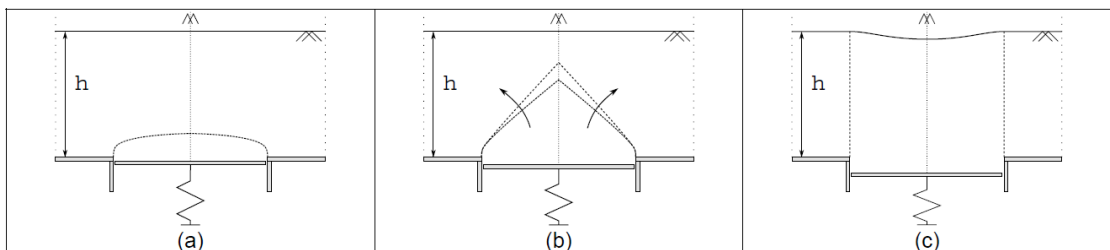


Figure 2-31: Three phases of failure mechanisms observed by Chevalier et al. (2009)

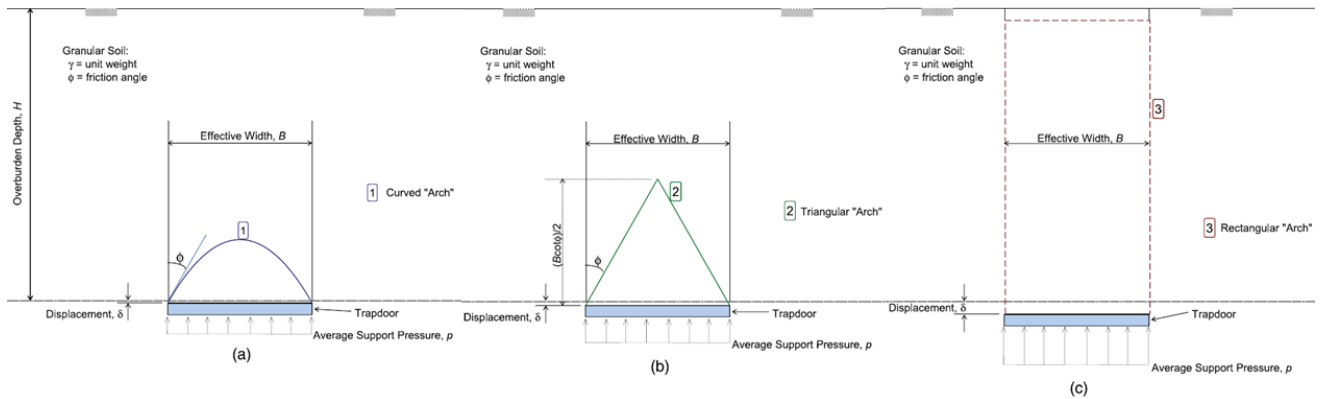


Figure 2-32: Three phases of failure mechanisms observed by Iglesia et al. (2014)

In all studies, Phase 1 consisted of a single pair of shear bands forming from the edges of the trapdoor and meeting at a line of symmetry in the centre of the trapdoor. Researchers differ on the shape of this initial phase, with Iglesia et al. (2014) and Chevalier et al. (2009) suggesting a parabolic shape while Evans (1983) based his theory on an initial triangular shape. However, all agree that this initial mechanism is formed by two shear bands forming from the edge of the trapdoor and meeting at a point along the trapdoor centreline.

Phase 2 was characterized by various secondary shear bands forming successively above one another. Tanaka (1993) described phase 2 as the continuous propagation of two symmetrical shear bands until they reach the top of the soil surface. Transition between successive shear bands in this phase have been observed to occur suddenly with deformation ceasing almost completely along the initial shear band and with the soil between the two shear bands playing very little role in either mechanism and remaining relatively rigid (Stone, 1988; Stone, 1992; Dewoolkar, 2007; Costa et al. 2009). Chevalier et al. (2009) noted that the transitional phase lasted until the dilatant zone (failure zone) reached the surface.

Finally, phase 3 consisted of a rectangular, chimney-like mechanism shearing on vertical sides that extended upwards from the trapdoor edges, similar to what Terzaghi (1943) assumed in his classical arching theory. When the zone of influence (or dilatant zone) reached the surface, the soil in this zone tended to settle down at a ratio of close to unity with that of the trapdoor's settlement.

It has been observed by various researchers (Stone, 1988; Santichaiant, 2002; Dewoolkar, 2007; Costa et al., 2009) that the angle formed between the vertical and a line tangent to any shear band is roughly equal to the dilation angle of the soil at the specific point and at the specific time of shear band formation. The angle of dilation ψ_{max} has been empirically

determined by Bolton (1986) to be a function of relative density and confinement/stress level in the soil, as defined in the following equation:

$$\psi_{max} = 6.25[I_D(10 - \ln p') - 1]$$

Where:

ψ_{max} = dilation angle (°)

I_D = relative density of the soil

p' = stress level (kPa)

A visual representation of Bolton's equation is shown in Figure 2-33 with the dilation angle plotted against stress level (increasing linearly with depth) for various relative densities (D_r).

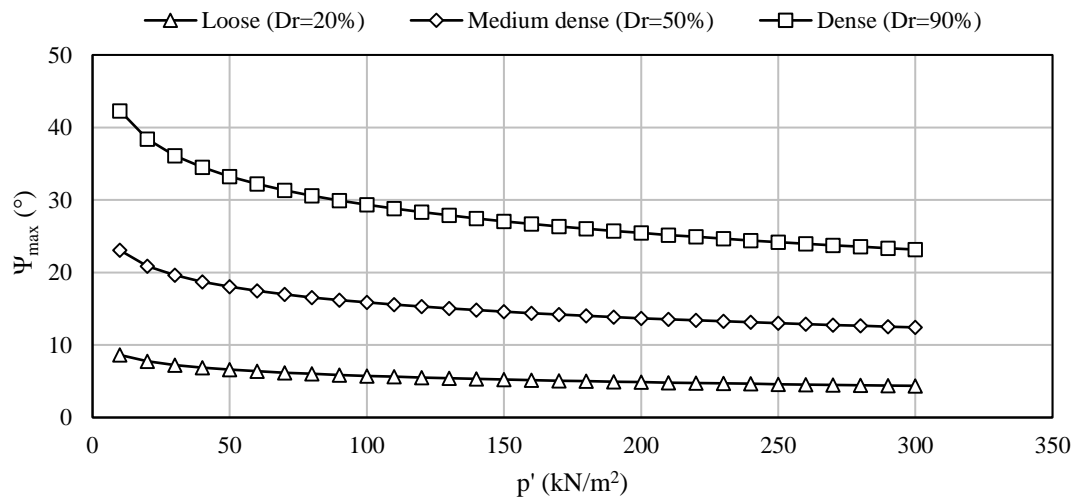


Figure 2-33: Comparison of dilation angle with depth for soils of various relative densities (D_r)

Consequently, the path and slope followed by a shear band is dictated by the relative density and stress level of the soil. A soil experiencing a greater stress would have a low dilation angle and thus a shear band at that location would form more vertically (smaller angle with the vertical) than in a region of lower stress. Dewoolkar (2007) showed physical evidence of this by noting that shear bands in high gravity tests (Figure 2-34b) curved inwards to a much greater degree than those in single gravity tests (Figure 2-34a). This occurred because stress levels were more varied across soil layers in higher-gravity tests, causing dilation angles to be more varied across soil layers. In addition, Bolton's equation also predicts that a region of soil with a low relative density would have a low dilation angle and thus a shear band forming in that region would form more vertical than in a region with a high relative density.

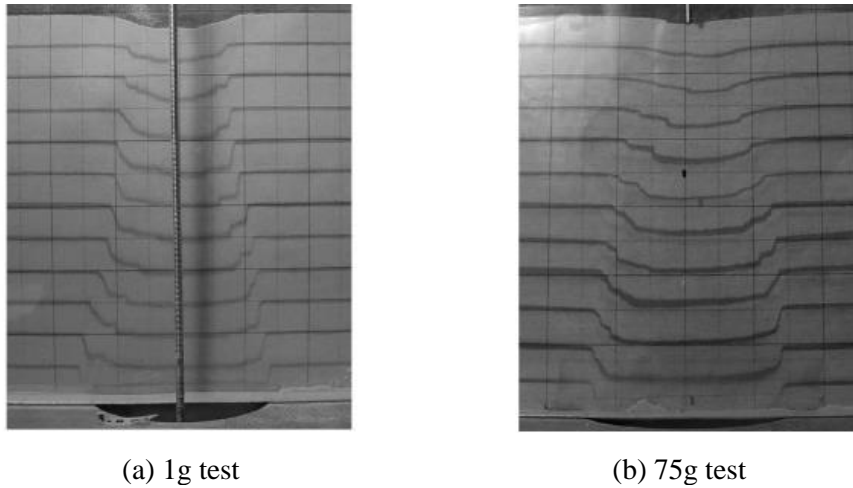


Figure 2-34: Shear band propagation at (a) single gravity and (b) in a centrifuge at 75g (Dewoolkar, 2007)

This concept is better described in a schematic by Costa et al. (2009) shown in Figure 2-35 in which the soil at point O directly above the trapdoor experiences a maximum stress level relative to the rest of the soil body, thus possessing a small dilation angle θ_{i-OA} . At a trapdoor settlement of δ_1 the initial shear band OA originating from this point thus forms at an angle θ_{i-OA} with the vertical. Soil particles higher up on the shear band experience progressively smaller stress levels due to smaller overburdens and thus have greater dilation angles. This results in shear band OA forming at a flatter slope as visible at point A where it forms at an angle $\theta_{i-A} > \theta_{i-OA}$ to the vertical. This continuous increase in dilation angle is the reason for the parabolic shape of the shear band (Costa et al. 2009).

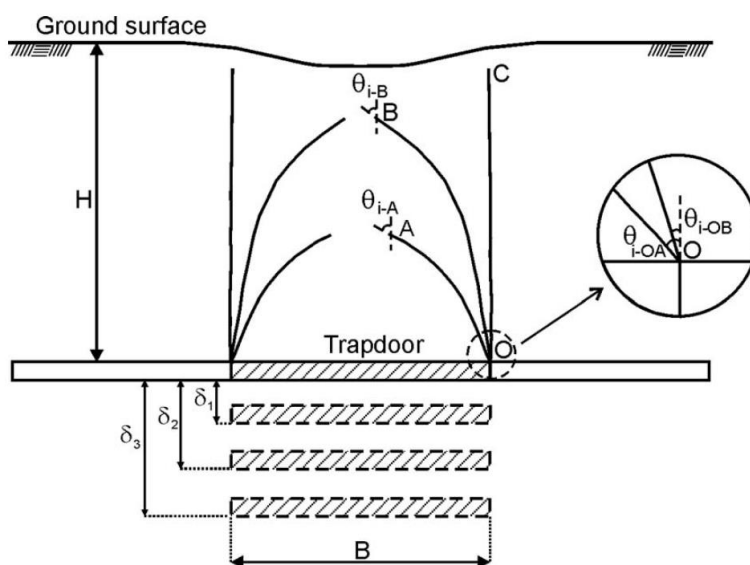


Figure 2-35: Schematic of propagation of shear bands above an active trapdoor (Costa et al., 2009)

At some trapdoor settlement $\delta_2 > \delta_1$ a secondary shear band OB will start forming above the initial shear band, but since the soil at point O had dilated and its relative density had been reduced, the new dilation angle θ_{i-OB} at that location is smaller than θ_{i-OA} , causing shear band OB to form at a more vertical angle. It has been observed that a series of successive shear bands will form in this way until a near-vertical shear band (shear band OC in Figure 2-35) finally forms from the edge of the trapdoor at some trapdoor settlement of $\delta_3 > \delta_2$. At this point, the soil at point O is assumed to have reached the critical state and have thus attained an insignificant dilation angle, resulting in a vertical shear band.

It has already been mentioned that deformation in a trapdoor test shifts abruptly from one shear band to the next. Stone (1988) shed some light on the criteria that dictates when such a shift takes place. He performed single gravity trapdoor tests and noted that shear band formation tended to be more complex in finer sand than coarse sand. He also noted that when comparing images with similar ratios of trapdoor settlement (Δ_B) to average particle size D_{50} , the shear band formation at various stages of the test tended to be similar regardless of the particle size, as seen in Figure 2-36. He concluded that the *magnitude* of relative movement of soil particles on both sides of a shear band play a role in the shape of the shear band and the onset of subsequent secondary shear bands, and that the formation of a secondary shear band is dictated by the point during the test where dilation along the initial shear band reduces to a point where deformation along that band is no longer kinematically admissible, thus triggering a halt of deformation along the initial shear band and a sudden shift to the secondary shear band.

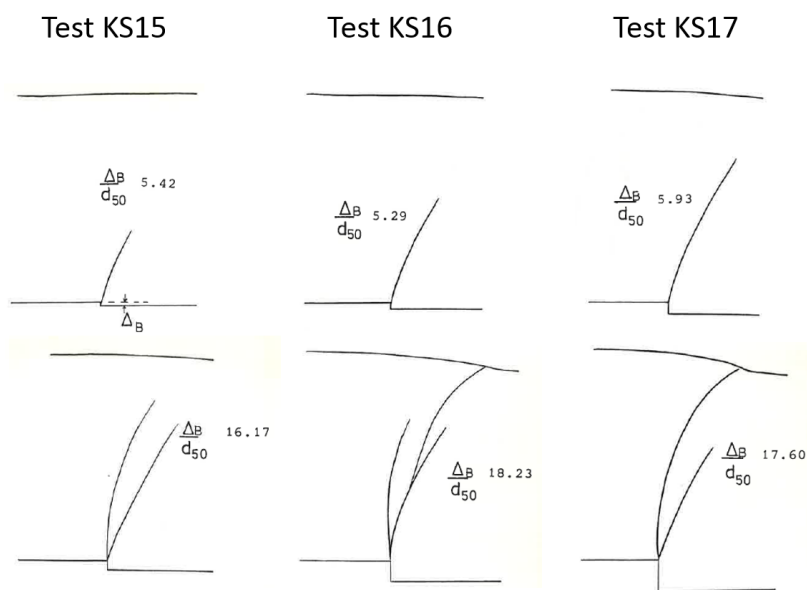


Figure 2-36: Shear bands of tests with similar ratios of trapdoor settlement (Δ_B) to D_{50} (Stone, 1988)

Stone (1988) also discussed the effects of stress level and particle size on the observations stated above. Firstly, an increased stress level (greater H/B ratio) will delay the formation of secondary shear bands because a greater relative movement is necessary to attain critical state along the first shear band and thus trigger formation of a secondary shear band. Second, a larger particle size requires a greater relative movement for the critical state to be reached along the first shear band. For this reason, formation of secondary bands in coarser sand is delayed because of greater trapdoor displacement necessary to trigger formation of a secondary shear band.

It can be concluded from this section that failure in a trapdoor occurs in three phases – an initial phase with one triangular or parabolic mechanism, a transitional phase with several parabolic shear bands propagating upwards and a final phase with a vertical, column-like mechanism. Shear bands form at angles with the vertical that are equal to the dilation angle in the soil at that point. In addition, deformation shifts abruptly from one shear band to the next at which point deformation on the initial shear band ceases entirely.

2.3.3.3 Surface Settlement Distributions

Research on surface settlement above a receding trapdoor has largely focused on finding an equation to describe the shape of the settlement trough. The volume of the settlement trough does not necessarily equate to the volume of soil being displaced by the trapdoor due to dilation in the soil (Evans, 1983) and thus a relationship between the two phenomena cannot be reached through pure geometric calculations.

Peck (1969) performed research on settlement troughs above a tunnel and suggested that a normal curve could be found that closely resembles the shape of such a trough. An example of this curve is shown in Figure 2-37, the equation of which requires the specification of the depth δ_{\max} of maximum settlement along the trapdoor centreline and the horizontal distance i from the centreline to the inflection point. Attewell (1977) also noted that the shape of a settlement trough resembles a normal curve at small trapdoor displacements, but then transitions to a V-shaped curve at higher displacements. Evans (1983) defined these larger displacements as models with an $H/B < 1$ and a trapdoor displacement $\delta/B > 0.3$ based on experimentation.

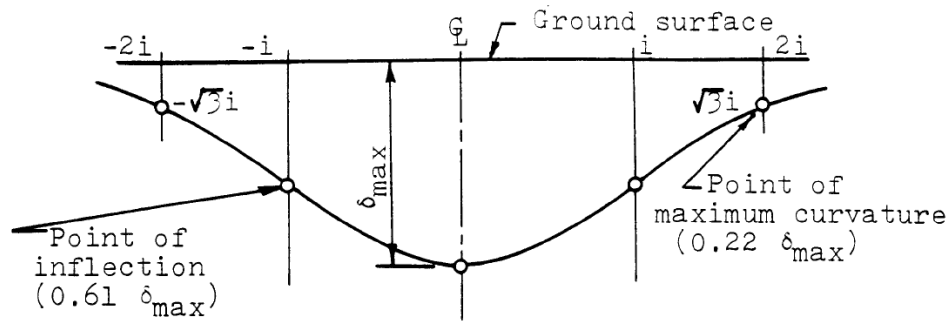


Figure 2-37: Normal curve resembling the shape of a settlement trough (Peck (1969) revised by Evans (1983))

In his trapdoor tests Evans (1983) approximated a perfect fit by choosing parameters of the normal curve to best fit his experimental data (Figure 2-38). He found good agreement between the two but noted that the width of the observed troughs tended to be somewhat narrower than that of the normal curve.

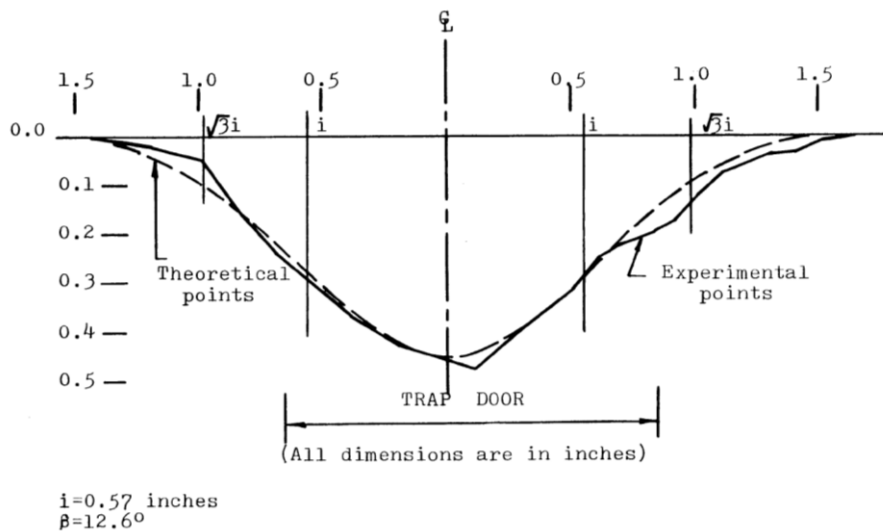


Figure 2-38: Shape of a settlement trough compared to a normal curve (Evans, 1983)

As an alternative method to describe surface settlement, Costa et al. (2009) noted that the shape of the soil surface after settlement closely resembled that of a Gaussian distribution as shown in Figure 2-39 and described by the equation below. The equation for a Gaussian curve does not contain soil parameters and is purely empirical, but it has proven to be a good prediction of surface settlement in tunnelling problems (Peck, 1969) and is now widely used in the geotechnical discipline.

$$s_x = s_{max} e^{-0.5 \left(\frac{x^2}{i^2} \right)}$$

Where:

s_{max} = maximum settlement

x = horizontal distance from centreline to where settlement is measured

i = horizontal distance from centreline to inflection point on Gaussian curve

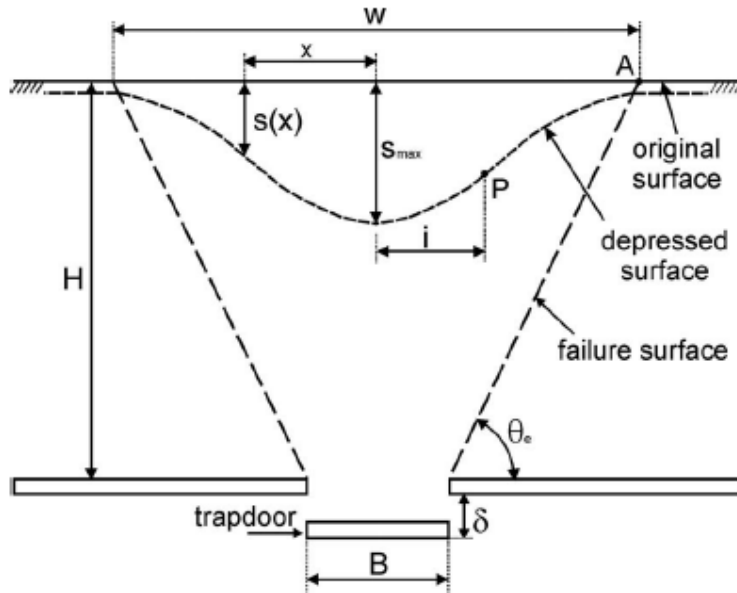


Figure 2-39: Gaussian curve resembling the shape of a settlement trough (Costa et al., 2009)

Factors that influence the amount of surface settlement include stress levels and soil density, with loose soils showing significantly more settlement than dense soils (Costa et al., 2009). Dewoolkar (2007) noted that high stress conditions caused shear bands to curve more towards the centre (Figure 2-40b), reaching the surface at a point closer to the trapdoor centreline and thus creating a smaller initial depression than in lower stress conditions (Figure 2-40a), where shear bands reach the surface at points directly above the trapdoor edges and thus creating a larger initial depression. Since stress levels greatly influence the dilation angle and thus the angle of shear bands as noted by Costa et al. (2009), these curved shear bands observed by Dewoolkar (2007) are in line with that of Costa et al (2009).



(a) 1g test

(b) 75g test

Figure 2-40: Surface depressions in (a) single gravity and (b) in a centrifuge at 75g (Dewoolkar, 2007)

Dewoolkar (2007) presented a plot of surface settlement against trapdoor settlement (Figure 2-41a) and noted that initial surface settlement was observed immediately after the onset of trapdoor displacement. He further noted that the plot demonstrated two distinct lines at different angles. The inflection point between these two sections occurs when the dilatant zone (or shear zone) reached the soil surface, corresponding to point 3 on the load-displacement plot (Figure 2-41b). Dewoolkar denoted this point 3 as the point of *minimum arching* since further retraction of the trapdoor would not result in a greater load. The angle of the second section was close to 45° , signalling a 1:1 ratio of surface settlement to trapdoor settlement. At this point, no more arching occurred in the sand and the entire column of soil above the trapdoor receded uniformly with the trapdoor. Dewoolkar further noted that in tests with very great overburden depths the second portion of the curve may not be detected, while in tests with very shallow overburdens the initial portion of the curve may merge with the second portion and also remain undetected.

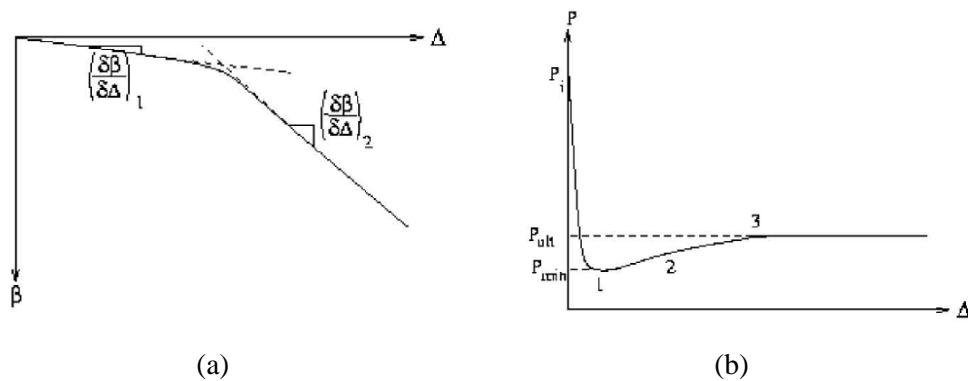


Figure 2-41: Relationship between graphs of (a) surface settlement to trapdoor displacement, and (b) trapdoor load to trapdoor displacement, with increasing trapdoor displacement (Dewoolkar, 2007)

It can be concluded from this section that surface settlement above a trapdoor can be approximated using a normal/Gaussian curve of which the parameters have been adjusted to attain a perfect fit. It was also concluded that stress levels and soil density affect the amount of surface settlement observed and that the ratio of surface settlement to trapdoor settlement increases to a value close to unity once the zone of influence reaches the surface.

2.3.3.4 Strain Distributions

Strain distributions in a trapdoor test can provide considerable insight into the test, but due to the difficulty of measuring such strains with conventional methods, they are sparse in literature. Stone (1988, 1992) placed discrete markers in his trapdoor tests and analysed the movement of these markers through digitisation of photographs and radiographs, enabling the visualization

of strain distributions throughout the soil. In plots of maximum shear strain (Figure 2-42) it was shown that shear strains occurred primarily along shear bands, while the rest of the soil body experienced insignificant shear strain.

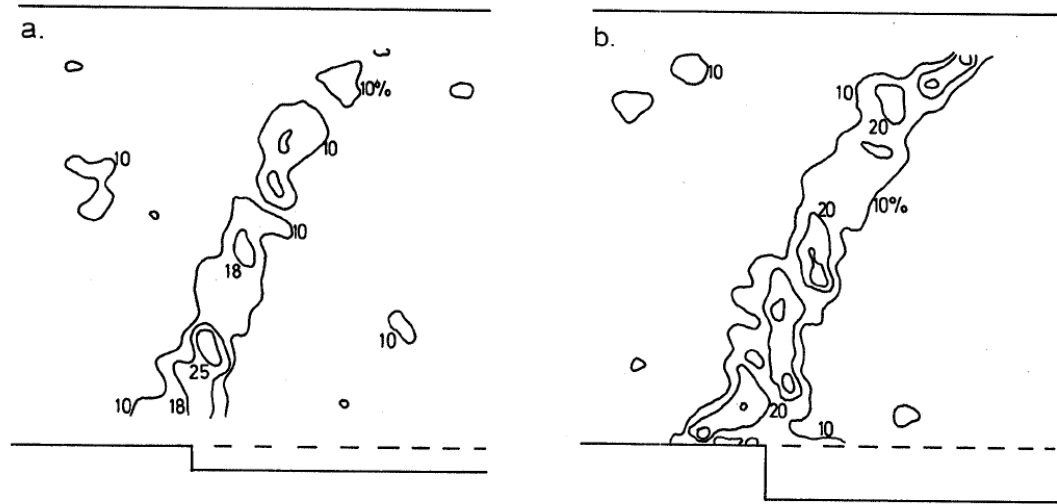


Figure 2-42: Typical maximum shear strain distributions in sand above a trapdoor at incremental trapdoor displacements (Stone, 1992).

Evans (1983) noted that excessive volumetric strains occurred in regions above the trapdoor as the soil dilated, and this was confirmed by Costa et al. (2009) who presented plots of vertical strain (ϵ_z) for several stages of a trapdoor test (Figure 2-43). Costa further noted that the observed horizontal strains were much lower than vertical strains and thus vertical strains were a close approximation of the overall volumetric strain.

It can be concluded from this section that most shear strain in soil above a receding trapdoor happens along the shear bands, with insignificant shear strains in the soil between these bands, and that excessive volumetric strains occur directly above the trapdoor as the soil dilates.

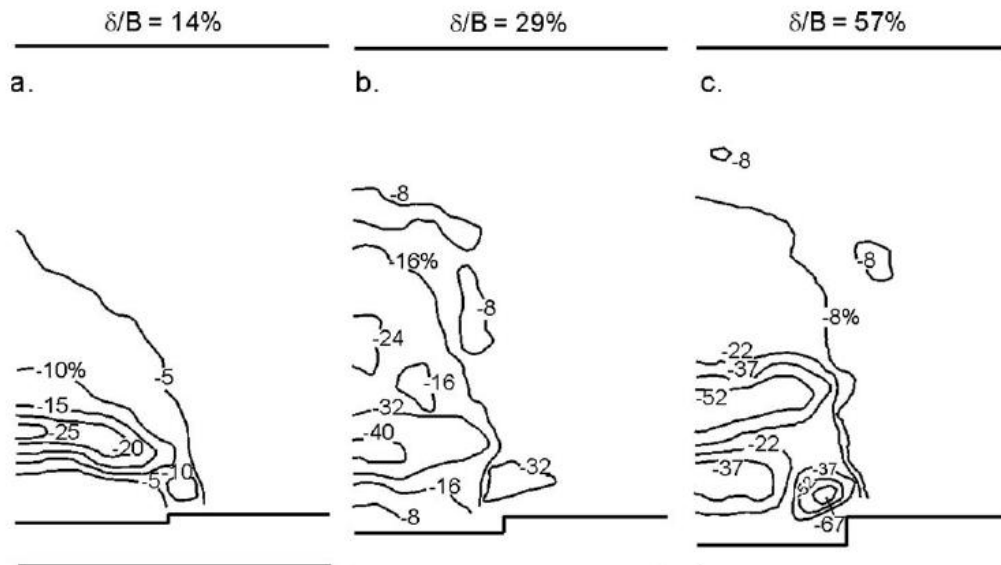


Figure 2-43: Plots of vertical strain (ϵ_z) for three stages during a trapdoor test performed at 45g acceleration (Costa et al., 2009)

2.4 REMAINING QUESTIONS

In this literature review the risk of sinkholes in South Africa was discussed together with existing measures to quantify risk and susceptibility of sinkhole formation in dolomitic areas. Research in this field is an on-going practice.

This review also summarized the current literature on classical soil arching theories and subsequent trapdoor tests that were performed both in single gravity and in centrifuge facilities. Numerous researchers described the test results through means of load-displacement tests, failure mechanism models, surface settlement plots and strain distributions.

Some unanswered questions from this review relate to the influence of moisture on the results of trapdoor tests since no literature was found on the subject. Answers to this scenario are attempted in the remainder of this dissertation, together with the main objective of ascertaining whether a cavity propagates to the surface in a chimney-like fashion rather than a funnel shape.

3 EXPERIMENTAL METHOD

3.1 INTRODUCTION

This chapter discusses the experimental equipment and testing techniques used in the current study. Descriptions of the geotechnical centrifuge, experimental model, measurement instrumentation and data acquisition system are given. A detailed geotechnical description of the materials used are presented. Methods deployed during model preparation and centrifuge tests are explained and imaging techniques and analysis of photographs using particle image velocimetry (PIV) are also described.

3.2 GEOTECHNICAL CENTRIFUGE

When a scaled model of a real-world problem is constructed, the self-weight of the model constituents is less than that of the original. This does not usually pose a problem in structural models since these can be tested accurately without any further modifications (Tien, 1990). However, problems arise when testing geotechnical models due to the stress-strain behaviour of soil. At small strains, soil behaves differently under varying confining stresses (Knappett & Craig, 2012). The shear modulus G (defined as the ratio of shear stress τ and shear strain γ as demonstrated in Figure 3-1a) exhibits a maximum value G_0 at small shear strains ($<0.001\%$) and then decrease nonlinearly to a constant value at larger strains ($>1\%$) as seen in Figure 3-1b. Although soils under various confining pressures converge to the same constant value of G at larger strains, the initial maximum value G_0 seems to increase under greater confining pressure. Strains experienced by the soil in a model would therefore differ from that in the real-world, and the model would thus not be a true representation of reality.

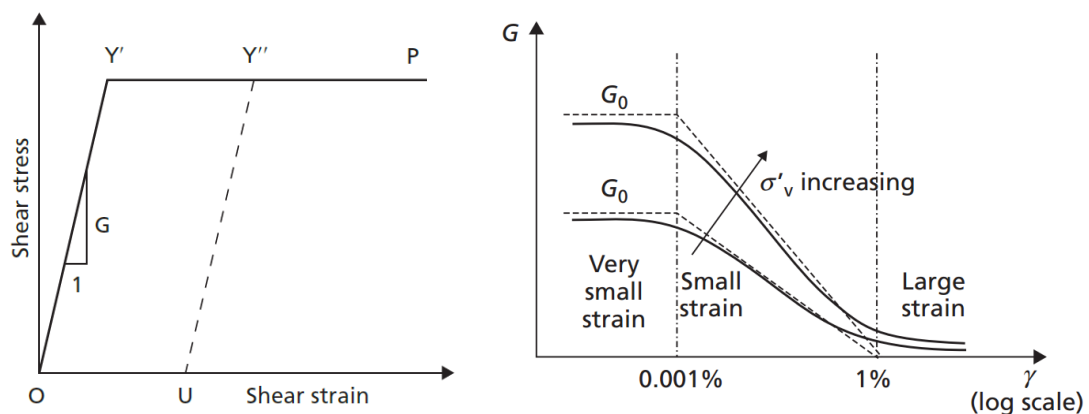


Figure 3-1: (a) Relationship of shear modulus to shear strain and shear stress and (b) non-linear behaviour of shear-modulus at small strains (Knappett & Craig, 2012)

To obtain similar behaviour in the model the confining pressure must be increased. Since geostatic self-weight is calculated by $\gamma = \rho gh$, one way to do this is to increase the gravitational acceleration g . A geotechnical centrifuge performs this task by spinning the model around a central point and increasing downward acceleration through centrifugal forces. The increased acceleration increases the self-weight, resulting in a greater confining pressure and consequently, a model that is more representative of conditions in the real world.

In a centrifuge, the increased gravitational acceleration experienced by the model is described as $N \cdot g$, where N is the scaling factor and g is earth's gravitational acceleration (9.81 m/s^2). The relationship between the two can be demonstrated by the following equation:

$$N = \frac{r\omega^2}{g}$$

Where:

- N = scaling factor
- r = centrifuge arm radius
- ω = angular velocity
- g = earth's gravitational acceleration (9.81 m/s^2)

When gravitational acceleration is scaled by N , other parameters of the model should be scaled accordingly to keep the model representative of reality. Taylor (1995) derived various such scaling factors, the applicable ones of which are given in Table 3-1. The most important of these is the scaling factor for length of $1/N$, showing that a $1/N$ scale model should be accelerated to an acceleration of $N \cdot g$ to represent reality.

Table 3-1: Applicable centrifuge scaling factors (Taylor, 1995)

Quantity (Reality)	Scaling factor (Model)
Length	$1/N$
Displacement	$1/N$
Density	1
Force	$1/N^2$
Stress	1
Strain	1

Models in this study were tested in the geotechnical centrifuge at the University of Pretoria, shown in Figure 3-2. The facility is a model C67-4 beam centrifuge manufactured by Actidyn. It has a 3m arm radius and can accelerate a model of 1 500kg to an acceleration of 100g at

maximum load and acceleration. Some relevant specifications of the apparatus are provided in Table 3-2.



Figure 3-2: Geotechnical centrifuge at the University of Pretoria

Table 3-2: Specifications of the geotechnical centrifuge at the University of Pretoria (Jacobsz et al., 2014)

Specification	Value
Model and Make	Actidyn C67-4
Arm length (radius)	3m
Basket dimensions	0.8m x 1.0m x 1.3m
Maximum acceleration	130g
Maximum load	1,500kg
Maximum acceleration at maximum load	100g
Maximum load at maximum acceleration	500kg

The facility is entirely controlled and monitored from an adjacent control room. Electrical connections to the room allow the operator to remotely control apparatus such as valves and actuators while the centrifuge is in flight. Data acquisition systems on the centrifuge allow for continuous monitoring of measurement equipment such as pressure transducers, displacement

transducers and load cells. A DSLR camera and video camera are also fitted inside the centrifuge basket and both can be remotely controlled and monitored from the control room. The entire centrifuge facility is described in detail by Jacobsz et al. (2014).

3.3 CENTRIFUGE TEST PACKAGE

The test package was constructed and prepared in an adjacent room and transferred onto the centrifuge basket for testing. Several elements make up the centrifuge test package and each part is described in the following sections.

3.3.1 Test Frame

The same test frame was used for all tests in this study. It was essentially an elevated rectangular container (referred to as the “sand box” henceforth) in which sand was held throughout the test and beneath which a trapdoor mechanism was installed. The frame and its supporting structures were made of aluminium and were held together with screws. An image of the unloaded test frame is shown in Figure 3-3 (top view) and Figure 3-4 (front view), and a technical drawing as seen from the same vantage points is shown in Figure 3-5.

The main structural support of the test frame came from two support columns, each consisting of three aluminium channel sections fastened back-to-back as seen in the top view in Figure 3-3. These columns supported the rest of the frame at an elevated height and formed the sides of the sand box. The bases of these two columns were bolted to a 100mm thick steel base plate as seen in Figure 3-4, that matched the size of the centrifuge basket and served as a sturdy base onto which all components of the frame were fixed in place.

The back of the container consisted of a 10mm thick aluminium plate that was bolted on both sides to the support columns as seen in Figure 3-3. Holes in the back plate that were utilized in a previous study had been covered up with several layers of aluminium tape.

The front of the sand box was formed by two 10mm thick glass panes as seen in Figure 3-6. These were glued to a rigid angle-iron U-frame that ran along the side and bottom edges of the glass panels and was strengthened at the corners with triangular gusset plates. The angle iron frame was bolted on both sides to the channel columns. Not only did the U-frame provide a means to keep the glass panes intact but the bottom part also served to restrain out-of-plane buckling of the bottom edge of the glass under lateral soil pressure during centrifuge acceleration. PIV marker dots (discussed later) printed on white paper were glued to the inside of the glass panes and covered with a layer of Desifix for a smooth surface.

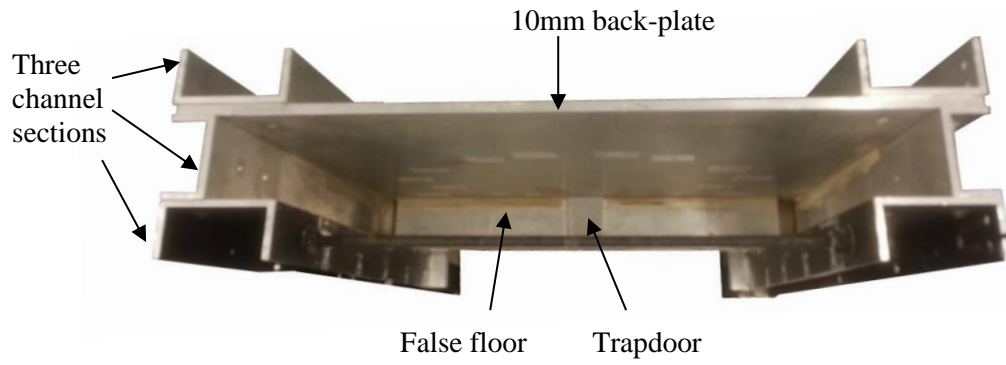


Figure 3-3: Top view of test frame (no sand loaded)

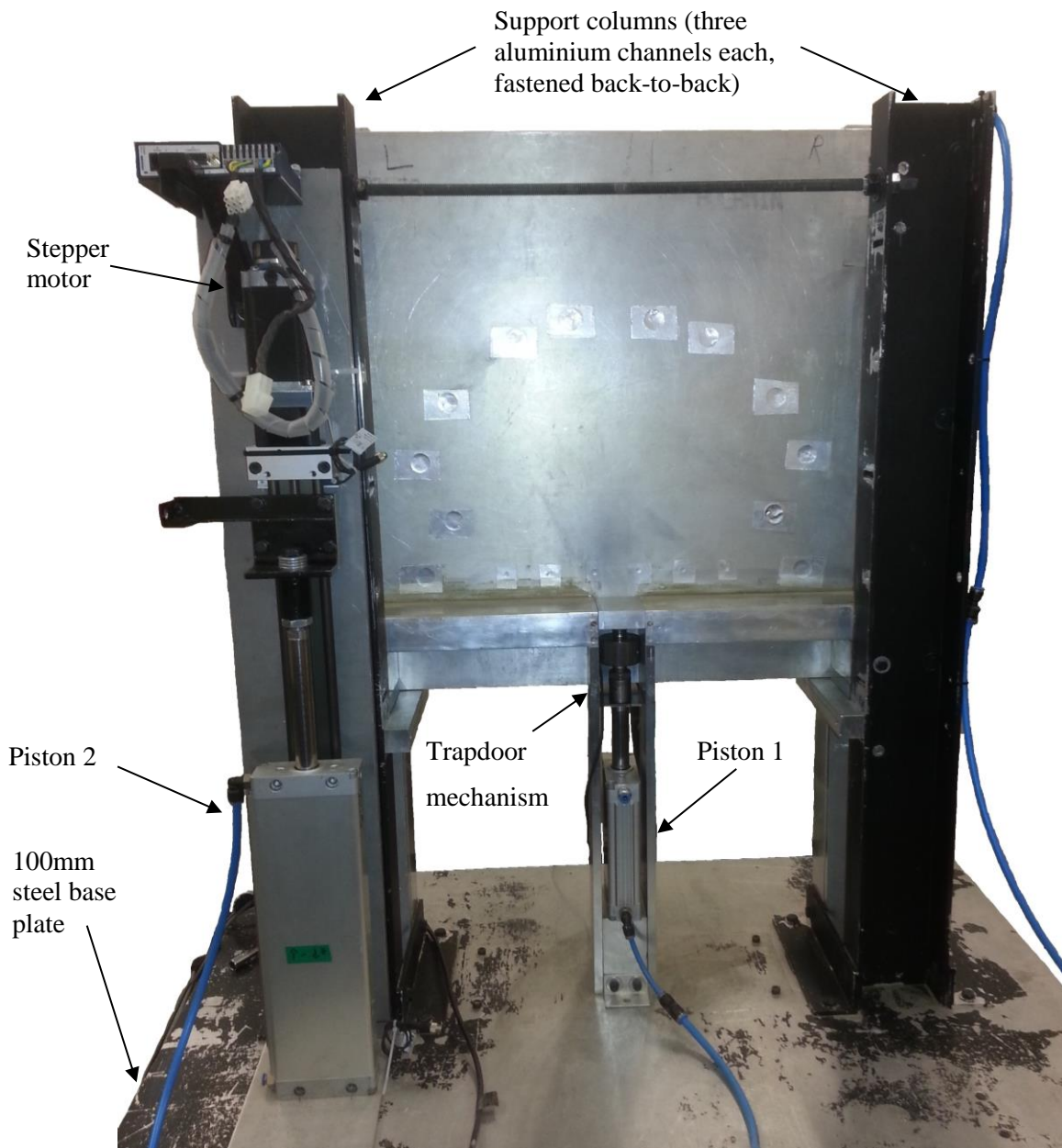


Figure 3-4: Front view of test frame (no sand loaded)

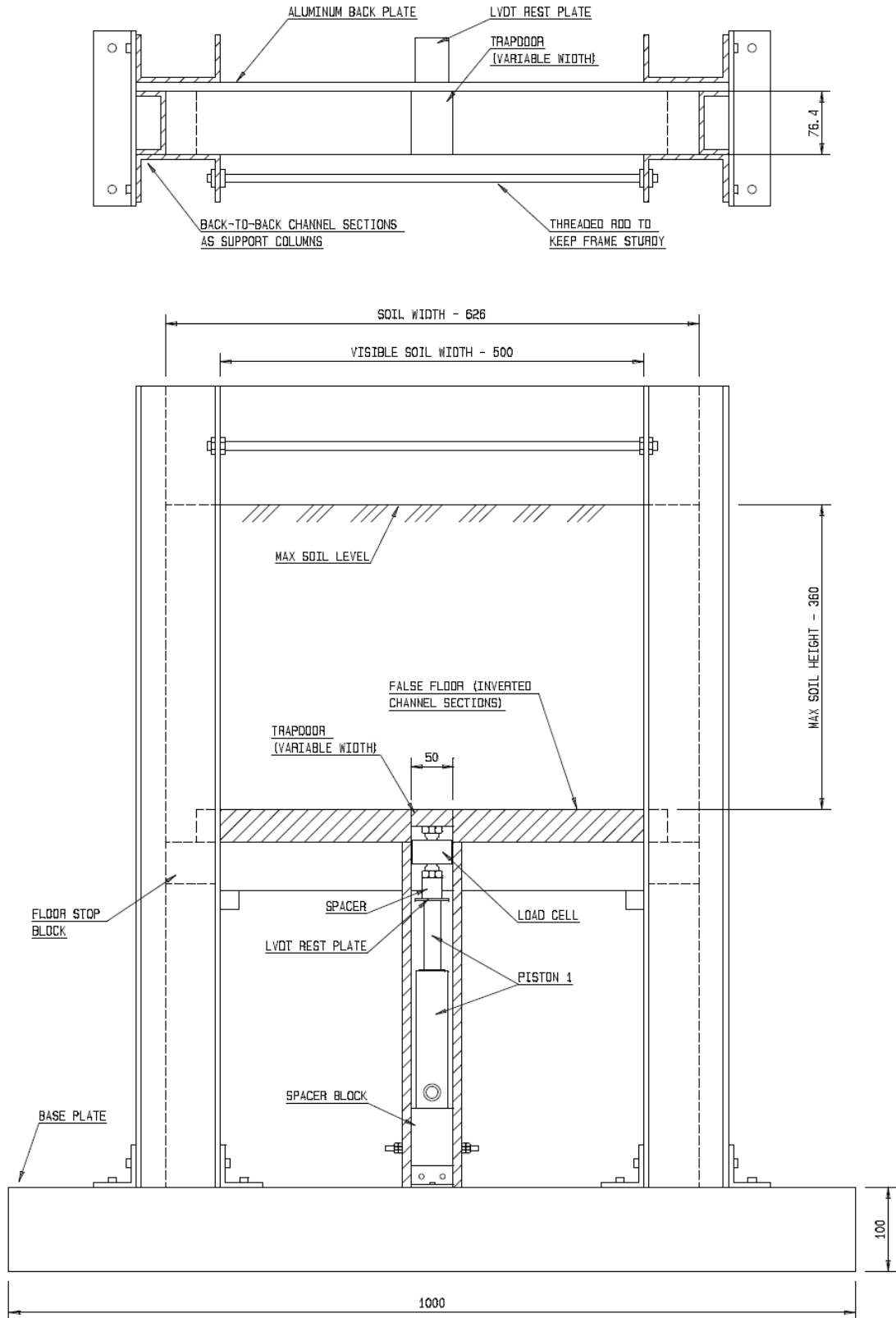


Figure 3-5: Schematic of test frame

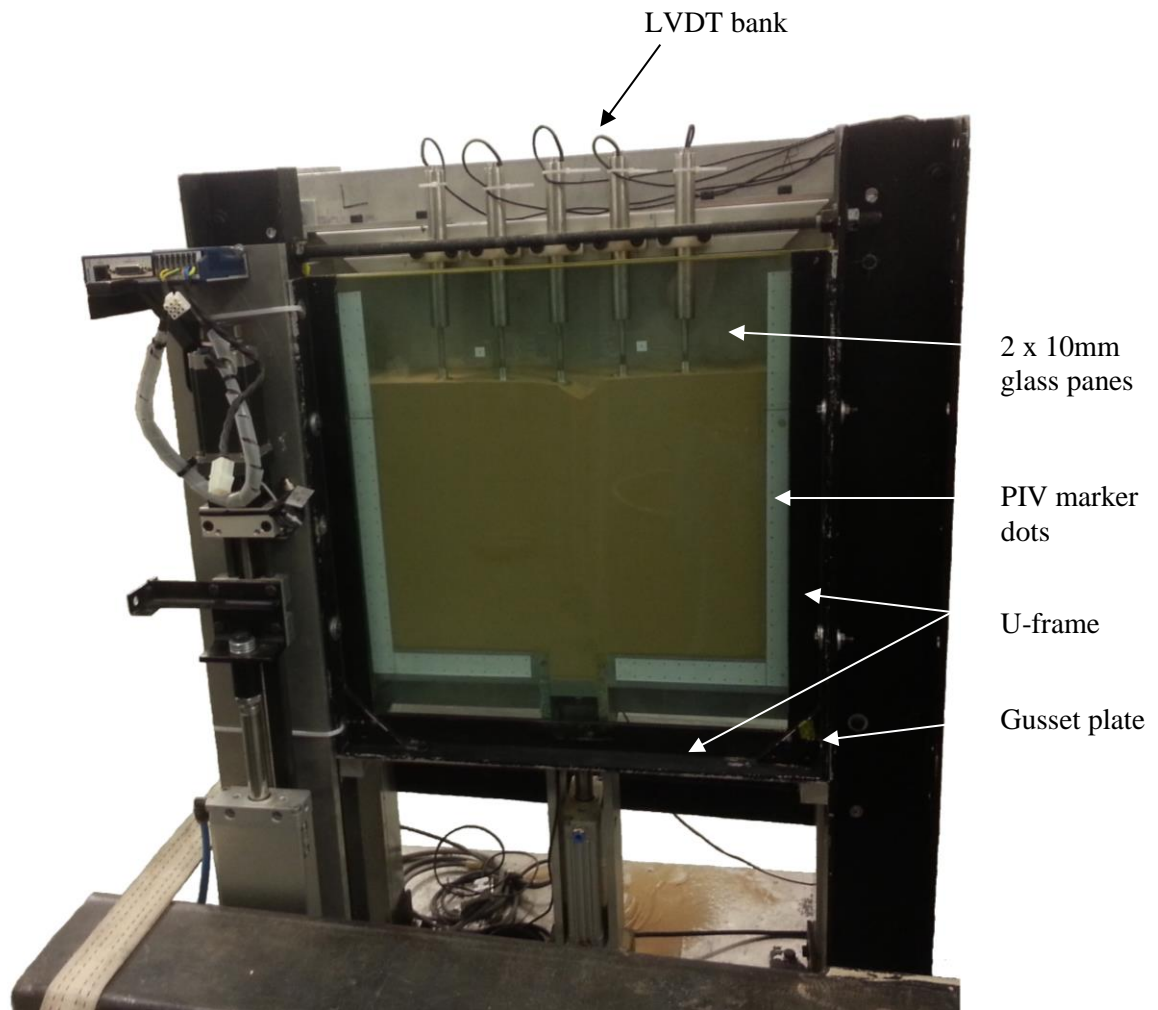


Figure 3-6: Front view of test frame (with sand loaded)

3.3.2 False Floor

Two inverted aluminium channel sections formed a false floor to the rectangular sand box, each composing half of the floor, and with a trapdoor mechanism placed between the two. This can be seen in Figure 3-7. The outer edge of each channel section rested on a stop bolted to the inside of the respective support columns while the inner edge was supported by a slender aluminium panel that extended downward and was bolted to the steel base plate via an aluminium floor spacer. The opening between these two vertical channel sections was the space in which the trapdoor could move up and down. Each channel section with its aluminium support could be moved sideways independently of one another to adjust the width of the opening between them, allowing the use of various trapdoor sizes. The channel sections were secured to the back plate with screws and to the aluminium floor spacer via a bolt and nuts.

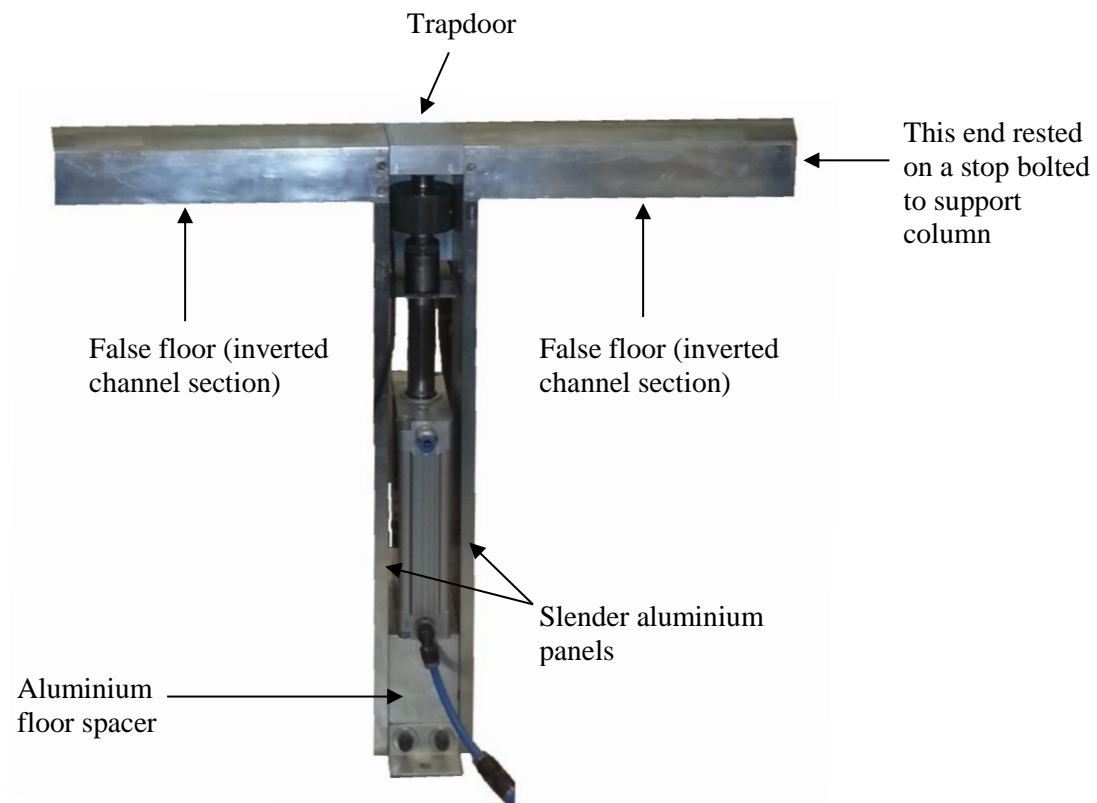


Figure 3-7: False floor with trapdoor mechanism

The glass front panel and aluminium back panel both extended below the false floor to act as sand guards around the trapdoor together with the two slender aluminium panels, preventing sand spillage during trapdoor settlement.

Viewed from the front, the interior dimensions of the sand box were 620mm wide, 76.4mm thick and 360mm high. The top of the sand box remained open and thus the depth of soil could be varied up to a maximum height of 360mm if no measurement instrumentation was present above the soil surface. A sand height of 290mm have been used in all tests.

3.3.3 Trapdoor Mechanism

As observed in the literature review, soil arching has often been tested with a trapdoor mechanism as pioneered by Terzaghi (1936). In previous studies, various methods were utilized to facilitate trapdoor settlement including a system of sliding wedges (Iglesia et al., 2014) and an electromagnet (Costa et al., 2009). The present study used a system of hydraulic pistons to lower the trapdoor, similar to that described by Da Silva (2014). The piston network controlling movement of the trapdoor was slightly altered after tests 1 and 2, as discussed next.

Trapdoor mechanism used in tests 1 and 2

In tests 1 and 2 an aluminium trapdoor 50mm wide, 76.4mm long and 25mm thick was fastened on top of a nylon spacer block as seen in Figure 3-8. The spacer block served to extend the height of the trapdoor rig and to reduce side friction during settlement. An aluminium rest plate was fastened to the bottom of the nylon block to act as a rest for the back-mounted displacement transducer that measured settlement of the trapdoor (discussed later). The nylon block was screwed into the top of a Festo DZF-50-80-P-A piston (referred to as Piston 1 henceforth) with a diameter of 50mm and a stroke of 80mm (total volume of 157cm³). Some specifications of this piston are given in Table 3-3. The base of the piston was connected to the steel base plate via an aluminium floor spacer.

Table 3-3: Specifications of pistons used in trapdoor mechanism

Specification	Festo DZF-50-80-P-A (Piston 1)	Festo DZF-50-250-P-A (Piston 2)
Internal diameter	50mm	
Stroke	80mm	250mm
Operating pressure	1-10 bar	
Operating medium	Primarily air, lubricated medium possible	
Theoretical force at 6 bar, retracting	990 N	

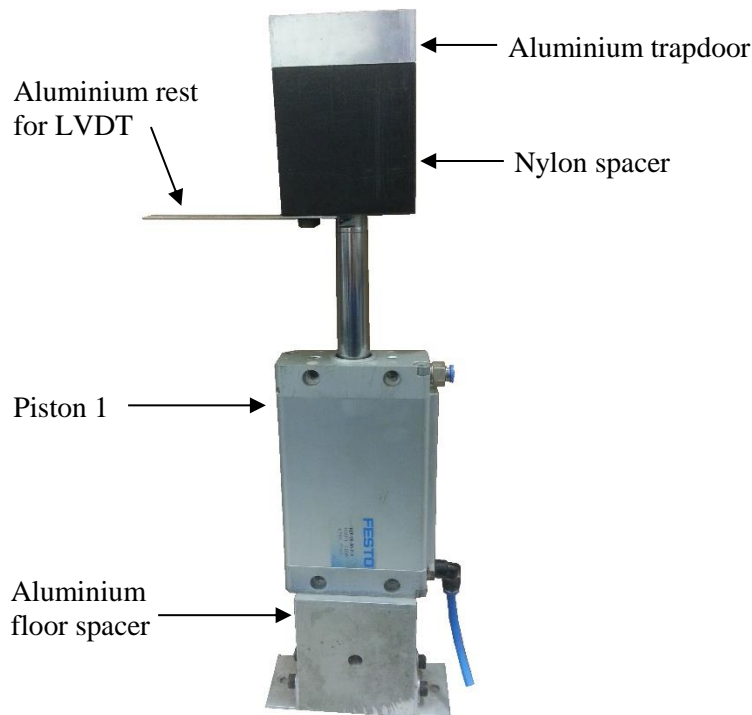


Figure 3-8: Trapdoor mechanism used in tests 1 and 2

Trapdoor mechanism used in tests 3 to 6

In tests 3 through 6 an HBM U9B/50kN load-cell was introduced between the trapdoor and the piston rod to measure the load of the soil on the trapdoor during settlement (the data obtained from this load cell was unreliable and therefore did not form part of this study). This modified trapdoor setup is shown in Figure 3-9. The load-cell screwed directly into the bottom of the aluminium trapdoor and into the top of the piston via an adapter. This removed the need for the nylon spacer and thus it was discarded. The same LVDT rest plate was installed above the piston, as seen in the schematic.

Plumbing network used in all tests

In all tests Piston 1 was connected via a plumbing network to a Festo DZF-50-250-P-A piston (labelled as Piston 2). Specifications of the piston can be found in Table 3-3. The rod of Piston 2 was attached to an actuator system with a stepper motor (as seen in Figure 3-10) that could be precisely controlled remotely. This enabled precise control of the position of the piston head and therefore the pressure in the system. When the head of Piston 2 was lowered, water was transferred from Piston 1 into Piston 2, effectively lowering the trapdoor fastened on top of Piston 1. The speed at which the trapdoor settled could thus be controlled by varying the speed of the stepper motor. The entire actuator system (Piston 2 and stepper motor) was fastened in an upright position and placed next to the test frame on the steel base plate.

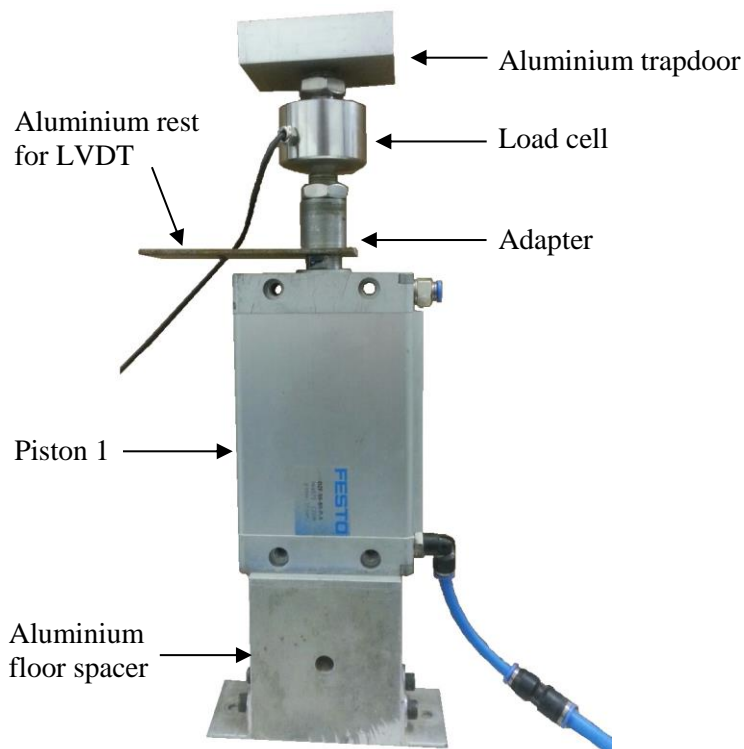


Figure 3-9: Trapdoor mechanism (with load cell) used in tests 3 through 6

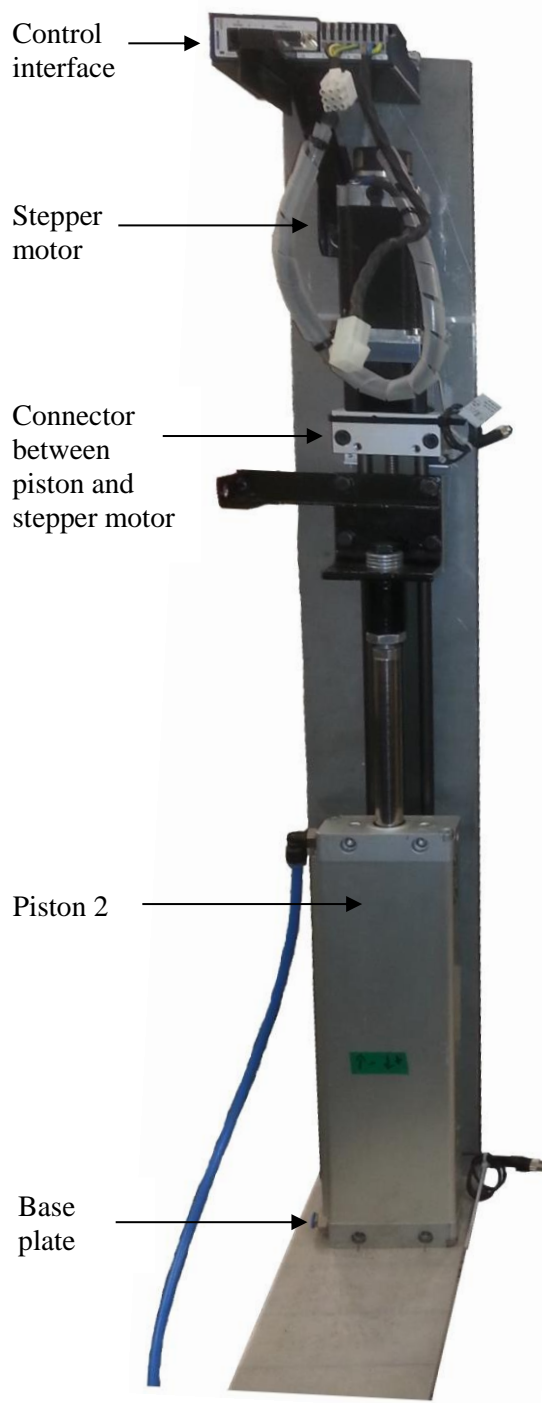


Figure 3-10: Piston 2 connected to stepper motor

The plumbing network that connected Piston 1 and Piston 2 is shown in Figure 3-11. Also included was a pressure transducer (shown in Figure 3-12) used to monitor the fluid pressure in the system during acceleration, as well as a dewatering valve used to expell any air in the

system during de-watering. Although Festo's equipment is primarily designed for an air medium, a fluid mixture of anti-freeze and water (mixed at a 1:1 ratio) was used due to it being much less compressible than air. The fluid had an oily consistency (though not as viscous as oil) that provided internal lubrication of the pistons and thus reduced sudden stick-and-slip movements during trapdoor settlement as was the case when water was used. The entire plumbing network was thoroughly de-aired before being fastened in place onto the test frame.

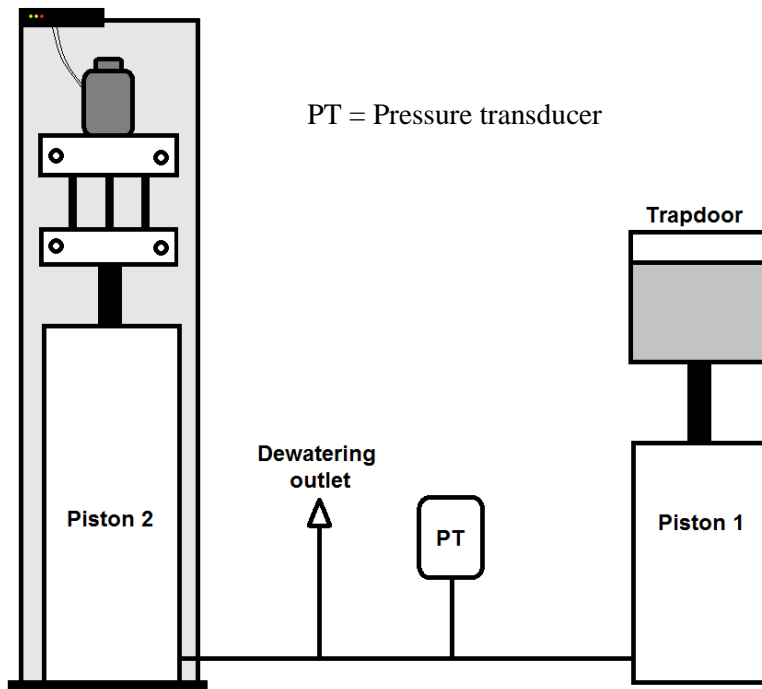


Figure 3-11: Trapdoor plumbing network



Figure 3-12: Pressure transducer (from O'Brien, 2013)

3.3.4 Measurement of Trapdoor Settlement

Trapdoor settlement was measured by two LVDTs, both mounted on the back of the test frame and labelled as LVDT 1 and LVDT 2 in Figure 3-13. LVDT 1 was a guided core Amatek S015.0 model (manufactured by Solartron) with a range of 30mm, which recorded trapdoor settlement

for the Digidaq data acquisition system. A close-up image of LVDT 1 is shown in Figure 3-14 and specifications are given in Table 3-4. LVDT 2 was a HBM WA/100-T model with a 100mm range which recorded trapdoor settlement for the HBM data acquisition system. Although the data from LVDT 2 (and the HBM data acquisition system) were not used in this study, the data did serve to check the data obtained from LVDT 1.

The extendable sections of both LVDTs rested on top of the aluminium rest plate fastened to the receding trapdoor mechanism. The bodies of both LVDTs were fastened to the back panel with clamps and screws to keep them steady during centrifuge acceleration.

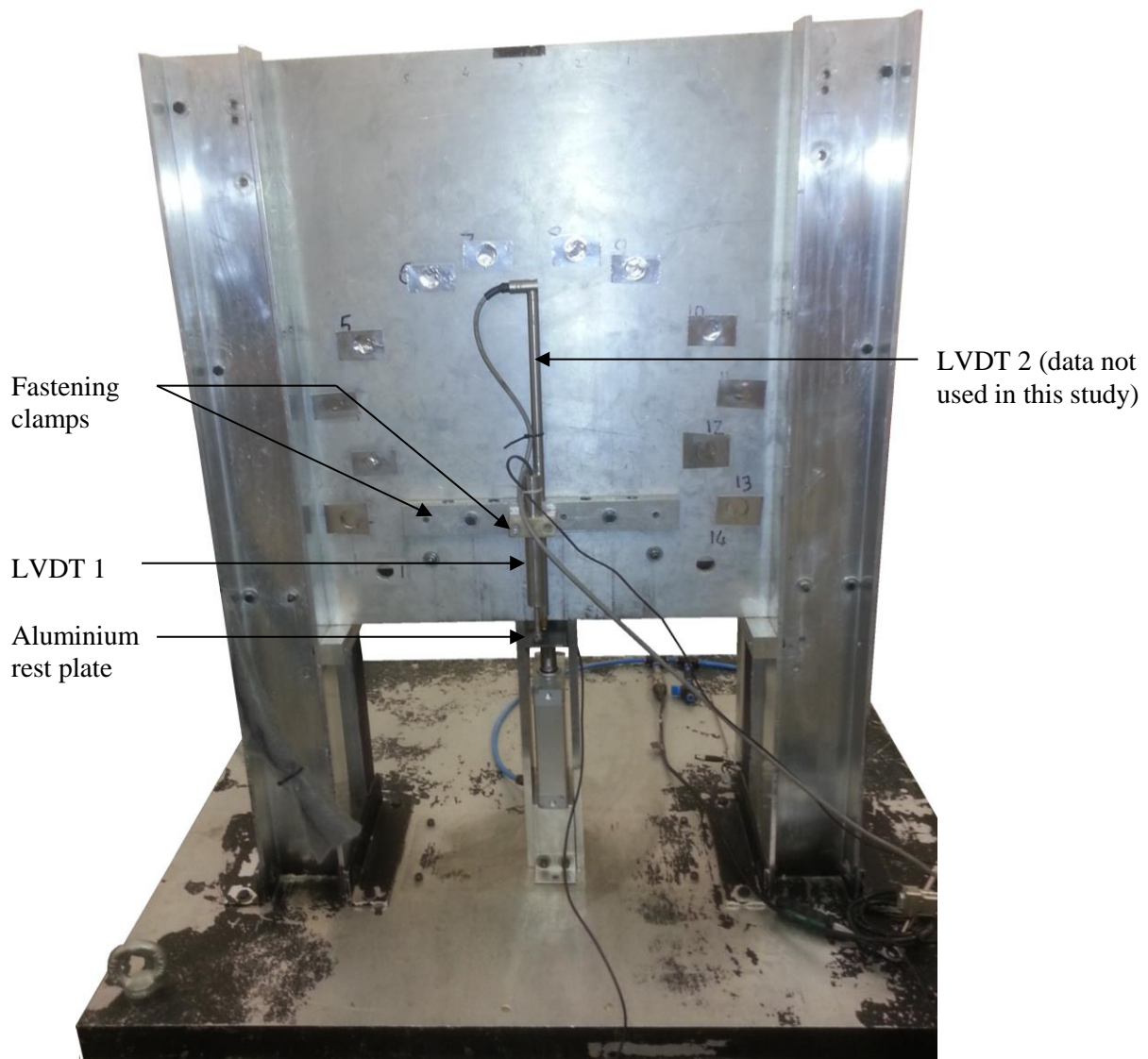


Figure 3-13: Back view of test frame and positioning of LVDTs tracking trapdoor settlement



Figure 3-14: Image of Solartron Amatek S015.0 LVDT (LVDT 1)

Table 3-4: Specifications of Amatek S015.0 LVDT (LVDT 1) used for tracking surface settlement

Specification	Value
Model	Amatek S015.0
Type	Guided core
Measurement range	$\pm 15\text{mm}$ (total of 30mm)
Sensitivity	60mV/V/mm
Resolution	$< 0.2 \mu\text{m}$
Tip force	1.2 N
Body type	19mm diameter stainless steel body with nickel core
Mass (body + core)	98.4 grams
Excitation voltage	1-10V

3.3.5 Measurement of Surface Settlement

To track surface settlement a bank of 5 Ametek S015.0 LVDTs (similar to LVDT 1 shown in Figure 3-14) was installed, each with a range of 30mm. The 5 LVDTs were spaced equally at 50mm intervals with the middle LVDT in line with the trapdoor centreline. They were fastened onto an aluminium collar frame that was bolted to the back plate near the top of the test frame as shown in Figure 3-15.

It was observed that the aluminium collar deflected during acceleration of the centrifuge but became stable once final, constant acceleration was reached. At this point the readings on the LVDTs could be zeroed to cancel out the effects of collar deflection.



Figure 3-15: Arrangement of surface settlement LVDTs above sand body

3.3.6 Introduction of Moisture

In tests conducted in moist sand, water was introduced before each test through a perforated pipe with holes along its length (Figure 3-16). This pipe was laid on top of the soil, separated by a layer of Bidim (a needle-punched, non-woven, polyester geotextile), which prevented small water jets from eroding the soil surface. A steel rod was used to keep the pipe straight throughout the test. The pipe was connected to the centrifuge water supply line which enabled the opening and closing of a moisture valve both in stationary and accelerated conditions. Before centrifuge acceleration, the soil body was completely saturated after which the moisture was allowed to drain slowly out of small openings in the bottom of the rig. This process was repeated again when the centrifuge reached final acceleration at 40G.



Figure 3-16: Perforated pipe on layer of Bidim, used to introduce moisture to the sample

The actual moisture content of the soil in each test was determined by measuring the moisture content of six samples collected at various locations in the body of sand. Three of these were taken on the left-hand side of the sand body (top, middle and bottom) and three on the right-hand side. The moisture content was measured after the completion of each test.

3.3.7 Calibration of Instruments

Instruments were calibrated once before initial tests were performed and these calibrated values were used for the duration of the study.

Calibration of LVDTs

All 5 of the Ametek S015.0 surface settlement LVDTs as well as the back-mounted trapdoor LVDT were calibrated using the apparatus shown in Figure 3-17. Each LVDT was fastened with a clamp to a rig that could be moved up or down. The tip of the LVDT rested on a stationary base plate as did the tip of an electronic calliper fastened to the same rig. The rig was then extended up and down while the displacement readings on the calliper and the LVDT volt readings, as displayed on the Digidaq data acquisition system (Gaudin et al., 2010), were noted down in 2mm intervals. The LVDTs were extended from 0mm to 30mm and back to 0mm and the process was repeated 3 times for each instrument. Graphs of output voltage against displacement yielded similar results for all instruments so only the graph of the back-mounted LVDT is shown in Figure 3-18. It was noted that all LVDTs exhibited excellent linear behaviour with the points on each curve correlating to a straight line with $R^2 = 0.999998$.

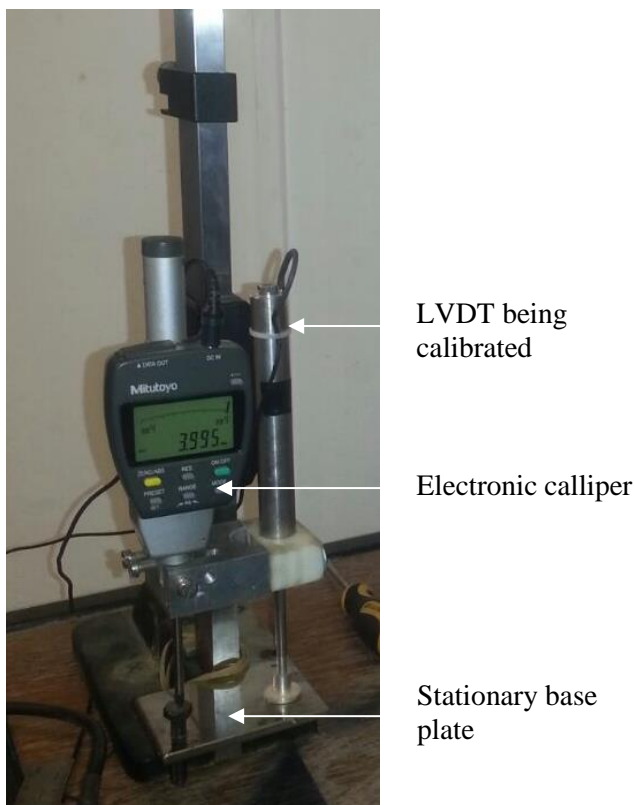


Figure 3-17: LVDT calibration rig

Calibration factors were calculated for each LVDT and values fell in the range of 2.935 – 3.006 mm/V. The same set of LVDTs were calibrated by Archer (2014) and showed calibration factors in the range of 2.971-2.977 mm/V. It was decided to use a calibration value of 3mm/V during data acquisition and the x-offset was measured in each test when readings were zeroed.

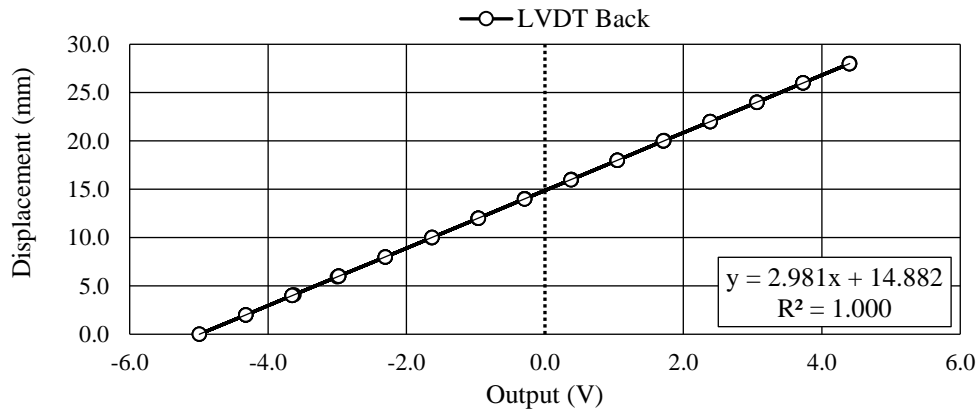


Figure 3-18: Voltage against displacement readings of LVDT 1, used in calibration procedures

Calibration of Pressure Transducer

The pressure transducer was calibrated by connecting it to an air-water interface and measuring response readings at various induced pressures. A compressor was used to create pressure in the system by inflating the air-side of the interface, consequently transferring the pressure to the water-side. Actual pressure readings were taken using a Bourdon tube gauge. Pressure was varied from 0kPa to 500kPa and back to 0kPa in increments of 100kPa for 3 cycles and readings of the pressure transducer was recorded at every increment. A graph of the readings obtained throughout all three cycles is shown in Figure 3-19. The pressure transducer records near-linear readings with $R^2 = 0.99996$ and shows very little hysteresis. The calibration factor used for this instrument was 0.002591 kPa/V and the offset was recorded for each test when readings were zeroed.

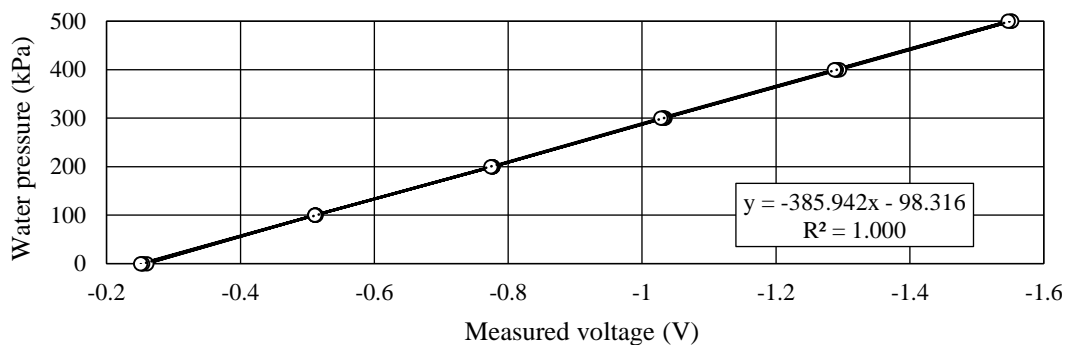


Figure 3-19: Voltage against pressure readings of pressure transducer, used in calibration procedure

3.3.8 Data Acquisition and Photographic Equipment

The centrifuge facility at the University of Pretoria uses two data acquisition systems – the German-built HBM system and the Digidaq system developed by the University of Western Australia as described by Gaudin et al. (2010). The latter was used in this study to record readings of the pressure transducer and the LVDTs. Instruments were plugged into a data acquisition box (Figure 3-20) on the centrifuge and data was then relayed in real time to a computer in the adjacent control room.

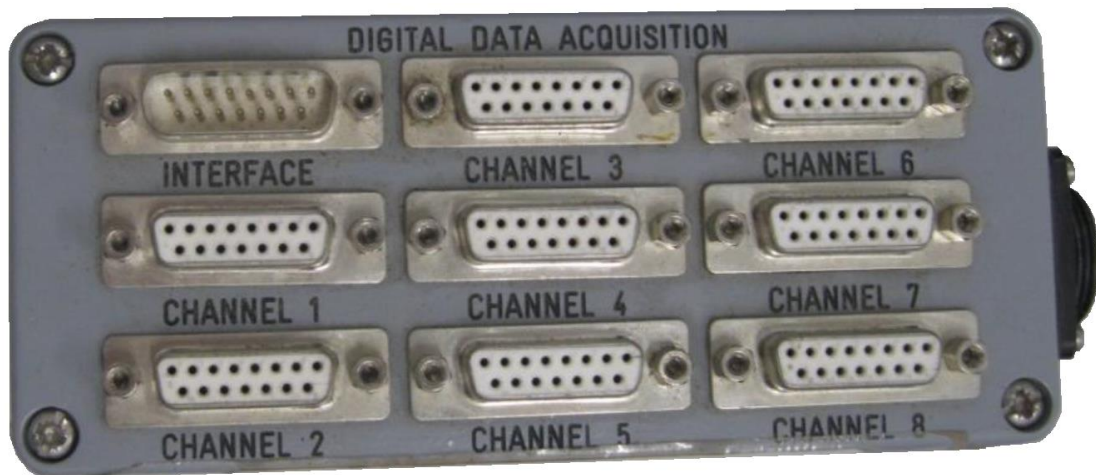


Figure 3-20: Digital data acquisition ports for the Digidaq system

The main form of data acquisition in this study was in the form of continuous photographs taken of the soil body during deformation. These photographs could then be analysed to determine displacements and strains within the deforming soil body. The camera used to capture these images was a modified Canon EOS 100D DSLR camera (Figure 3-21) with a Canon EF 40mm f/2.8 STM lens. These cameras typically have an internal mirror that lowers during focus and raises when the photograph is taken, but due to the high accelerations experienced in the centrifuge, the mirror would fall flat and could not be raised again to take a photograph. To prevent this, the mirror was jammed open using cardboard. This prohibited the use of the automatic focus feature and manual focus had to be performed before the start of each test.



Figure 3-21: Canon EOS 100D camera used to capture images of soil deformation

The camera was mounted within the centrifuge basket opposite the trapdoor model and was attached to an aluminium bar that allowed manual adjustments up, down, left and right. Due to space constraints within the centrifuge basket, the camera could not be positioned directly in front of the soil body but instead photographed it from below. This introduced a level of parallax as seen in Figure 3-22, causing the lower part of the sand body to appear wider than the top. However, this error could later be corrected when calibrating PIV results by making use of the PIV marker dots along the sides and bottom of the glass. This process is described in detail in Section 3.6.5.

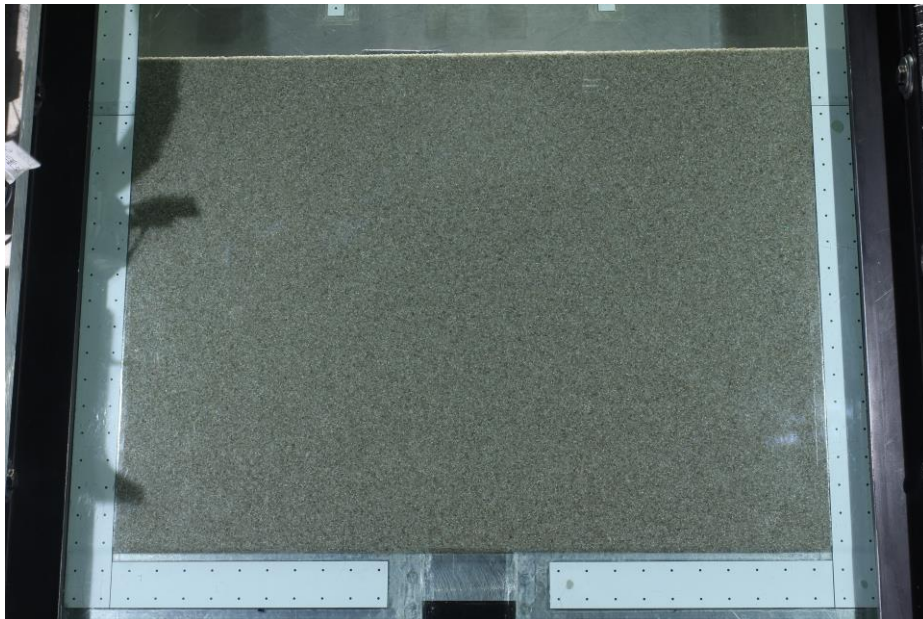


Figure 3-22: Actual image captured, used to illustrate parallax

Images were taken at a resolution of 5184 x 3456px (equating to roughly 18MP) at an ISO of 200, f-stop of f/10, and the exposure was 1/10 seconds. Ample lighting was provided by the centrifuge lighting system so the use of the flash was not necessary.

The camera was controlled remotely via the DSLR Remote software which allowed setting an interval at which images could be taken. Although the camera was theoretically capable of capturing 4 images per second, the relay of the data to the computer software took additional time depending on the complexity of the photograph. It was found with trial and error that an interval of 6 seconds ensured all photographs could be securely transferred and recorded in time for the next photograph to be taken. This interval was used in all tests in this study.

3.4 MATERIAL PROPERTIES

Two soil types were used in this study – Cullinan sand (also referred to as *fine sand*) and Consol sand (also referred to as *coarse sand*). Images of the Cullinan and Consol sands are shown in Figure 3-23a and Figure 3-23b, respectively. The Cullinan sand is a fine, yellowish, slightly silty sand obtained from a commercial source near Cullinan while the Consol sand is a medium to coarse sand (calibrated to a specific particle size distribution) commercially available from Consol with a greyish-white appearance.

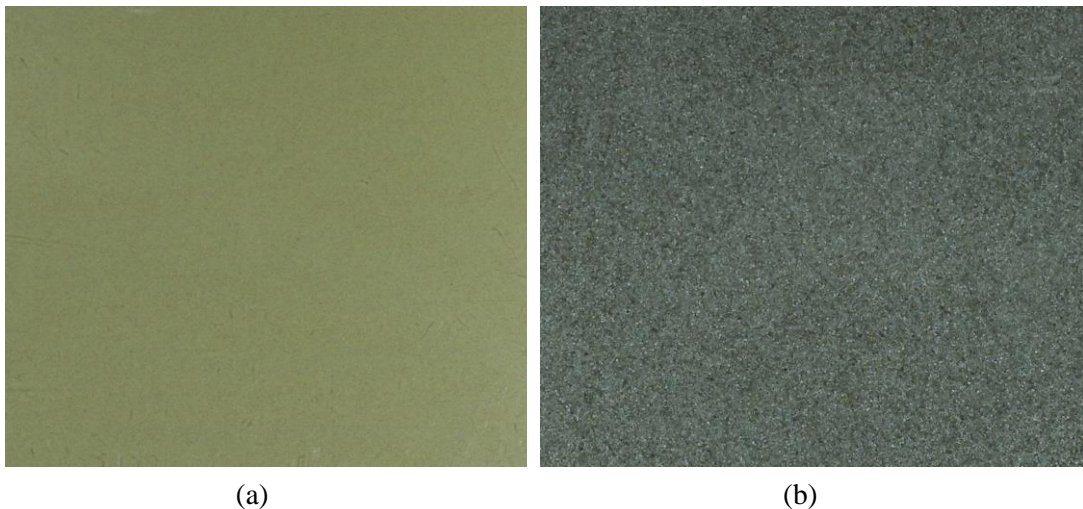


Figure 3-23: Physical appearance of (a) Cullinan sand and (b) Consol sand

This section presents an in-depth comparison of geotechnical parameters of the two sands including grading, density, specific gravity and triaxial properties. An extensive characterisation of the fine Cullinan sand has been performed by Archer (2014) and some of his results are reproduced here.

3.4.1 Particle Size Distribution

Typically, the particle size distribution (PSD) of a soil is measured by performing a sieve analysis of a sample and recording the percentage by mass of sand retained on a range of sieve sizes (Knappett & Craig, 2012). These percentages are used to calculate a cumulative percentage which is then plotted on a logarithmic graph. For this study, however, the PSDs of both sands were measured using the Mastersizer 2000 manufactured by Malvern Instruments. The instrument operates by shining a laser light beam onto the soil particles, capturing the light that reflects off the particles and using refraction theories to determine the size of the particles reflecting the light. The PSD is then given as a range of percentages by *volume* of soil between two particle sizes, rather than by *mass*. Because volume and mass are linearly related via the specific gravity (SG) of the material, the curves representing percentage mass and percentage volume are identical in this case. Archer (2014) compared the results of the Mastersizer 2000 to that of a conventional sieve analysis and found good correlation.

The particle size distribution of both soils as obtained from the Mastersizer 2000 is given in Figure 3-24. Both sands exhibited uniformly-graded curves with a concentration of fine to medium sand-sized particles, and with Cullinan sand being noticeably less uniform than Consol sand.

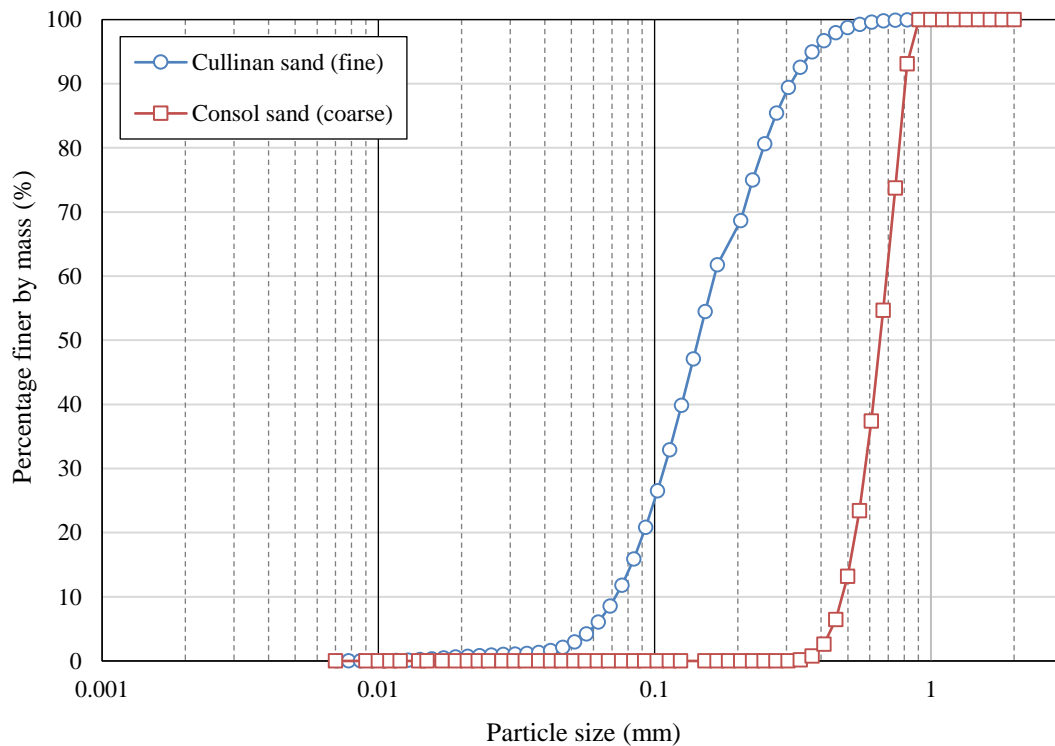


Figure 3-24: Particle size distribution of Cullinan sand (Archer, 2014) and Consol sand

The average particle size (D_{50}) of Cullinan sand is 0.152mm while that of Consol sand is 0.742mm, showing that the particles of the latter are on average 4.9 times larger than that of the former. The grading curve can further be described by the coefficient of uniformity (C_U) and the coefficient of curvature (C_Z). These are calculated according to the following equations:

$$C_U = \frac{D_{60}}{D_{10}}$$

$$C_Z = \frac{D_{30}^2}{D_{60}D_{10}}$$

Where:

D_{10} = the particle size such that 10% of particles are smaller

D_{30} = the particle size such that 30% of particles are smaller

D_{60} = the particle size such that 60% of particles are smaller

These parameters are shown in Table 3-5 for both soils. The C_U value of both soils is less than 3, confirming that both are indeed uniformly graded. Using the particle size range classification system suggested by Knappett & Craig (2012) as shown in Figure 3-25, the Cullinan sand can be classified as a coarse silt to fine to medium sand, while the Consol sand can be classified as a medium to coarse sand.

Table 3-5: Particle size distribution parameters of both soils (including data by Archer, 2014)

	D₁₀ (mm)	D₃₀ (mm)	D₆₀ (mm)	C_U	C_Z
Cullinan Sand (fine)	0.072	0.108	0.165	2.29	0.98
Consol Sand (coarse)	0.477	0.578	0.692	1.45	1.01

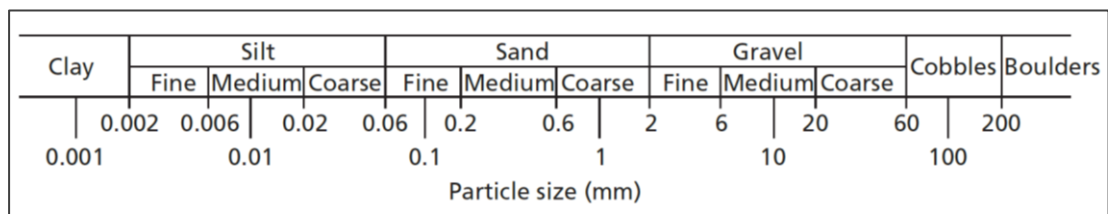


Figure 3-25: Classification of typical particle size ranges (Knappett & Craig, 2012)

3.4.2 Density

In previous literature the behaviour of soil in trapdoor tests was greatly influenced by the relative density (RD) of the material. Since density is in direct correlation to the degree of packing of a soil, a denser soil will exhibit a greater degree of particle interlock and would therefore be able to support a greater overburden pressure during arching.

It is therefore important to know the relative density of the soil being tested. Relative density is calculated as a percentage of the range between the minimum and maximum densities of a soil. A relative density of 0% would mean that the soil is at its minimum density while a relative density of 100% would indicate that the soil is at its maximum density. It is therefore important to accurately determine the minimum and maximum densities of a soil beforehand. The minimum and maximum densities of the Cullinan sand were measured by Archer (2014) and that of the Consol sand were measured in this study according to ASTM Standards D4253 and D4254 and are presented in Table 3-6. Soils in all tests were placed at a high density when compared to the maximum dry densities given here.

Table 3-6: Maximum and minimum dry densities of both sands (including data by Archer, 2014)

	Min dry density (kg/m ³)	Max dry density (kg/m ³)
Cullinan sand (Archer, 2014)	1392.0	1669.1
Consol sand	1595.4	1756.9

3.4.3 Specific Gravity

The specific gravity of both sands was measured using an AccuPyc II 1340 Pycnometer manufactured by Micromeritics, which measures the particle density through the gas displacement method known as pycnometry. The sand sample is placed in a container with a known volume after which helium (or some other inert gas) is injected into the container. Helium is then expelled into a second container of known volume. Pressure readings taken in both containers can then be used to determine the exact volume of the solids inside the container. Since the exact mass of the sample is known, the particle density can then be calculated.

The instrument measured the particle density three times and produced an average reading. The measured particle density of both sands is given in Table 3-7. The specific gravity of the Consol sand was measured in this study while Archer (2014) measured that of the Cullinan sand using the same instrument.

Table 3-7: Particle density of Cullinan sand (Archer, 2014) and Consol sand

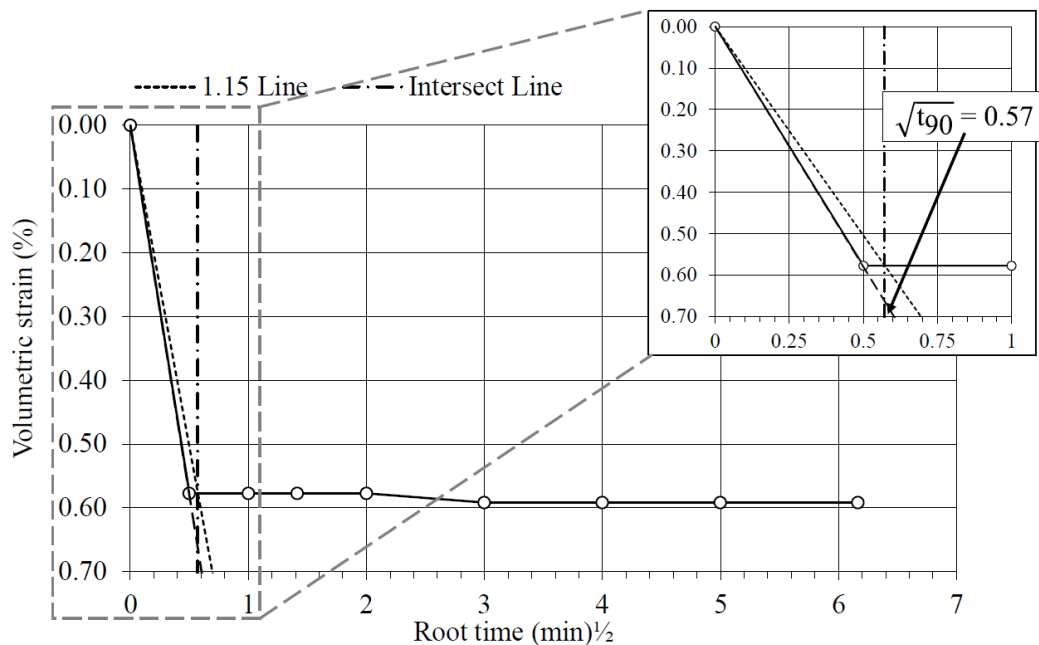
	Particle density (g/cm ³)
Cullinan sand (Archer, 2014)	2.666
Consol sand	2.648

3.4.4 Strength Parameters from Triaxial Tests

Triaxial tests were performed on both soils to assess their strength properties. This section presents the results of the triaxial tests performed on Cullinan sand by Archer (2014) as well as those performed on Consol sand in the current study. Both studies utilized the same equipment in the same laboratory.

Consolidation stage

Archer performed a series of 9 consolidated drained triaxial tests on the Cullinan sand, divided into 3 sets with relative densities of 20%, 50% and 80% respectively. Each set contained 3 tests that were consolidated to effective stresses of 50kPa, 200kPa and 500kPa. The consolidation curve of the 20% RD 200eff test is shown in Figure 3-26 and Archer reported that all other tests showed similar results. Archer used Taylor's method to determine a coefficient of consolidation c_v greater than 31 000 m²/year.

**Figure 3-26: Consolidation curve of 20% RD 200eff test on Cullinan sand (Archer, 2014)**

A series of 3 consolidated undrained triaxial tests were performed on the Consol sand in the current study at effective stresses of 100kPa, 300kPa and 450kPa. Several initial conditions of the three Consol samples are presented in Table 3-8 (initial conditions of the Cullinan samples are given in Archer (2014)). The samples were close to 100% relative density when compared to the values in Table 3-6.

Table 3-8: Initial conditions of triaxial test samples on Consol sand

	Triaxial 1 ($p_0' = 100\text{kPa}$)	Triaxial 2 ($p_0' = 300\text{kPa}$)	Triaxial 3 ($p_0' = 450\text{kPa}$)
Initial volume (cm^3)	193.7	198.6	198.1
Initial mass (g)	340.8	340.5	340.5
Initial water content (%)	0.0	0.0	0.0
Dry density (g/cm^3)	1.759	1.715	1.719
Relative density (%)	101.6	73.7	76.4
Initial void ratio	0.51	0.55	0.54

The samples were consolidated to 100kPa, 300kPa and 450kPa effective stresses prior to shearing. As with the Cullinan sand, consolidation happened quickly. The consolidation curve for sample 3 ($p_0' = 450\text{kPa}$) is shown in Figure 3-27. Using Taylor's method, the coefficient of consolidation c_v was calculated to be greater than 31 000 m^2/year , similar to that of the Cullinan sand.

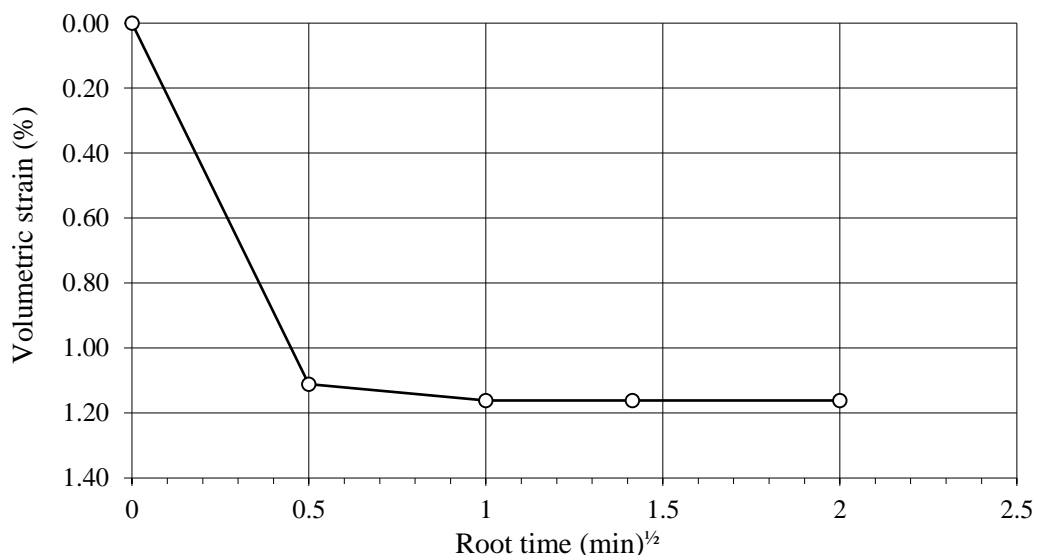


Figure 3-27: Consolidation curve of 100% RD 450eff for Consol sand

Shear stage

After consolidation all samples were sheared and stress paths in t' and s' space were constructed. In this study, the Consol sand was tested undrained with base pore pressure measurements, allowing effective stress paths and parameters to be measured. The stress paths for the 80% RD tests on Cullinan sand are shown in Figure 3-28 while that of the 100% RD Consol sand are shown in Figure 3-29.

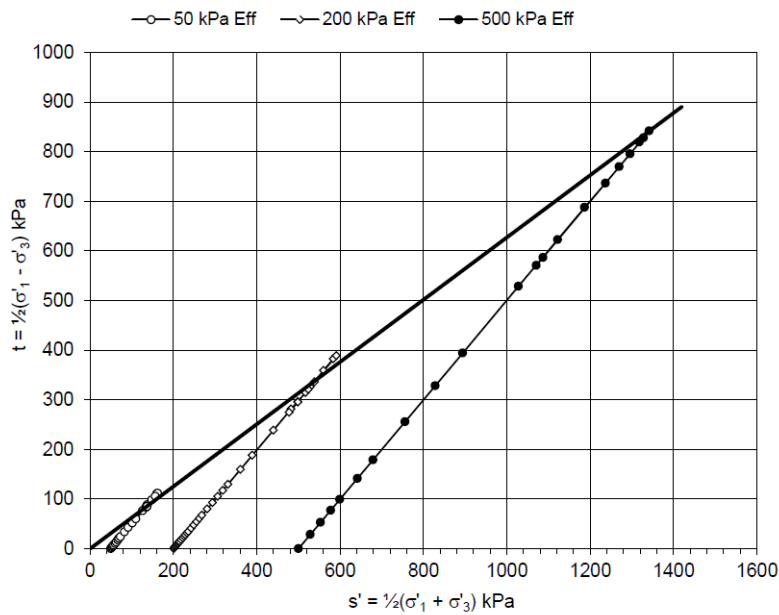


Figure 3-28: Stress paths of Cullinan sand at 80% D_r at various effective stresses (Archer, 2014)

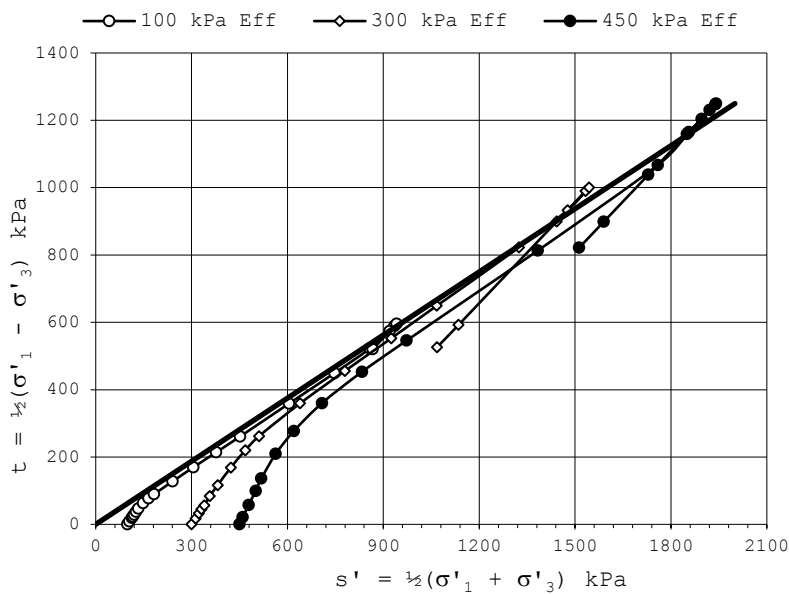


Figure 3-29: Stress paths of Consol sand at 100% D_r at various effective stresses

A failure envelope was fitted to the stress paths to determine the friction angle (slope of failure envelope) and cohesion (y-intercept of failure envelope) as displayed in Table 3-9.

Table 3-9: Strength parameters of Cullinan sand at 80% RD (Archer, 2014) and Consol sand at 100% RD

	Cullinan sand (Archer, 2014)	Consol sand (current study)
Peak friction angle (°)	39	32
Cohesion (kPa)	0	0

3.5 MODEL PREPARATION

The following steps were taken during preparation, sand placement, centrifuge acceleration and lowering of the trapdoor of each model. References are made to particle image velocimetry (PIV) which is described in detail in Section 3.6.

3.5.1 Preparation of the Test Frame and Trapdoor System

The following steps were followed to prepare the test frame and trapdoor system before sand placement:

1. The test frame and trapdoor system were cleaned thoroughly and wiped with Acetone and Alcohol solutions to sterilize the area.
2. The trapdoor plumbing network was filled up with a 1:1 water/antifreeze solution and thoroughly de-aired under pressure. This was done by sequentially lowering and raising the trapdoor and then rotating the apparatus into various positions to collect any air bubbles at an elevated point within the network. The air was then expelled and more fluid was introduced through an open valve to replace it. The process was performed so that a certain amount of residual fluid pressure remained in the system that later assisted in supporting the load of the sand body during centrifuge acceleration.
3. Adhesive strips were stuck along the top perimeter of the trapdoor block. These strips rested against the adjacent aluminium and glass panels and served to keep any small sand particles from leaking at those interfaces.

4. The trapdoor system with its plumbing network was then fastened with screws onto the base plate of the test frame to complete the floor of the sand box. Care was taken not to introduce any air into the system.
5. In tests conducted in moist sand, all interfaces between aluminium sections were sealed with silicone to reduce the amount of water that escaped, except the trapdoor-to-false-floor and trapdoor-to-back-panel interfaces which required freedom of movement during the test. The aim was not to make the test frame entirely waterproof but to make it waterproof to such an extent that moisture would build up inside the test frame and saturate the sand before slowly draining out. This method was found to be the best method of creating a homogenous moisture distribution throughout the soil.
6. The two 10mm glass front panels were thoroughly cleaned with Acetone and Alcohol to produce a non-stick surface free of any marks that could disturb PIV analyses.
7. PIV Marker dots were printed onto white paper strips which were then stuck to the inside of the glass panels (the side against which the soil would later rest) as seen in Figure 3-6. The strips were covered with a layer of Desifix to prevent disturbance from the soil during settlement and to provide a smooth surface against which soil could move. It was decided to stick the paper strips to the *inside* of the glass panels, because if they were stuck to the *outside* (and thus removed 20mm from the soil) they would cast shadows onto the soil during testing that would interfere with PIV analyses.
8. The glass panels were then bolted in place onto the test frame via angle-iron sections to form the front of the sand box.
9. Silicone and adhesive strips were used to seal the interfaces between the aluminium test frame sections and the glass panel. Care was taken not to inhibit freedom of movement of the trapdoor during this step.
10. The entire test frame (without sand) was weighed using an overhead crane scale.

3.5.2 Sand placement

The method of sand placement typically has a significant effect on the relative density and homogeneity of the soil and should be conducted with care. Soil packing, and consequently

relative density, can be controlled by varying both the rate of deposit as well as the drop height. The ultimate relative density of the soil is dictated by a combination of these two factors.

The following steps were performed to place the sand into the test frame and weigh the model:

1. Sand was introduced into the test frame by pluviation from an elevated sand hopper as seen in Figure 3-30. With the aim of achieving a homogenous relative density throughout the soil body, care was taken to ensure a constant rate of deposit during pluviation. This was done by controlling the size of the hopper mouth via a ball valve. The drop height was kept constant as the sand level increased by continually lowering the entire test frame during pluviation. Various drop heights ranging from 1m to 2m were used in this study to attain a compact density for each specific soil type. A flexible pipe attached to the bottom of the hopper allowed manual control over where the soil fell in the test frame. The end of the pipe was moved sideways across the test frame, using visual judgement to ensure an even distribution of placement. Care was taken not to have sand particles pile up on one another and roll down, which would ultimately disturb the relative density and homogeneity of the sample. The exact weight of all soil deposited into the hopper was measured using a laboratory scale.



Figure 3-30: Sand being pluviated from a hopper into test frame

2. Excess soil was scooped off the top of the sand body to attain the desired sand height. Care was taken during this step not to disturb the packing of any particles below the desired sand height.
3. The bank of surface settlement LVDTs was then bolted in place above the sand surface, again taking care not to disturb the sand body during placement.
4. In tests done in moist sand, a perforated pipe was wrapped in a layer of Bidim (a needle-punched polyester geotextile) and placed on top of the soil (behind the LVDT bank). This would later be used to introduce moisture into the soil from the centrifuge water supply line.
5. The entire test frame (with sand) was weighed once again using an overhead crane scale to determine the final weight of the model.

3.5.3 Preparation of Centrifuge

The following steps were performed to install the model on the centrifuge and prepare for testing:

1. The model was placed onto the centrifuge test basket and all measurement instruments (LVDTs and pressure transducer) were connected to data acquisition ports. The perforated pipe was also connected to the water supply line (in tests run in moist sand).
2. All 6 LVDTs and the pressure transducer were loaded onto the computer system and tested to see that they were all at the start of their reading ranges.
3. The DSLR camera and video camera were connected and positioned correctly.
4. In tests done in moist sand, the water supply line was opened to introduce moisture into the sample. The sand body was saturated from the top and excess moisture was drained out of small openings at the bottom of the test frame.

3.5.4 Centrifuge Acceleration and Lowering of the Trapdoor

The following steps were performed during centrifuge acceleration and lowering of the trapdoor:

1. The doors to the centrifuge were closed and locked and the centrifuge was started. The centrifuge accelerated to 4g at which point it calibrated the weight distribution by measuring out-of-balance forces and adjusting the counterweight accordingly. This eliminated the need to manually calculate the position of the counterweight beforehand. It then accelerated up to a final acceleration of 50g.
2. For tests done in moist sand, moisture was again introduced at the top of the sand body to ensure the sample remained saturated. Excess moisture was drained out of small openings at the bottom of the test frame.
3. All LVDTs were zeroed at this point to correct any extension that could have taken place during acceleration.
4. The DSLR camera was set to photograph the sand body at intervals of 6 seconds.
5. The trapdoor was then slowly lowered by controlling the stepper motor. The test was stopped whenever the trapdoor reached maximum retraction or when sand started to leak from the test frame. At this point image capture was also stopped and the centrifuge was decelerated to a stop.

3.5.5 Post-experiment Procedures

The following steps were performed after the experiment was completed and the centrifuge was brought to a stop:

1. After the test, the model was removed from the centrifuge basket. End-of-test photographs were taken of the sand body as well as the model.
2. The soil was then removed by scooping it out of the test frame. In tests in moist sand, soil samples were taken at 6 locations within the soil body to determine the moisture content. The samples were weighed in a moist condition, dried overnight in an oven and then weighed again in a dry condition.
3. LVDT data was then exported from the centrifuge computer to be analysed in a spreadsheet. Image data were downloaded to be analysed using PIV.

3.5.6 Test schedule

A total of 6 trapdoor tests were performed with various soil types, moisture conditions and particle sizes. These are summarized in Table 3-10. All tests were performed at an acceleration of 50g.

Inaccuracies occurred when measuring the exact weight of the soil body in each test, and therefore the relative density of each test could not be exactly computed. However, when taking into account the results of preliminary pluviation tests, in which the same material was dropped from the same sand hopper from the same drop height, it was deduced that the models were all deposited at a high relative density. Hence, they are marked as “dense” in Table 3-10.

The tests were named using the following convention: a chronological test number followed by two capital letters that provide a method for easy identification of the particular test’s soil properties, as seen in the first column of Table 3-10. The first letter denotes the moisture condition (‘D’ for dry and ‘M’ for moist) and the last letter denotes the particle size (‘C’ for coarse and ‘F’ for fine). The standard trapdoor width used in most of these tests was 50mm. In tests where a different width was used, an additional number was added at the end of the test name to indicate the trapdoor size in millimetres.

Table 3-10: Centrifuge test schedule

Test name	Sand type	Density description	Wet/Dry	Moisture content range (w)	Soil height (H)	Trapdoor width (B)	H/B ratio	Surface settlement LVDTs present
				(%)	(mm)	(mm)		
Test 1DC	Coarse	Dense	Dry	-	290	50	5.8	No
Test 2MC	Coarse	Dense	Wet	2.00 – 3.25	290	50	5.8	No
Test 3DF	Fine	Dense	Dry	-	290	50	5.8	Yes
Test 4MF-50	Fine	Dense	Wet	3.50 – 7.50	290	50	5.8	Yes
Test 5MF-75	Fine	Dense	Wet	2.50 – 8.50	290	75	3.86	Yes
Test 6MF-100	Fine	Dense	Wet	2.00 – 5.50	290	100	2.9	Yes

3.6 PARTICLE IMAGE VELOCIMETRY

This section introduces Particle Image Velocimetry (PIV) and describes the software used for analyses. The process of analysis in this study is then described and values chosen for certain software parameters are presented.

3.6.1 Introduction

Particle Image Velocimetry is a technique used to determine movements and strains of various regions within a deforming body by comparing sequential photographs of the deformation. This technique was initially developed to track the movement and velocity of particles in a fluid (Adrian, 1991) and has proven to be equally useful in tracking the movement of sand particles in a deforming soil body.

Various image-based techniques have been used to measure soil deformation in the past including X-rays, stereo-photogrammetric methods and image-processing algorithms that track physical targets within the soil, such as lead shot or coloured beads (White et al., 2003). White et al. (2003) mentioned several limitations of conventional target tracking methods:

- Target markers could influence the behaviour of the soil on a local level.
- Target markers could easily become obscured by soil particles during deformation.
- The resolution of the deformation measurements depends on the spacing of the target marker grid.
- Positioning of the target markers during soil placement tends to be a meticulous undertaking prone to human error.

These problems were mostly eliminated by using PIV which tracks the movement of soil particles by correlating image texture across two or more sequential digital images. The granularity of soil provides ample texture to track this movement, thus eliminating the need for target markers entirely.

3.6.2 GeoPIV Software

PIV analyses were performed in this study using the GeoPIV8 software package developed by David White and Andy Take (White & Take, 2002; White et al., 2003). The software consists of several scripts that run in Matlab. It operates by dividing the image up into patches and then finding patches in sequential images that most resembles the initial patch. Since the data of a digital colour image is essentially contained in 3 matrices (one matrix for each primary colour), each containing a value of colour intensity per pixel, these patches can be compared through matrix correlation techniques.

3.6.3 Analysis Technique

Typically, the software performed the following steps when analysing the deformation across two images, Image 1 (the reference image) and Image 2 (the compared image):

1. The area of analysis in Image 1 (reference image) was divided into a grid-like mesh of test patches of size $L \times L$ pixels. Figure 3-31 shows the grid of patches in image 1 with the first test patch at location $(\mathbf{u}_1, \mathbf{v}_1)$.
2. For the first *test patch*, a slightly larger *search patch* was extracted from Image 2. The search patch extended a distance s in each direction beyond the extents of the original test patch and therefore had equal sides of length $L + 2s$. This search patch marked the area in which the test patch was searched for.

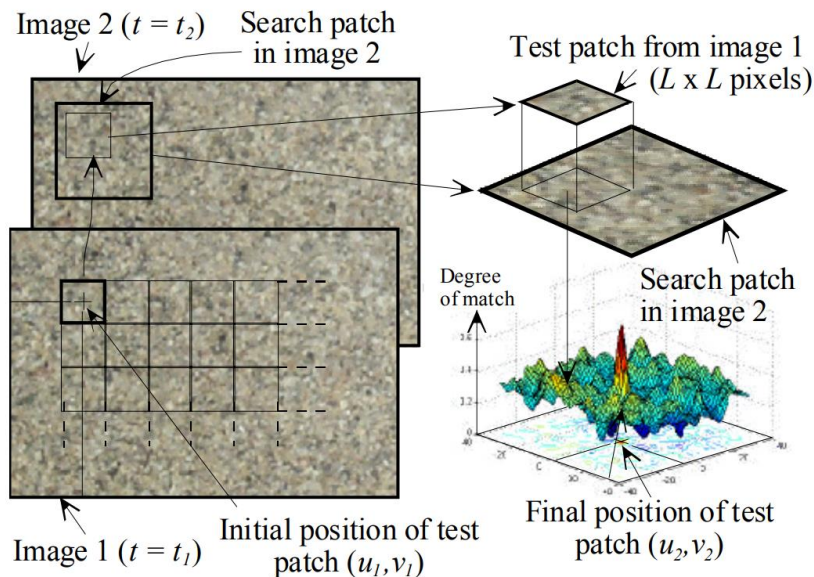


Figure 3-31: Principles of PIV analysis (from White & Take, 2002)

3. The correlation between the test patch in Image 1 and the search patch in Image 2 was then evaluated using matrix correlation techniques which produced a correlation plane (Figure 3-32a) that showed the “degree of match” at all locations within the search patch.
4. The point of highest correlation on the correlation plane was enlarged (Figure 3-32b) and a cubic interpolation was used to identify the exact position $(\mathbf{u}_2, \mathbf{v}_2)$ of the greatest correlation to sub-pixel precision (Figure 3-32c).
5. The \mathbf{u} and \mathbf{v} locations of the matched patch in Image 2 were then stored in a data file.
6. Steps 2 to 5 were repeated for every patch in the mesh to complete the comparison between Image 1 and Image 2.

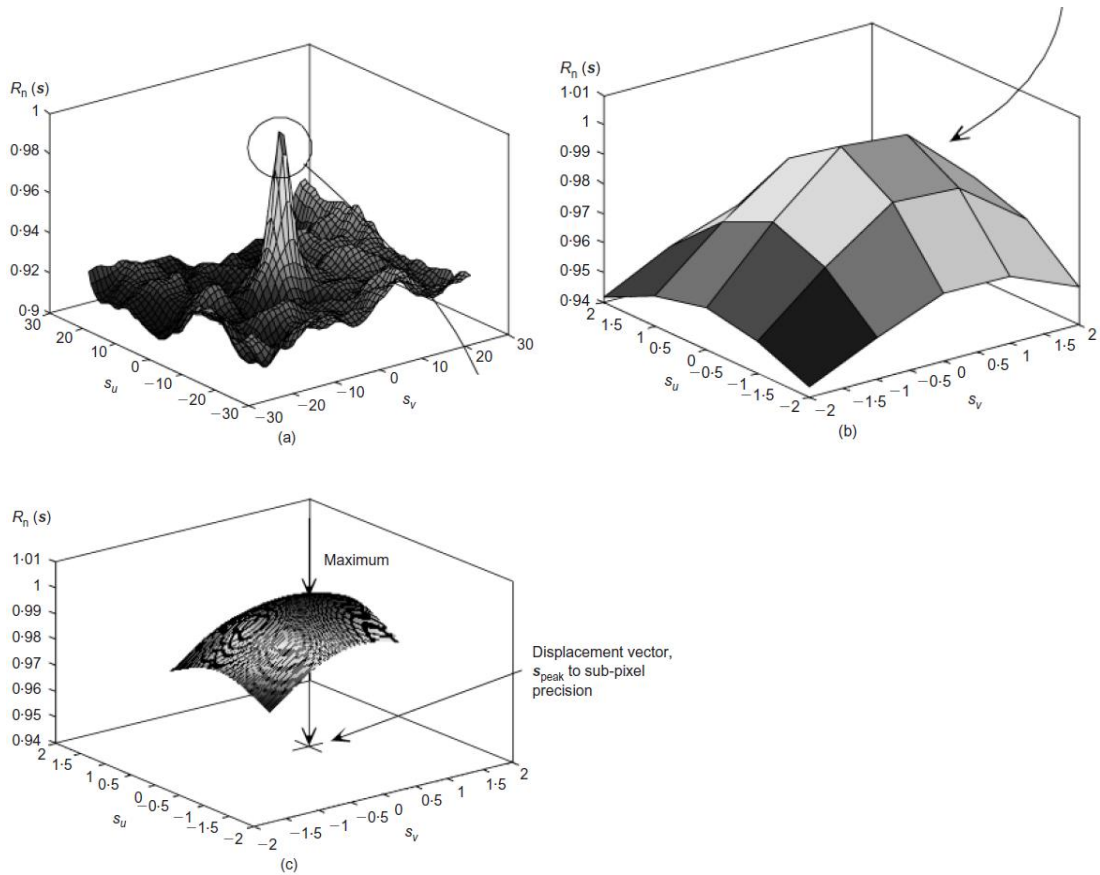


Figure 3-32: Finding displacement vector using PIV by (a) determining a correlation plane, (b) enlarging the peak of the correlation plane and (c) fitting a cubic function over the peak (White et al., 2003)

PIV analyses are usually done between a sequence of images taken during the deformation and thus the steps above were repeated for the entire sequence of images, comparing each image to the one before it.

Patch size and spacing

White et al. (2003) performed an experiment to determine the best patch size to use in an analysis. They ran analyses that compared various image pairs (both real and artificially generated) with known displacements using patch sizes of 6, 8, 10, 16, 24, 32 and 50 pixels. The results, shown in Figure 3-33, indicated that a larger patch size produced a smaller standard error on average, therefore having a higher precision.

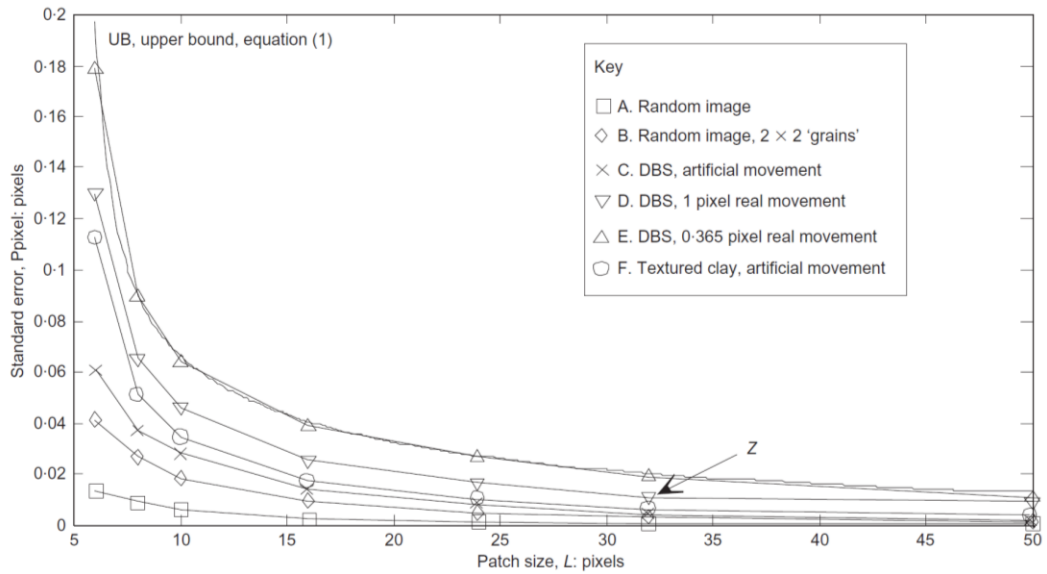


Figure 3-33: PIV precision against patch size (White et al., 2003)

A large patch size was therefore selected for analyses in this study. All experiments were analysed with a mesh of test patches sized 48 x 48px spaced at 16px horizontally and vertically. This created an overlap between patches that increased the resolution of data points without sacrificing precision. A typical mesh (shown in Figure 3-34) covered the portion of soil in the centre of the soil body stretching vertically from the bottom of the trapdoor to the soil surface and horizontally by approximately 50mm on either side of the trapdoor centreline. The search zone used in each comparison stretched 10 pixels in each direction beyond the extents of the test patch.

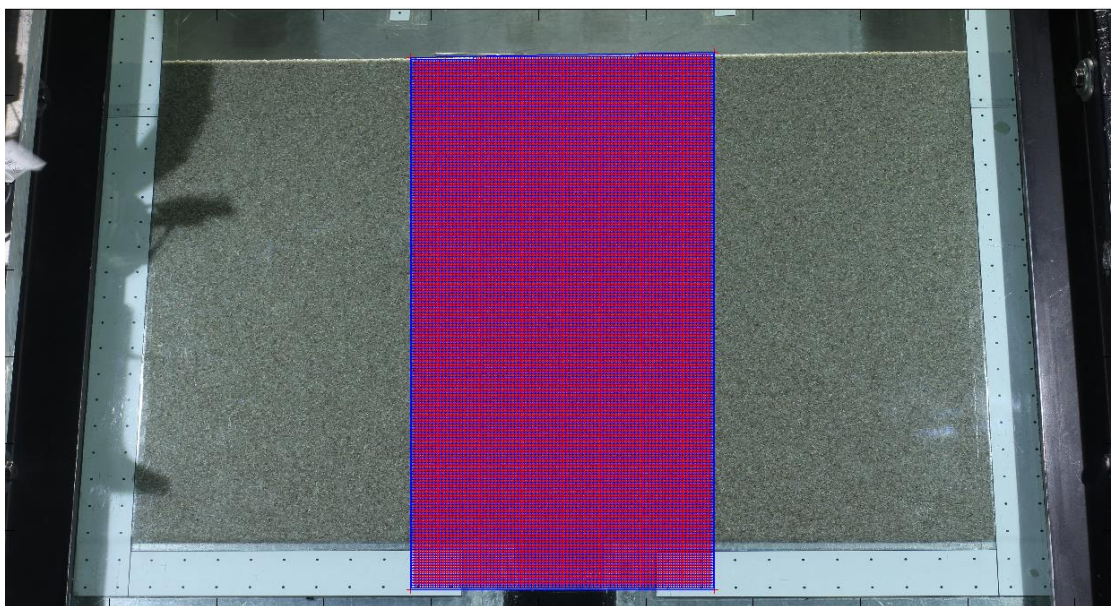


Figure 3-34: Typical mesh used in PIV analysis

Images

Images were analysed at a full resolution of 5184 x 3456px equating to roughly 15 image pixels per millimetre on the model. The first analysed image was taken just before trapdoor movement started and the final image was taken when the trapdoor reached its maximum retraction or when sand started to leak from the test frame.

Although images were taken roughly 6 seconds apart, the settlement rate of the trapdoor was slow enough to allow analysis of every second or third image without the risk of patches not being able to match. This equated to a time between analysed images of between 12 and 18 seconds (the exact time between images are listed in Chapter 4 along with the results of each test).

Leapfrog parameter

Since the output from GeoPIV is an approximation (best fit) of the deformation it is inevitable that small measurement errors will be introduced with each comparison. Every time the reference image is updated a new initial location (\mathbf{u}_1 , \mathbf{v}_1) is set for each patch, as computed in the previous comparison. Each new comparison therefore builds upon the error.

It would thus be better to compare as many consecutive images as possible to a single reference image before updating the reference image. For this reason, the software utilizes a leapfrog parameter which specifies how often the reference image is updated. If the leapfrog parameter is set to 1, GeoPIV compares images 1 and 2, 2 and 3, 3 and 4, etc. If the leapfrog parameter is set to 2, GeoPIV compares images 1 and 2, 1 and 3, then updates the reference image, and then continues to compare 3 and 4, 3 and 5, etc. This is illustrated in Figure 3-35. A high leapfrog parameter will yield high precision since the error carried forward is small but will increase the chances of not finding a match since too much deformation will have taken place. Consequently, a low leapfrog parameter will have lower precision but a high likelihood of finding a match.

A calibration experiment was run to test the precision of PIV under various leapfrog parameters. In the experiment a photograph from one of the experiments was artificially displaced by moving the image horizontally to the right by 3 pixels. In other words, 3 rows of pixels were removed from the right side of the image while 3 rows of clear pixels were added onto the left side of the image. A total of 34 images were created this way, each displaced horizontally by 3px more than the previous one, creating a total displacement of 102px. In this way, the displacement of the image could be precisely controlled.

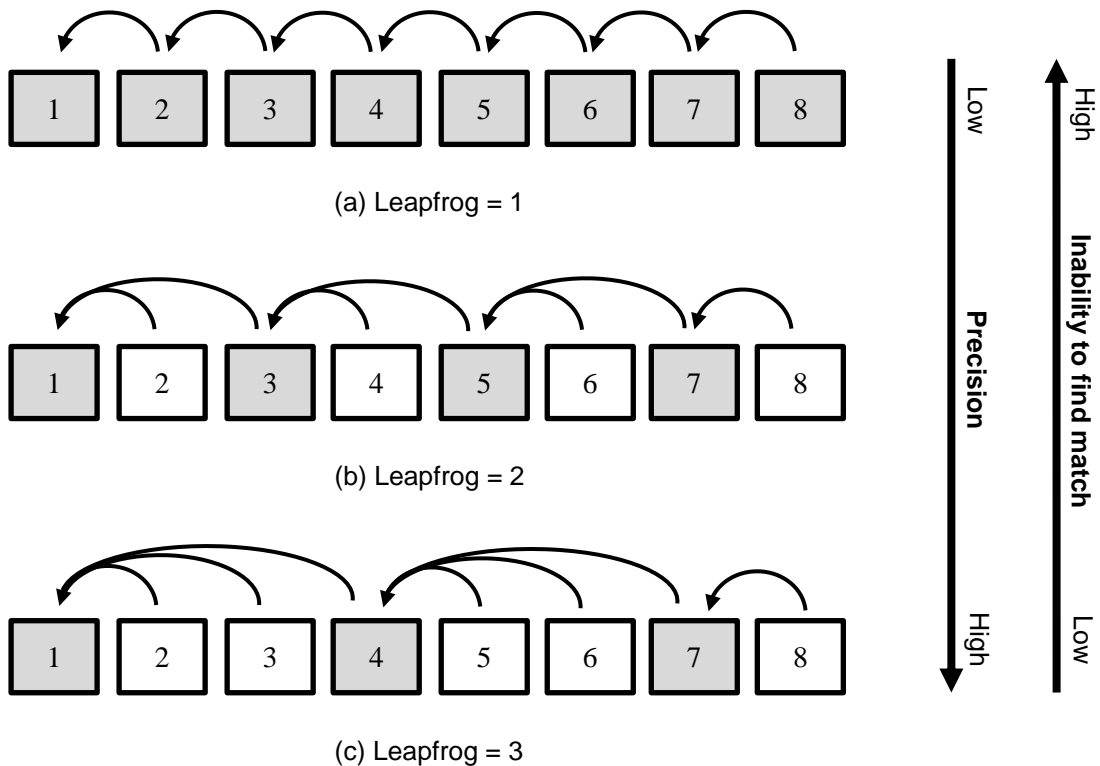


Figure 3-35: Illustration of leapfrog parameter (grey blocks represent updated reference images)

A series of PIV analyses were then performed on the image sequence using patches of 48 x 48px spaced at 48px (thus no overlap) with a search zone of 64px beyond the patch extents in all directions. Each analysis was performed with a different leapfrog parameter ranging from 1 to 10 in increments of 1. Results of these analyses were compared to the original known displacements and the average absolute error of each image in the sequence was then calculated, as seen in Figure 3-36.

As was expected, a leapfrog parameter of 1 induced the largest error, equalling 0.083px (0.0055mm) on average over a displacement of 100px (6.66mm) or roughly 0.083% of actual displacement. Precision increased significantly with greater leapfrog parameters. It is interesting to note, however, that the greatest precision was obtained by using a leapfrog parameter of 8, showing an average error of 0.0006px. Any leapfrog parameter above this saw a decrease in precision, probably due to the limited size of the search zone patch. The search zone could be increased, but this would also increase computation power significantly. In addition, it is also interesting to note that precision increased by between 5 and 6 times whenever actual displacements equalled a multiple of $\frac{1}{2}$ the patch size. Errors in the vertical direction were also measured and were found to be almost identical to that of the horizontal direction, although no artificial vertical movement was induced.

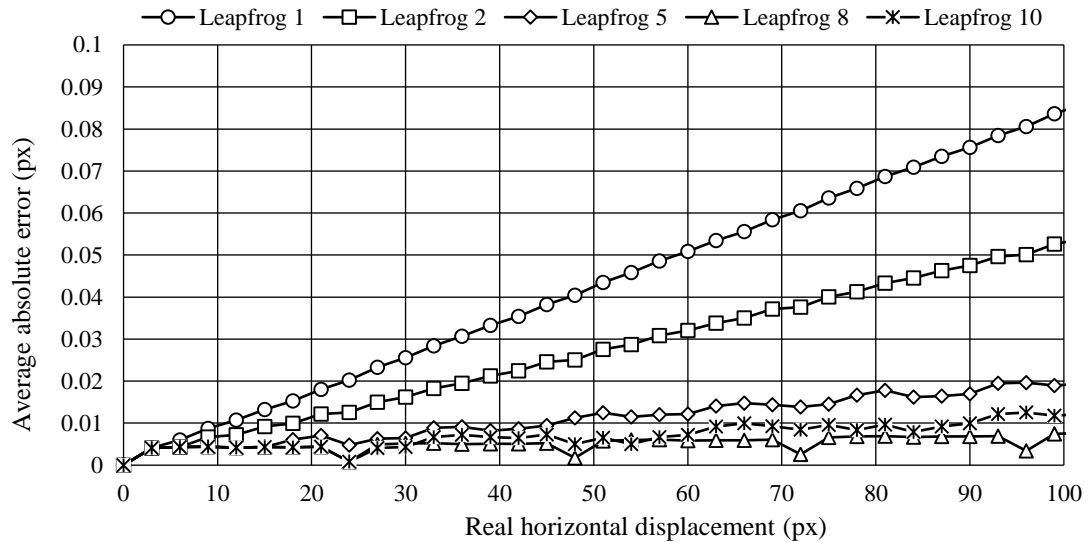


Figure 3-36: Error induced in horizontal displacements by various leapfrog parameters

In this study, initial analyses were performed with leapfrog parameters of 3 and 4, but it was quickly noted that the deformations experienced in some of the models were too excessive to be analysed with a leapfrog parameter greater than 1, thus resulting in the software not being able to match various patches. A leapfrog value of 1 was therefore used in the analysis of all tests.

3.6.4 Cleaning of Data

The output from the analyses were in the form of matrices that contained the initial position ($\mathbf{u}_1, \mathbf{v}_1$) and final positions ($\mathbf{u}_2, \mathbf{v}_2$) of each test patch in the grid, for every image in the sequence. Displacement vector fields (as seen in Figure 3-37) could then be generated by subtracting the initial position of each patch from the final position.

In each comparison some patches could not be matched due to excessive deformations and therefore produced wild vectors (an artefact of the program) that point in random directions and are much larger in size than the vectors around it. Using built-in functions in GeoPIV, these wild vectors were deleted from the data by removing all data from the specific test patch, leaving only a matrix of clean data.

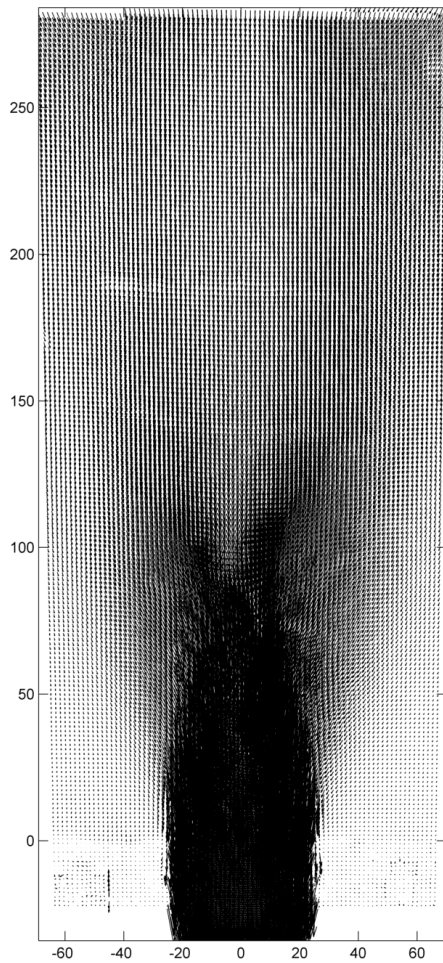


Figure 3-37: Typical vector displacement field

3.6.5 Calibration and Correcting for Parallax

Due to the camera being slightly lower than the midpoint of the sand body as mentioned in Section 3.3.8, some parallax was introduced into the images, causing the lower part of the model to appear wider than the top. These errors could be corrected by including and analysing PIV marker dots in the analysed images.

As mentioned, PIV marker dots were stuck to the inside of the glass panel along the sides and bottom of the soil body as seen in Figure 3-34. The markers were carefully positioned and stuck onto the glass so that the exact distance between them was known. A separate PIV analysis was then performed on these marker dots using a function that determined the exact centroid of each marker dot and traced its individual movement across the sequence of images. By specifying the exact object coordinates of each marker dot in millimetres, the software could then calibrate the model to correct for parallax, camera distortion and camera movement. This was done using a built-in function of GeoPIV that warped the test patch locations to correlate with results from

the analysis run on the marker dots. As a result, the function also converted the data from image coordinates (as they appear on the image) to object coordinates (as they appear on the actual model).

3.6.6 Displacement and Strain Plots

Using the output data matrix, various plots related to displacements could then be drawn such as displacement fields and settlement plots. Knowledge of the original distances vs. final distances between patches could also be used to calculate various strains in the soil body, which in turn allowed the creation of strain plots such as incremental maximum shear strain plots and total maximum shear strain plots. These plots are now explained with the results in Chapter 4.

4 RESULTS AND DISCUSSIONS

4.1 INTRODUCTION

This chapter presents results of all experiments conducted in this study and discusses the findings. The methods used to determine exact trapdoor settlement are discussed first. Results of each test are then presented individually in the form of figures and graphs. The results are discussed and comparisons are made between the shearing behaviour of different soil types varying in moisture content and particle size. Also discussed in this section are surface settlement and the influence of cavity propagation on surface movement. Finally, the information gathered from this chapter is applied to real life sinkholes and the implications of this are discussed.

4.2 SETTLEMENT OF TRAPDOOR

Settlement of the trapdoor was measured with an LVDT or by means of image correlation in the absence of an LVDT. Figure 4-1 shows trapdoor settlement readings of Test 3DF (graphs for trapdoor settlement of the other tests showed similar results). Also shown is a linear trend-line fitted through the LVDT data. The graph indicates an average trapdoor settlement rate of 2.49mm/min. Note that settlement does not start at zero due to premature settlement of the trapdoor during centrifuge acceleration. This could, however, be neglected since the objective of the test was to investigate failure mechanisms at larger trapdoor movements.

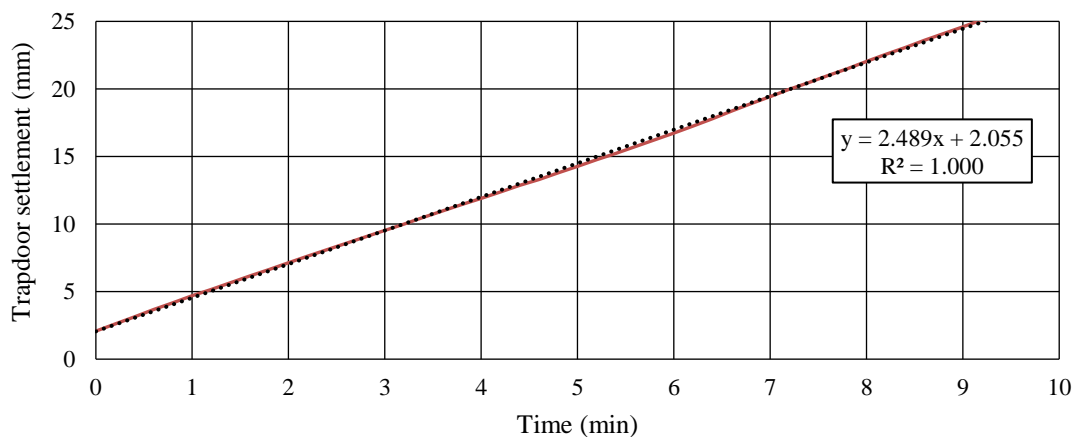


Figure 4-1 Settlement of trapdoor with time during Test 3DF

The equation of the trend-line in the graph shows an R^2 value close to 1, indicating good linear fit. This shows that extrapolation could be used to estimate trapdoor settlement for the entire

movement range of 85mm when the trapdoor LVDTs reached their maximum extension of 30mm, or when tracking of the trapdoor using image correlation was not possible. Based on the availability of data, the following hierarchy was used to determine final settlement values:

1. LVDT readings
2. Trend line equations based on LVDT readings
3. PIV results
4. Trend line equations based on PIV results

4.3 PRESENTATION AND DISCUSSION OF RESULTS

Results from each of the tests are presented below. Details of the test arrangements are given after which plots of vertical displacement, incremental maximum shear strain and total maximum shear strain are presented. Tests are described in chronological order as they appear in Table 4-1. The first test is described in more detail while notable deviations from these results are pointed out in subsequent tests.

Table 4-1 Sequence of presentation of results

Nr.	Sand type	Density	Moisture Content	Trapdoor size	Test name
1	Coarse	Dense	Dry	50mm	Test 1DC
2			Moist		Test 2MC
3	Fine	Dense	Dry	50mm	Test 3DF
4			Moist		Test 4MF-50
5			Moist	75mm	Test 5MF-75
6			Moist	100mm	Test 6MF-100

In literature, trapdoor test results are often presented as normalised trapdoor settlement (δ/B) with δ the trapdoor settlement and B the trapdoor width. This provides a dimensionless parameter that can therefore be used to compare results from many different tests. The same convention was used when reporting results in this study.

Throughout this chapter, several terms will be used to describe the results relating to shear behaviour of the soil inside the trapdoor experiments. They are defined here:

1. *Shear band*. A line or curve in a body of sand on which the soil is sheared beyond failure.
2. *Zone of influence*. The area in a body of soil bounded by the trapdoor at the bottom, the leftmost and rightmost shear bands on the sides and either the highest-reaching shear

band or the soil surface at the top. This zone typically increases in size as the tests progress.

3. *Trapdoor centreline.* An imaginary line extending vertically upwards from the centre of the trapdoor in a trapdoor experiment. This line also coincides with the centre of the soil body.

The results of each test are now presented, starting with test 1DC.

4.3.1 Test 1DC – Dry Coarse Sand

4.3.1.1 Test Arrangement

Parameters of the test arrangement of Test 1DC are given in Table 4-2. Settlement of the trapdoor was measured by one 30mm range LVDT throughout the test. Through inspection of images, premature settlement (δ_0) of the trapdoor during centrifuge acceleration was determined to be 0.28mm ($\delta/B = 0.6\%$) when acceleration reached 50G. This value was taken to be the settlement at the first analysed image and LVDT readings were zeroed at this point. All subsequent LVDT readings were adjusted by δ_0 to obtain corrected settlement values.

Table 4-2: Test arrangement parameters of Test 1DC

Parameter	Value
<u>Soil Characteristics</u>	
Sand type	Coarse sand
Moisture content	Dry
Density	Very Dense
<u>Geometry of Test Package</u>	
Sand depth (H)	290 mm
Trapdoor width (B)	50 mm
H/B ratio	5.8
Rate of trapdoor settlement	2.54 mm/min
Time between analysed images	12 secs (every 0.51mm of settlement)

Although the LVDT provided readings only up to a trapdoor settlement of 28mm, a linear trend line equation was used to estimate settlement up to a final value of 81mm ($\delta/B = 162\%$).

4.3.1.2 Photographic Record

The first analysed photograph of Test 1DC is shown in Figure 4-2 below. Also indicated is the area of interest that was analysed using PIV.

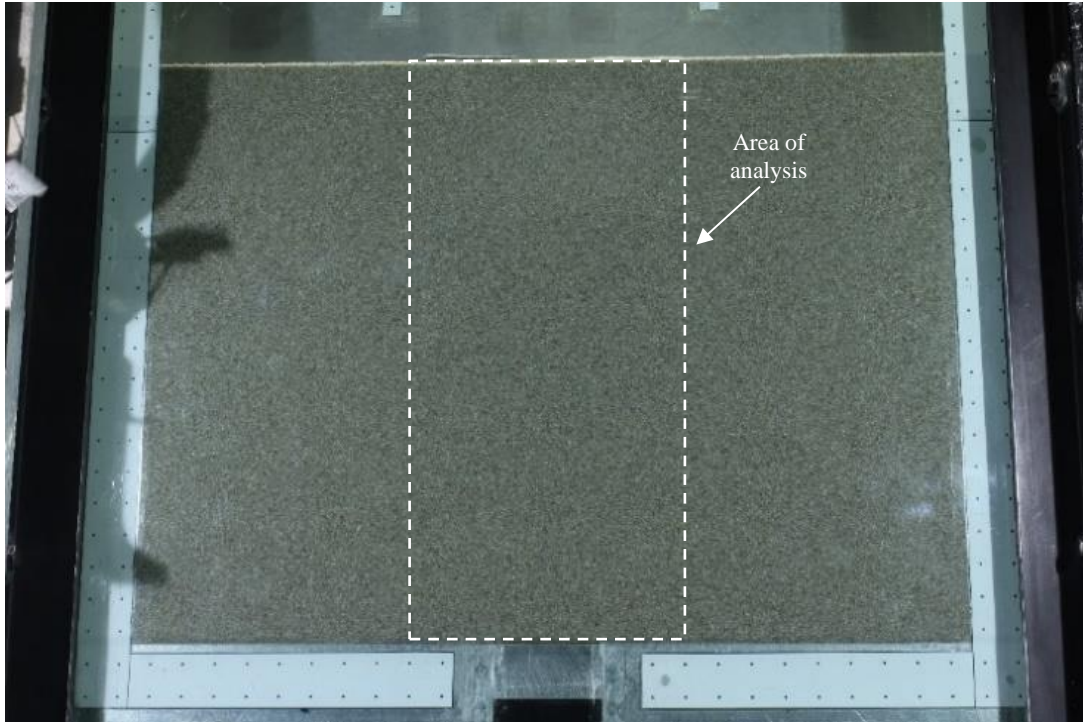
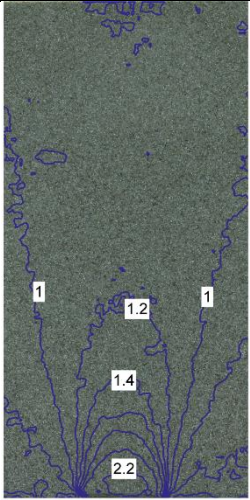
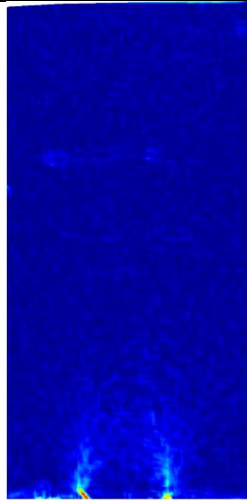
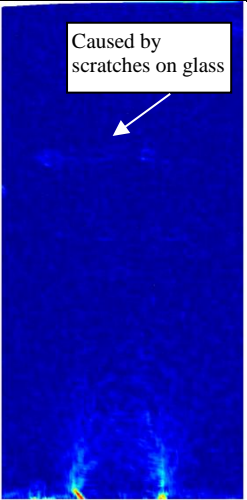
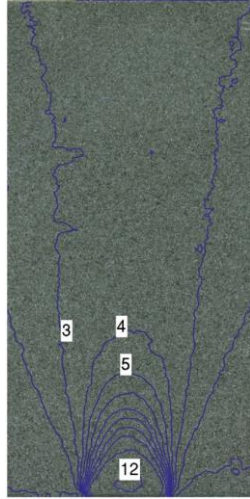
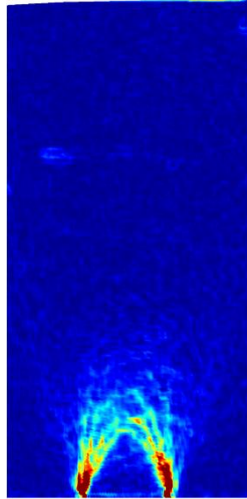
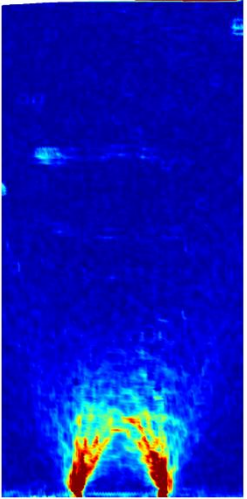
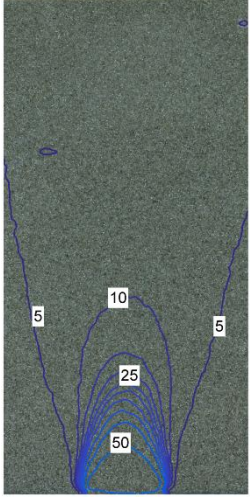
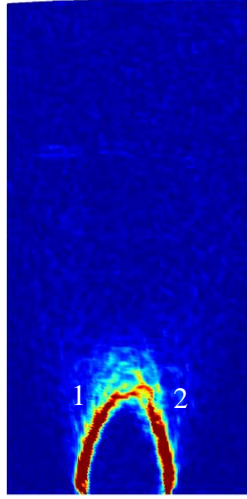
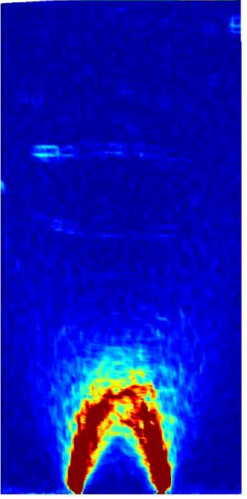


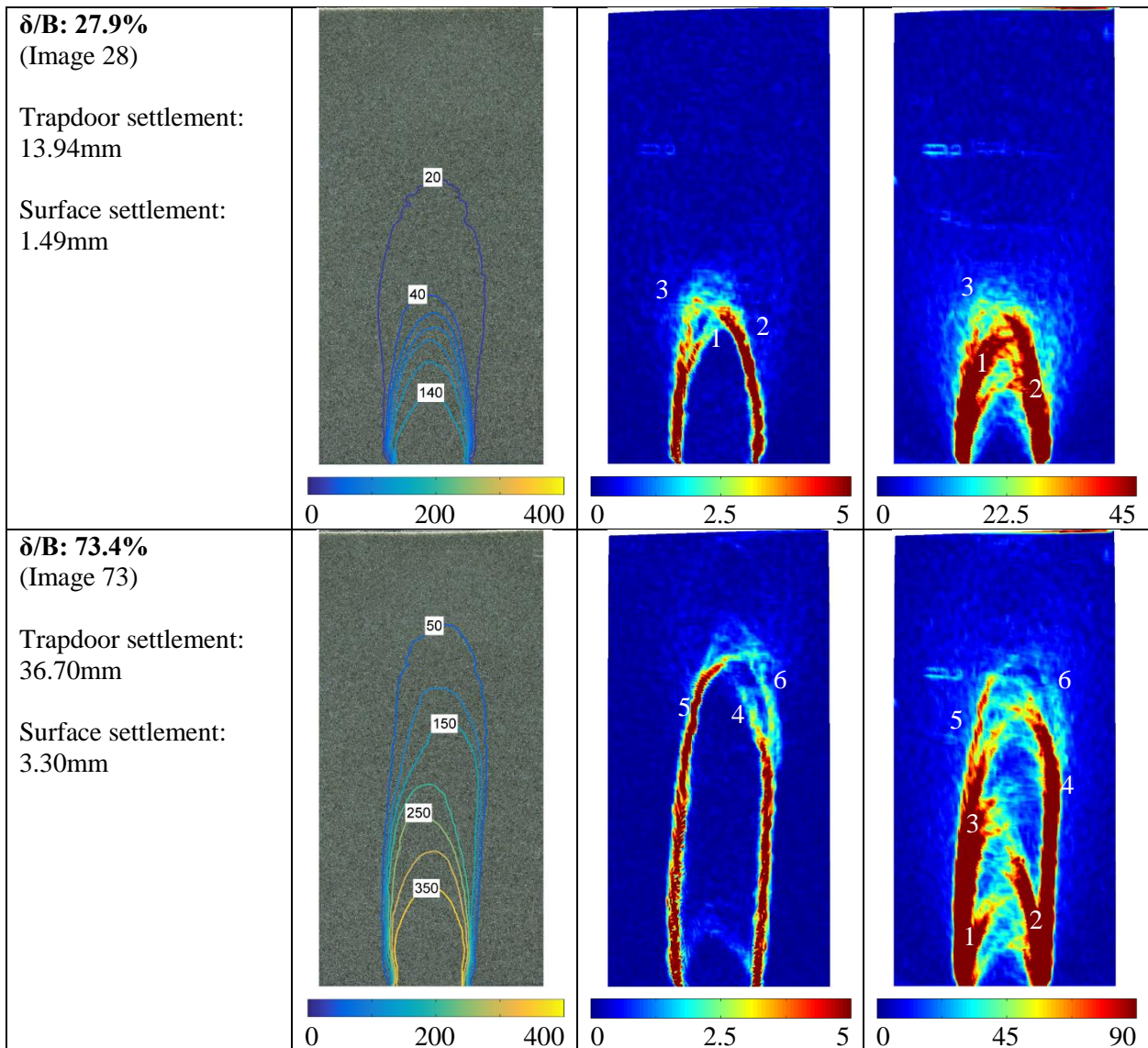
Figure 4-2: First analysed photo of Test 1DC

4.3.1.3 Shear Zone Propagation

Movements in the soil body were tracked using PIV from which several plots of displacement and strains could be generated as described in Section 3.6.6. Table 4-3 below shows distributions of vertical displacement, incremental maximum shear strain and total maximum shear strain at several selected stages during the test. The respective stages shown here were selected to illustrate prominent changes in the soil behaviour during the test. In the table, vertical displacement plots show contours of vertical displacement throughout the test in units of pixels. Incremental maximum shear strain plots show the change in maximum shear strain between the current image and the image before it (at a settlement rate of 2.54 mm/min and an image spacing of 12 seconds, this would equate to 0.508mm of trapdoor settlement or a δ/B ratio of 1.0% between the two compared images). Plots of total maximum shear strain show cumulative maximum shear strains, calculated with the first image ($\delta/B = 0.6\%$) as baseline. Strains, however, could only be computed up to a δ/B ratio of 73.4% after which calculations became impractical due to the large magnitudes of accumulated strains. Small scratches on the glass panel introduced minor irregularities into the shear strain results as indicated on the plots below. These apparent strains were present in most of the tests in this study but do not form part of the actual strain distribution of the soil body and can thus be ignored.

Table 4-3 Selected results of Test 1DC

	Vertical displacement (px)	Incremental max. shear strain (%)	Total max. shear strain (%)
<p>δ/B: 1.1% (Image 2)</p> <p>Trapdoor settlement: 0.54mm</p> <p>Surface settlement: 0.09mm</p>	 <p>0 200 400</p>	 <p>0 2.5 5</p>	 <p>Caused by scratches on glass</p> <p>0 2.5 5</p>
<p>δ/B: 3.0% (Image 4)</p> <p>Trapdoor settlement: 1.48mm</p> <p>Surface settlement: 0.32mm</p>	 <p>0 200 400</p>	 <p>0 2.5 5</p>	 <p>0 3.5 7</p>
<p>δ/B: 10.4% (Image 11)</p> <p>Trapdoor settlement: 5.19mm</p> <p>Surface settlement: 0.77mm</p>	 <p>0 200 400</p>	 <p>0 2.5 5</p>	 <p>0 10 20</p>



4.3.1.4 Discussion of Displacement and Strain Plots

It is evident from Table 4-3 that shear bands started forming from the two edges of the trapdoor as soon as the test started. This was followed by a group of smaller shear bands radiating outward from each corner of the trapdoor. Two prominent shear bands (labelled 1 and 2) remained from this group and joined up at the centre of the soil body, taking on the approximate shape of a triangle. As the trapdoor receded further, new shear bands formed above these, expanding the zone of influence upwards. New shear bands continually formed, alternating from left to right, from both sides of the zone of influence.

As pointed by Terzaghi (1936), horizontal stresses in the soil above an arch temporarily increase beyond that created due to self-weight (see Figure 2-17), providing soil in that region with enough shear resistance to temporarily carry the load of the soil mass above it. This is further

illustrated in Figure 4-3 below. In Figure 4-3a, the shear resistance in the sand above the trapdoor is greater or equal to the stress caused by the soil weight above it ($\tau \geq \sigma_v$) and thus the arch is stable. However, as the trapdoor recedes further, shear failure causes a decrease in shearing resistance along the two vertical lines extending from the edges of the trapdoor (in effect the “feet” of the arch). This in turn causes more material lying on and above the arch to be drawn downwards, thus collapsing the arch and reducing the shear resistance in the region, as seen in Figure 4-3b. The concentration of horizontal stresses (σ_v) is thus disturbed and a new stress concentration is formed at a slightly higher location. This new stress concentration is strong enough to support the weight of the soil above it and consequently a new, similarly shaped failure arch forms above the first one. This process repeats itself several times and causes the zone of influence to extend upwards as the trapdoor recedes. Similar behaviour was reported in a summary by Costa et al. (2009) for tests done in shallow material.

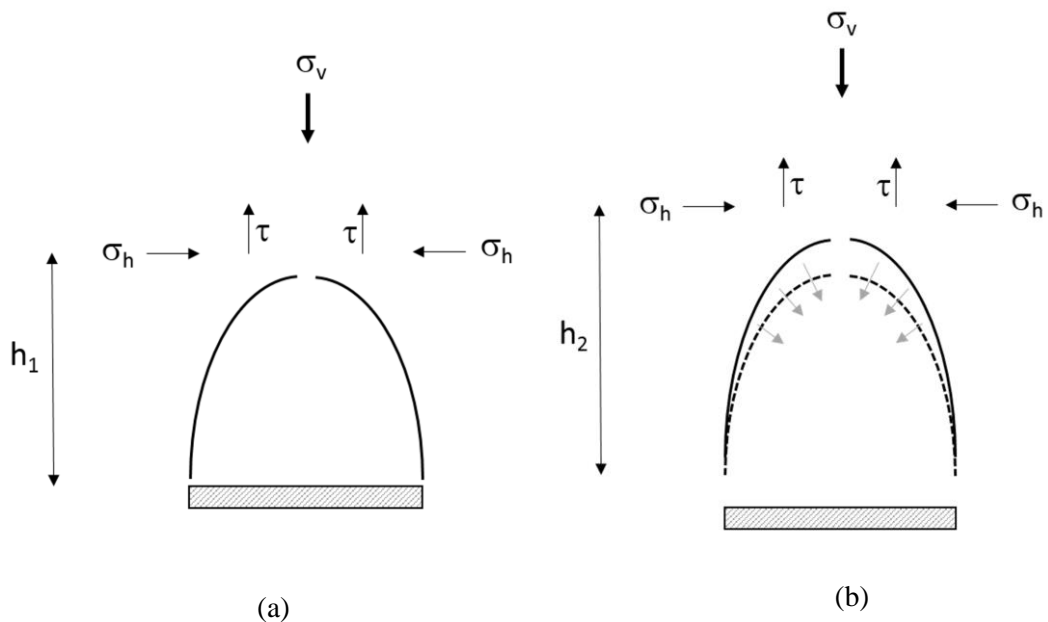


Figure 4-3 Upwards movement of the zone of influence

Similar movement of the zone of influence was also recorded in this study. At a δ/B ratio of 10.4%, the series of arching shear bands gradually extended upwards and took on an approximate parabolic shape, rather than the initial triangular shape. The zone of influence grew increasingly taller and the side slopes of the shear bands became increasingly steeper, becoming near vertical at a δ/B ratio of 73.4% (similar to the shear bands predicted by Terzaghi (1936) to occur when the shear zone came close to the surface). The top ends of the shear bands however, continued to be parabolic in shape.

Three different mechanisms were thus observed in this test – triangular, parabolic and finally vertical, in that order. These mechanisms are shown in Figure 4-4 below. Costa et al. (2009) and Dewoolkar (2007) noted that shear bands formed at angles with the vertical equal to the angle of dilation as mentioned in Section 2.3.3.2, and the same type of behaviour was observed in this study. Shear bands initially formed at inclined angles in the form of a triangle. As the soil supporting the arch then receded down, movement along the triangular shear band pattern ceased and new mechanisms formed above it, albeit more vertically due to a decrease in local density (due to dilation) at that point and thus a decreased dilation angle. This process repeated itself with the upper radius of each successive mechanism being larger than the previous. This caused the mechanism to change to a parabolic shape and eventually a vertical shape. All three mechanisms are also in line with mechanisms postulated by Iglesia et al. (2014) in their analysis of the load on the trapdoor.

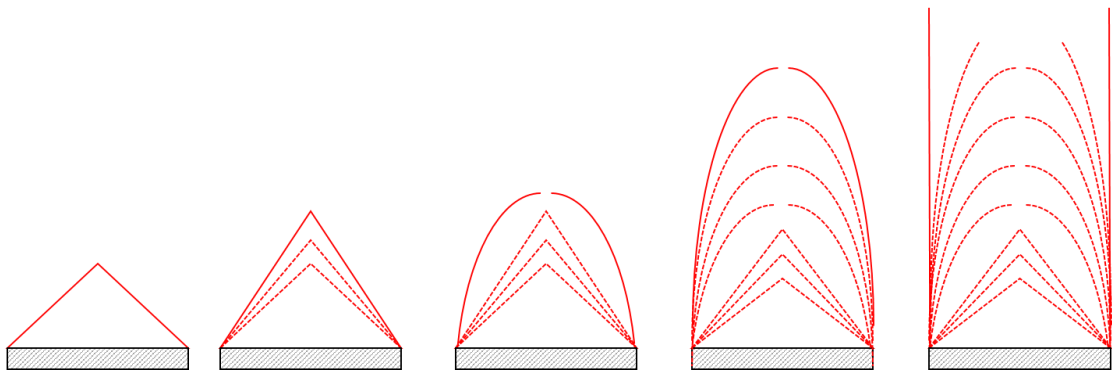


Figure 4-4 Progression of failure mechanisms

For the first part of the test, soil deformation was largely confined to a zone of influence bound by two lines extending vertically upwards from the trapdoor edges, with very little to no deformation visible beyond these boundaries. Small deformation beyond these boundaries became visible at a δ/B ratio of 27.9% but the greatest amount of deformation remained directly above the trapdoor. In addition, formation of shear bands was mostly symmetric up to the appearance of the triangular-shaped mechanism at around 14mm trapdoor displacement, after which shear band development became increasingly more asymmetrical.

Horizontal and vertical movement of the soil body are shown in Figure 4-5 below. In these images, blue represents movement towards the right and red represents movement towards the left, while green represents no movement. Vertical movement is represented by deflection of the horizontal lines. As visible in the figures, horizontal movement in this test appeared to be dictated by the location of shear bands. Whenever a shear band formed, the wedge of soil above

it tended to settle vertically downward and move horizontally in the direction of the trapdoor centreline.

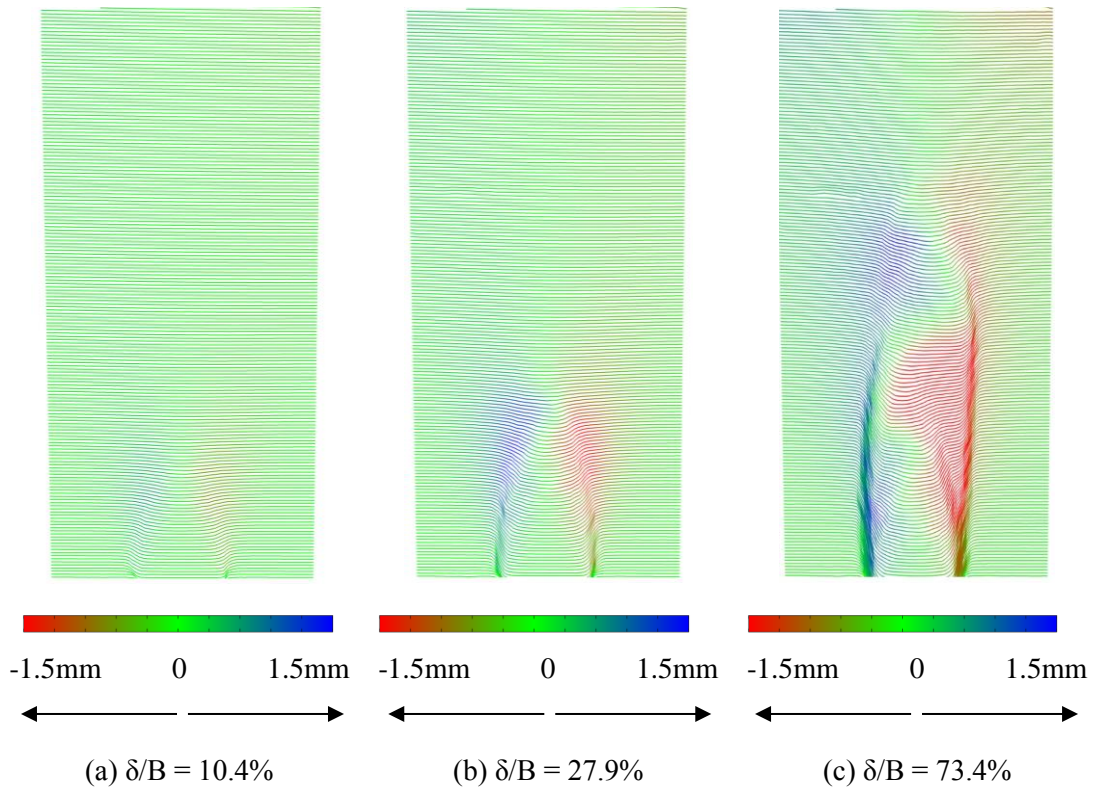


Figure 4-5: Settlement plots of test 1DC

It is also worth noting that, close to the soil surface, shear bands on either side of the shear zone tended to move closer together and join in the middle, reaching the soil surface at a single location near the trapdoor centreline, similar to that observed by Dewoolkar (2007). Once the soil surface was reached, adjacent soil started sliding into the newly created space left open by the receding soil column and by doing so progressively increased the diameter of the depression at the soil surface.

4.3.1.5 Strain Behaviour at Selected Points

Several points of interest in the sand body were selected to investigate changes in strain behaviour over time as the trapdoor settled. The first set of points were selected on four different shear bands that formed close to the vertical boundary of the zone of influence. These are shown in Figure 4-6 below.

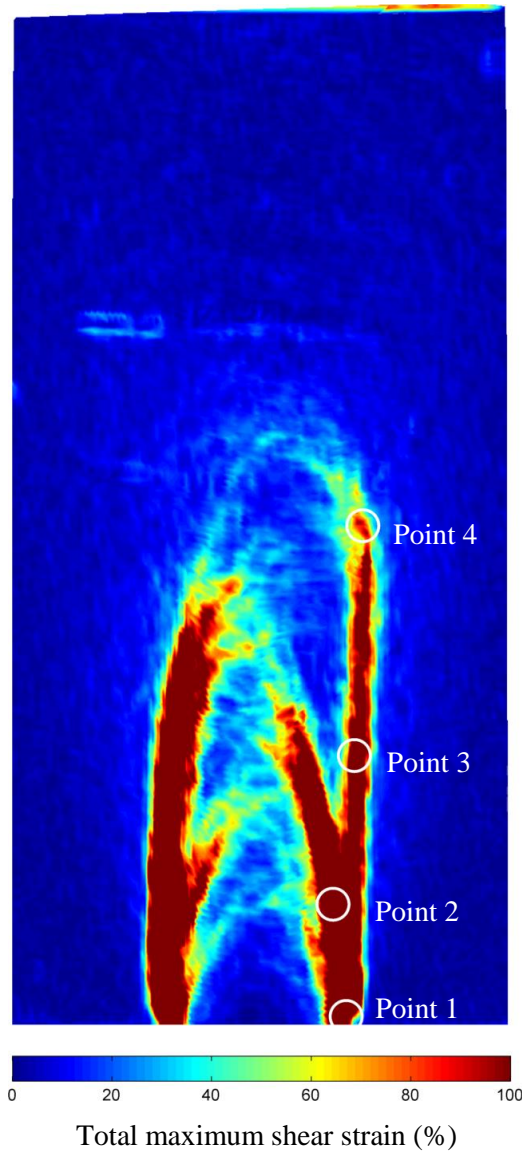


Figure 4-6: Distribution of total maximum shear strain above the trapdoor showing the location of selected points 1 to 4 in Test 1DC

Graphs showing total maximum shear strain (%) against normalized trapdoor movement (δ/B) are shown for the entire calculated shear strain range in Figure 4-7 and for smaller strains in Figure 4-8. It is evident from these figures that the inspected points experienced an increase in shear strains at different stages during the test, illustrating the progressive development of shear zones in response to trapdoor movement. Point 1 experienced shear strains increasing at a constant rate from the beginning of the test which continued up to the end of the test. As shown by Stone & Muir Wood (1992), strains at the edges of the trapdoor are much higher compared to strains along the rest of the shear band.

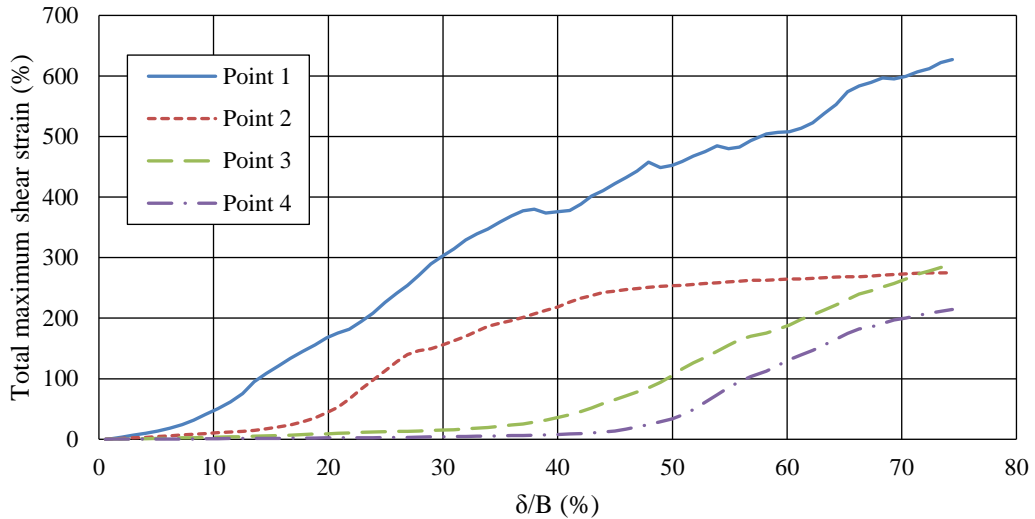


Figure 4-7: Total maximum shear strain of points 1 to 4 in Test 1DC (entire strain spectrum)

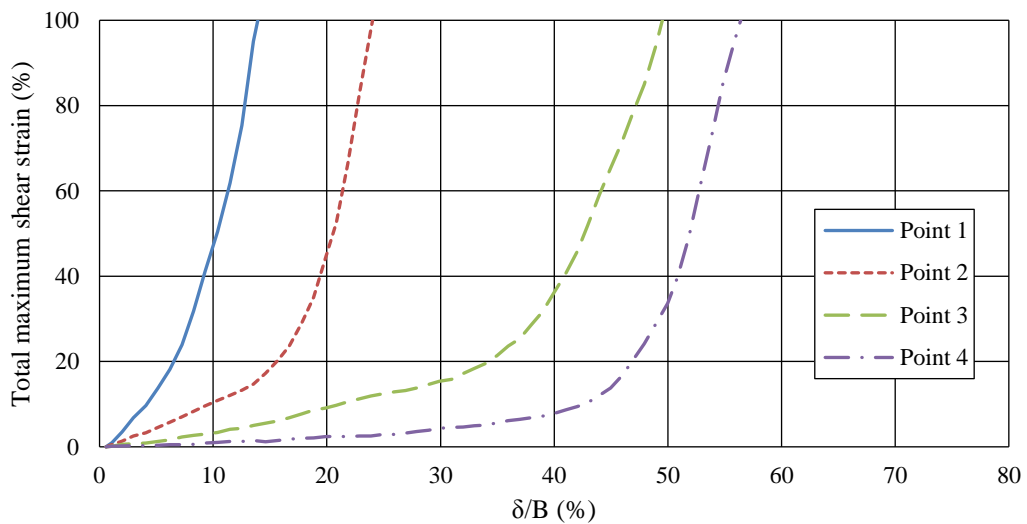


Figure 4-8: Total maximum shear strain of points 1 to 4 in Test 1DC (small strains)

Shear strains at point 2 commenced at a later point in time before increasing and attaining a constant value at a δ/B ratio of 50%. This demonstrates strain increasing at this location while the shear band formed, but then remaining constant as it moved down uniformly with the rest of the column of soil without showing any further strain. Points 3 and 4 both lie on a vertical shear band and thus showed similar behaviour with shear strains increasing at constant rates until the end of the test, albeit starting at different stages.

The location of the second set of points that was investigated is shown in Figure 4-9. These points were selected to be at roughly the same height above the trapdoor, tracking different

points of interest in the failing soil mass. Point 6 was selected to act as a reference outside the zone of influence in a region where no significant strains occurred. Points 7 and 10 were selected on a near-vertical shear band while point 9 was selected on an inclined shear band. Point 8 was selected at the top of a shear band near the middle of the zone of influence.

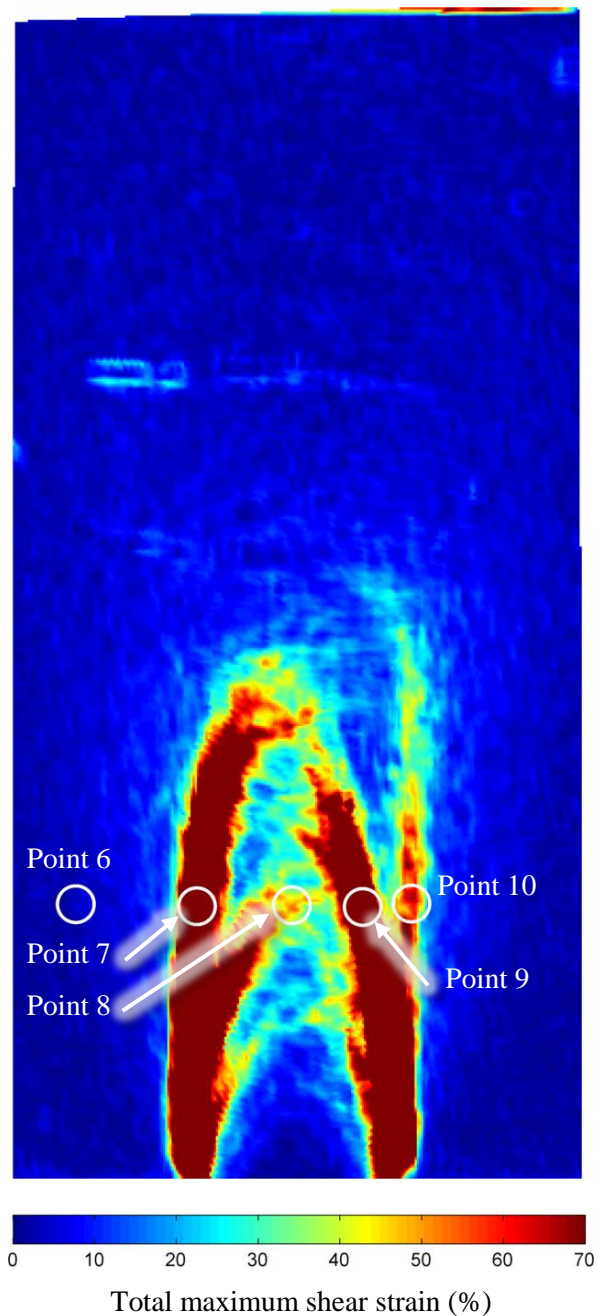


Figure 4-9: Distribution of total maximum shear strain above the trapdoor showing the location of selected points 6 to 10 in Test 1DC

Graphs showing total maximum shear strain against trapdoor movement (δ/B) are shown for the entire calculated shear strain range in Figure 4-9 and for smaller strains in Figure 4-10.

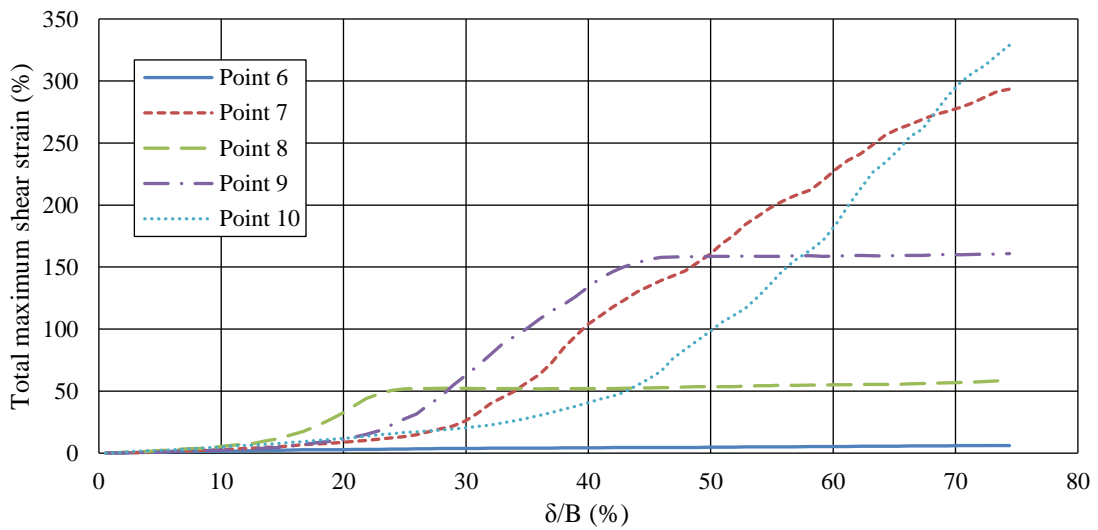


Figure 4-10: Total maximum shear strain of points 6 to 10 in Test 1DC (entire strain spectrum)

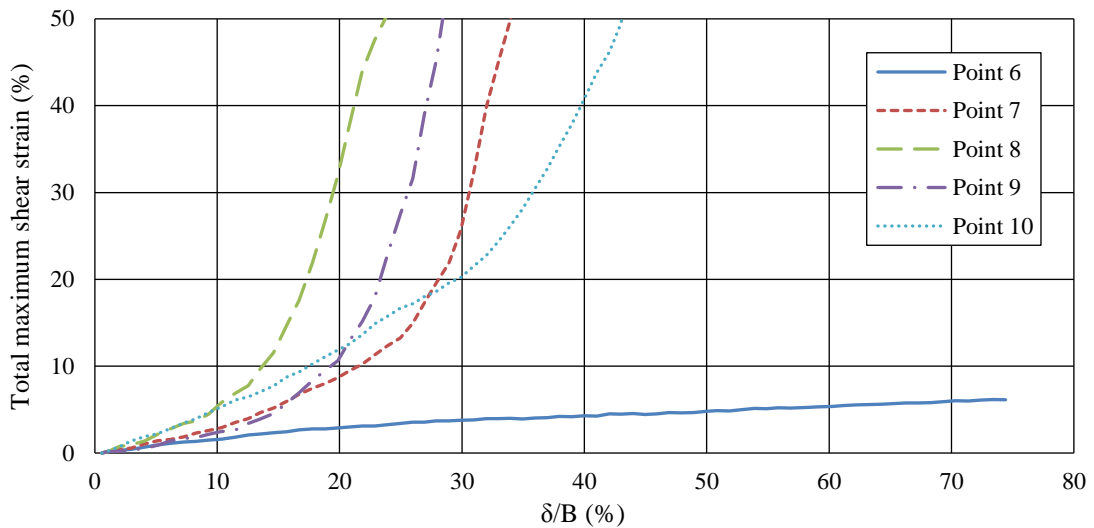


Figure 4-11: Total maximum shear strain of points 6 to 10 in Test 1DC (small strains)

Point 6 (chosen as a point of reference) experienced a small but constant increase in strain from the start of the test. All four of the other points (points 7 to 10) experienced this same constant increase in shear strain up to the point where the influence of a nearby shear band overshadowed this effect. Point 8, being at the centre of the zone of influence, experienced a sharp increase in shear strain before assuming a constant value for the duration of the test, indicating downward movement without any further shear strain. Point 9, being on an inclined shear band,

experienced a relatively similar phenomenon, deforming constantly up to a δ/B ratio of 45% and also remaining at a constant strain up to the end of the test. On the contrary, points 7 and 10, which lay on the vertical boundaries of the zone of influence, strained continually up to the end of the test. Although these two points were at roughly the same depth, straining commenced at different stages throughout the test (different values of δ/B) illustrating the asymmetrical nature of alternating shear bands during propagation of the failure zone.

It is evident that the greatest amounts of shear strain occurred on the vertical boundaries of the zone of influence as seen in the results of points 1, 3, 4, 7 and 10. These points experienced an increase in strain up to the end of each test, showing that continual shearing happens along these vertical boundaries. All other points were stationed between these two vertical boundaries and experienced strains only up to a certain value after which strains remained constant for the remainder of the test as the zone of active shearing gradually migrated upward past those points. This shows that points in the column of soil directly above the trapdoor tended to move down uniformly with little strain except when influenced by a nearby shear band. After the shear band had formed, strains at these locations stabilized again and continued their previous behaviour of uniform settlement.

4.3.1.6 Volumetric strain

Figure 4-12 depicts the volumetric strain distribution at the end of Test 1DC. Blue regions indicate negative volumetric strain (dilation) while red regions indicate positive volumetric strain (contraction). It is evident that large amounts of dilation occurred in the soil directly above the trapdoor, particularly along the lengths of all shear bands. Similar observations were noted by Evans (1983). Movement of soil particles over one another was hampered due to their angularity and interlock and as a result these particles were forced to dilate in a direction perpendicular to the shear band, consequently increasing the volume at that specific location. Contraction in the zone of influence was negligible.

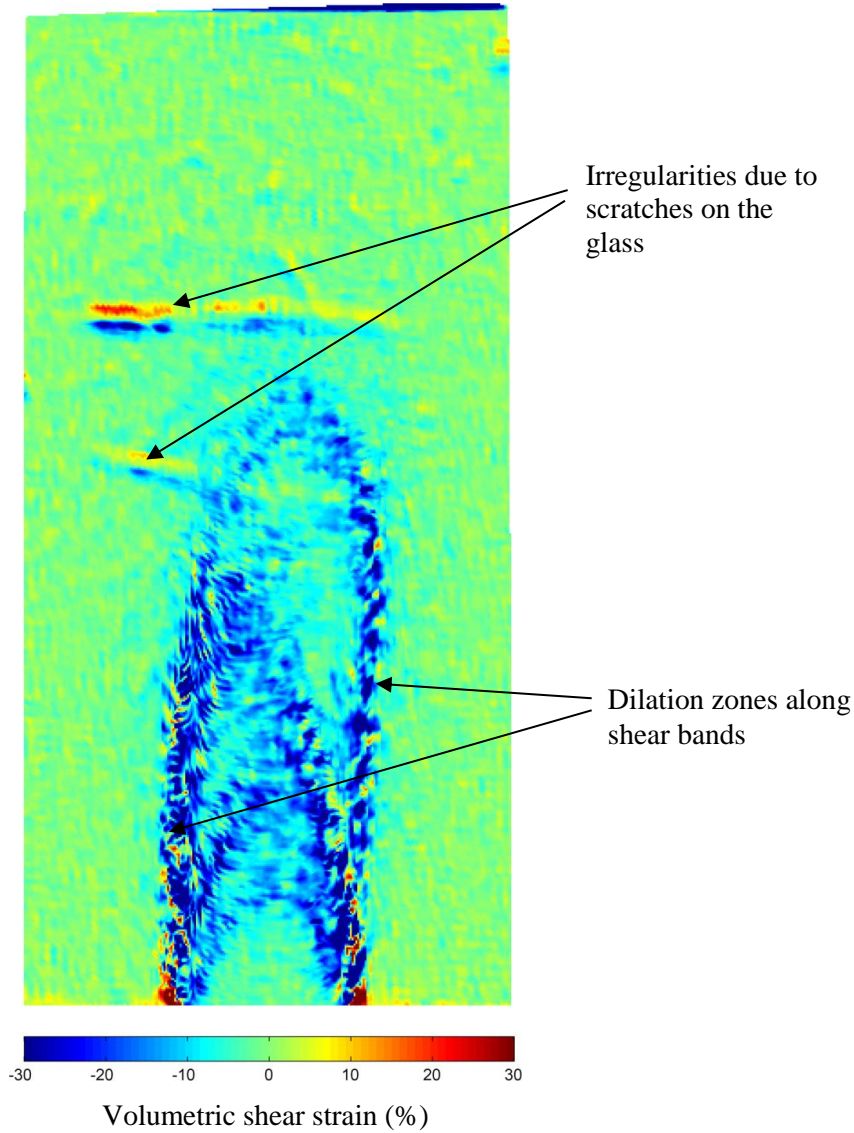


Figure 4-12: Distributions of volumetric strains at the end of Test 1DC

4.3.1.7 Surface Settlement

Settlement distributions were measured by tracking the movement of patches of soil near the surface using PIV. These results provided high-resolution data that correlated well with the measurements of the bank of LVDTs that rested on the soil surface. Vertical settlement of the soil (referred to hereafter as s) at various δ/B ratios throughout the test are shown as solid lines in Figure 4-13 below, with downward movement exaggerated. The settlement troughs were compared to a Gaussian curve as suggested by Costa et al. (2009) and discussed in Section 2.3.3.3. The best-fit Gaussian curve of each trough was obtained programmatically by varying

values of S_m , i and the position of the trough minimum to obtain the least squared error across the entire curve. Such curves are shown as dashed lines for each measured curve in Figure 4-13.

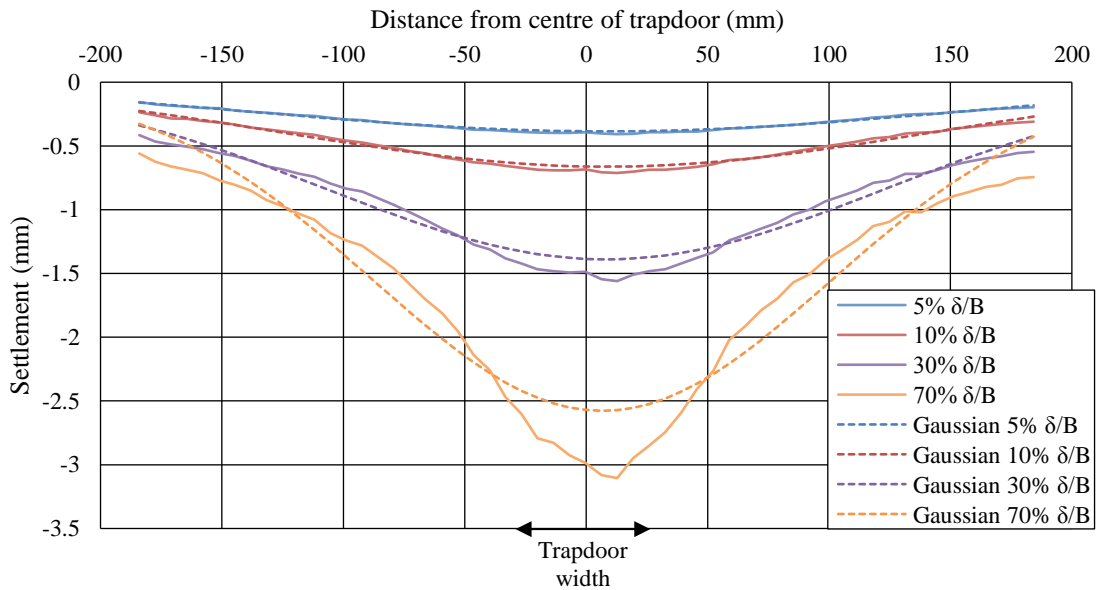


Figure 4-13: Surface settlement distribution of Test 1DC

As is evident from the graph, soil settled initially in the shape of a Gaussian curve while close to the surface, but later deviated from this shape as the test progressed and the observed settlement trough became deeper. This deviation occurred because significant vertical movement was confined to an area directly above the trapdoor, thus causing more surface settlement in those areas than in surrounding areas.

It is worth noting from Figure 4-14, showing normalized surface settlement (s/B) directly above the trapdoor against normalized trapdoor displacement (δ/B), that the *ratio* of surface settlement to trapdoor displacement remained constant at a value of about 10%, similar to what has been observed by Dewoolkar (2007). At a δ/B ratio of 95%, when the zone of influence has reached the surface, the *ratio* changed to 84% which was maintained up to the end of the test. This ratio is less than unity, as can be seen when viewing it against the 1:1 line. This is indicative of dilation in the soil above the trapdoor since the top of the settling soil column is not moving down at the same rate as the bottom.

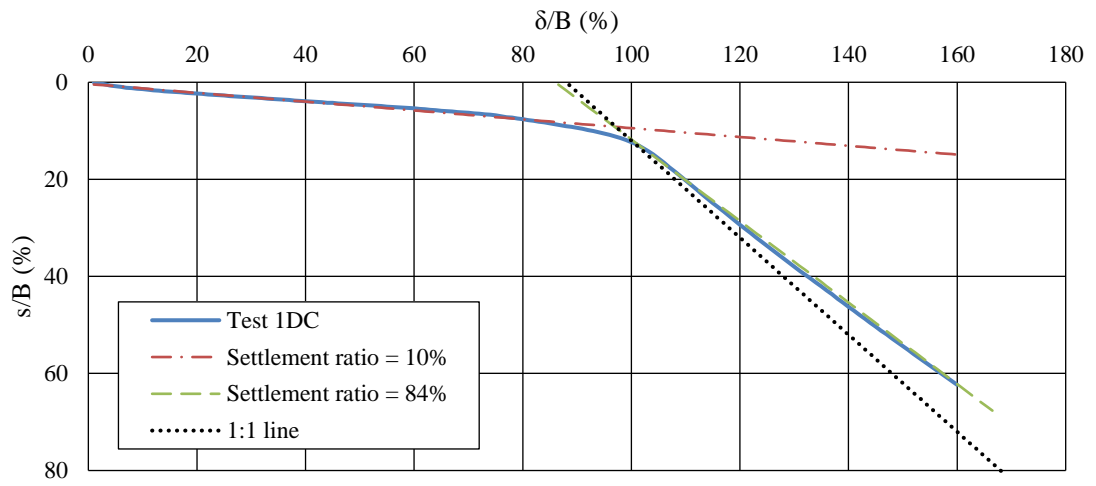


Figure 4-14: Ratio of normalized surface settlement against normalized trapdoor settlement during Test 1DC

4.3.2 Test 2MC – Moist Coarse Sand

A replica of Test 1DC was performed in moist sand to investigate the influence that moisture would have on the failure mechanism. Since sinkholes are primarily caused by leaking water-bearing infrastructure, the soil in its vicinity would likely contain substantial moisture, making this test an important addition. Moisture can provide a certain degree of inter-particle tensile forces due to matric suction.

4.3.2.1 Test Arrangement

Several parameters of the test arrangement are shown in Table 4-4 below. Through inspection of images, settlement (δ_0) of the trapdoor during centrifuge acceleration was determined to be 0.38mm when acceleration reached 50G. This value was taken to be the settlement at image 1 of the test and LVDT readings were zeroed at this point. All subsequent LVDT readings were adjusted by δ_0 to obtain corrected settlement readings.

Table 4-4: Test arrangement parameters for Test 2MC

Parameter	Value
<u>Soil Characteristics</u>	
Sand type	Coarse sand
Moisture content	2.1% - 3.1%
Density	Very Dense
<u>Geometry of Test Package</u>	
Sand depth (H)	290 mm
Trapdoor width (B)	50 mm
H/B ratio	5.8
Rate of trapdoor settlement	2.53 mm/min
Time between analysed images	12 secs (every 0.51mm of settlement)

After completion of the test, the moisture content was measured at six locations within the soil mass near the top, middle and bottom on both the left- and right-hand sides. Moisture content results for this test are (Figure 4-15) show that moisture in the sample was uniform with readings varying between 2.1 and 3.1%. Moisture was allowed to drain under centrifuge acceleration, thus leaving the sand at roughly the same residual moisture content, depending on the particle size and grading of the material.

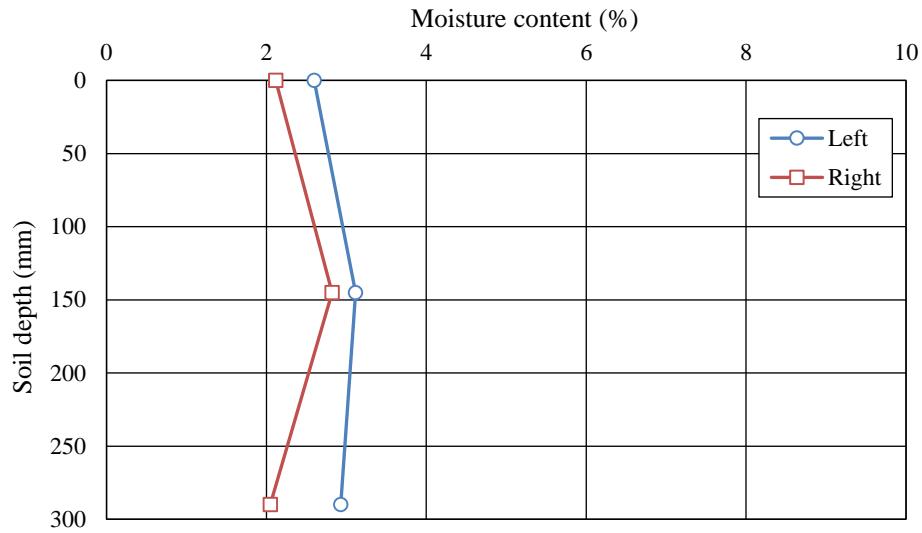


Figure 4-15: Moisture content with soil depth (Test 2MC)

4.3.2.2 Photographic Record

The first analysed photograph of Test 2MC is shown in Figure 4-16 below. Also indicated is the area of interest that was analysed using PIV. The layer of Bidim that prevents soil erosion during moisture introduction (discussed in Section 3.3.6) is visible on top of the soil.

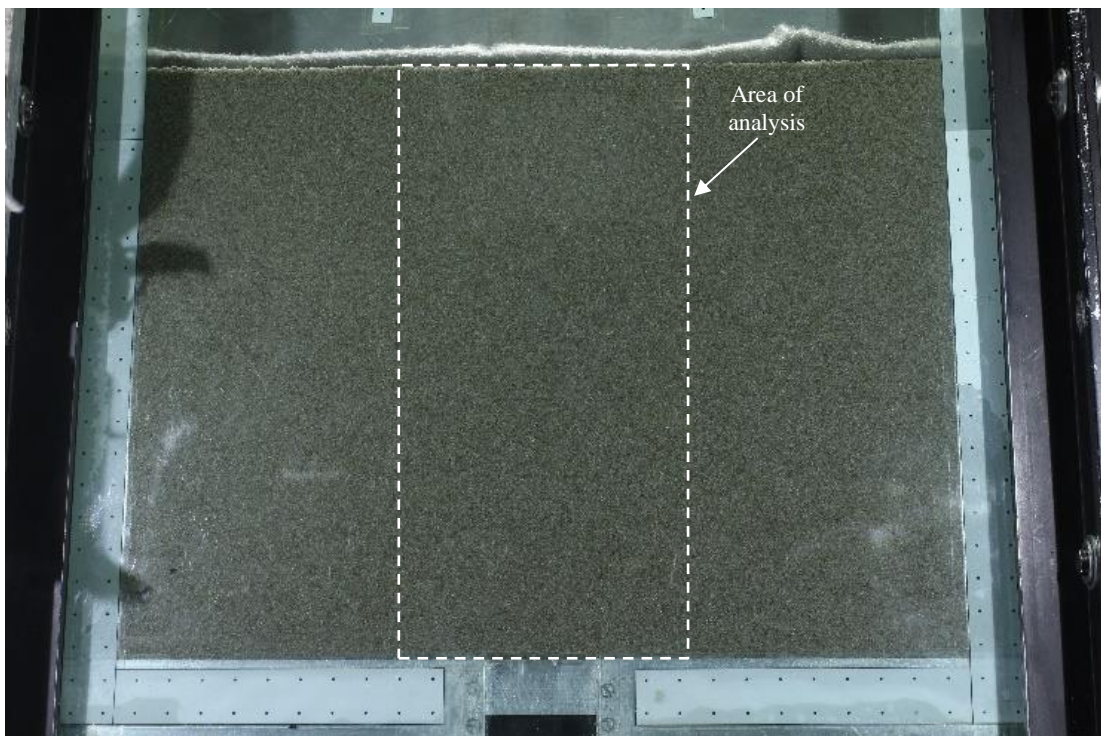
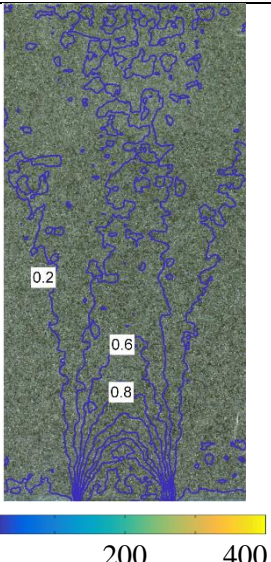
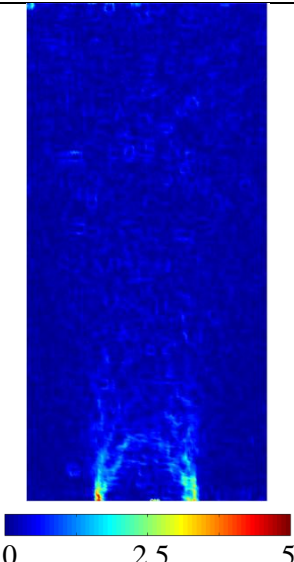
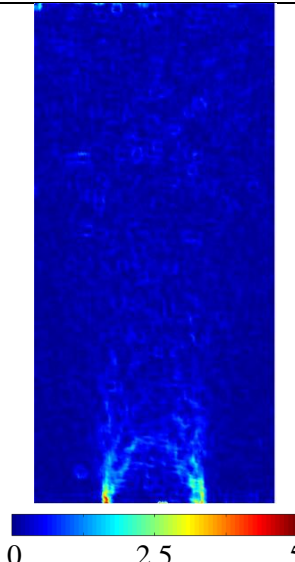
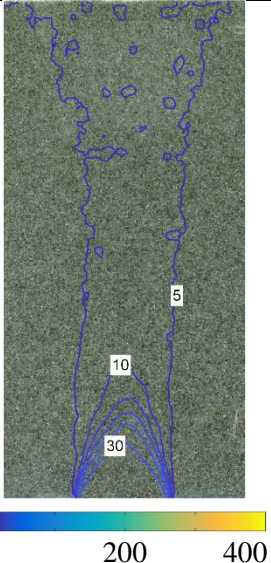
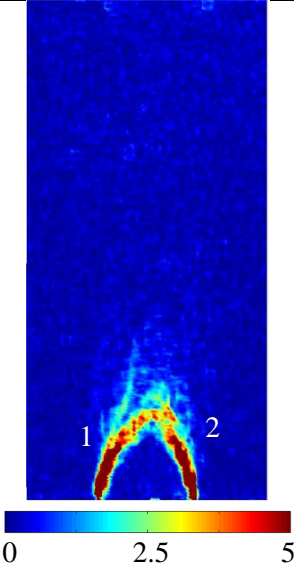
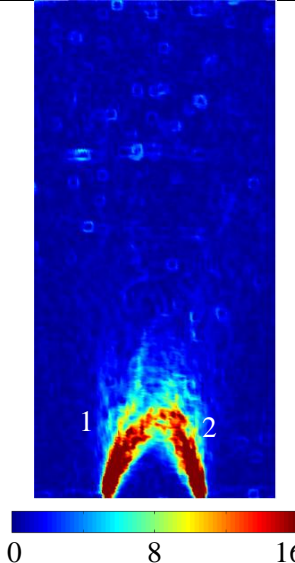


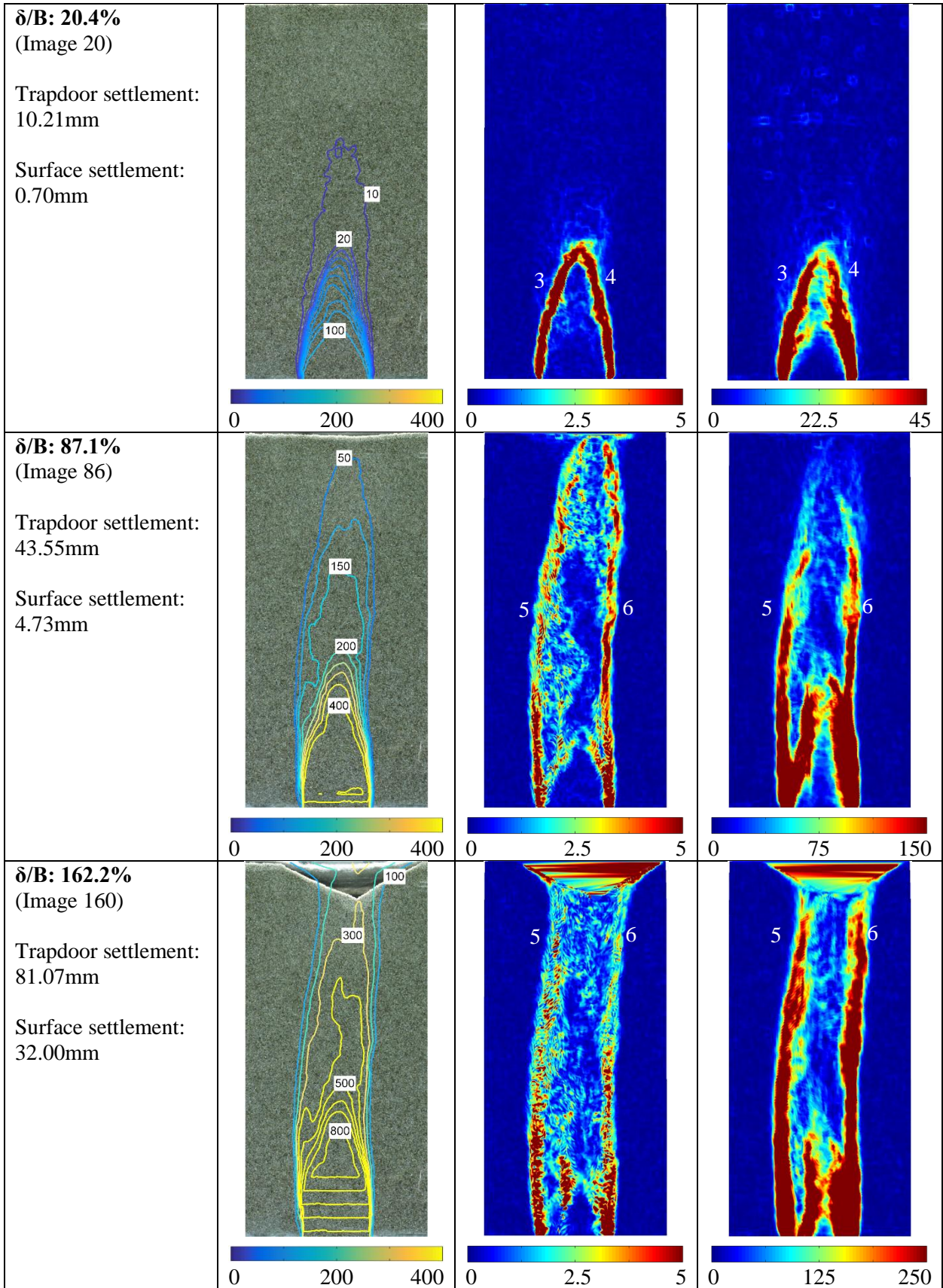
Figure 4-16: First analysed photo of Test 2MC

4.3.2.3 Shear Zone Propagation

Table 4-5 below shows plots of vertical displacement, incremental maximum shear strain and total maximum shear strain for test 2MC.

Table 4-5: Selected results of Test 2MC

	Vertical displacement (px)	Incremental max. shear strain (%)	Total max. shear strain (%)
<p>δ/B: 1.4% (Image 2)</p> <p>Trapdoor settlement: 0.69mm</p> <p>Surface settlement: 0.06mm</p>			
<p>δ/B: 6.8% (Image 7)</p> <p>Trapdoor settlement: 3.38mm</p> <p>Surface settlement: 0.36mm</p>			



4.3.2.1 Discussion of Displacement and Strain Plots

No literature could be found of trapdoor test in moist sand. However, when comparing test 2MC to the corresponding test in dry soil (Test 1DC), there are noticeable differences. Similar to Test 1DC, deformation in this test began with localised shear bands at the edge of the trapdoor at a δ/B of 1.4% which transitioned into a shear zone of several small shear bands radiating from the trapdoor edge and finally two prominent shear bands (labelled 1 and 2). These two shear bands curved inward and joined in the centre to form a triangular shaped failure mechanism at a δ/B of about 6.8%, although somewhat more rounded than that of Test 1DC.

As the test progressed, new shear bands were continually created above the initial ones, and the mechanism evolved from triangular to a parabolic shape by a δ/B ratio of 16.3%. The parabolic failure mechanism seen here were slightly more pointed than the ones observed in Test 1DC, indicating the presence of a stronger stable arch above the mechanism. During the remainder of the test, several more shear bands formed, alternating in an unsymmetrical fashion between the left and right sides of the zone of influence, each gradually advancing the zone of influence upwards until reaching the surface at a δ/B ratio of 86.1%. Shear bands reached the soil surface at a single location close to the centre before gradually moving outwards and finally reaching a near-vertical mechanism at a δ/B ratio of about 101.3%. This was accompanied by horizontal movement of the soil at the surface towards the trapdoor centreline.

Shear bands in this test formed in a more symmetrical fashion than in dry sand (Test 1DC). In addition, triangular and parabolic failure mechanisms tended to take on a more pointed shape and formed at a steep angle (slanted towards the centre of the zone of influence) as opposed to that in dry tests which tended to form more vertically before curving towards the centre (compare Image 73 of Test 1DC in Table 4-3 and Image 86 of Test 2MC in Table 4-5).

As before, horizontal movement of the soil appeared to be dictated by the shapes and slopes of shear bands, as seen in Figure 4-17. Soil above a shear band that originated from the right side of the zone of influence tended to move leftward while soil above one originating from the left side tended to move rightward.

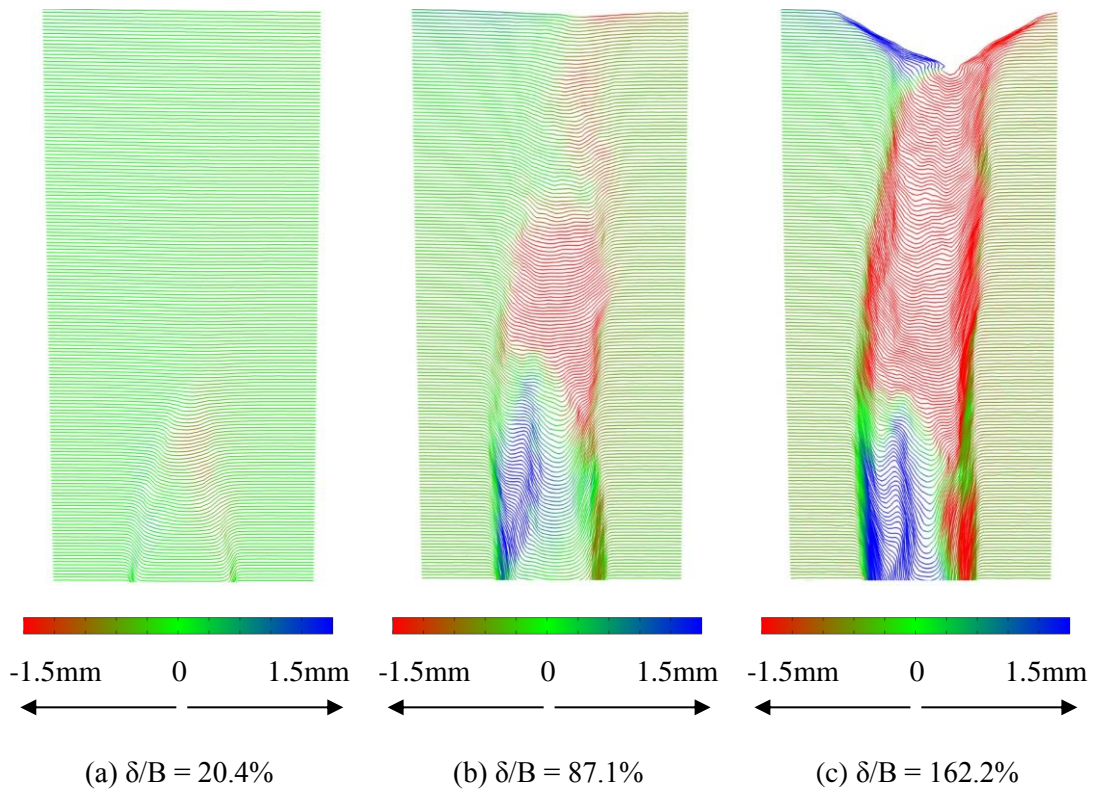


Figure 4-17: Settlement plots of test 2MC

It is notable that the entire zone of influence leaned slightly to the right, but never extended beyond vertical lines drawn from the trapdoor edges. This slight leaning was observed in numerous tests in this study. Similar leaning was also observed by Da Silva (2014), albeit in dry sand. It is reasoned that this might be caused due to small irregularities in the sand density.

4.3.2.2 Surface Settlement

Surface settlement of Test 2MC, shown in Figure 4-18, progressed almost identical to that in dry material (Test 1DC). Settlement appeared to follow a Gaussian curve at first but deviated from this trend at later stages, becoming steeper along the slopes and slightly deeper near the centre. This can once again be attributed to soil column directly above the trapdoor being pulled down and settling faster than the adjacent soil.

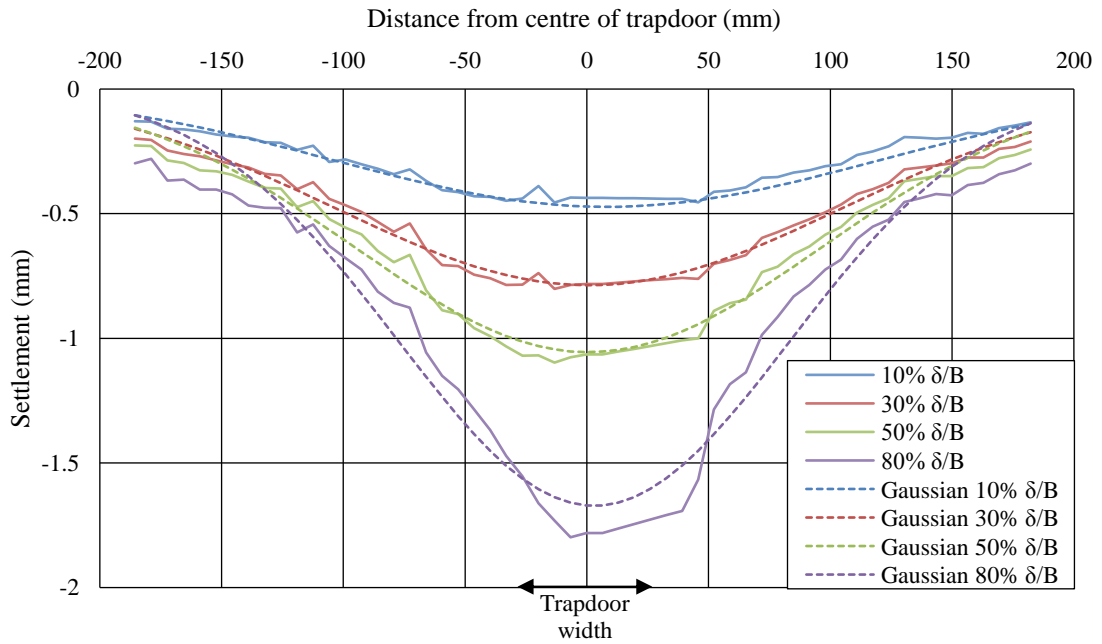


Figure 4-18: Surface settlement distribution of Test 2MC

Similar to that of Test 1DC, soil at the surface settled slowly at first when compared to trapdoor settlement and then sped up when the zone of influence reached the surface at a δ/B ratio of about 86%. This is visible in Figure 4-19 below. In general, surface settlement appeared to progress more slowly than that in the dry material of Test 1DC (compare with Figure 4-14). It should once again be mentioned that the settlement rate during the second part was less than unity (1:1 line) indicating dilation of the sand.

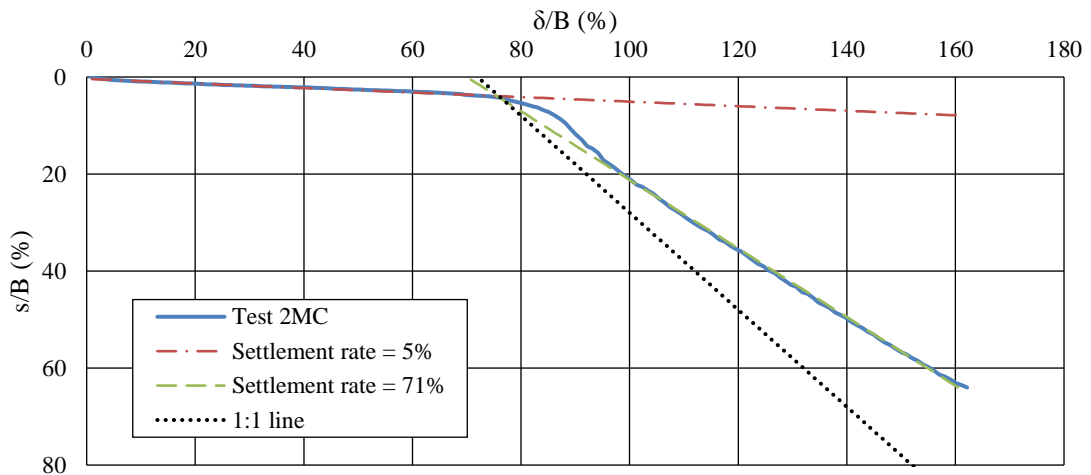


Figure 4-19: Ratio of normalized surface settlement against normalized trapdoor settlement during Test 2MC

4.3.3 Test 3DF – Dry Fine Sand

Following the tests on coarse sand in both dry and moist conditions, this test and the ones thereafter investigate the same experiment performed on fine Cullinan sand. The properties of both sand types were discussed in Section 3.4.

4.3.3.1 Test Arrangement

Several parameters of the test arrangement for Test 3DF are given in Table 4-6. Through inspection of images, settlement (δ_0) of the trapdoor during centrifuge acceleration was once again determined to be 2.07mm when acceleration reached 50G. This value was taken to be the settlement at image 1 of the test and PIV readings were zeroed at this point. All subsequent PIV readings were adjusted by δ_0 to obtain corrected settlement readings. The test ended with a sand leak at about 26.7mm ($\delta/B = 53.3\%$) of trapdoor settlement.

Table 4-6: Test arrangement parameters of Test 3DF

Parameter	Value
<u>Soil Characteristics</u>	
Sand type	Fine sand
Moisture content	Dry
Density	Dense
<u>Geometry of Test Package</u>	
Sand depth (H)	290 mm
Trapdoor width (B)	50 mm
H/B ratio	5.8
Rate of trapdoor settlement	2.49 mm/min
Time between analysed images	12 secs (every 0.50mm of settlement)

4.3.3.2 Photographic record

The first analysed photograph of Test 3DF is shown in Figure 4-20 below. Also indicated is the area of interest that was analysed using PIV.

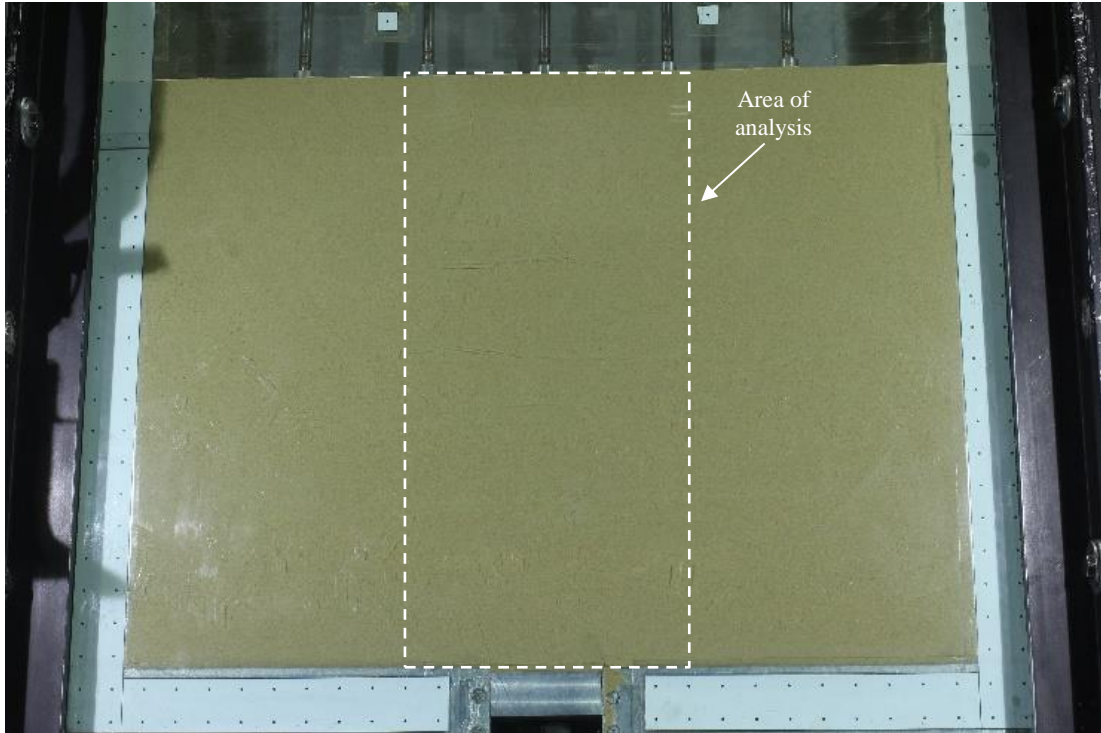
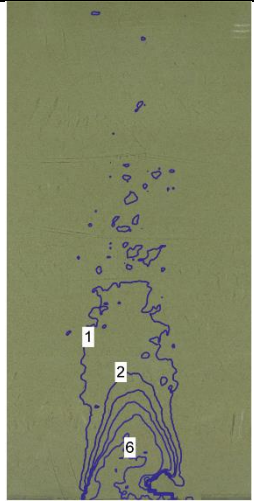
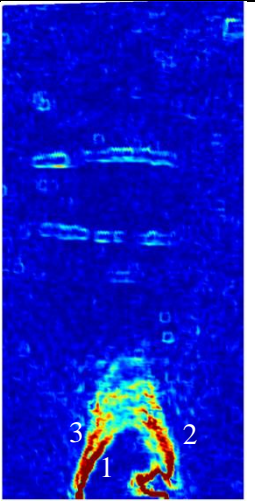
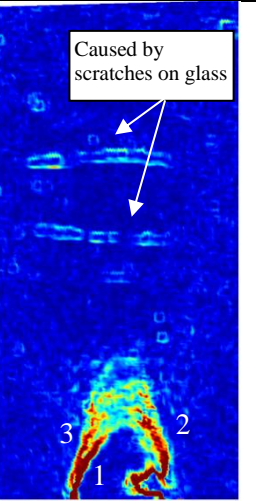
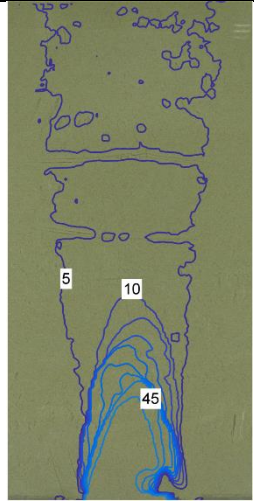
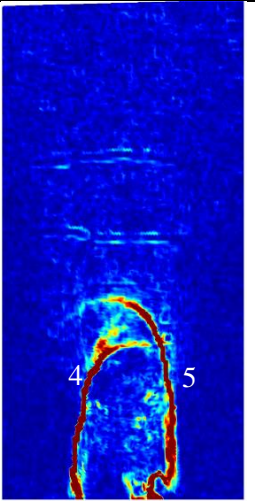
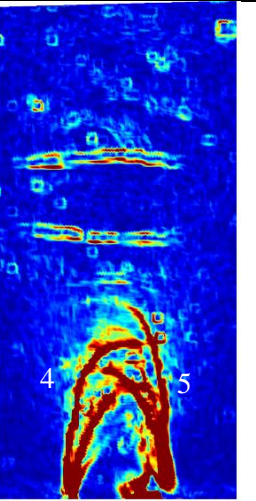
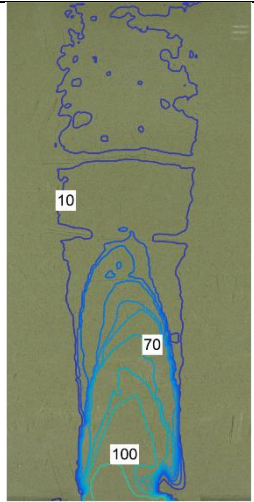
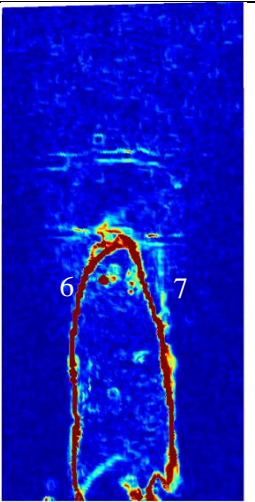
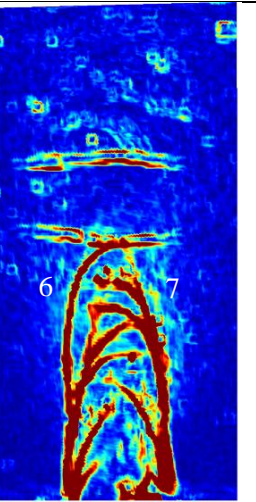


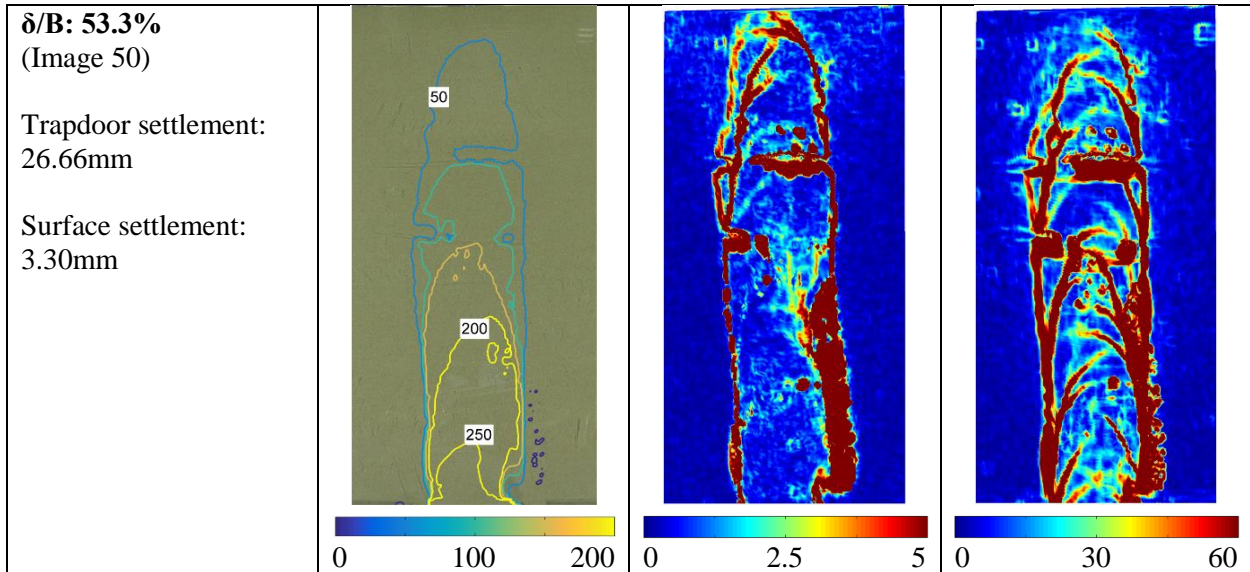
Figure 4-20: First analysed photo of Test 3DF

4.3.3.3 Shear Zone Propagation

Table 4-7 below shows distributions of vertical displacement, incremental maximum shear strain and total maximum shear strain at several stages throughout the test. Compared images were spaced 12 seconds apart which equates to 0.50mm of trapdoor settlement or δ/B of 1.0% between images. Once again, small scratches on the glass created two distinct lines of irregularities that should be disregarded.

Table 4-7: Selected results of Test 3DF

	Vertical displacement (px)	Incremental max. shear strain (%)	Total max. shear strain (%)
<p>δ/B: 5.2% (Image 2)</p> <p>Trapdoor settlement: 2.61mm</p> <p>Surface settlement: 0.09mm</p>	 <p>0 100 200</p>	 <p>0 2.5 5</p>	 <p>0 2.5 5</p>
<p>δ/B: 13.3% (Image 10)</p> <p>Trapdoor settlement: 6.64mm</p> <p>Surface settlement: 0.60mm</p>	 <p>0 100 200</p>	 <p>0 2.5 5</p>	 <p>0 7.5 15</p>
<p>δ/B: 22.9% (Photo 20)</p> <p>Trapdoor settlement: 11.45mm</p> <p>Surface settlement: 1.02mm</p>	 <p>0 100 200</p>	 <p>0 2.5 5</p>	 <p>0 12.5 25</p>



4.3.3.4 Discussion of Displacement and Strain Plots

Since the first comparison could only be made at a δ/B ratio of 5.2% due to premature trapdoor settlement, the first image shows a group of shear bands that have already formed from the edges of the trapdoor. As the trapdoor settled further, shearing continued along several prominent shear bands (labelled 1, 2 and 3) that tended to join up at the centre and form an approximately symmetrical parabolic-shaped failure arch, similar to that in coarse sand (Test 1DC). The remnants of a triangular mechanism created during premature settlement of the trapdoor was observed at $\delta/B = 5.2\%$. Shear strain development soon ceased along these initial shear bands and continued along a secondary pair of more vertically inclined shear bands with parabolic shaped “heads” as shown in the plot of incremental maximum shear strain at $\delta/B = 13.3\%$.

These results agree with that of Stone & Muir Wood (1992) and Costa et al. (2009) in which secondary shear bands developed from the edges of the trapdoor and extended beyond the initial shear bands at a steeper slope than the first. As noted by Stone & Muir Wood, movement shifted suddenly from the initial set of shear bands to the secondary shear bands, causing deformation to cease altogether along the former and continue along the latter.

This near-vertical mechanism with parabolic-shaped heads tended to continue up to the end of the test with new shear bands forming above previous ones as the test progressed. The zone of influence reached the surface at a single location at a δ/B ratio of about 53.3% before widening outwards into a vertical mechanism. At this point a sand leak formed near the trapdoor as is evidenced by a large band of strains near the right edge of the trapdoor. Thus, the test was stopped.

It is evident from the strain plots that shear bands initially appeared symmetric but became increasingly asymmetric as the zone of influence extended upwards. There was no discernible pattern indicating at what stage and from which side of the zone of influence the next shear band would develop, but in general they alternated between left and right with each shear band reaching a slightly higher elevation than the previous one before curving inwards at the top and stopping. There was a tendency for the zone of influence to maintain near-vertical side slopes.

When comparing this test to the test performed in dry coarse sand (Test 1DC), there are notable differences in the way that shear bands formed. Firstly, it is evident that shear bands formed much more frequently in fine sand than in coarse sand. When considering the packing of particles, it is evident that there are more potential planes on which shearing can take place in fine sand than in coarse sand, as seen in Figure 4-21 below. For this reason, several smaller shear bands formed in fine sand in the place of a single, wider shear band in coarse sand.

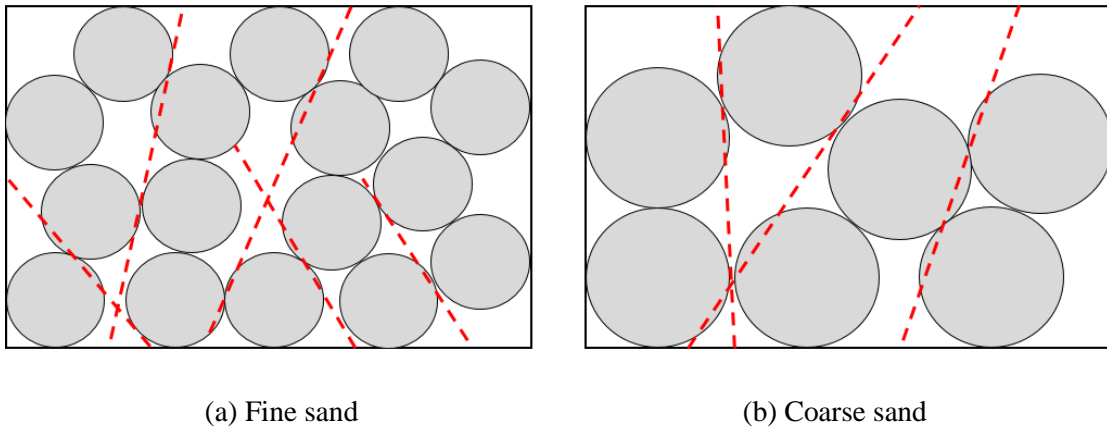


Figure 4-21 Possible shear band locations in (a) fine vs. (b) coarse sand

Secondly, shear bands in fine sand tended to be much narrower than in coarse sand. Literature suggests that the width of a shear band is directly related to the mean particle size D_{50} (Roscoe, 1970; Costa et al. 2009).

It was also observed that shear bands in fine sand tended to be spaced closer together directly above the trapdoor, but further apart near the centre of the soil body. Closer to the surface, the spacing of shear bands was once again denser. This could possibly be a function of the mean stress level in the soil mass.

Horizontal movement in this test was once again governed by the location of shear bands (as shown in Figure 4-22). It is clearly visible that soil above a shear band forming from the left

trapdoor edge tended to move rightward while soil above one forming from the right trapdoor edge tended to move leftward.

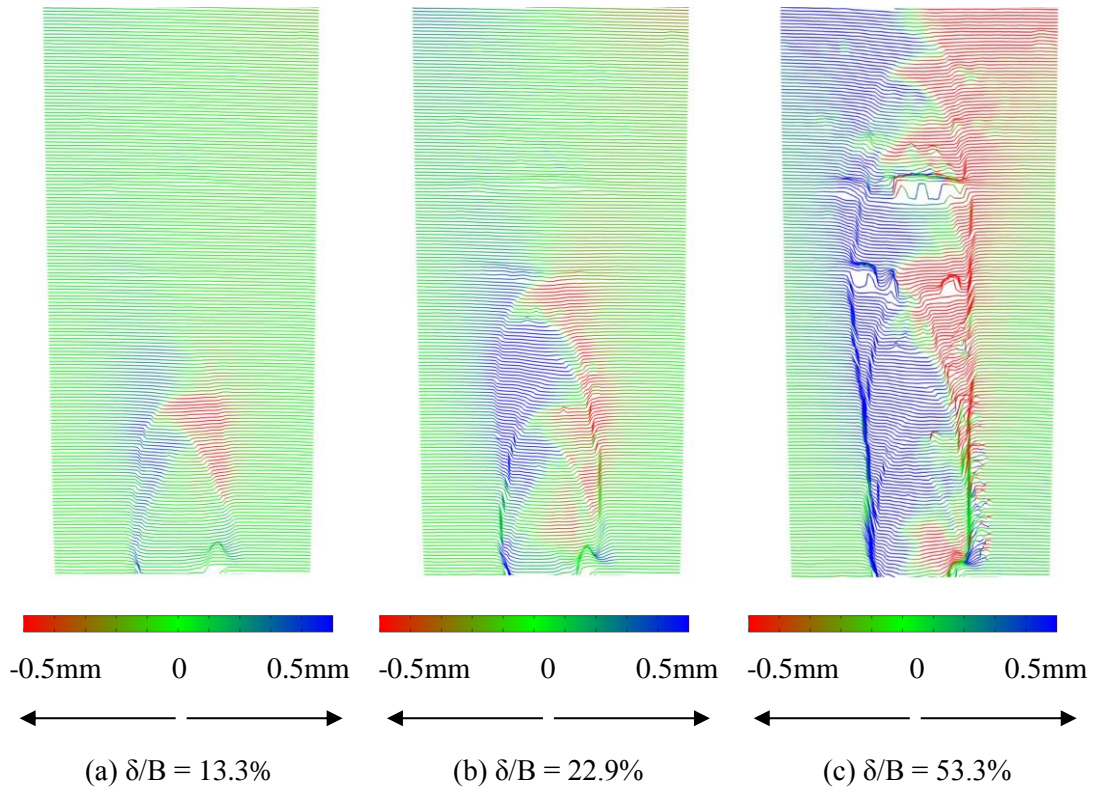
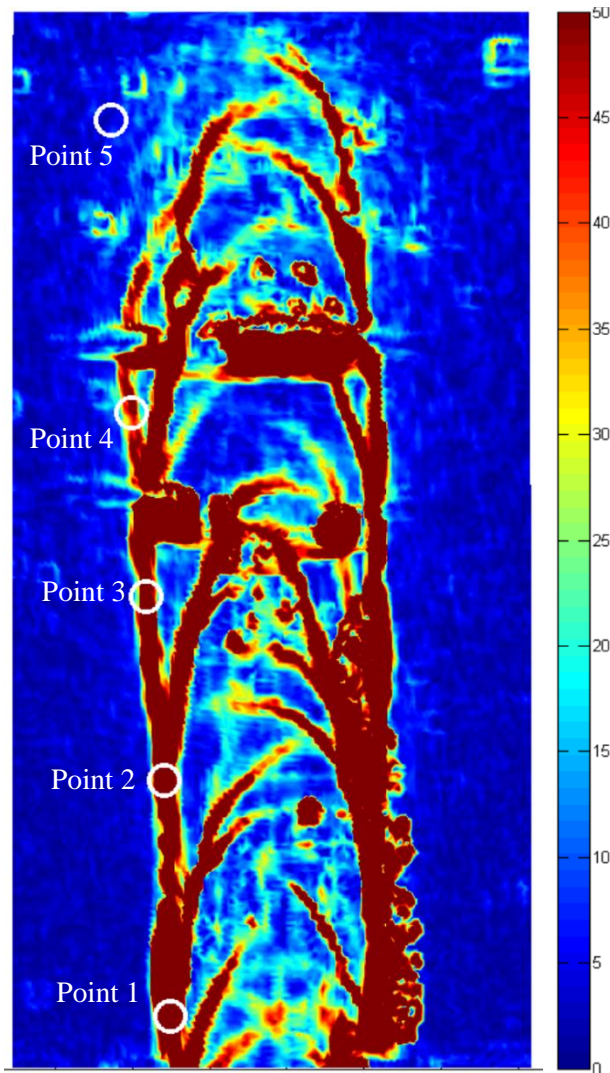


Figure 4-22: Settlement plots of Test 3DF

4.3.3.5 Strain Behaviour at Selected Points

Similar to what was displayed in Test 1DC, several points of interest in the sand mass were once again selected to investigate changes in strain behaviour over time. The first set of points were selected on four different shear bands that formed a vertical boundary to the zone of influence as shown in Figure 4-23 below. Graphs showing maximum shear strain against trapdoor displacement (δ/B) are shown for the entire calculated shear strain range in Figure 4-24 and for smaller strains in Figure 4-25.



Total maximum shear strain (%)

Figure 4-23: Distribution of maximum shear strain above the trapdoor showing the location of selected points 1 to 5 in Test 3DF

Shear strains were visible along all points right from the start of the test, as is visible in Figure 4-25. This shows that even the slightest amount of trapdoor movement had a noticeable effect at all locations above the trapdoor. After this initial shear strain, each point experienced a sudden increase in shear strain rate when the zone of influence reached that particular point. The increased strain rate then prevailed for the duration of the test. This corresponded with previous observations that shearing along any particular shear band stopped as soon as another shear band formed above it. Shearing continued along new shear bands and along the two vertical boundaries of the zone of influence, with soil inside the zone of influence settling near-uniformly at roughly the same rate as the trapdoor.

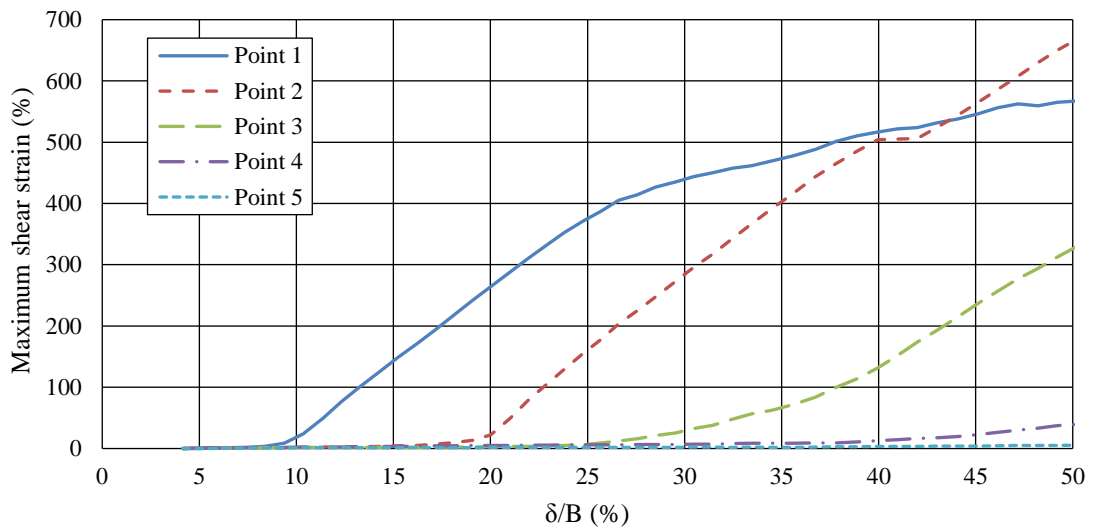


Figure 4-24: Maximum shear strain of points 1 to 5 in Test 3DF (entire strain spectrum)

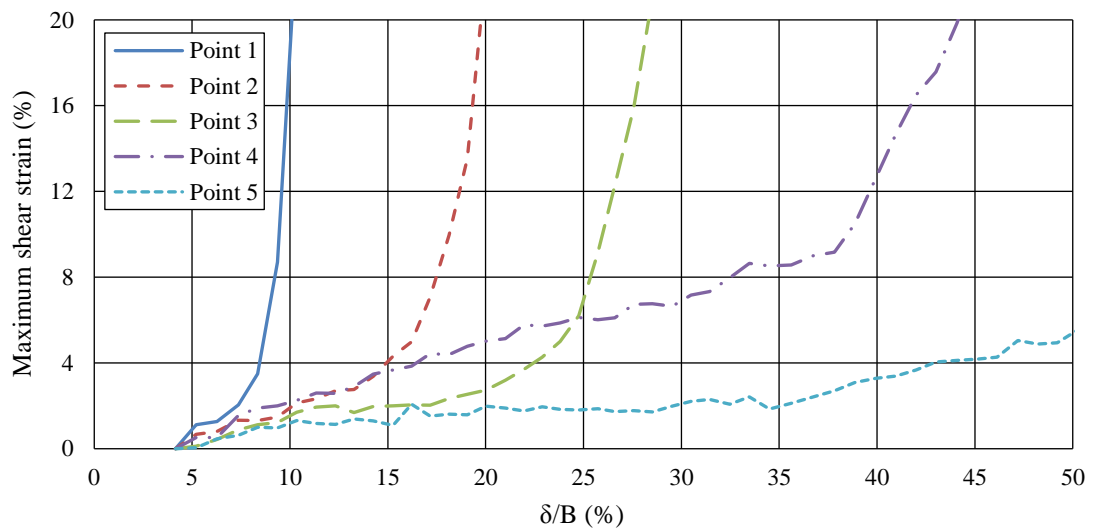


Figure 4-25: Maximum shear strain of points 1 to 5 in Test 3DF (small strains)

The location of a second set of points that was investigated is shown in Figure 4-26. These points were selected to be at roughly the same height above the trapdoor, tracking different points of interest in the soil mass. Once again, point 6 was selected to act as a reference outside the zone of influence in a region where no significant strains occurred. Point 7 was selected on a near-vertical shear band while points 8 and 10 were selected on inclined shear bands on either side of the zone of influence. Point 9 was selected at the top of a shear band near the middle of the chimney.

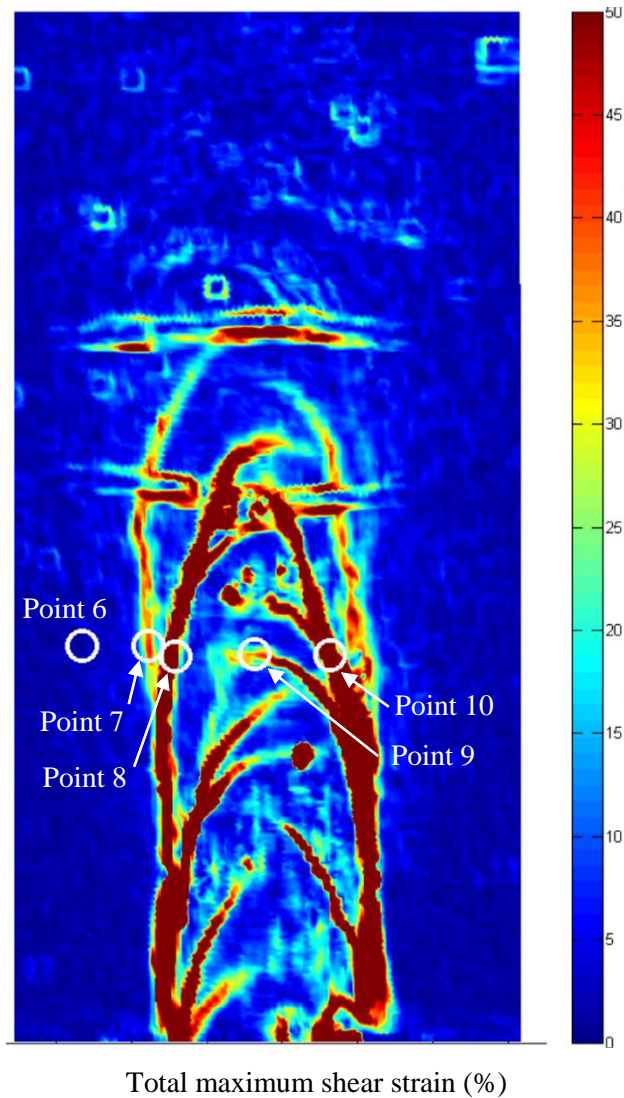


Figure 4-26: Distribution of maximum shear strain above the trapdoor showing the location of selected points 6 to 10 in Test 3DF

Maximum shear strain plots for these points are shown in Figure 4-27. It is evident from the graphs that point 6 (reference point) experienced little deformation and shear strains were thus negligible. Point 9 (directly above the trapdoor centre) experienced initial strain during the formation of a shear band at that location, but local shear strains soon stabilised and remained constant for the remainder of the test. Shearing at point 9 ceased at a δ/B ratio of 15% after which the soil at this location settled uniformly with the soil around it. Maximum shear strains at points 8 and 10 experienced the same phenomenon. Both experienced an increase in strain up to a δ/B ratio of 35% and then attained constant strain coupled with uniform downward settlement. Maximum shear strains at point 7 exhibited behaviour similar to points 1 to 4, in which straining occurred continuously throughout the test, indicating constant shear along the borders of the zone of influence. This continued up to the end of the test as the column of soil continued to shear along this line.

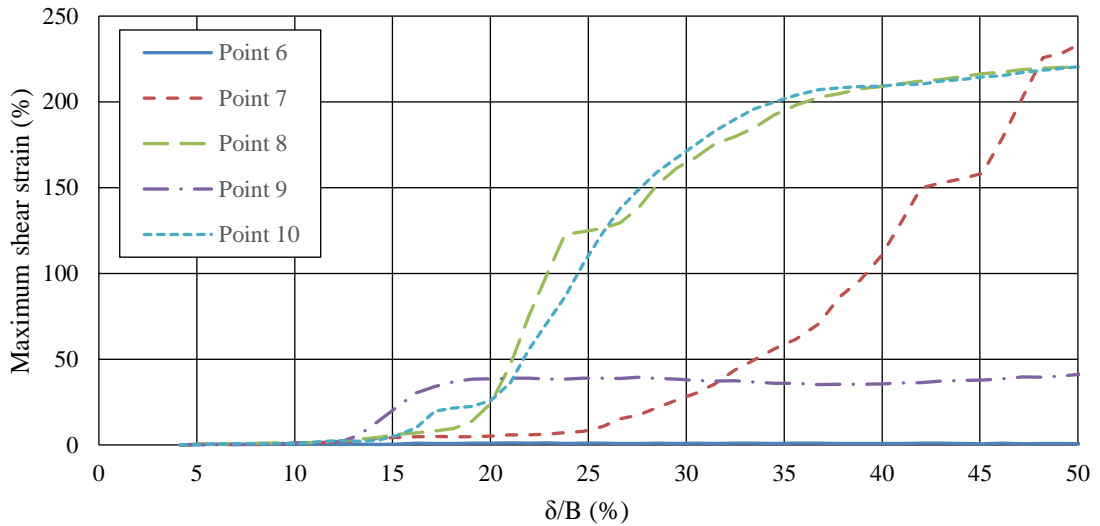


Figure 4-27: Maximum shear strain of points 6 to 10 in Test 3DF (entire strain spectrum)

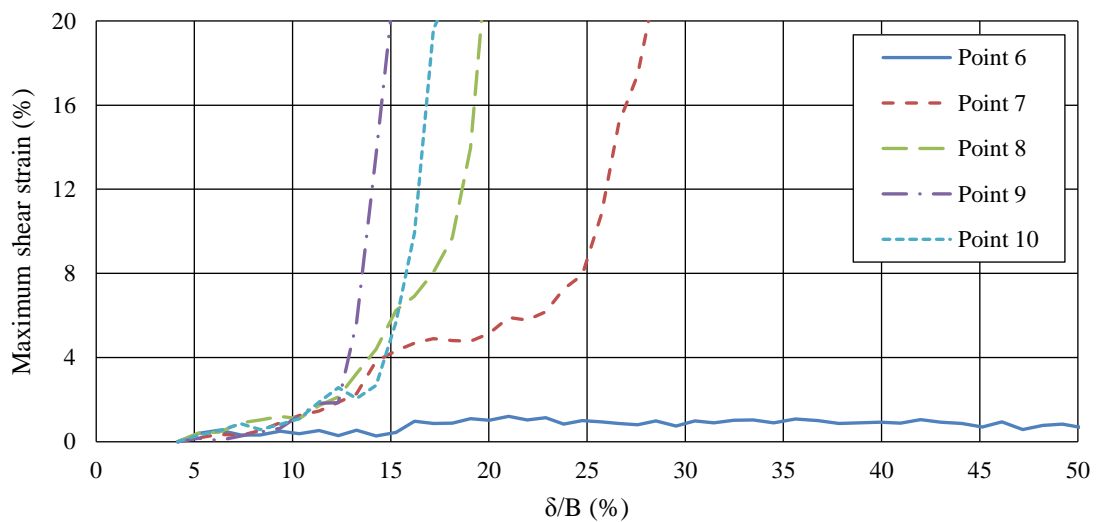


Figure 4-28: Maximum shear strain of points 6 to 10 in Test 3DF (small strains)

When focussing on the smaller strain range in Figure 4-28, it is evident that points that lie directly above the trapdoor initially experienced a linearly increasing shear strain. This rate of shearing continued until the zone of influence grew large enough to form a shear band close to that location, at which point the rate of shear increased significantly. Point 6, which lies to the left of the zone of influence, experienced insignificant shear strain.

4.3.3.6 Surface Settlement

Surface settlement distributions at selected times throughout the test are shown in Figure 4-29. As with previous tests, soil initially settled in the form of a Gaussian curve, but later deviated from this trend.

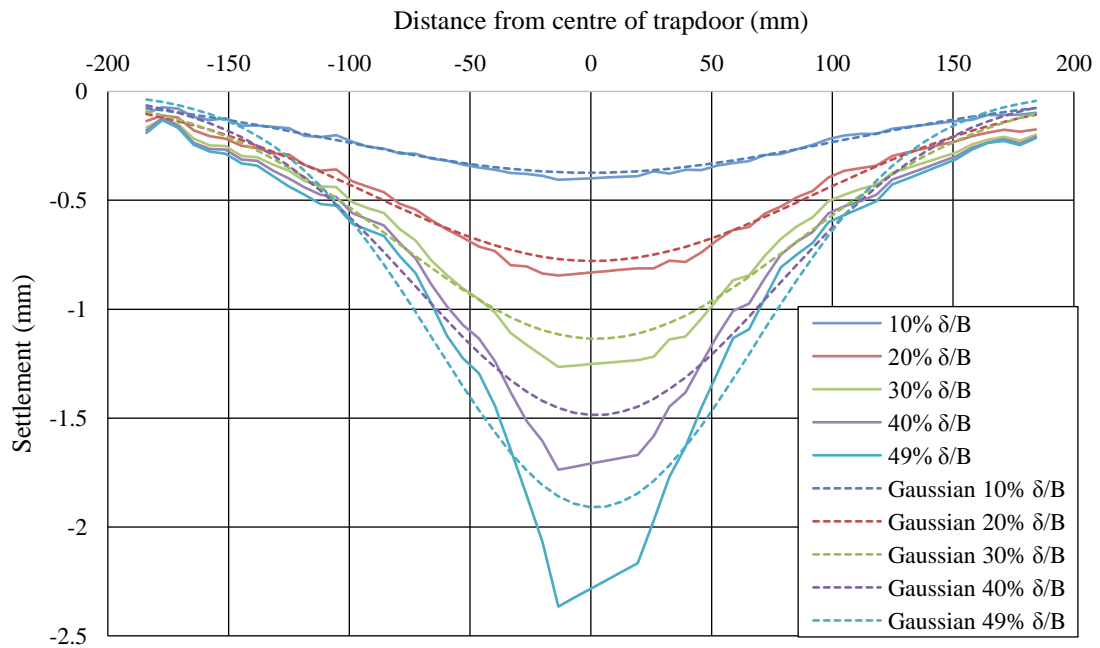


Figure 4-29 Surface settlement distribution of Test 3DF

A graph of surface settlement against δ/B , tracked by a bank of 5 LVDTs resting on top of the soil surface, is shown in Figure 4-30. LVDT 3 measured settlement directly above the trapdoor, LVDT 2 and 4 were positioned at 50mm from the centre and LVDTs 1 and 5 were positioned at 100mm from the centre on either side of the trapdoor. The measurements taken by LVDTs that were at equal distances from the centre were similar. It is evident from the graph that surface settlement commenced immediately after the trapdoor started retracting and progressed at a rate dependent on the distance from the centreline of the soil body. This rate remained approximately constant for the initial part of the test but then increased as the zone of influence reached the surface at a δ/B ratio of 53.3%, marked as (1) on the graph. The test was also stopped at this time due to the sand leakage. Also shown on the graph are the mechanisms that were observed at various stages throughout the test.

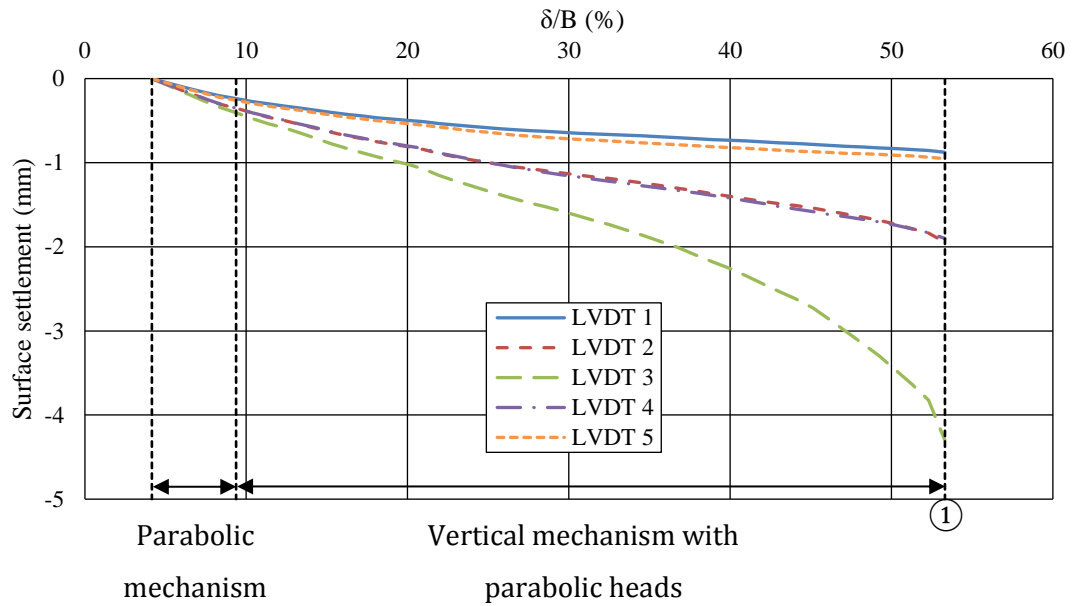


Figure 4-30 Surface settlement (LVDT bank) - Test 3DF

As is evident from a plot of normalized surface settlement against trapdoor settlement (Figure 4-31), settlement at the surface occurred at a constant rate of 8% initially and then accelerated as the zone of influence neared the surface. This test had to be stopped early due to a sand leak and so no conclusions could be drawn about the rate of settlement after the zone of influence reached the surface.

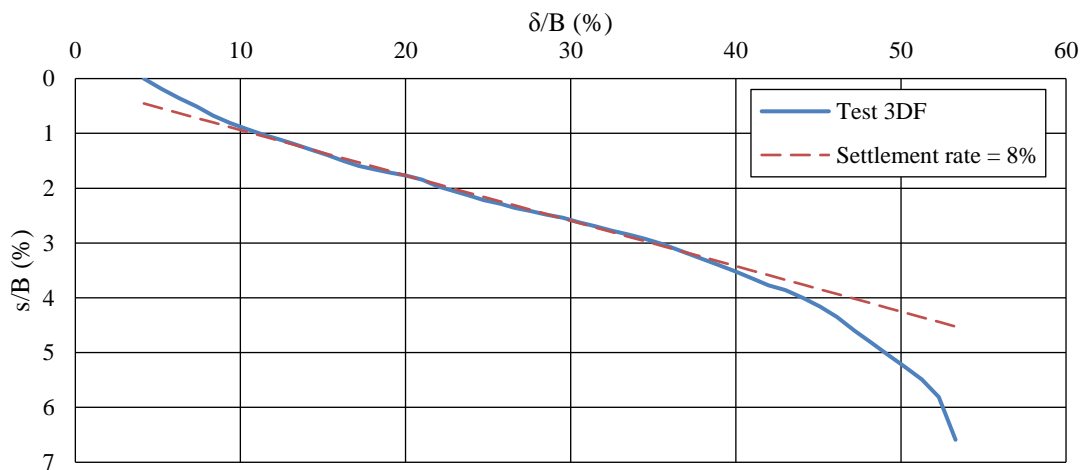


Figure 4-31: Ratio of normalized surface settlement to normalized trapdoor settlement during Test 3DF

4.3.4 Test 4MF-50 – Moist Fine Sand with 50mm Trapdoor

This test was a duplication of Test 3DF with the exception that it was done in moist sand. It also served as a reference for the two remaining tests (Test 5MF-75 and 6MF-100) in which the influence of trapdoor width was tested.

4.3.4.1 Test Arrangement

Table 4-8 below shows several parameters of the test arrangement of Test 4MF-50. Through inspection of images, settlement (δ_0) of the trapdoor during centrifuge acceleration was determined to be 1.51mm when acceleration reached 50g. This value was taken to be the trapdoor settlement at image 1 of the test and PIV readings were zeroed at this point. All subsequent PIV readings were adjusted by δ_0 to obtain corrected settlement readings.

Table 4-8: Test arrangement parameters for Test 4MF-50

Parameter	Value
<u>Soil Characteristics</u>	
Sand type	Fine sand
Moisture content	3.5% - 7.5%
Density	Dense
<u>Geometry of Test Package</u>	
Sand depth (H)	290 mm
Trapdoor width (B)	50 mm
H/B ratio	5.8
Rate of trapdoor settlement	2.52 mm/min
Time between analysed images	12 secs (every 0.50mm of settlement)

The moisture content in the soil was measured after the test at 6 locations (on both sides of the body of soil and at several depths) as was done in Test 2MC. This data is displayed in Figure 4-32 below. It is immediately apparent from the graph that the distribution of moisture in the fine sand (ranging between 3.6% and 7.5%) was less uniform than that in the coarse sand (ranging roughly between 0.5% and 2.5%). This was deemed to be due to the applied acceleration forcing the moisture downwards and causing the water content to increase with depth. However, since this type of moisture distribution would also be present in fine, near-homogenous soil above a real-life cavity, the distribution was deemed to be satisfactory and representative.

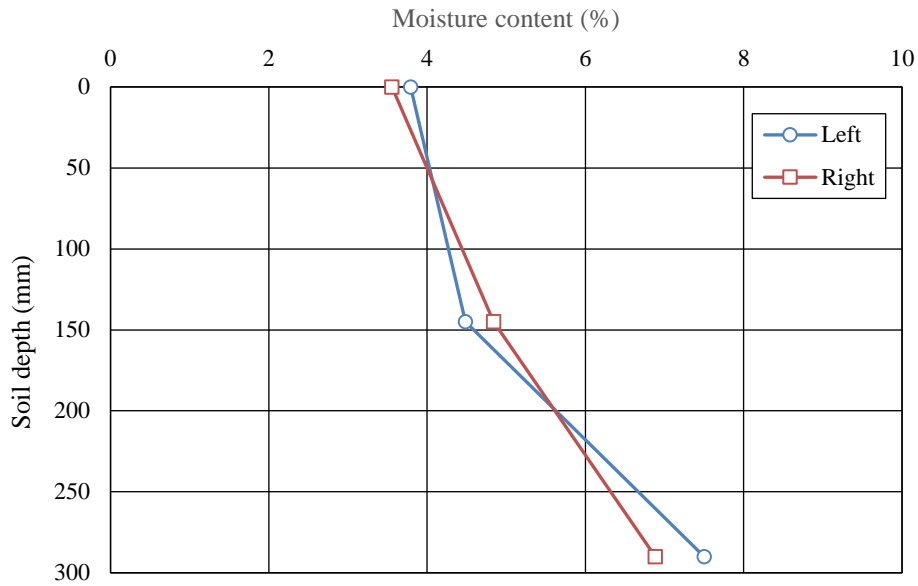


Figure 4-32: Moisture content with soil depth (Test 4MF-50)

4.3.4.2 Photographic Record

The first analysed photograph of Test 4MF-50 is shown in Figure 4-33 below. Also indicated is the area of interest that was analysed using PIV. Alternating light and dark horizontal lines in the photograph show layers in which sand was placed in the test frame.

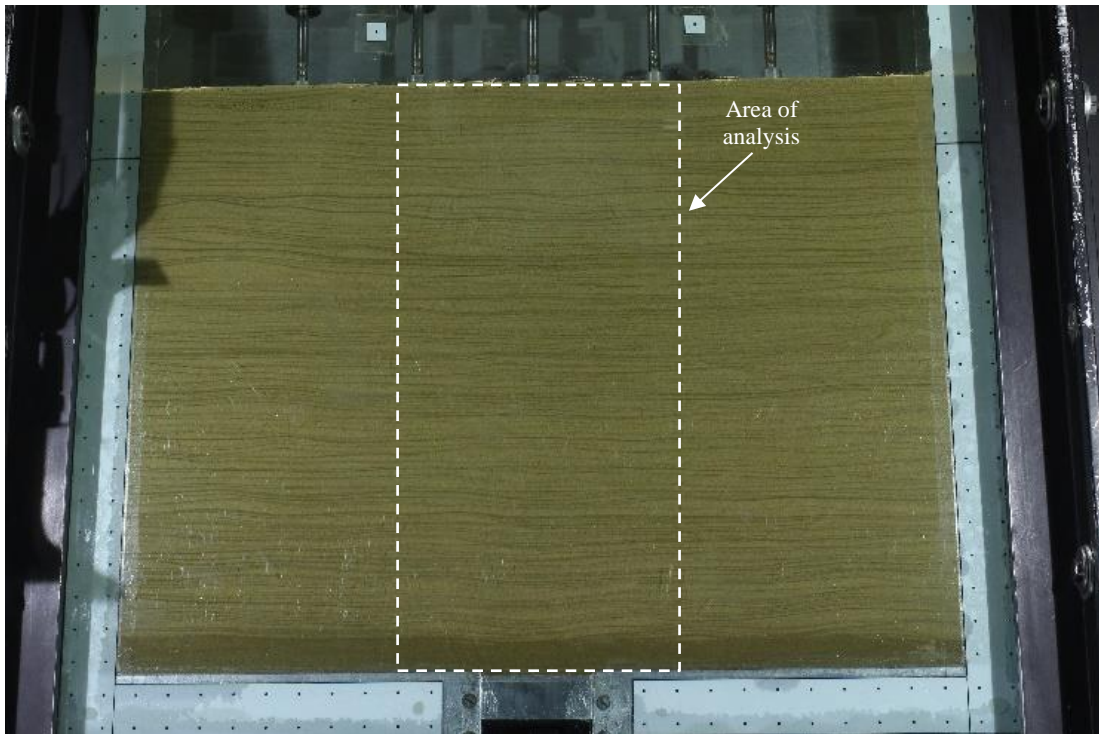


Figure 4-33: First analysed photo of Test 4MF-50

In a sequence of photographs taken at the beginning of the test, the occurrence of dilation at the onset of shearing can be observed, as seen in Figure 4-34 below. During shearing, adjacent soil particles attempted to slide past one another but was prevented from doing so due to particle interlock. As a result, particles had to move in a direction perpendicular to the direction of sliding to overcome the particle interlock. Consequently, soil at these locations experienced a slight increase in volume (dilation) and therefore a slight decrease in the local volumetric water content. These areas can be observed as lines that appear slightly lighter in colour than their surroundings. As expected, shearing of the soil occurred exactly along these curves. Figure 4-34b shows a slight drying of the soil and Figure 4-34c shows consequent shearing at this location. The same process was visible in a second, larger shear bands as shown in Figure 4-34e and Figure 4-34f. The general curvature of these lines corresponded to the parabolic-shaped mechanisms mentioned previously while the amount of curvature appeared to be a function of the dilation angle which decreases with depth as the soil becomes more confined and therefore less prone to volume expansion during shearing.

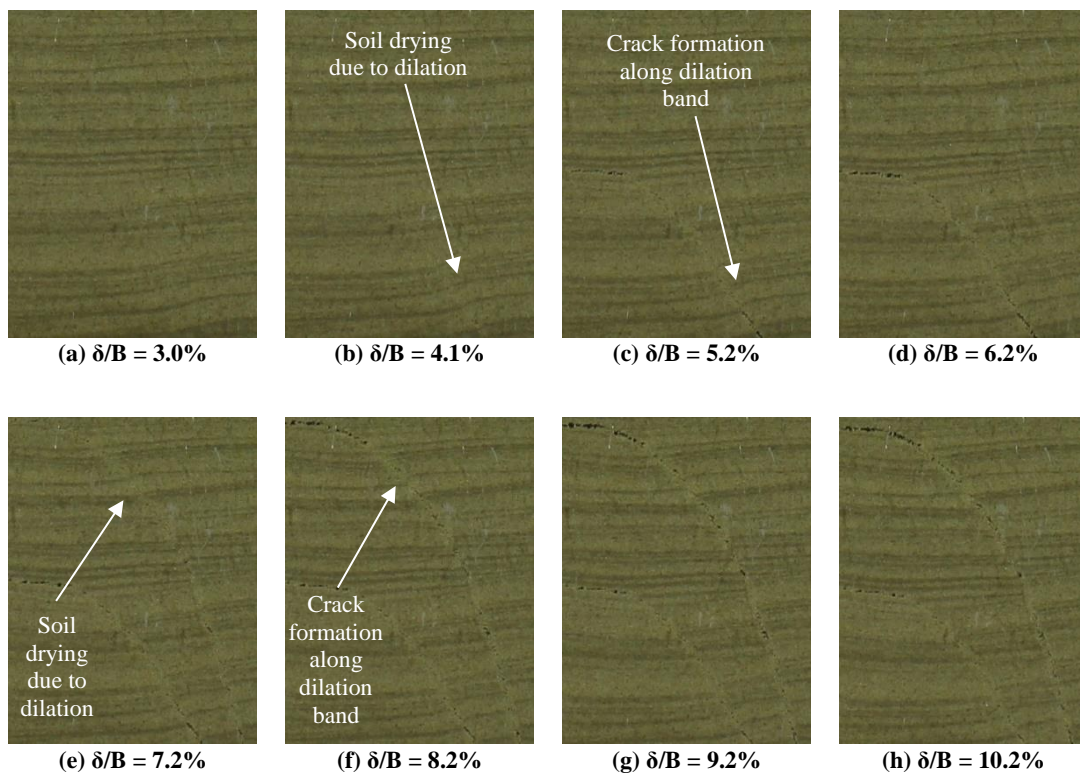

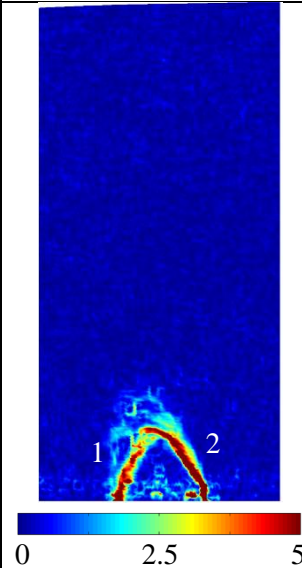
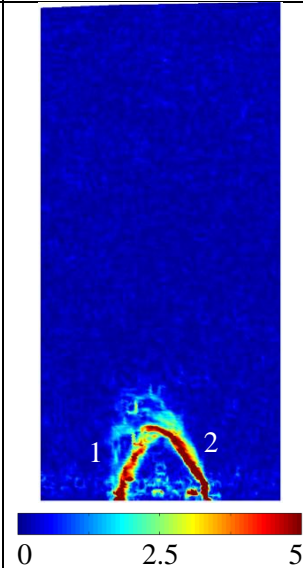
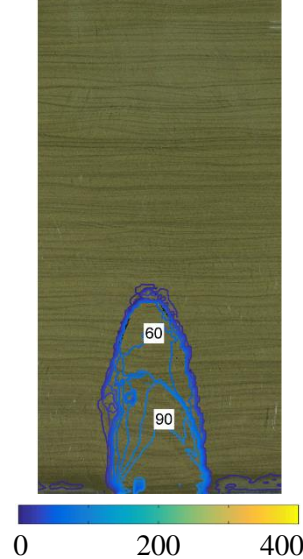
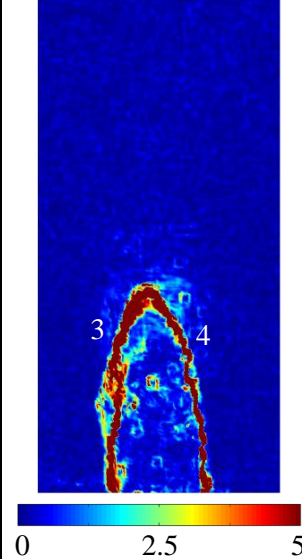
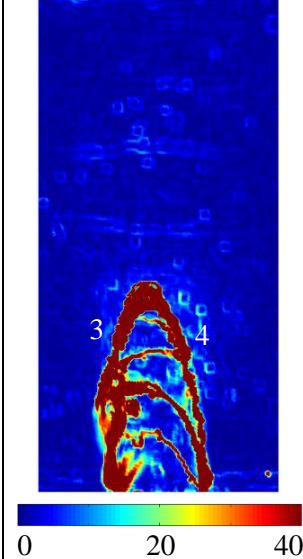



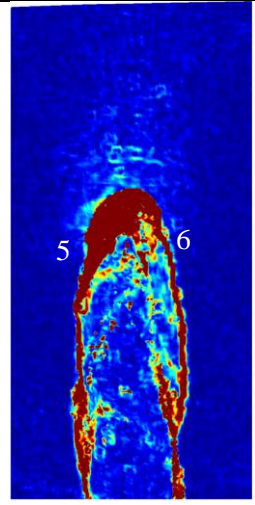
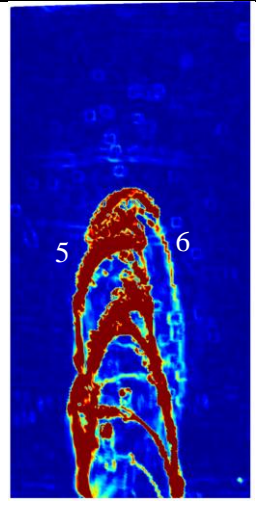
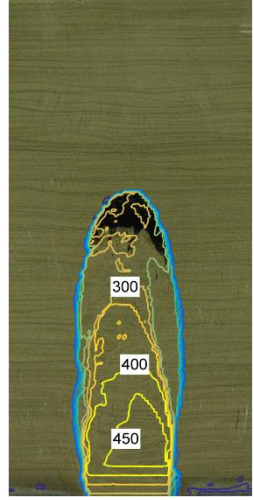
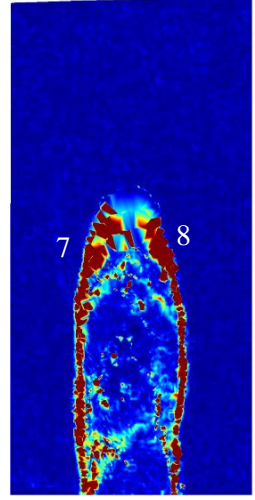
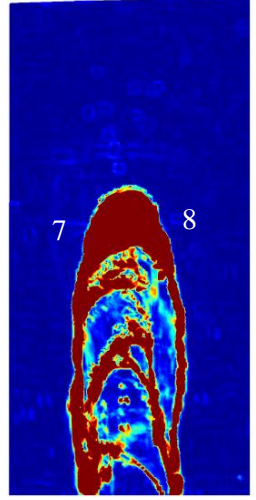
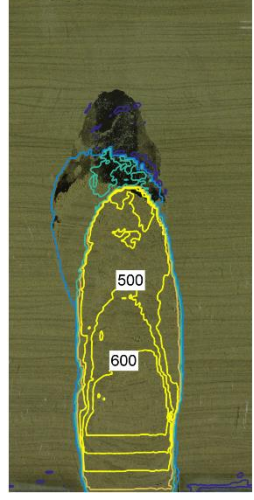
Figure 4-34: Images illustrating visible dilation along shear bands

4.3.4.3 Shear Zone Propagation

Table 4-9 below shows distributions of vertical displacement, incremental maximum shear strain and total maximum shear strain at several stages throughout Test 4MF-50. As mentioned previously, the marks created due to small scratches on the glass can be disregarded.

Table 4-9: Selected results of Test 4MF-50

	Vertical displacement (px)	Incremental maximum shear strain (%)	Total maximum shear strain (%)
<p>δ/B: 4.1% (Image 2)</p> <p>Trapdoor settlement: 2.07mm</p> <p>Surface settlement: 0.02mm</p>			
<p>δ/B: 21.3% (Image 19)</p> <p>Trapdoor settlement: 10.63mm</p> <p>Surface settlement: 0.42mm</p>			

<p>δ/B: 40.2% (Image 38)</p> <p>Trapdoor settlement: 20.09mm</p> <p>Surface settlement: 0.74mm</p>	 <p>0 200 400</p>	 <p>0 2.5 5</p>	 <p>0 45 90</p>
<p>δ/B: 90.9% (Image 88)</p> <p>Trapdoor settlement: 45.46mm</p> <p>Surface settlement: 0.89mm</p>	 <p>0 200 400</p>	 <p>0 2.5 5</p>	 <p>0 90 180</p>
<p>δ/B: 134.4% (Image 132)</p> <p>Trapdoor settlement: 67.18mm</p> <p>Surface settlement: 1.15mm</p>	 <p>0 200 400</p>	<p>(not available)</p>	<p>(not available)</p>

4.3.4.4 Discussion of Displacement and Strain Plots

Shortly after the start of the test, at a δ/B of 4.1%, two shear bands had grown from the edges of the trapdoor, meeting up at the centre to form a triangular shaped mechanism. After this initial mechanism, a new pattern of shear band formation emerged. Parabolic-shaped shear bands formed above the existing triangular mechanism from one side of the trapdoor and reached up to the centre of the body of soil. However, there was no immediate shear band from the other side that formed to meet the first band in the centre. Instead, soil “hanging” underneath the shear band dislodged and moved down along with the trapdoor. Soil from the opposite side tore away from adjacent material, effectively forming a shear band from the top downwards. This process repeated itself with shear bands forming in alternating fashion from the left and right of the trapdoor edge. A similar phenomenon was also observed by Jennings et al. (1956) in the roofs of sinkholes where he referred to it as “onion peeling.”

By a δ/B ratio of 21.3%, shear bands 6 and 7 had formed and joined up at the centre, forming a triangular-shaped failure mechanism, albeit slightly resembling a parabolic arch. By a δ/B ratio of 40.2%, another pair of shear bands (labelled 5 and 6) had formed once again in a parabolic-shape. At this point, a stable arch had formed immediately above the failure arch that was strong enough to support the weight of the soil above it. Soil beneath this arch settled with the trapdoor and created a void within the soil body and continued to grow in size as the trapdoor receded. At a δ/B ratio of 90.9%, strain computations became impossible due to excessive amounts of strain. As was observed in previous tests, the zone of influence in this test was confined to the column of soil directly above the trapdoor while adjacent soil experienced little to no soil movement, as seen in Figure 4-35 below.

By a δ/B ratio of about 95%, the stable arch had collapsed and a new stable arch had formed at a shallower depth and slightly to the left of the first arch. This second arch had formed slightly beyond the boundary extending upwards from the left trapdoor edge, thus deviating from trends seen in other tests. The second arch remained intact up to the end of the test and no further deformation occurred above it.

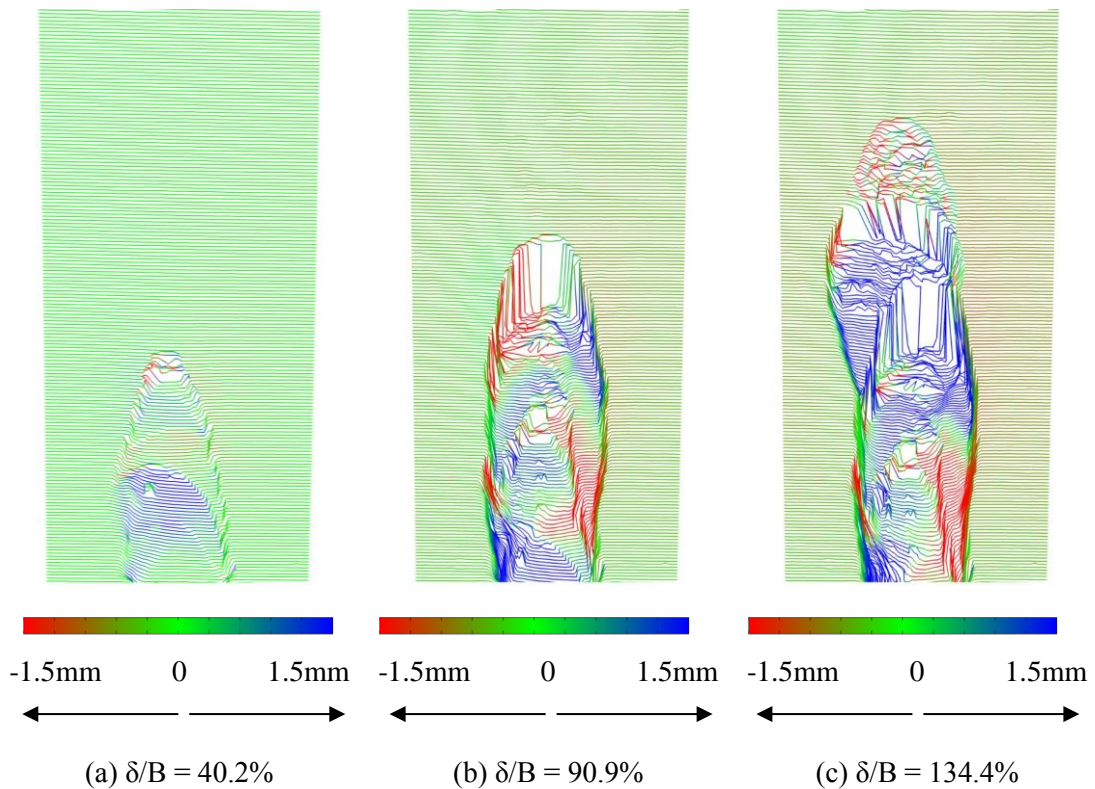


Figure 4-35: Settlement plots of Test 4MF-50

4.3.4.5 Surface Settlement

Settlement of soil at the surface is shown in Figure 4-36 with settlement exaggerated. Although no opening manifested at the soil surface as was the case in all previous tests, the settlement profile followed a similar trend. Maximum settlement occurred along the trapdoor centreline and gradually reduced with distance from the centreline. Since the cavity did not propagate all the way to the surface, a maximum downward settlement of about 1.2mm was recorded. Nevertheless, settlement still occurred in the shape of a Gaussian distribution at the start of the test and deviated slightly from this trend as the test progressed.

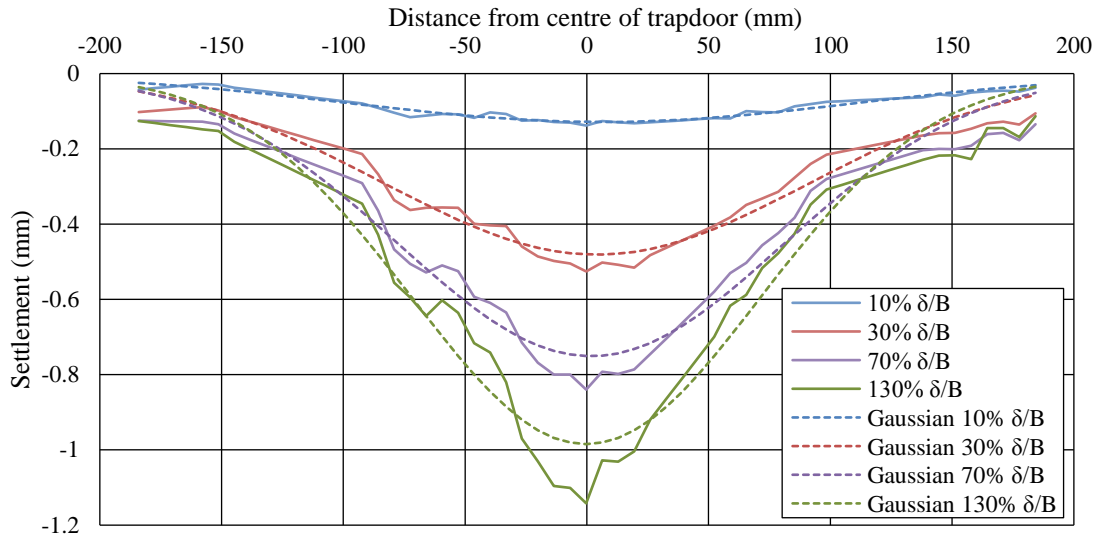


Figure 4-36: Surface settlement distribution of Test 4MF-50

A ratio of surface settlement to trapdoor settlement is shown in Figure 4-37. Initial settlement occurred at a rate of 4% before a stable arch was formed at a δ/B of about 40%. At this stage, further settlement at the surface became insignificant, increasing at a rate of merely 0.5%. Ultimate failure of the initial stable arch saw the creation of a second stable arch at a δ/B of 95%. This caused an instantaneous settlement of about 0.5mm before stabilising once again. This stable state continued up to the end of the test.

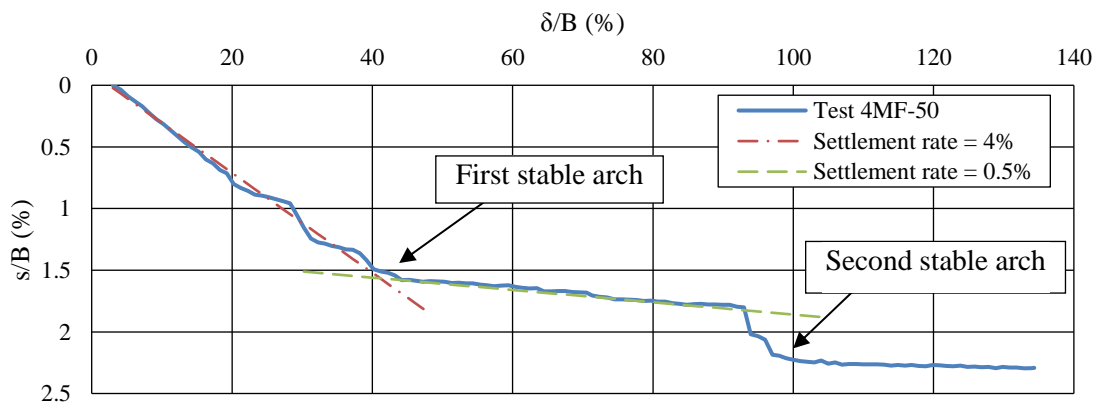


Figure 4-37: Ratio of normalized surface settlement against normalized trapdoor settlement during Test 4MF-50

4.3.5 Test 5MF-75 – Moist Fine Sand with 75mm Trapdoor

Up to this point all test had been performed using a 50mm trapdoor, which represents a cavity with a full-scale diameter of 2.5m (taking into the account a 1:50 scaling factor). It was decided to simulate a larger cavity with a diameter of 3.75m (75mm trapdoor) as well as one with a width of 5m (100mm trapdoor). The current test was similar to Test 4MF-50 with the exception of having a 75mm trapdoor.

4.3.5.1 Test Arrangement

The table below shows several parameters of the test arrangement of Test 5MF-75. Through inspection of images, settlement (δ_0) of the trapdoor during centrifuge acceleration was determined to be 2.53mm when acceleration reached 50G. This value was taken to be the trapdoor settlement at image 1 of the test and PIV readings were zeroed at this point. All subsequent PIV readings were adjusted by δ_0 to obtain corrected settlement readings.

Table 4-10: Test arrangement parameters for Test 5MF-75

Parameter	Value
<u>Soil Characteristics</u>	
Sand type	Fine sand
Moisture content	2.7% - 9.4%
Density	Dense
<u>Geometry of Test Package</u>	
Sand depth (H)	290 mm
Trapdoor width (B)	75 mm
H/B ratio	3.9
Rate of trapdoor settlement	2.56 mm/min
Time between analysed images	12 secs (every 0.51mm of settlement)

The moisture content distribution in the soil is shown in Figure 4-38 below. Similar to the corresponding test in moist fine sand (Test 4MF-50), the distribution of moisture within the soil had a wider range than in coarse sand, ranging from 2.7% - 9.4%. The high moisture content at the bottom of the soil mass is probably not representative of the entire soil mass since water was drawn down under the applied acceleration.

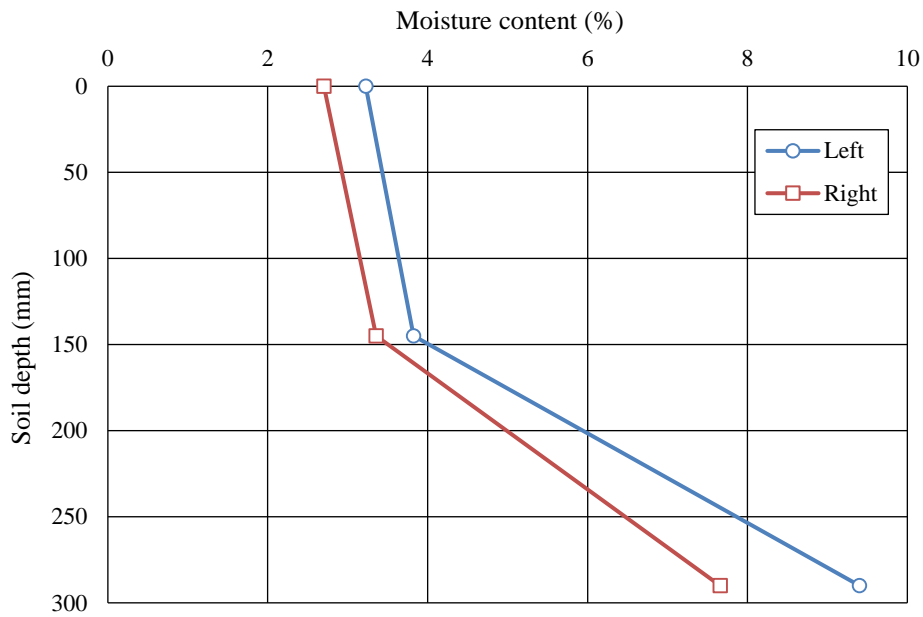


Figure 4-38: Moisture content with soil depth (Test 5MF-75)

4.3.5.2 Photographic Record

The first analysed photograph of Test 5MF-75 is shown in Figure 4-39 below. Also indicated is the area of interest that was analysed using PIV.

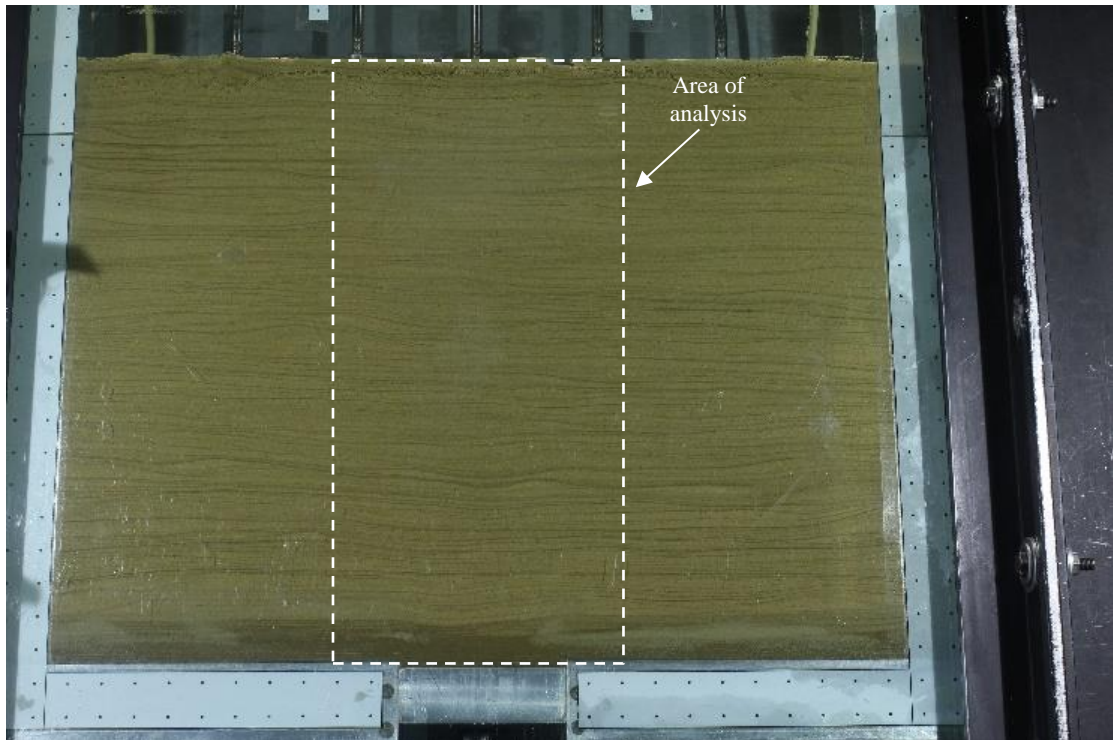
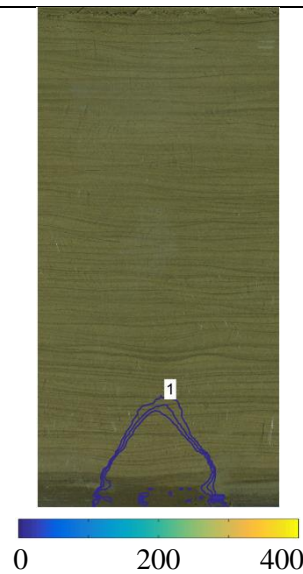
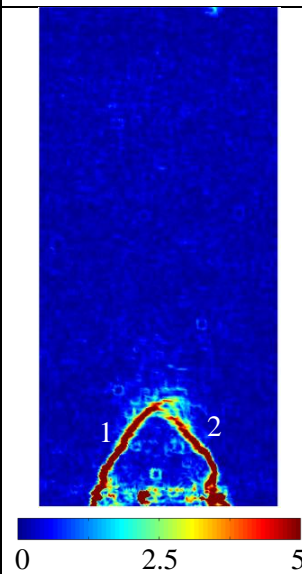
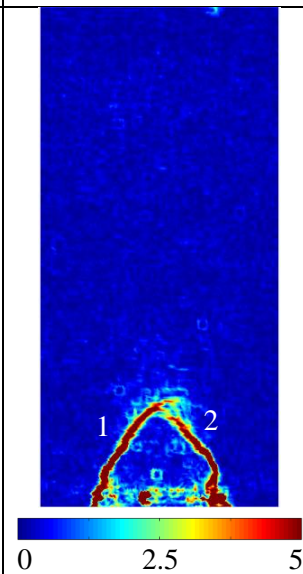
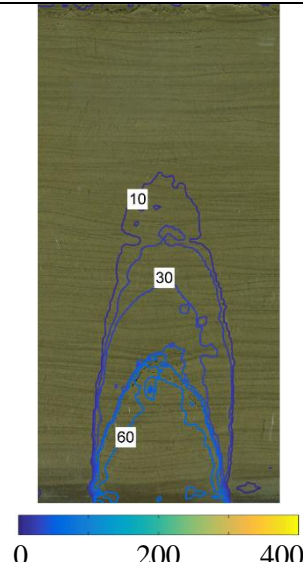
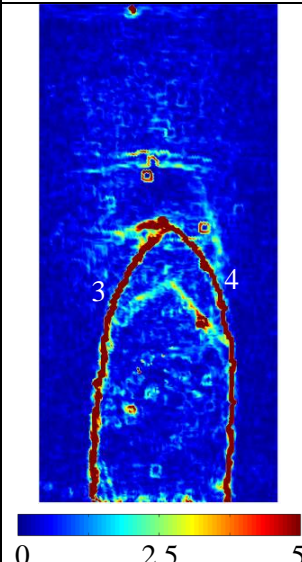
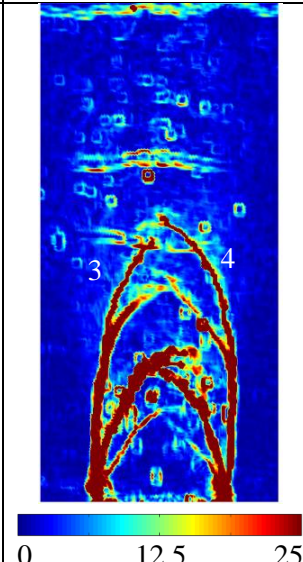


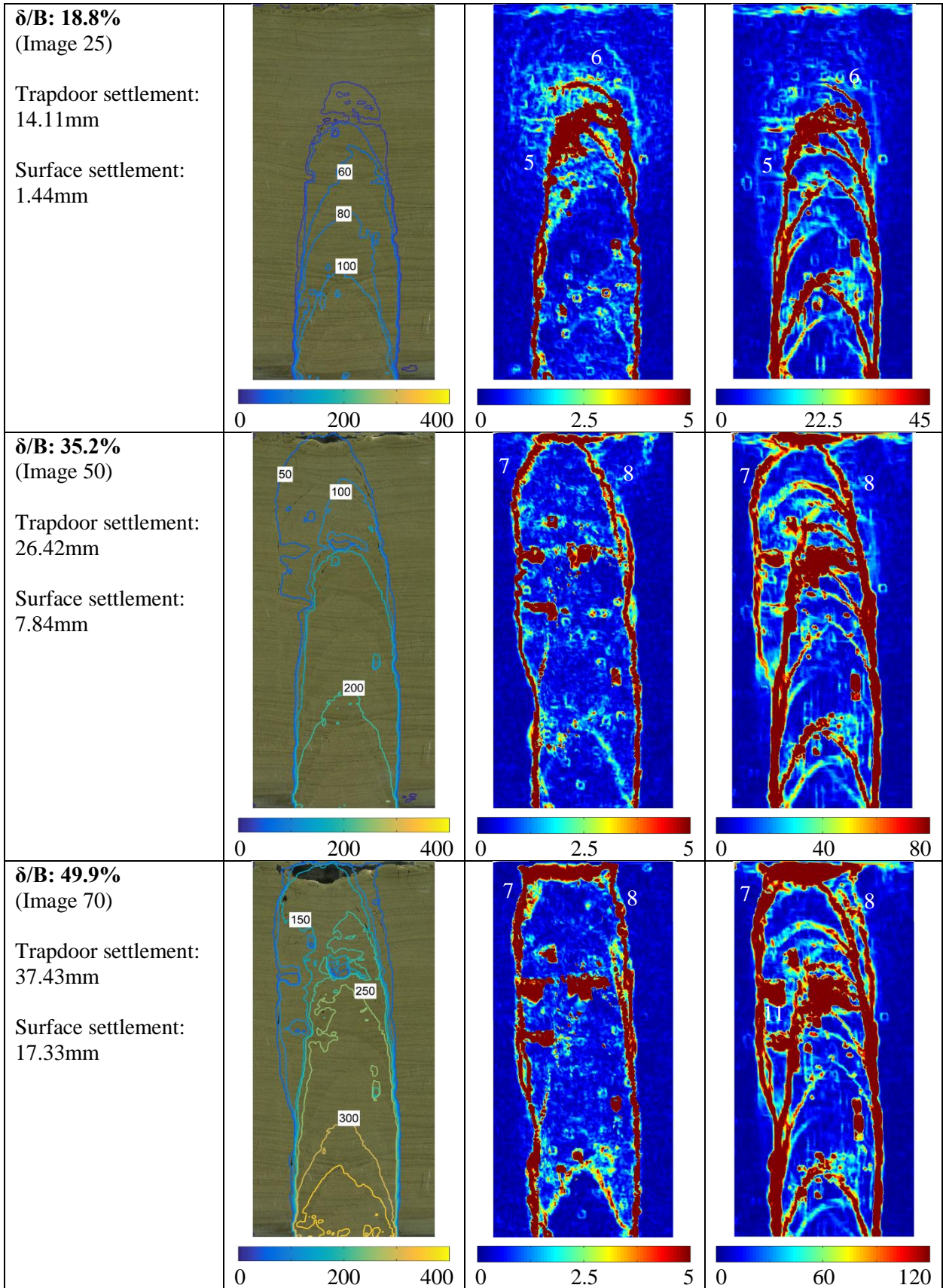
Figure 4-39: First analysed photo of Test 5MF-75

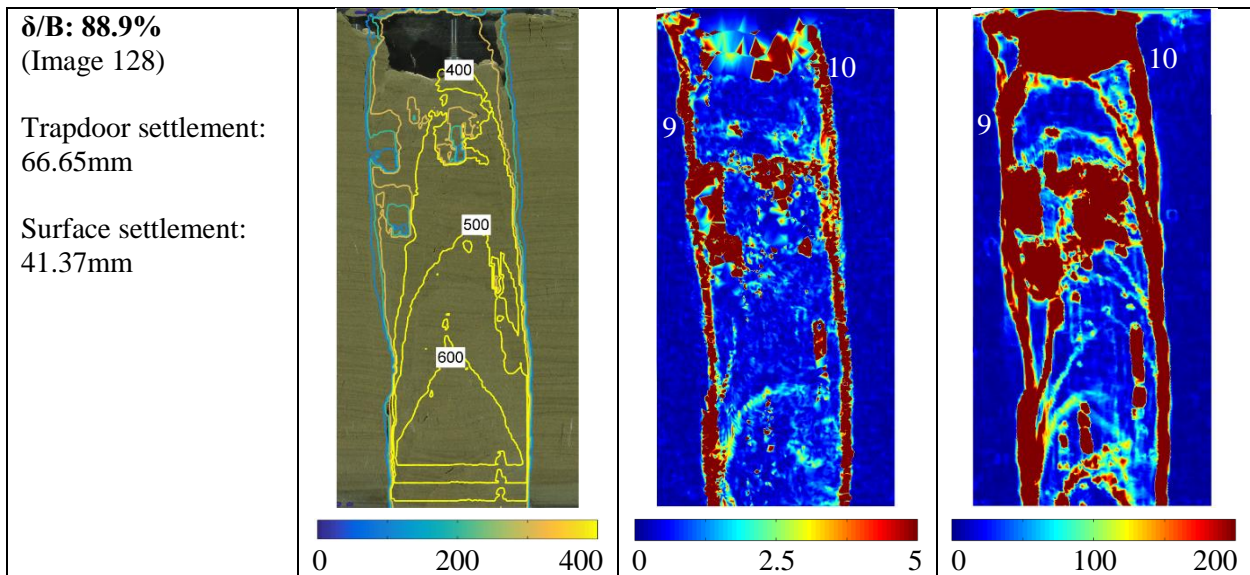
4.3.5.3 Shear Zone Propagation

Table 4-11 below shows distributions of vertical displacement, incremental maximum shear strain and total maximum shear strain at several stages throughout the test.

Table 4-11: Selected results of Test 5MF-75

	Vertical displacement (px)	Incremental maximum shear strain (%)	Total maximum shear strain (%)
<p>δ/B: 4.1% (Image 2)</p> <p>Trapdoor settlement: 3.10mm</p> <p>Surface settlement: 0.01mm</p>			
<p>δ/B: 11.8% (Image 15)</p> <p>Trapdoor settlement: 8.86mm</p> <p>Surface settlement: 0.76mm</p>			





4.3.5.4 Discussion of Displacement and Strain Plots

At a δ/B ratio of 4.1%, two shear bands (labelled 1 and 2) had formed symmetrically from each edge of the trapdoor, joining up at the centre to form a triangular shaped failure mechanism. As with the previous tests in moist fine material (Test 4MF-50), the shear bands in this test appeared to be narrower than that of tests in moist coarse sand (Test 2MC). Several more pairs of shear bands had formed in a symmetrical fashion up to a δ/B ratio of 10.2%, with each pair joining up in the centre at a higher elevation than the previous pair.

The typical parabolic-shaped mechanism seen in previous tests was prominently visible at a δ/B of 11.8% with shear bands 3 and 4 joining up at the centre. As before, shear bands tended to form symmetrical at first but became increasingly asymmetrical. It appeared that the zone of influence became narrower at shallower depths, which is in contrast with the test performed using the smaller trapdoor (Test 4MF-50) where the boundaries of the zone of influence tended to rise near-vertically.

At a δ/B of 23.3%, shear band 7 formed on the left-hand side, reaching beyond the boundary of the existing zone of influence, curving slightly inwards near the surface and then reaching the surface at a location close to the trapdoor centreline. Shear band 8 formed at a δ/B of 27.3% and eventually joined up with shear band 7 at the surface. Both are visible at a δ/B of 35.2%. As in previous tests, the zone of influence reached the soil surface near the centre of the zone of influence and then gradually branched outwards to widen the diameter of the subsequent depression, continuing up to the end of the test.

At this stage, horizontal movement appeared to have been largely towards the right, as seen in Figure 4-40 below, probably due to the far-reaching extents of shear band 7. However, even at

the end of the test there appeared to be portions of soil within the zone of influence that experienced no horizontal movement and only settled downward uniformly with the surrounding soil.

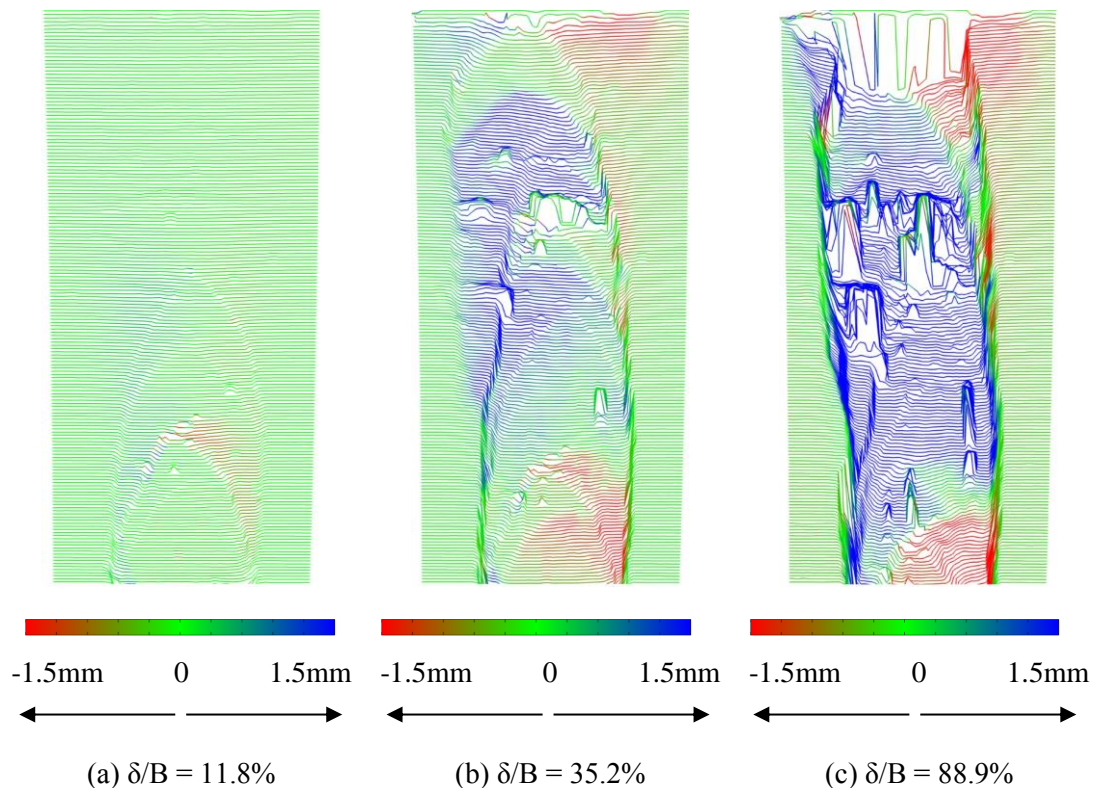


Figure 4-40: Settlement plots of Test 5MF-75

Matric suctions in the soil and interlock at high densities allowed for near vertical slopes of the depression sides. Rather than individual particles rolling into the depression as it deepened, soil along the edges remained upright for a longer period of time before sliding into the depression in larger chunks. This is visible at a δ/B of 88.9% with shear band 9 forming from the surface downwards and widening the zone of influence.

4.3.5.5 Surface Settlement

Surface settlement of Test 5MF-75 are shown in Figure 4-41. As with previous tests, soil at the surface initially appeared to settle in the shape of a Gaussian curve, but soon deviated from this trend. Matric suction in the soil and interlock due to a high density and compaction effects under high acceleration made it possible for steep slopes at the sides of the depression, as can be seen in the shape of the surface depression at δ/B of 70%. The centre of the curve was shifted towards the left of the trapdoor centreline, primarily due to the formation of shear band 7.

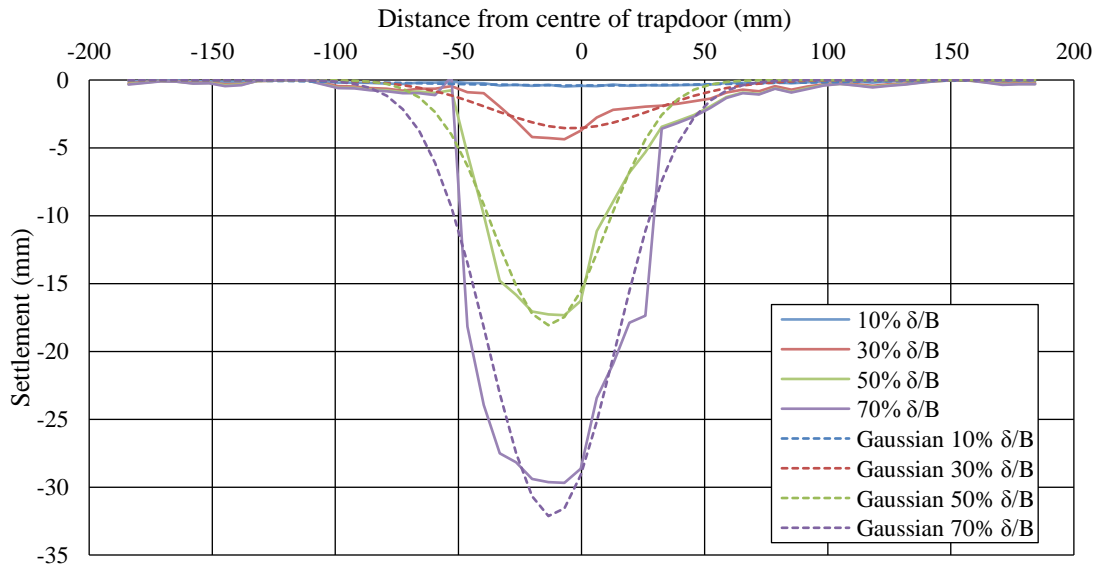


Figure 4-41: Surface settlement distribution for Test 5MF-75

A graph of surface settlement against δ/B , tracked by the bank of 5 LVDTs resting on the soil surface, is shown in Figure 4-42. It is evident from the graph that LVDTs 1 and 5 registered negligible settlements, supporting the fact that the greatest influence of the depression is directly above the trapdoor. LVDTs 2 and 4 registered similar settlement readings up to a δ/B ratio of 73%, after which a large chunk of soil failed underneath LVDT 2. LVDT 3, located directly above the trapdoor, registered slow settlement up to the point when the zone of influence reached the surface, which happened at a δ/B ratio of 23% (marked as ① on the graph). It then registered an increased settlement rate until reaching its maximum extension at a δ/B ratio of about 60%. Also shown on the graph are a timeline of failure mechanisms observed at various stages throughout the test.

The ratio of normalized surface settlement to normalized trapdoor settlement is shown in Figure 4-43, along with trend lines of the two distinct linear parts of the curve. The soil settled at a slow rate up to δ/B of 23% when the zone of influence reached the soil surface, after which the rate of settlement increased to a greater value, slightly less than the settlement rate of trapdoor. This rate remained constant up to the end of the test. The two separate slopes of this curve most closely resemble that of the test on dry, coarse sand (Test 1DC).

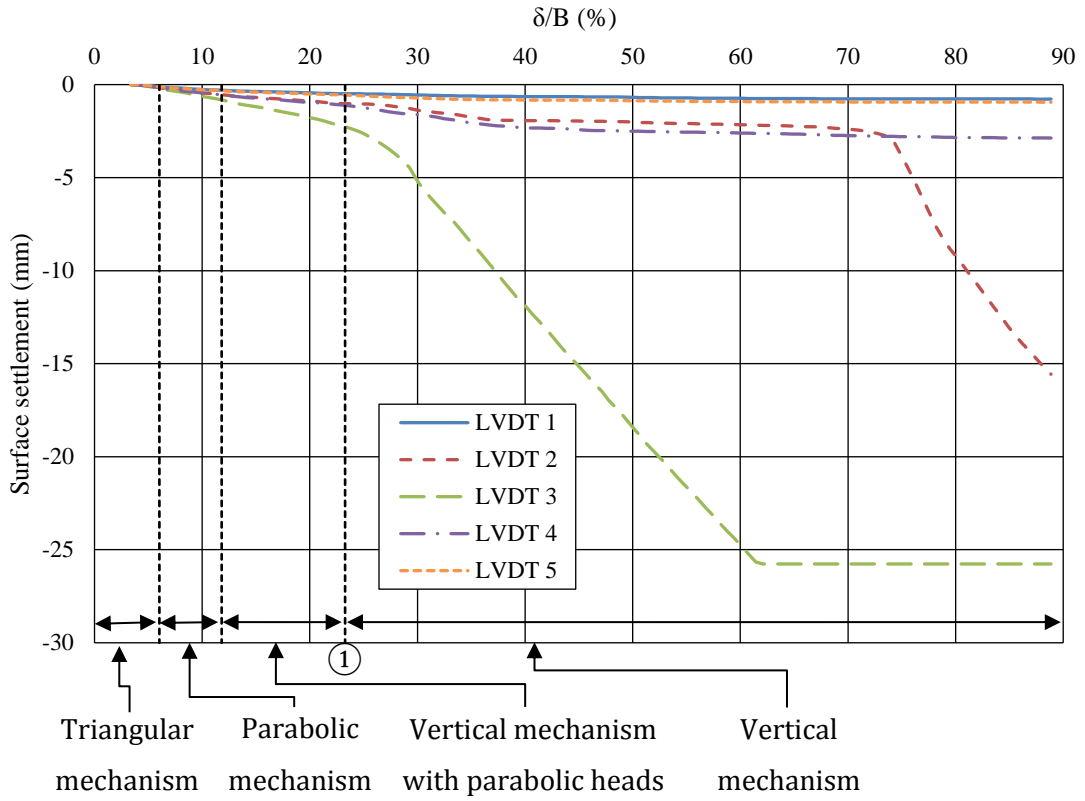


Figure 4-42: Surface settlement (LVDT bank) - Test 5MF-50

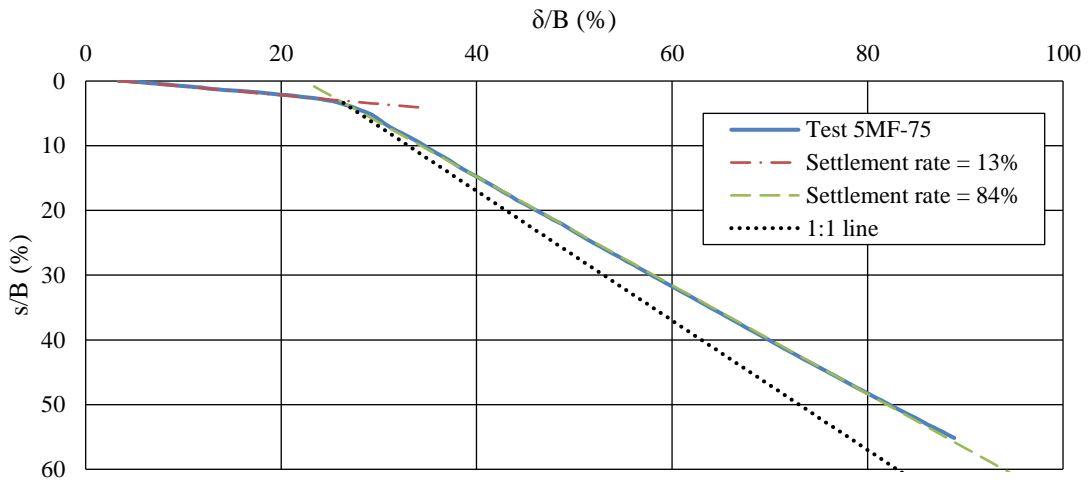


Figure 4-43: Ratio of normalized surface settlement against normalized trapdoor settlement during Test 5MF-75

4.3.6 Test 6MF-100 – Moist Fine Sand with 100mm Trapdoor

This test was the third in the series of three tests to investigate the impact of the trapdoor width on failure mechanisms. It was similar to Tests 4MF-50 and 5MF-75 with the only difference being a change in trapdoor width to 100mm.

4.3.6.1 Test Arrangement

Shown in the table below are several parameters of the test arrangement of Test 6MF-100. Through inspection of images, settlement (δ_0) of the trapdoor during centrifuge acceleration was determined to be 0.47mm when acceleration reached 50G. This value was taken to be the settlement at image 1 of the test and PIV readings were zeroed at this point. All subsequent PIV readings were adjusted by δ_0 to obtain corrected settlement readings.

Table 4-12: Test arrangement parameters for Test 6MF-100

Parameter	Value
<u>Soil Characteristics</u>	
Sand type	Fine sand
Moisture content	2.0% - 5.6%
Density	Dense
<u>Geometry of Test Package</u>	
Sand depth (H)	290 mm
Trapdoor width (B)	100 mm
H/B ratio	2.9
Rate of trapdoor settlement	2.57 mm/min
Time between analysed images	12 secs (every 0.51mm of settlement)

The moisture content in the sample, as measured after the test, is shown in Figure 4-44 and ranges between 2.06% and 2.9%. Similar to Tests 4MF-50 and 5MF-75, the moisture content increased with depth which can once again be attributed to the applied acceleration forcing the moisture downwards.

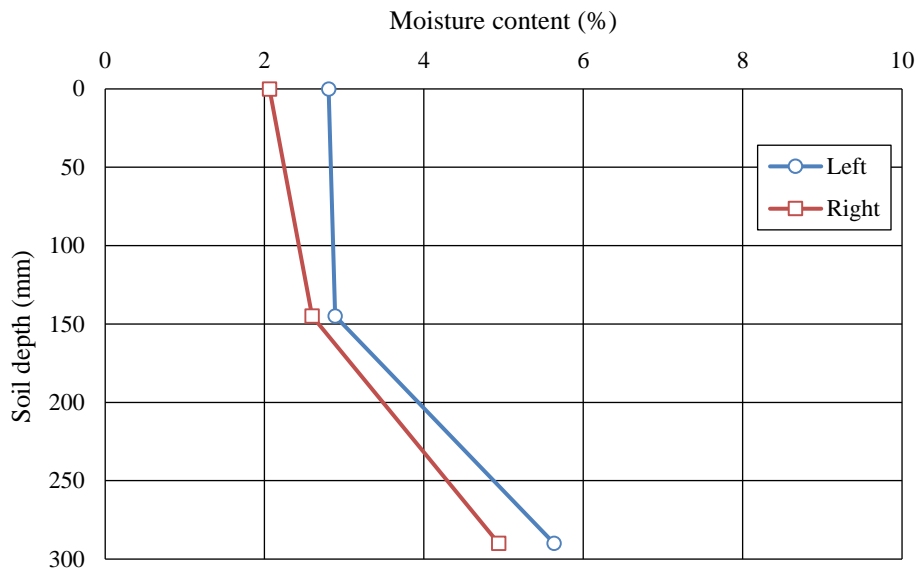


Figure 4-44: Moisture content with soil depth (Test 6MF-100)

4.3.6.2 Photographic Record

The first analysed photograph of Test 6MF-100 is shown in Figure 4-45 below. Also indicated is the area of interest that was analysed using PIV.

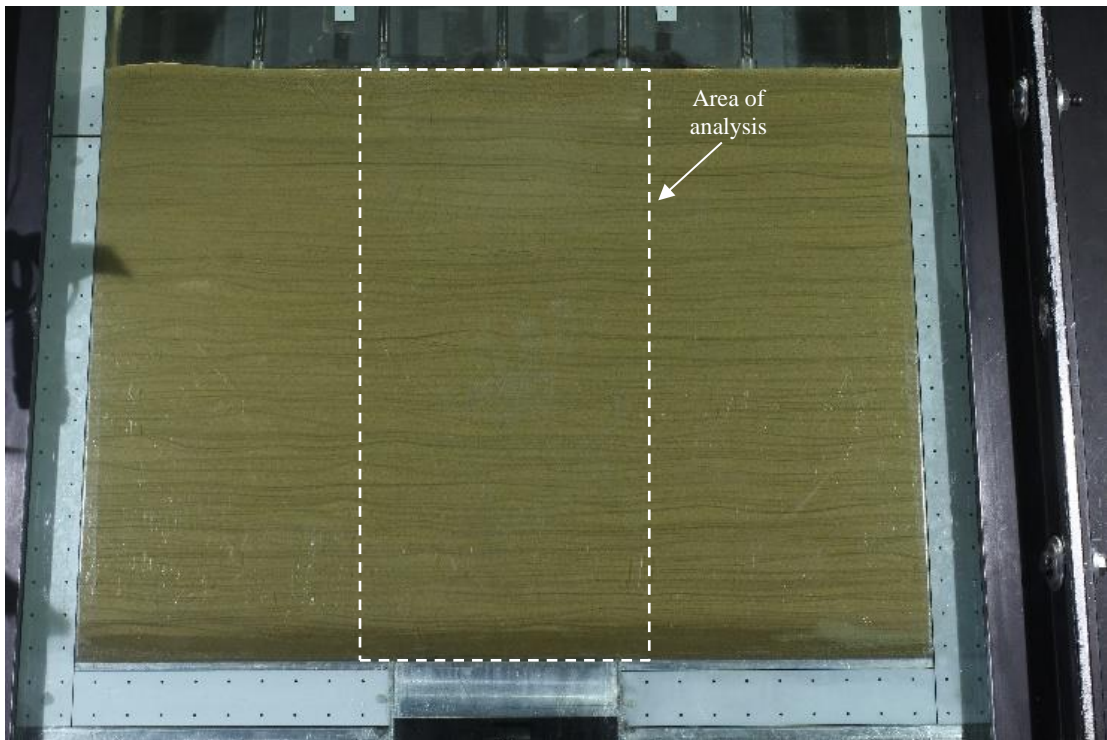
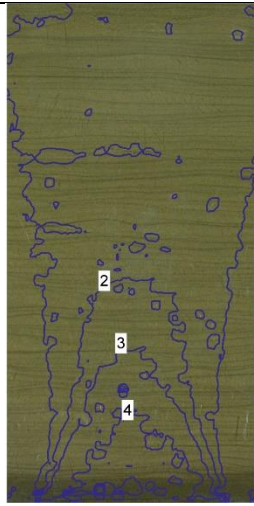
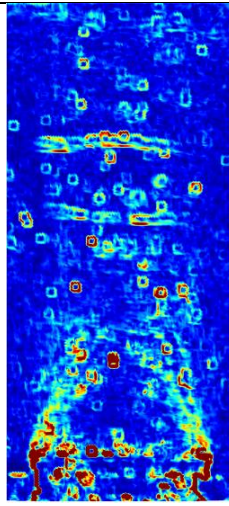
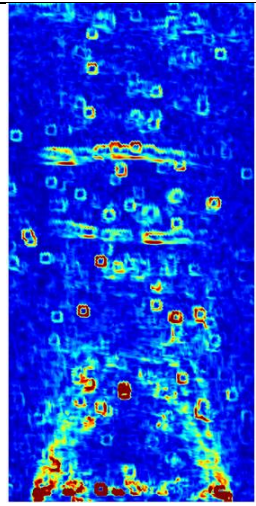

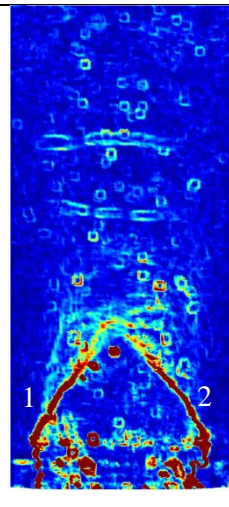
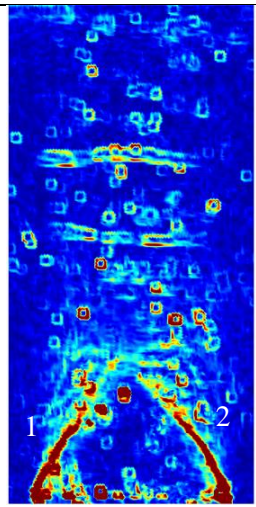


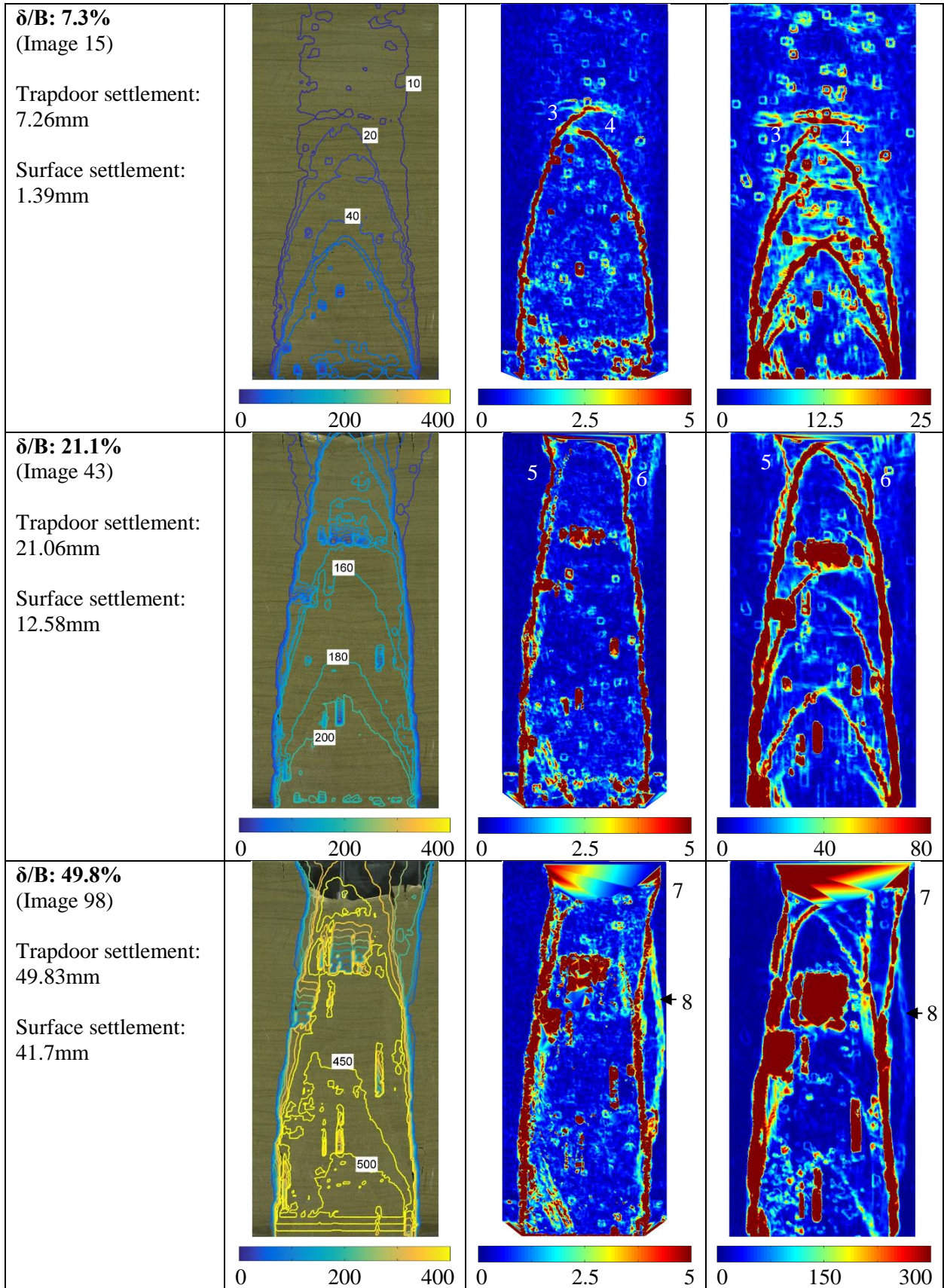
Figure 4-45: First analysed photo of Test 6MF-100

4.3.6.3 Shear Zone Propagation

Table 4-13 below shows distributions of vertical displacement, incremental maximum shear strain and total maximum shear strain at several stages throughout the test.

Table 4-13: Selected results of Test 6MF-100

	Vertical displacement (px)	Incremental maximum shear strain (%)	Total maximum shear strain (%)
<p>$\delta/B: 1.0\%$ (Image 2)</p> <p>Trapdoor settlement: 0.96mm</p> <p>Surface settlement: 0.19mm</p>	 <p>0 200 400</p>	 <p>0 2.5 5</p>	 <p>0 2.5 5</p>
<p>$\delta/B: 2.0\%$ (Image 4)</p> <p>Trapdoor settlement: 1.54mm</p> <p>Surface settlement: 0.42mm</p>	 <p>0 200 400</p>	 <p>0 2.5 5</p>	 <p>0 6 12</p>



4.3.6.4 Discussion of Displacement and Strain Plots

Propagation of the zone of influence occurred in much the same way as in the test with the 75mm trapdoor (Test 5MF-75). At a δ/B of 1.0% a family of shear bands developed from each edge of the trapdoor. By a δ/B of 2.0% two prominent shear bands (labelled 1 and 2) remained and met up in the centre of the shear zone to form a triangular-shaped failure mechanism. Several more pairs of shear bands formed from each edge of the trapdoor, more symmetric than in narrower trapdoor tests, with each pair joining up near the centre at a depth slightly shallower than the previous pair.

As with the previous test (Test 5MF-75) there were large areas within the shear zone where no horizontal movement was observed, as seen in Figure 4-46. Horizontal displacement was confined to regions directly above shear bands while the entire column of soil directly above the trapdoor settled uniformly. Similar to the previous test, the zone of influence became narrower closer to the surface and only widened to the full width of the trapdoor after reaching the surface.

The triangular-shaped failure arch formed upwards and grew increasingly parabolic in shape before reaching the soil surface by a δ/B of 9.9%, much sooner than in previous tests and at a location close to the trapdoor centreline. As with most of the previous tests, this initial depression widened and became larger during the remainder of the test. At this stage, another pair of shear bands (5 and 6) started forming away from the trapdoor centreline, curving outwards and stretching from the top of the existing shear zone to the soil surface. However, the mechanism at this stage remained parabolic in shape, continuing beyond the point where the zone of influence reached the surface.

At a δ/B of 17.5%, the mechanism transitioned from parabolic to vertical. This widening was, however, accomplished by shear bands forming from the surface downwards and meeting up with the parabolic mechanism below the surface. At a δ/B of 24.5%, shear band 7 started forming from the soil surface on the right-hand side and extended downwards, joining up with the rest of the shear zone at a distance of about $H/3$ below the surface. Similar to Test 5MF-75, a block of soil on the right edge of the developing depression became too heavy to be held upright by shear strength alone and thus started to tear away from the rest of the soil body with the initial crack forming downwards from the surface. Another shear band of this kind (shear band 8) started forming at δ/B of 34.5% just below shear band 7.

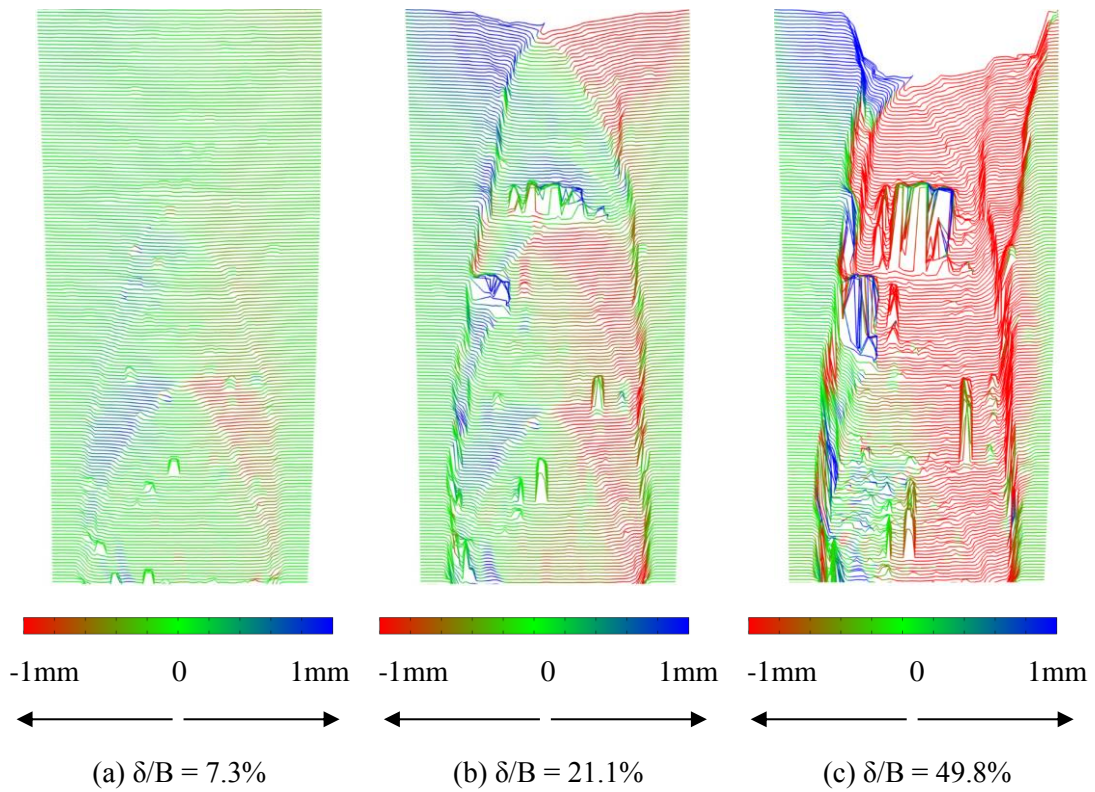


Figure 4-46: Settlement plots of Test 6MF-100

In contrast with the previous test, the shear zone tended to lean towards the right and consequently, horizontal movement appeared to be predominantly towards the left, as seen in Figure 4-46.

4.3.6.5 Surface Settlement

Settlement of soil at the surface is shown in Figure 4-47. As with most other tests, settlement initially occurred in the form of a Gaussian distribution, but then deviated from this trend soon after the zone of influence reached the surface. The slopes of the surface depression becoming near-vertical in the latter stages of the test, owing to the fact that the moisture in the soil provided enough matric suction to support steep sides.

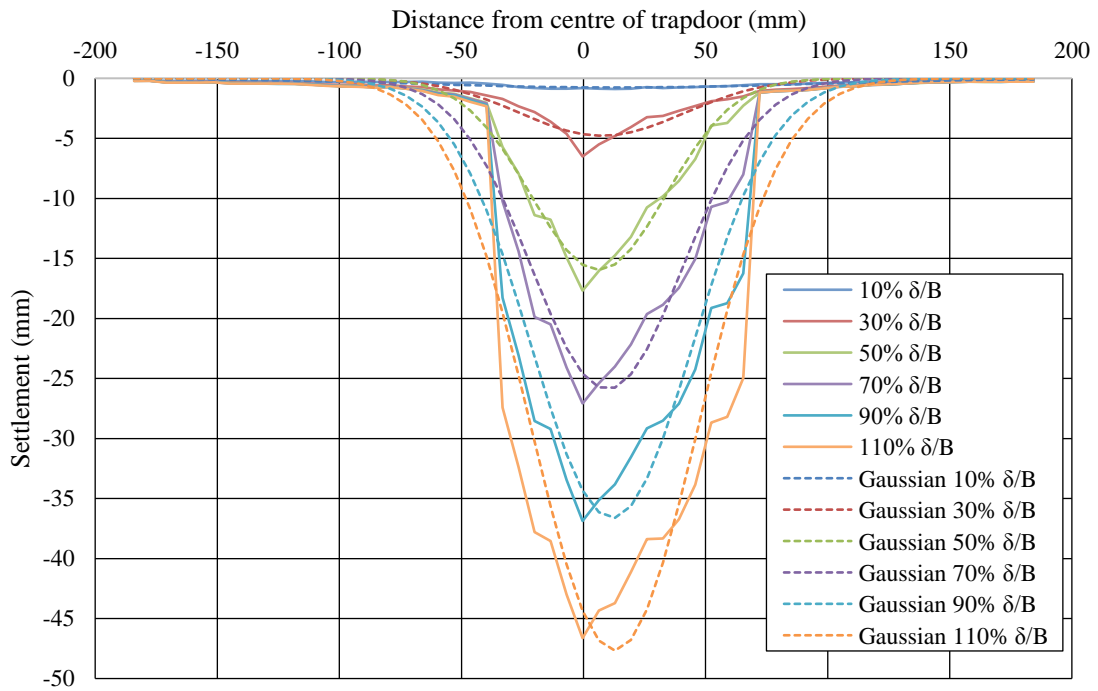


Figure 4-47: Surface settlement distribution of Test 6MF-100

A graph of surface settlement against δ/B , tracked by the bank of LVDTs resting on the soil surface, is shown in Figure 4-48. LVDTs 1 and 5 registered negligible settlements as before. LVDT 4 registered a greater settlement than LVDT 2, although they were located at equal distances from the centreline, due to the fact that the column of failure leaned to the right. LVDT 3, located directly above the trapdoor, registered a similar reading to the same LVDT in the previous test. Settlement was initially slow up to the point where the zone of influence reached the surface, which happened at a δ/B ratio of 9.9% (marked as ① on the graph). A greater settlement rate of nearly 97% that of trapdoor settlement was then registered before the LVDT reached its maximum extension. Also shown on the graph are a timeline of failure mechanisms that were observed at various stages throughout the test.

The ratio of normalized surface settlement to normalized trapdoor settlement is shown in Figure 4-49. The change from a low rate of settlement to a higher one occurred at a δ/B of around 12% when the zone of influence reached the surface. It is notable that the rate of surface settlement is equal to 97% of the rate of trapdoor settlement, compared to 84% in Test 5MF-75. This shows that a wider trapdoor causes the surface settlement rate after the zone of influences reaches the surface to increase, with the rate of trapdoor settlement being the upper limit.

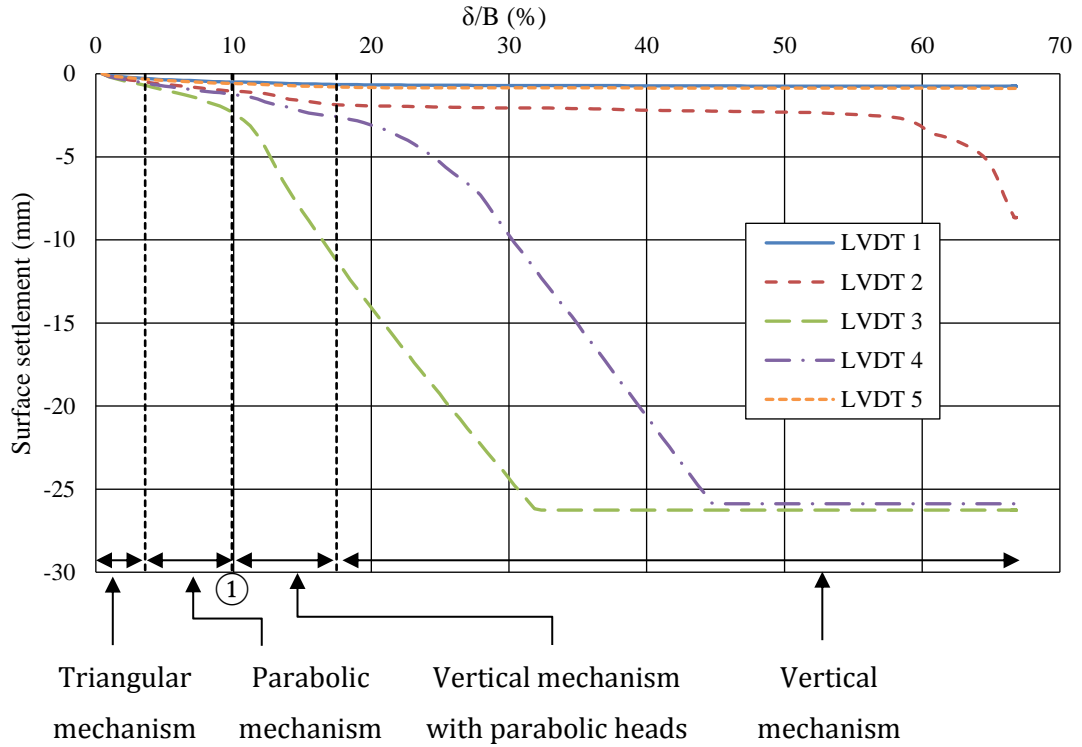


Figure 4-48: Surface settlement (LVDT bank) - Test 6MF-100

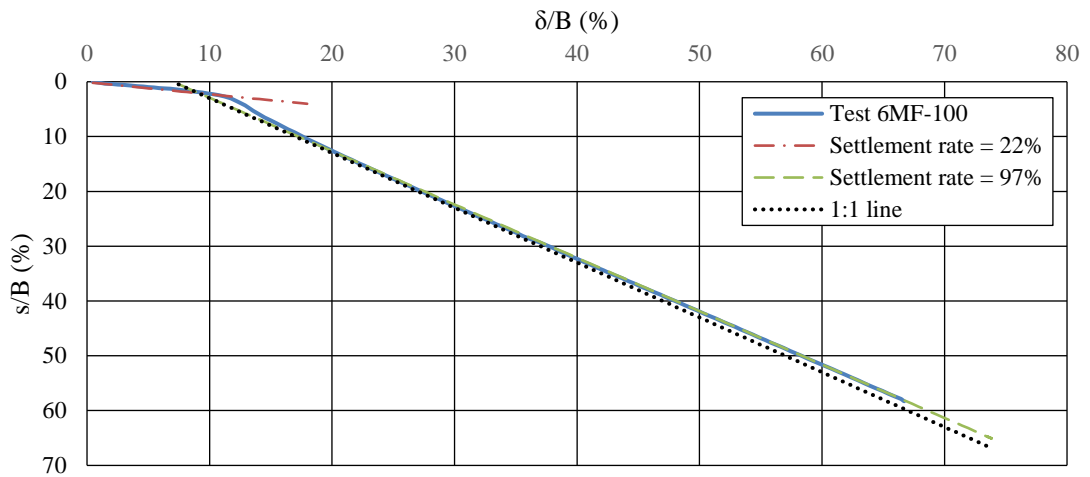


Figure 4-49: Ratio of normalized surface settlement against normalized trapdoor settlement during Test 6MF-100

4.4 COMPARISON OF SHEAR BEHAVIOUR IN VARIOUS CONDITIONS

Several comparisons were made between results of the tests presented to highlight the influence that various parameters have on shearing behaviour. These are discussed in the sections below.

4.4.1 Comparison Between Coarse and Fine Material

The first comparison is made between coarse and fine material, as presented in the table below. Since behaviour of the soil varied significantly with varying moisture conditions, comparisons will be made separately for dry and moist conditions.

Table 4-14: Comparison between coarse and fine material

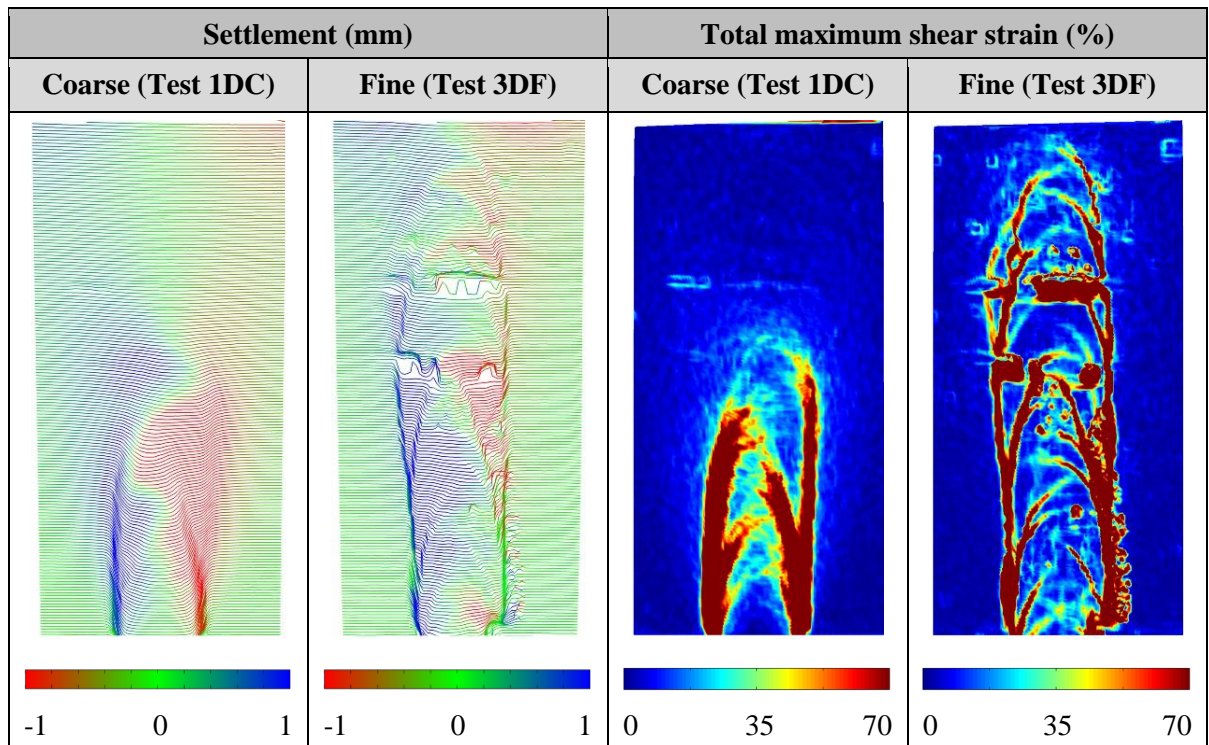
	Dry	Moist
Coarse	Test 1DC	Test 2MC
Fine	Test 3DF	Test 4MF-50 Test 5MF-75 Test 6MF-100

Dry conditions

Table 4-15 below shows a comparison of failure mechanisms between coarse material (Test 1DC) and fine material (Test 3DF) in a dry state at a δ/B of 53% (the highest value for which shear strains could be determined for Test 3DF).

It is immediately apparent that shear bands appeared more complex and densely spaced in fine material than in coarse material. This could be due to more shear planes being available between fine grains than between coarser grains. Stone (1988) suggested that the larger particles in coarser sand requires a greater relative movement to shear past one another and reach the critical state which would then trigger the formation of a new shear band. Finer materials reach this state faster and thus new shear bands form more regularly and in various directions.

Shear bands in fine material also appeared thinner than in coarse material, although actual measurements of shear band thickness were not performed in this study. Literature suggests that thickness (t) of shear bands is greatly dependent on the mean particle diameter (D_{50}). Roscoe (1970) advocated an average t/D_{50} value of 10. Experimental results by Costa et al. (2009) found these values to be in excess of 30. Noting that the D_{50} of the coarse Consol sand is 4.9 times that of the finer Cullinan sand (Section 3.4.1), the order of magnitude of the shear band width in this test seems to agree with these values found in literature.

Table 4-15: Comparison of failure mechanisms between coarse and fine conditions in dry material at $\delta/B = 53\%$ 

It is notable that the zone of influence propagated faster to the surface in fine material than in coarse material as is evident from a comparison of normalized surface settlement in Figure 4-50. Surface settlement initially occurred at the same rate in both tests, but the shear zone in fine material reached the surface at half the normalized trapdoor displacement recorded in coarse material. The end of Test 3DF (fine material) is visible in Figure 4-50 at a δ/B of roughly 55%, at which point the shear zone had reached the surface and a change in the settlement rate is clearly visible. This indicates more efficient arching in fine material (more capable of supporting the overburden load), with the amount of surface settlement being the same for a shallow shear zone in fine material than a deeper shear zone in coarse material.

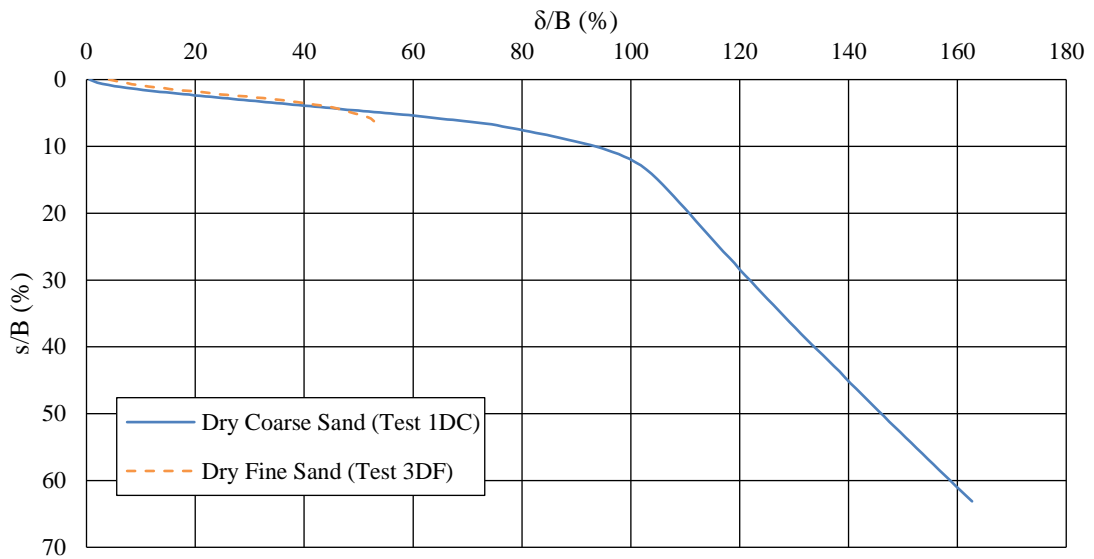


Figure 4-50: Comparison of normalized settlement between coarse and fine conditions in dry material

Moist conditions

Table 4-16 below shows comparison of failure mechanisms between coarse material (Test 2MC) and fine material (Test 4MF-50) at a δ/B of 91%, which was the highest value for which strains could be determined for Test 4MF-50. As in the case of dry conditions, shear bands in fine sand were once again thinner, more complex and more densely spaced in fine material than in coarse material. The width of the shear zone seemed to be relatively equal between the two tests, roughly bound by vertical lines from the trapdoor edges in both cases.

In dry conditions, it was observed that a cavity in fine sand propagated faster to the surface than in coarse sand in terms of normalized trapdoor settlement. Under moist conditions, however, this trend was obscured by a stable arch forming in the fine sand which remained intact until the end of the test, as observed in the normalized settlement plot in Figure 4-51, further illustrating the more efficient arching capability of fine material. A stable arch formed in fine sand due to it possessing sufficient matric suction to support the weight of the soil above it. Pores within the coarse material were too large to sustain small capillary radii and thus moisture drained faster from soil body. Without sufficient moisture between particles, there was not enough shear strength in the coarse sand to sustain a stable arch for a prolonged period and therefore any possible arches that could have formed collapsed before they could be detected.

Table 4-16: Comparison of failure mechanisms between coarse and fine conditions in moist material at $\delta/B = 91\%$

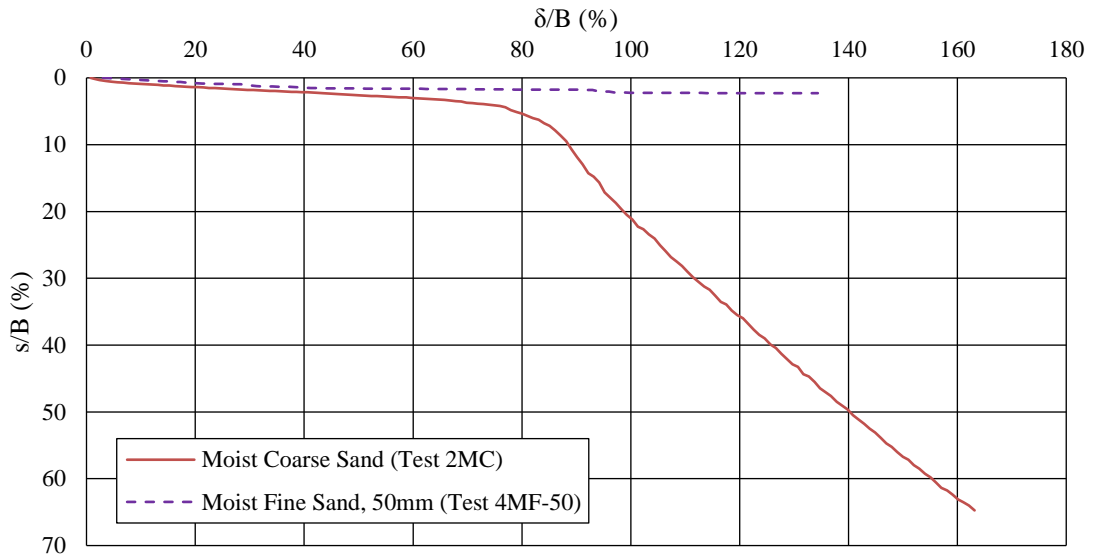
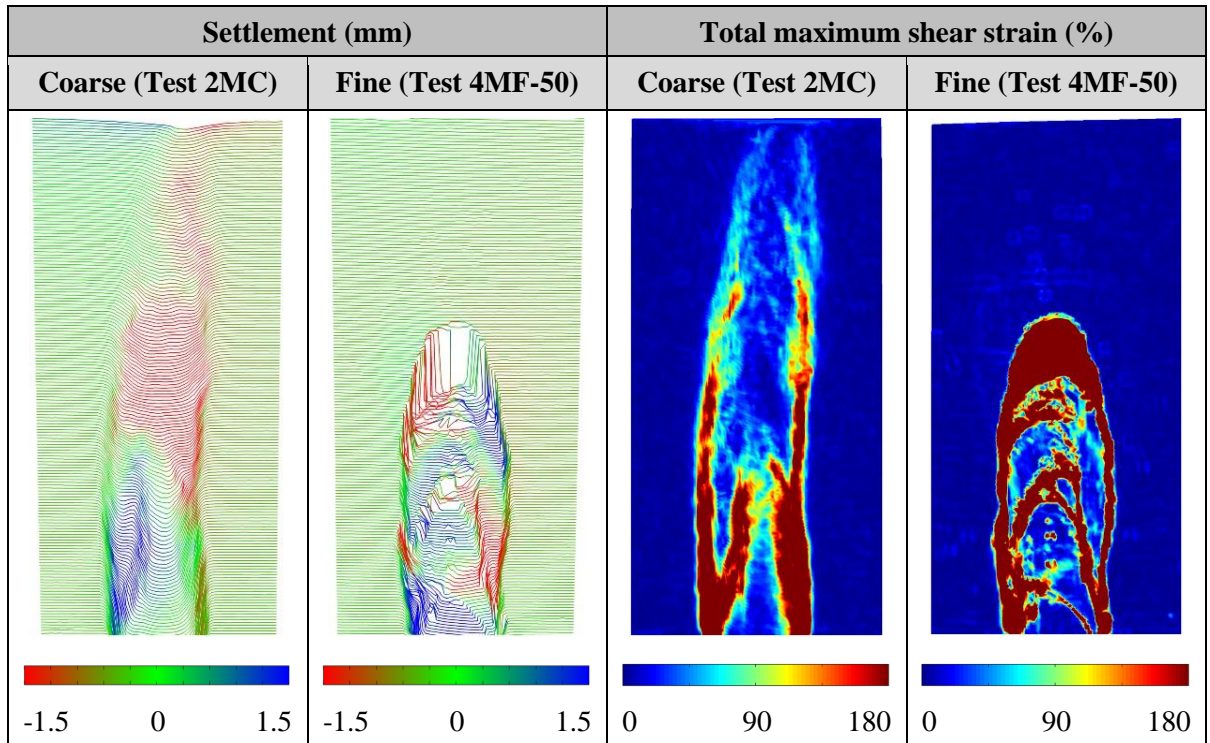


Figure 4-51: Comparison of normalized settlement between coarse and fine conditions in moist material

4.4.2 Comparison Between Dry and Moist Material

Although tests in both dry and moist states have been discussed separately in the previous section, a direct comparison is made between them here. Comparisons are made between Test

1DC (dry) and Test 2MC (moist), and between Test 3DF (dry) and Test 4MF-50 (moist), pairs with similar particle sizes, as demonstrated in Table 4-17.

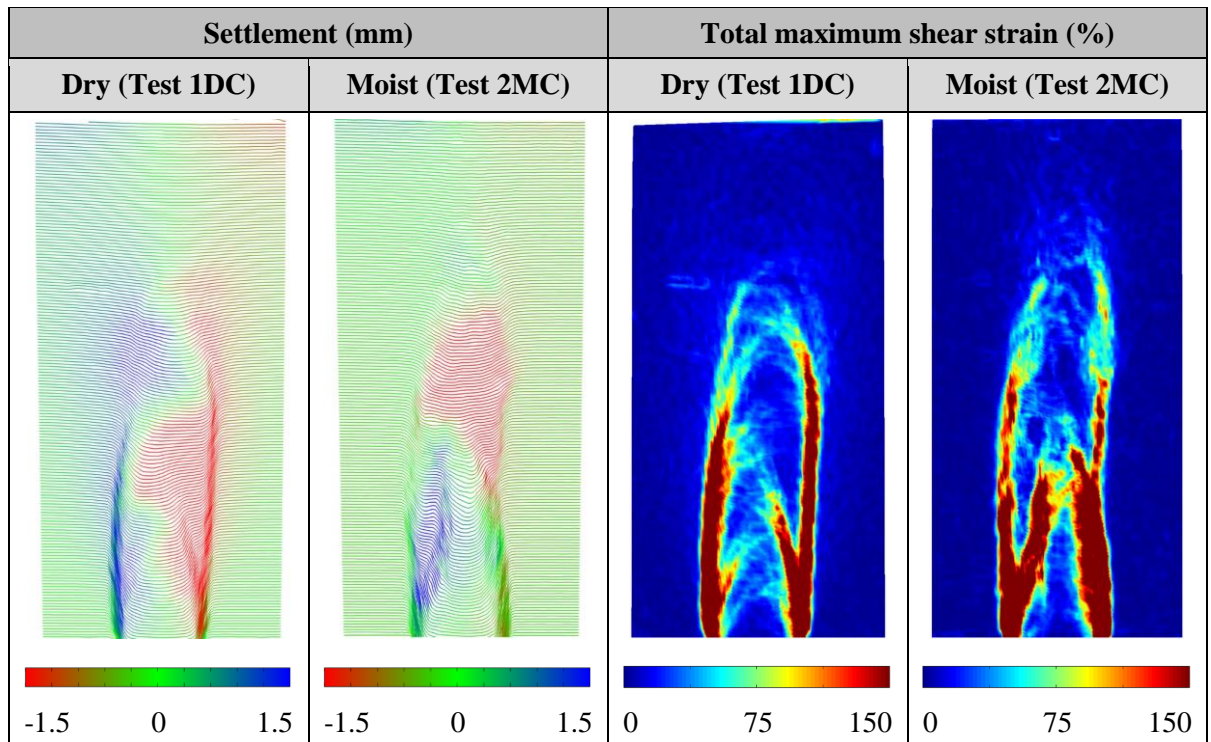
Table 4-17: Comparison between dry and moist material

	Dry	Moist
Coarse	Test 1DC	Test 2MC
Fine	Test 3DF	Test 4MF-50 Test 5MF-75 Test 6MF-100

Coarse material

As seen in Table 4-18, the zones of influence in Test 1DC and Test 2MC had propagated the same distance towards the surface at a δ/B ratio of 73% (the highest value for which strain data was available for Test 1DC). This contrasts with comparisons between coarse and fine material which showed a definite difference in propagation time. This is also evident in Figure 4-52, showing that dry sand settled slightly faster initially and the settlement rate gradually increased when the zone of influence reached the surface. This increase was more sudden and abrupt in moist material due to the fact that it settled and broke off in chunks while dry material gradually flowed into the depression from adjacent locations.

Table 4-18: Comparison of failure mechanisms between dry and moist conditions in coarse material at $\delta/B = 73\%$



These observations indicate that the presence of moisture had little effect on the speed of propagation when compared to the influence of particle size as discussed in the previous section. The small amount of matric suction provided by the moisture contributed only a small amount of shear strength. Although a fully saturated soil would have little shear strength that would result in imminent failure, a small amount of moisture seemed to have the opposite effect and rather strengthened the soil to ensure more effective arching behaviour (as discussed in the next section).

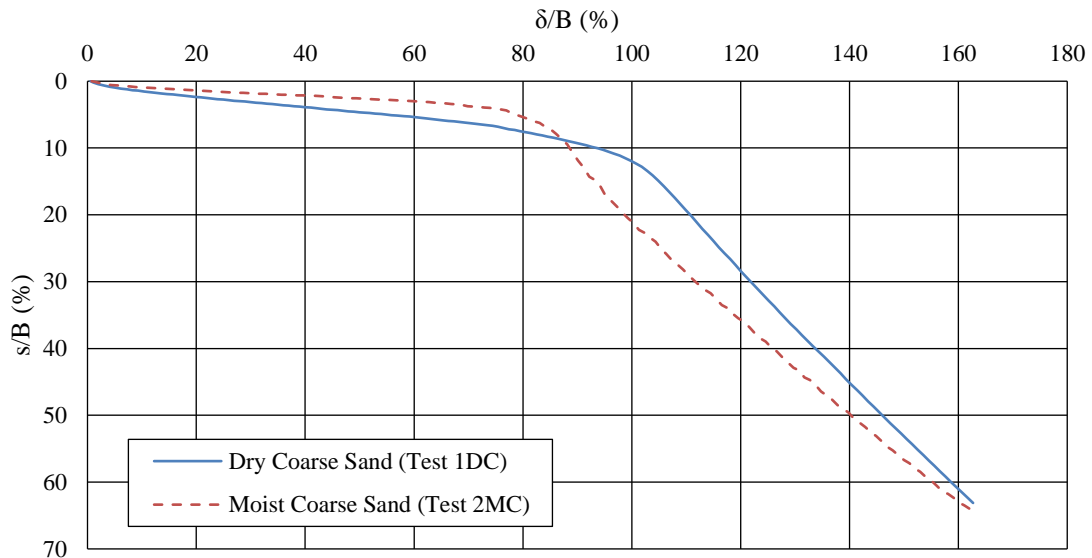


Figure 4-52: Comparison of normalized settlement between dry and moist conditions in coarse material

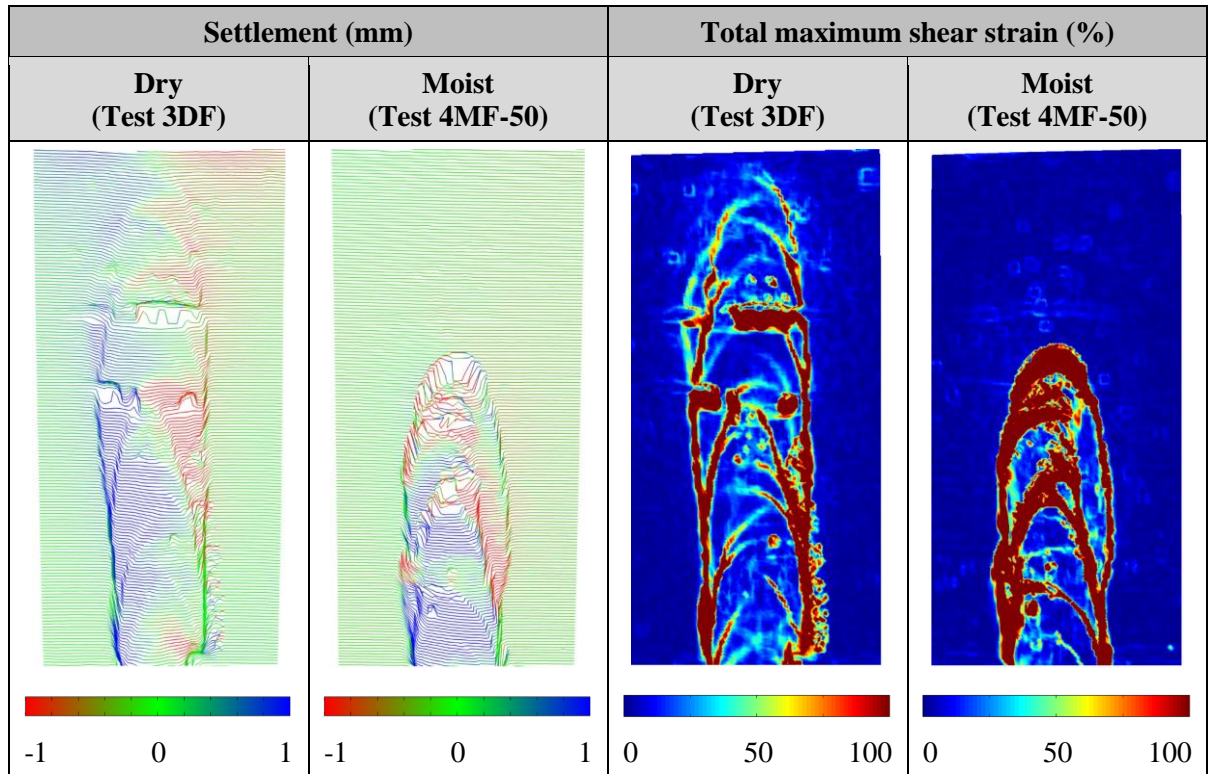
Fine material

A comparison of failure mechanisms is made between two tests in fine sand, Test 3DF (dry) and Test 4MF-50 (moist), as shown in Table 4-19. The images show the state of failure at a δ/B ratio of 53% (the highest value for which strains could be calculated for Test 3DF).

Shear bands in dry sand formed symmetrically at first but deviated from this pattern at later stages during the test while shear bands in moist sand formed asymmetrically from the beginning. From the variables tested in this study, moisture content seemed to have the largest influence on the slope of shear bands. From Table 4-19 it is visible that shear bands in dry material tended to form near-vertically upwards and curving sharply inwards at the top of the shear band before deformation transferred to a new, similarly-shaped shear bands above it. In contrast, shear bands in moist material tended to form at more slanted angles that curve inwards near the apex of the zone of influence. This is due to the moisture in the soil providing cohesion

and increasing the shear strength, consequently resulting in a more curved shear band than would be formed in cohesion-less soil.

Table 4-19: Comparison of failure mechanisms between dry and moist conditions in fine material at $\delta/B = 53\%$



Lateral soil pressure alone is not sufficient to ensure the formation of a stable arch like that in Test 4MF-50 and therefore some additional shear strength in the soil was required. To support this statement, consider an element at the intrados of an air-filled cavity and an analysis of the stresses acting on it using the Mohr-Coulomb failure criterion as shown in Figure 4-53. Assuming vertical and horizontal stresses as principal stresses and assuming atmospheric pressure within the cavity, there are no possible stresses acting on the element from below. Therefore, $\sigma_3 = 0$ and consequently the cavity roof is not supported from below. Stability of the arch is due only to increased horizontal stresses (σ_1) in the soil. From inspection of Figure 4-53a, showing a family of Mohr circles that fit the criteria given above, it is evident that no possible stress state can exist entirely inside the failure envelope when no shear strength is present at zero normal stress (illustrated by the dashed circles). Thus, a purely frictional material is not capable of arching across a cavity roof. When a certain amount of shear strength at zero normal stress is assumed, as shown in Figure 4-53b, the stress state at the cavity roof becomes permissible (as indicated by the solid circles).

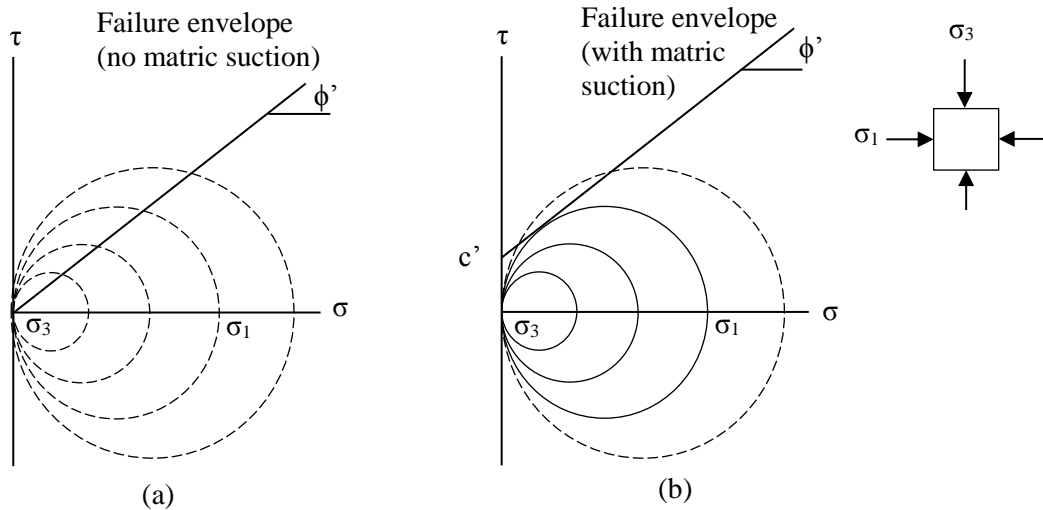


Figure 4-53: Mohr circle diagram of the strength of a cavity roof

Additional shear strength can be contributed by particle interlock, cementation and matric suction in the soil. Due to the arch forming in moist fine sand and not forming in dry sand with the same density and particle size, it can be deduced that moisture and matric suction was the largest contributor to the additional shear strength that supported the arch.

A comparison of normalized surface settlement between the two tests is shown in Figure 4-54. Settlement of the surface in moist sand was small compared to that of dry sand due to the stable arch that formed in the moist sand. Even though both tests demonstrated slow surface settlement when compared to coarse sand, the test in moist sand tended to settle slower still even though the two stable arches only formed later during the test.

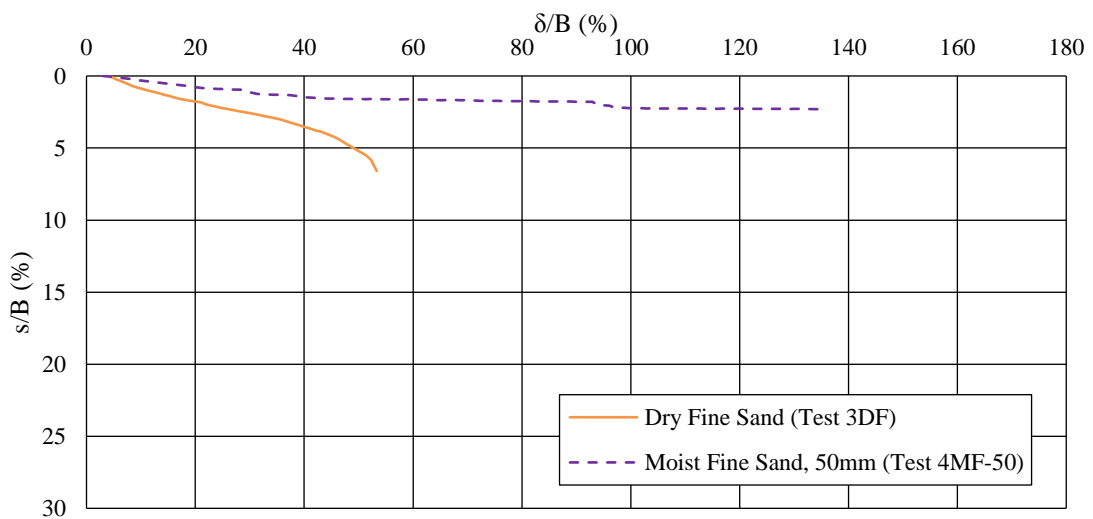
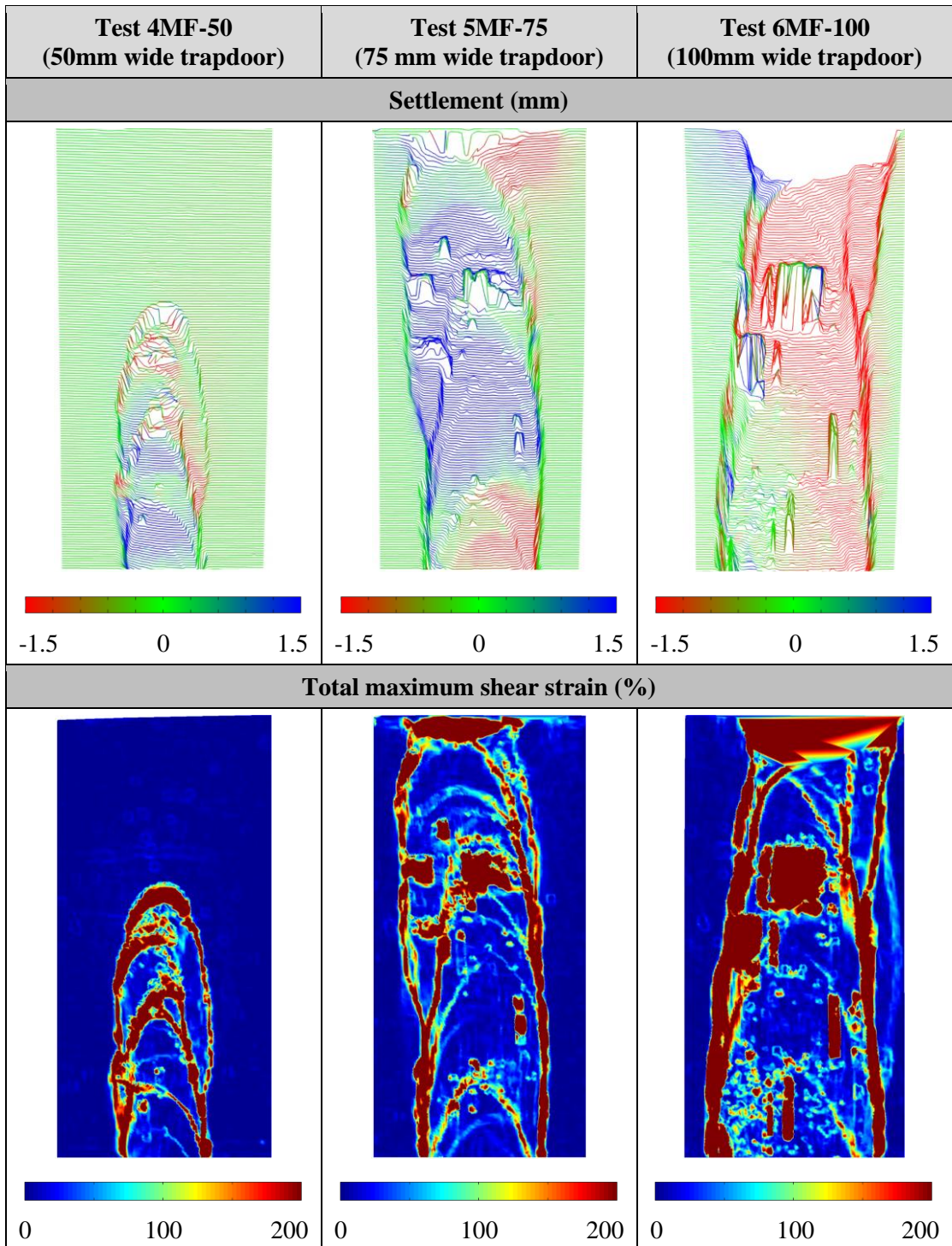


Figure 4-54: Comparison of normalized settlement between dry and moist conditions in fine material

4.4.3 Comparison Between Different Trapdoor Widths

To compare the effects of the trapdoor width on cavity propagation, a comparison of the failure mechanisms in Tests 4MF-50, 5MF-75 and Test 6MF-80 is shown in Table 4-20 at a δ/B ratio of 50% (the highest value for which strains could be calculated for Test 6MF-100).

Table 4-20: Comparison of failure mechanisms between tests with different trapdoor widths in moist fine material at $\delta/B = 50\%$



The effects of trapdoor widths on the failure mechanisms in moist fine material seemed minimal, only affecting the spacing of shear bands and the width of the zone of influence. In each case, the width of the zone of influence and the resulting sinkhole at the surface was roughly the same width as the trapdoor. The thickness, slope, and shape of shear bands appeared to be similar between the three tests, demonstrating that shear band formation and size are more dependent on soil properties and less on the geometry of the trapdoor test.

It is evident that the H/B ratio was the defining factor that gave the fine material sufficient shear strength to span a cavity for a prolonged period. As mentioned in Section 2.3.3.1, researchers agree that arching was possible in any soil with an H/B ratio greater than 2. According to this, Tests 4MF-50, 5MF-75 and 6MF-100, having H/B ratios of 5.8, 3.68 and 2.9 respectively, would all be able to develop an arch for a *short* period of time. Arching behaviour was observed in all of these tests, but these arches soon collapsed as the trapdoor receded, making way for new arches above them. The stable arch capable of supporting the overburden for a *longer* period formed only at an H/B ratio of 5.8 with all other parameters being equal.

Normalized surface settlement of the three tests are shown in Figure 4-55. It is immediately apparent that the surface settled faster above a wider trapdoor (Test 6MF-100) than above a narrower one (Test 5MF-75) as the zone of influence reached the surface faster in Test 6MF-100 than in Test 5MF-75. Even though Evans (1983) noted that the area of the surface depression does not equal the area of the soil displaced above the trapdoor due to dilation, an increase in trapdoor width increases the volume of the soil column that settles with the trapdoor. A wider trapdoor therefore increases the relative volume of the surface depression and therefore increases the surface settlement reading.

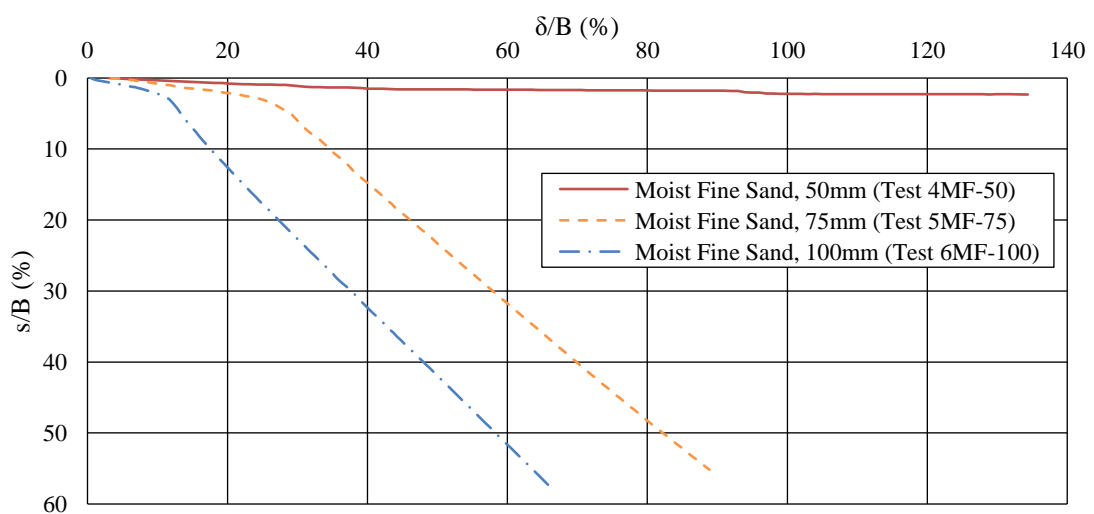


Figure 4-55: Comparison of normalized settlement between tests with different trapdoor widths in moist fine material

4.5 PROGRESSION OF FAILURE MECHANISMS

In all results presented up to this point, the general pattern of failure mechanisms as reported in literature (Costa et al, 2009; Dewoolkar et al., 2007; Evans, 1983) had been confirmed. A qualitative description of the transition between mechanisms as observed in most tests are presented in the next paragraphs.

Initially, several small shear bands formed from both corners of the trapdoor, stretching upwards and inwards towards the centre. These shear bands eventually became inactive and made way for two prominent shear bands that propagated diagonally upwards and joined up in the centre, forming a triangular-shaped mechanism as seen in Figure 4-56a. The zone of influence then continued to grow upwards with several similarly shaped mechanisms forming above it, but still retained a triangular shape as visible in Figure 4-56b.

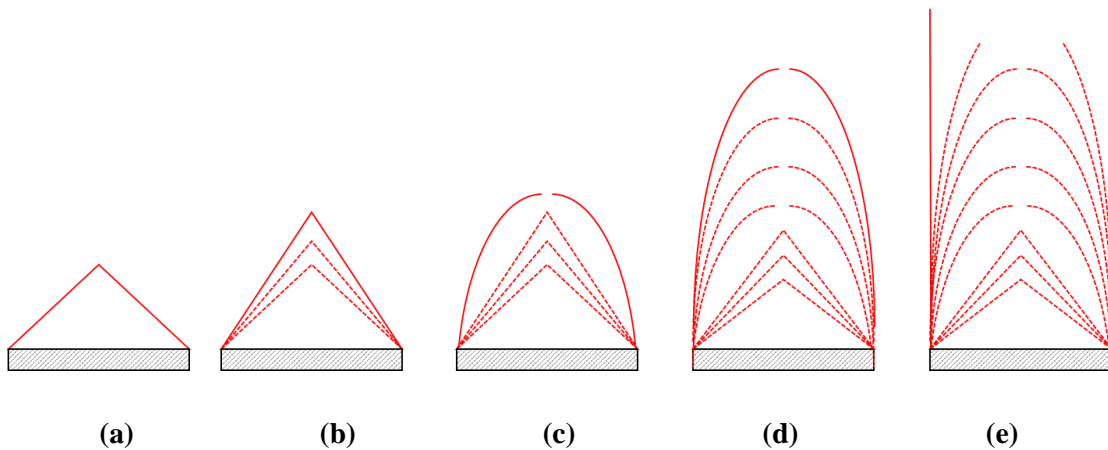


Figure 4-56: Summary of failure mechanisms as the sinkhole propagates to the surface

The mechanism eventually changed to a parabolic-shaped one as in Figure 4-56c, with two parabolic-shaped shear bands forming from both corners of the trapdoor and joining up in the centre, supporting the notion that shear bands formed at angles equal to the dilation angle (Stone, 1988; Costa, 2009; Dewoolkar, 2007). The zone of influence continued to grow upwards with new, similarly-shaped parabolic mechanisms forming above one another as seen in Figure 4-56d. As the zone of influence increased in height, the mechanisms became increasingly column-like with approximately parabolic-shaped “heads”.

Eventually, the zone of influence reached the surface at a location roughly above the trapdoor centreline. After this initial daylight event, the depression widened outwards with sand particles either sliding down from adjacent locations as in the case of dry soil, or breaking off in chunks

with shearing starting from the surface and progressing downwards, as in the case of moist soil. The depression widened to form a column-like zone of influence with failure continuing along the vertical sides and soil in the middle settling uniformly as the trapdoor retracted. This created the column-like mechanism shown in Figure 4-56e. This column-like mechanism continued up to the end of the test.

This transition between failure mechanisms – triangular to parabolic to column-like – are therefore in agreement with observations by Evans (1983), Dewoolkar (2007), Costa et al. (2009) and Da Silva (2014) but disagrees with the parabolic to triangular to column-like progression proposed by Iglesia et al. (2014).

4.6 DISCUSSION ON SURFACE SETTLEMENT

A comparison of normalized surface settlement between all 6 tests are seen in Figure 4-57. It is apparent that surface settlement started immediately at the onset of trapdoor settlement in all tests, confirming the fact that the slightest failure underground can trigger a detectable response at the surface.

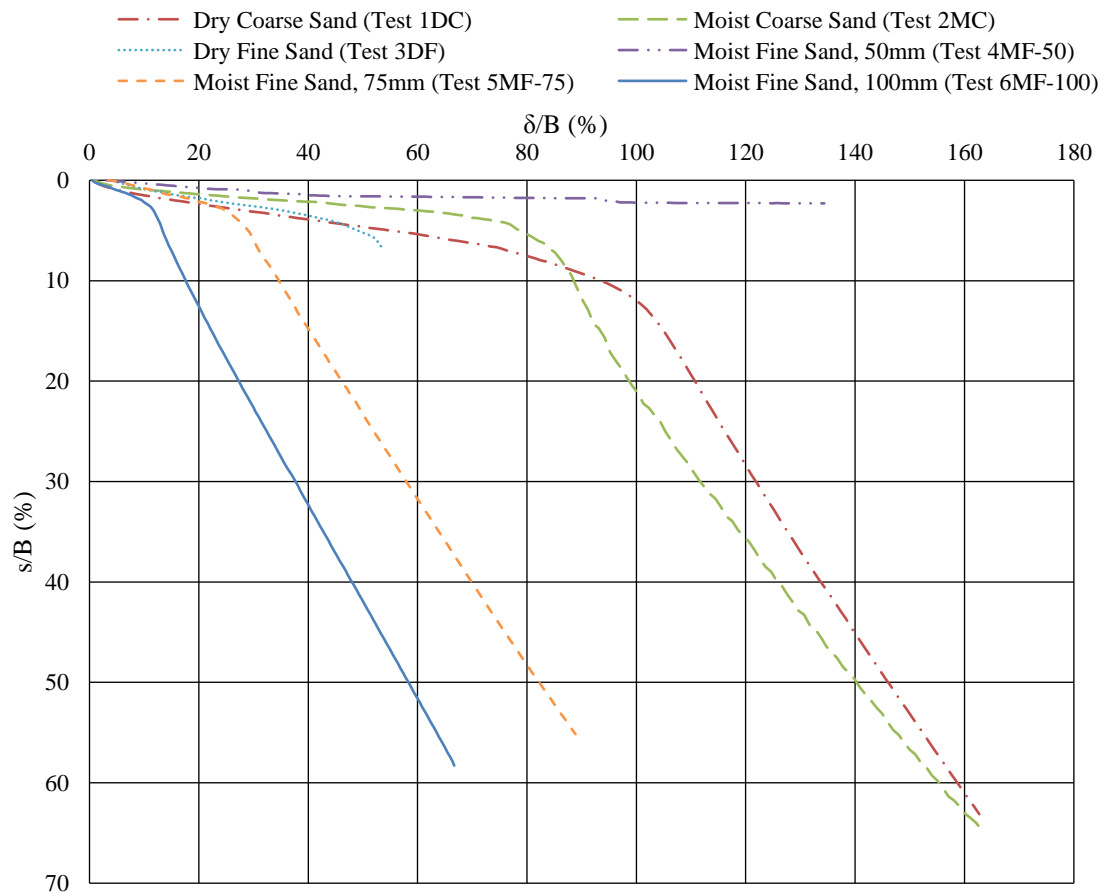


Figure 4-57: Comparison of normalized surface settlement across all tests

It is apparent that the zone of influence reached the surface at different times in each of the tests. Trapdoor width (or cavity size) seemed to have the most significant effect on this (when comparing Tests 6MF-100 and 5MF-75), with a larger trapdoor providing a shorter warning time between start of movement and the time at which the zone of influence reaches the surface. Particle size also had a significant effect on the speed of propagation of the zone of influence (comparing Tests 3DF and 1DC), with fine sand failing much faster than coarse sand. It is notable that the addition of moisture to both tests greatly decreased this effect (comparing Tests 4MF-50 with 2MC). Moisture content had little effect on the speed of propagation for the materials tested and rather reduced the amount of surface settlement when compared to similar tests in dry sand (comparing Tests 1DC and 2MC).

It has been observed in all tests that soil settled in the shape of a Gaussian curve until just before the zone of influence reached the surface. After that event, the shape of the depression became deeper in the centre and steeper along the sides, regardless of the δ/B ratio at which it occurred. Similar results were found by Costa et al. (2009).

4.7 IMPLICATIONS FOR ACTUAL SINKHOLES

Based on the discussions presented in this chapter, several of the results and conclusions can be applied to real-life sinkholes:

1. It is evident from the results seen above that cavities can be expected to propagate vertically upwards in the shape of a chimney rather than a funnel. This is in contrast with the method of scenario supposition (Buttrick & Van Schalkwyk, 1998) showing that a cavity propagates in a funnel shape, therefore having a much larger footprint at the soil surface.
2. The diameter of the actual surface depression might be wider than that of the cavity/shear zone depending on the size of the receptacle cavity and soil parameters. If the receptacle is large, a considerable amount of soil can be displaced from the “chimney” above the cavity, causing adjacent particles at the surface to roll down and widen the depression. However, if the soil has sufficient shear strength in the form of moisture or particle interlock, it will be able to support near-vertical walls as seen in Test 6MF-100 that would prevent further increase of the depression diameter. A smaller receptacle would also limit the amount of soil displaced and would therefore prevent the depression from widening.
3. Surface settlement was observed from the first movement of the trapdoor, indicating that any underground cavity collapse, however small in magnitude, will trigger an

immediate measurable response at the surface. Monitoring of ground levels in dolomitic areas with LIDAR drones, satellite interferometry, or by physical measurements could therefore aid in early discovery of underground cavities. All tests showed nearly identical surface settlement up to the point where the zone of influence reached the surface. Therefore, upon discovery of an underground cavity, it would be difficult to predict the time of daylighting without considering additional information such as soil parameters and cavity depth. Any surface settlement should be recognized as an immediate hazard.

5 CONCLUSIONS AND RECOMMENDATIONS

This chapter presents conclusions based on results of this study and previous studies, provides an outcome to the objectives of this study and gives recommendations for future work.

5.1 CONCLUSIONS

The conclusions from this study, arranged into the following categories, are presented: zone of influence propagation, surface settlement and failure mechanisms.

Zone of Influence Propagation

- Contrary to the funnel shape suggested in current South African building regulations for dolomitic regions, cavities propagated near-vertically upwards in a chimney-like shape. Large strains were confined by vertical shear bands extending approximately vertically upwards from the trapdoor/cavity edges. This was true in both fine and coarse material, in both dry and moist conditions.
- Cavity propagation tended to occur more rapidly in fine sand than in coarse sand, with the shear zone in fine sand reaching the surface in roughly half the amount of normalized trapdoor displacement recorded in its coarser counterpart, the latter having an average particle size 4.9 times greater than the former.
- Soil moisture content had an insignificant effect on the speed of cavity propagation when compared to the effects of particle size, except in the case of moist fine material where a stable arch hampered further propagation up to the end of the test.
- A stable arch formed in moist fine sand above a narrow trapdoor and was strong enough to support the weight of the overburden layer up to the end of the test. Moisture and matric suction appeared to be the largest contributors of cohesive shear strength that supported the arch. Limited arching behaviour was observed in other soil profiles as evidenced by shear bands in this study and load-displacement graphs in literature (McNulty, 1965; Ladanyi and Hoyaux, 1969; Dewoolkar, 2007; Iglesia et al., 2014), with the arch failing within moments of formation.

Surface Settlement

- Settlement at the surface was visible immediately after the onset of trapdoor settlement in all tested soil profiles.
- Although the zone of influence in fine sand reached the surface in roughly half the amount of trapdoor settlement recorded for coarse sand, initial settlement at the surface occurred at a near-identical rate for both soils, and only accelerated after the zone of influence had

reached the surface. This indicated more efficient arching in fine sand, with it being capable of supporting the overburden to a greater extent.

- Surface settlement appeared to follow a Gaussian distribution initially and deviated from this trend when the zone of influence reached the surface, with the centre of the trough becoming deeper so that the Gaussian curve was no longer accurate.
- Surface settlement occurred at a slow rate (5-15% of trapdoor settlement rate) until large strains (the zone of influence) reached the surface, after which the rate of settlement increased considerably to approximately 70-90% of trapdoor settlement rate.
- An increase in trapdoor size realized an increase in the volume of the surface depression due to a wider column of soil being displaced.

Failure Mechanisms

- Initially, shear bands developed from the edges of the trapdoor and joined up near the trapdoor centreline. Additional shear lines then developed from the edges of the trapdoor, each one reaching higher than the preceding one. Failure mechanisms transitioned from triangular to parabolic to vertical as recorded in literature (Evans, 1983; Dewoolkar et al., 2007; Costa et al, 2009; Da Silva, 2014).
- In all tested soil profiles, the shear bands on the outer edges of the shear zone converged just below the surface, piercing the surface at a single point before widening to the trapdoor width as the trapdoor receded. This produced a slight narrowing of the zone of influence in the overburden material as observed in literature by Abdulla and Goodings (1996) and also in real-life sinkholes.
- Dry material tended to produce shear bands that formed vertically upwards, alternating from left and right, before curving towards the centre and then ceasing. Moist material tended to produce more inclined shear bands in pairs that curve slightly inwards near the apex of the zone of influence, with each pair forming an isosceles triangle (this was more pronounced in coarse material than in fine material).
- Shear bands in coarse material tended to be much wider than in finer material as mentioned in literature. The paths of shear bands in fine material tended to be more complex and unpredictable than in coarse material due to the fact that the smaller particles in finer material travelled a shorter distance to shear past one another and reach the critical state, with the result that shear band formation happened easier in fine material.
- Trapdoor size tended to have little effect on the size and shape of failure mechanisms, only affecting the spacing of shear bands. However, an increase in trapdoor size resulted in a

faster propagation of the failure zone to the surface due to a larger column of soil above the trapdoor being displaced.

- A stable arch formed in moist fine sand above a narrow trapdoor at an H/B ratio of 5.8, but not in similar tests at smaller H/B ratios. Literature shows consensus that *limited* arching can only take place at an H/B ratio above 2, but a stable arch requires a larger H/B ratio and enough cohesive shear strength to support the overburden for a prolonged period of time.

5.2 RECOMMENDATIONS

Considering the initial hypothesis of this study, claiming that cavities propagate vertically in a chimney-like fashion rather than in a funnel shape, the following recommendations can be made regarding building regulations around actual sinkholes:

- Results from this study show that a cavity propagates vertically to the surface, pierces the surface at a single location, and then widens with soil falling into the chimney or sliding down from adjacent areas. The ultimate size of the resulting sinkhole depends on the amount of soil that can be drawn in from adjacent areas. A shallow cavity or one with a small receptacle will therefore result in a sinkhole diameter roughly equal to the diameter of the cavity. A deeper cavity or one with a large receptacle will be able to accept more adjacent material and therefore produce a wider sinkhole diameter. These considerations should be taken into account when estimating the risk of development on a particular region of dolomite land.
- As observed in this study, a cavity with a large diameter will propagate faster to the surface than one with a smaller diameter, thus providing a shorter warning time from the onset of surface settlement to the point where the zone of influence reaches the surface. Development regulations in the vicinity of larger cavities (on the order of 5m diameter and above) should thus be more stringent.
- A stable arch was observed in fine, moist sand, supporting the weight of the overburden material. It is, however, not recommended to regard an area with these conditions as more favourable for development due to long-term consequences that could result from the cavity as well as differential settlement that could take place.
- It was observed that soil at the surface settled immediately after the onset of trapdoor movement, indicating that a slight increase in the size of the cavity will trigger a response at the surface. This fact can be used to search for new undiscovered cavities or to track the progressive failure of known cavities.

Considering the recommendations above, the hypothesis is still in its infant stages and considerable additional research remains in order to fully understand the propagation of a cavity in reality. Further research should investigate the following aspects:

- The response of a less homogenous material containing more angular particles should be investigated, such as chert and wad typically found in a residual dolomite soil profile prone to sinkholes.
- The response of material at various relative densities should be investigated. Preliminary tests performed alongside the current study showed a widening of the zone of influence in loose material.
- The response of a multi-layered profile should be investigated, such as is more typical in a natural situation.
- The influence of the overburden depth should be investigated.
- It is recommended that additional measurements be taken of the model during testing, including the load on the trapdoor, horizontal and vertical forces in the soil directly above the trapdoor and in-situ measurements of moisture content using buried probes.
- Future models should be constructed such that the trapdoor has a greater range of movement (effectively increasing the size of the receptacle), to ensure that the zone of influence can propagate entirely without being limited by the range of the trapdoor.

6 REFERENCES

- Abdulla, W.A. & Goodings, D.J. 1996. Modeling of Sinkholes in Weakly Cemented Sand. *Journal of Geotechnical Engineering* 1-4.
- Adrian, R.J. 1991. Particle imaging techniques for experimental fluid mechanics. In *Annual review of fluid mechanics.*, 1991.
- Archer, A. 2014. *Using small-strain stiffness to predict the settlement of shallow foundations on sand*. Unpublished M.Eng Thesis. Pretoria: University of Pretoria.
- Attewell, P. 1977. Ground movements caused by tunnelling in soil. In *Proceedings, Large Ground Movements and Structures*. New York, 1977. Institute of Science and Technology, University of Wales.
- Augarde, C.E., Lyamin, A.V. & Sloan, S.W. 2003. Prediction of Undrained Sinkhole Collapse. *Journal of Geotechnical and Geoenvironmental Engineering* 129(3): pp. 197-205.
- Bjerrum, L., Frimann Clausen, C.J. & Duncan, J.M. 1972. Earth pressures on flexible structures - A state-of-the-art report. In *Proceedings, Fifth European Conference on Soil Mechanics and Foundation Engineering*. Madrid, Spain, 1972.
- Bolton, M.D. 1986. The strength and dilatancy of sands. *Geotechnique* 36(1): 65-78.
- Buttrick, D. & Van Schalkwyk, A. 1995. The method of scenario supposition for stability evaluation of sites on dolomitic land in South Africa. *Journal of South African Institute of Civil Engineering* Fourth Quarter: 9-14.
- Buttrick, D. & Van Schalkwyk, A. 1998. Hazard and risk assessment for sinkhole formation on dolomite land in South Africa. *Environmental Geology* 36(1-2): 170-78.
- Chevalier, B., Combe, G. & Villard, P. 2009. Experimental and numerical study of response of granular layer in the trap-door problem. In *Powders and Grains 2009: Proceedings of the 6th International Conference on the Micromechanics of Granular Media*. Melville, NY, 2009. American Institute of Physics.
- Costa, Y.D., Zornberg, J.G., Bueno, B.S. & Costa, C.L. 2009. Failure mechanisms in sand over a deep active trapdoor. *Journal of Geotechnical and Geoenvironmental Engineering* 135(11): 1741-53.

- da Silva, T. 2014. *Centrifuge modelling of the behaviour of geosynthetic-reinforced soil over voids*. Unpublished PhD Thesis. Cambridge, UK: Trinity College, University of Cambridge.
- Davis, R.E. & Bacher, A.E. 1968. California's culvert research program - Description, current status, and observed peripheral pressures. *Highway Research Record* 249: 14-23.
- Dewoolkar, M.M., Santichaiant, K. & Ko, H.Y. 2007. Centrifuge modeling of granular soil response over active circular trapdoors. *Soils and Foundations* 47(5): 931-45.
- Drumm, E.C., Akturk, O., Akgun, H. & Tutluoglu, L. 2009. Stability Charts for the Collapse of Residual Soil in Karst. *Journal of Geotechnical and Geoenvironmental Engineering* 135(7): 925-31.
- Evans, C.H. 1983. *An examination of arching in granular soils*. Unpublished M.S Thesis. Cambridge, MA: MIT.
- Gaudin, C., White, D.J., Boylan, N. & Breen, J. 2010. Development of a miniature high speed wireless data acquisition system for geotechnical centrifuges. In *7th International Conference on Physical Modelling in Geotechnics (ICPMG)*. Zurich, 2010.
- Harris, G.W. 1974. A sandbox model used to examine the stress distribution around a simulated longwall coal-face. *International Journal of Rock Mechanics, Mining Sciences and Geomechanical Abstracts* 11: 325-35.
- Hyatt, J.A. & Jacobs, P.M. 1996. Distribution and morphology of sinkholes triggered by flooding following Tropical storm Alberto at Albany, Georgia, USA. *Geomorphology* 17: 305-16.
- Iglesia, G.R. 1991. *Trapdoor experiments on the centrifuge: A study of arching in geomaterials and similitude in geotechnical models*. Unpublished PhD Thesis. Cambridge, MA: MIT.
- Iglesia, G.R., Einstein, H.H. & Whitman, R.V. 2011. Validation of centrifuge model scaling for soil systems via trapdoor tests. *Journal of Geotechnical and Geoenvironmental Engineering* 137(11): 1075-89.
- Iglesia, G.R., Einstein, H.H. & Whitman, R.V. 2014. Investigation of soil arching with centrifuge tests. *Journal of Geotechnical and Geoenvironmental Engineering* 140(2).
- Jacobsz, S.W. 2014. Research on dolomitic sinkhole development at the University of Pretoria. In *Proceedings of Dolomite Seminar 2014*. Pretoria, 2014. Proceedings of the Dolomite Seminar 2014, University of Pretoria.

- Jacobsz, S., Kearsley, E. & Kock, J. 2014. The Geotechnical Centrifuge Facility at the University of Pretoria. In *Proceedings of the 8th International Conference on Physical Modelling in Geotechnics*, Perth, 2014. CRC Press.
- Jennings, J.E., Brink, A.B., Louw, A. & Gowan, G.D. 1965. *Sinkholes and subsidence in the Transvaal dolomites of South Africa*.
- King, H. 2017. *Geology.com*. [Online] Available at: <http://geology.com/minerals/dolomite.shtml> [Accessed 28 September 2017].
- Knappett, J.A. & Craig, R.F. 2012. *Craig's Soil Mechanics*. 8th ed. New York: Spon Press.
- Ladanyi, B. & Hoyaux, B. 1969. A Study of the Trap-Door Problem in a Granular Mass. *Canadian Geotechnical Journal* 6(1): 1-15.
- Marston, A. 1930. The theory of external loads on closed conduits in the light of the latest experiments. In *Bulletin 96*. Ames, Iowa, 1930. Iowa Engineering Experiment Station.
- McNulty, J.W. 1965. *An experimental study of arching in sand*. Unpublished PhD Thesis. Champaign, IL: University of Illinois.
- Nel, D.T. & Haarhoff, J. 2011. The failure probability of welded steel pipelines in dolomitic areas. *Journal of South African Institution of Civil Engineering* 53(1): 9-21.
- Peck, R.B. 1969. Deep Excavations and Tunneling in Soft Ground. State of the Art Report. In *Proceedings of the 7th International Conference on Soil Mechanics and Foundations Engineering*. Mexico City, 1969.
- Pilecki, Z. & Baranowski, A. 2006. *Estimation of dimensions of a rectangular type sinkhole activated by abandoned shafts*. Report M-29 (395). Warsaw: Institute of Geophysics of the Polish Academy of Sciences.
- Richardson, S. 2013. *Sinkhole and Subsidence Record in the Chuniespoort Group Dolomite, Gauteng, South Africa*. MSc Thesis. Pretoria: University of Pretoria.
- Roscoe, K.H. 1970. The influence of strains in soil mechanics. *Geotechnique* 20(2): 129-70.
- SABS 2012. *SANS 1936 Development of Dolomite Land*. Pretoria: SABS Standards Division.
- Santichaianant, K. 2002. *Centrifuge modeling and analysis of active trapdoor in sand*. Unpublished PhD Thesis. Boulder, CO: University of Colorado at Boulder.

- Sloan, S.W., Assadi, A. & Purushothaman, N. 1990. Undrained stability of a trapdoor. *Geotechnique* 40(1): 45-62.
- Stone, J.K. 1988. *Modelling of rupture development in soils*. Unpublished PhD Thesis. Cambridge, UK: Wolfson College, University of Cambridge.
- Stone, J.K. & Muir Wood, D. 1992. Effects of dilatancy and particle size observed in model tests on sand. *Soils and Foundations* 32(4): 43-57.
- Tanaka, T. & Sakai, T. 1993. Progressive failure and scale effect of trap-door problems with granular materials. *Soils and Foundations* 33(1): 11-22.
- Taylor, R. 1995. Centrifuges in modelling: principles and scale effects. In *Geotechnical centrifuge technology*, 1995. Blackie Academic & Professional.
- Terzaghi, K. 1936. Stress distribution in dry and saturated sand above a yielding trap-door. In *Proceedings of the First International Conference on Soil Mechanics and Foundation Engineering*. Cambridge, MA, 1936. Graduate School of Engineering, Harvard University.
- Terzaghi, K. 1943. *Theoretical soil mechanics*. New York: Wiley.
- Tien, H. 1990. *A Literature Study of the Arching Effect*. Unpublished M.Eng Thesis. Cambridge, MA: MIT.
- Trollip, N. 2006. *The Geology of an Area South of Pretoria with Specific Reference to Dolomite Stability*. Unpublished M.Sc Thesis. Pretoria: University of Pretoria.
- Van Schalkwyk, A. 1981. Ontwikkelingspatroon en Risiko-Evaluasie in Dolomietgebiede. In *Proceedings of the Seminar on the engineering geology of dolomitic areas*. Pretoria, 1981. University of Pretoria.
- Vardoulakis, I., Graf, B. & Gudehus, G. 1981. Trap-door problem with dry sand: A statistical approach based upon model kinematics. *International Journal for Numerical and Analytical Methods in Geomechanics* 5: 57-78.
- Wagener, F. 1984. *Engineering Construction on Dolomite*. Johannesburg: Geotechnical Division of the South African Institution of Civil Engineers.
- White, D.J. & Take, W.A. 2002. *Particle Image Velocimetry (PIV) software for use in geotechnical testing*. Technical Report. Cambridge, UK: Cambridge University Engineering Department.

White, D.J., Take, W.A. & Bolton, M.D. 2003. Soil deformation measurement using particle image velocimetry (PIV) and photogrammetry. *Geotechnique* 53(7): 619-31.